



The  
University  
Of  
Sheffield.

**Diode Area Melting of Ti6Al4V:  
Probing the Multi-laser Interaction  
and Residual Stress Evolution**

**By:**

Sarath Alayil Veetil

The University of Sheffield  
Faculty of Engineering  
Department of Electronics & Electrical Engineering

January 2024

## Abstract

Developed at the University of Sheffield, Diode Area Melting (DAM) represents a novel development in Laser Powder Bed Fusion (L-PBF) technologies. This method diverges from traditional mirror galvanometer-controlled laser techniques by employing an array of low-powered diode lasers, each with a power output of less than 5 watts. In contrast to traditional L-PBF, which employs high-powered fibre lasers with outputs exceeding 100 watts at speeds ranging from 300 to 3000 mm/s, DAM operates these diode lasers at significantly reduced speeds of 1 to 10 mm/s.

The essence of this research involves exploring the interactions between multiple diode lasers and powder materials within the DAM process. It focuses on forming single tracks and two-dimensional layers, crucial for constructing three-dimensional final parts. The study investigates how the quantity of lasers affects the melt pool size and cooling rates, utilising multiple lasers arranged in a linear array. In the modelling phase, the study utilises up to six lasers arranged in a linear array and employs Finite Element Method (FEM) simulations, analytical approaches, and thermal camera measurements to analyse the intricate dynamics of the multiple laser-powder interactions within the DAM process.

In the processing of Ti6Al4V, the experimental findings shows that a single laser achieves a cooling rate of 778 K/s, which decreases to 191 K/s when employing six lasers, closely resembling the slower cooling rates observed in some casting processes. Furthermore, a single layer of Ti6Al4V processed using DAM demonstrates lower residual stresses, with a reduction in stress noted as the number of lasers is increased and the scanning speed is decreased. Microstructural analysis indicates the presence of both  $\alpha + \beta$  crystal structures, with variations mainly influenced by scanning speed. These enhancements, along with the ability of DAM to process larger areas through the use of multiple lasers, potentially improve both efficiency and throughput, marking an important shift from conventional L-PBF methods. Consequently, leading to important benefits for large-scale production with enhanced part quality and reduced need for post-processing.

## Acknowledgements

I extend heartfelt appreciation to Dr. Kristian Groom, my principal academic supervisor, and Professor Kamran Mumtaz, my secondary supervisor, for dedicated support and invaluable guidance throughout this project. The expertise and insights from both have been pivotal in shaping my research. Constant encouragement from these mentors has been a source of motivation. I am profoundly grateful for the significant role each has played in my academic journey.

Additionally, I extend my sincere gratitude to my industrial supervisors, Matt Thomas, David Wimpenny, and Nick Cruchley, at the Manufacturing Technology Centre (MTC). Their support and contributions have been influential throughout my journey. A heartfelt thanks goes to the Engineering and Physical Sciences Research Council (EPSRC) for funding my research. The financial support has been crucial; without it, none of this work would have been possible. Their commitment to advancing science and engineering has not only enabled me to pursue my research but has also significantly contributed to the broader field of study.

The 2019/2020 academic year was profoundly disrupted by the Covid-19 pandemic, which significantly hampered my research progress. The enforced interruption from university access for several months presented considerable challenges, markedly delaying the advancement of my studies and research activities. In these challenging times, particularly, Dr. Kristian Groom support were instrumental in steering me in the right direction amidst the uncertainties and constraints imposed by the pandemic.

Lastly, and most importantly, my deepest gratitude goes to my wife, Savina Sarath, and daughter, Sriya Sarath, who have provided unwavering support and patience throughout this and every journey. Their love and encouragement have been the bedrock of my resilience and perseverance. Equally, I extend my heartfelt thanks to my parents, whose constant support and encouragement have been a guiding force in all my endeavours.

# Contents

<b>Abstract</b> .....	<b><i>i</i></b>
<b>Acknowledgements</b> .....	<b><i>ii</i></b>
<b>Contents</b> .....	<b><i>iii</i></b>
<b>List of Figures</b> .....	<b><i>ix</i></b>
<b>List of Tables</b> .....	<b><i>xx</i></b>
<b>List of Abbreviations</b> .....	<b><i>xxii</i></b>
<b>List of Symbols</b> .....	<b><i>xxiv</i></b>
<b>1 Chapter 1: Introduction</b> .....	<b>1</b>
<b>1.1 Novelty Statement</b> .....	<b>2</b>
<b>1.2 Thesis Overview and Structure</b> .....	<b>4</b>
Chapter 2 .....	4
Chapter 3: .....	4
Chapter 4: .....	4
Chapter 5: .....	5
Chapter 6: .....	5
Chapter 7: .....	5
<b>2 Chapter 2: Literature Review</b> .....	<b>7</b>
<b>2.1 Additive Manufacturing (AM)</b> .....	<b>7</b>
<b>2.2 Powder Bed Fusion (PBF) Process</b> .....	<b>9</b>
2.2.1 Laser Powder Bed Fusion (L-PBF) .....	10
2.2.2 Challenges in L-PBF .....	12
2.2.3 Lasers in L-PBF .....	15

<b>2.3</b>	<b>Enhancing L-PBF with Diode Laser Technology .....</b>	<b>17</b>
2.3.1	The Diode Area Melting (DAM).....	19
2.3.2	Use of fibre-coupled lasers in DAM:.....	21
2.3.3	Area Melting with Multi-Laser Array.....	22
<b>2.4</b>	<b>Diode Lasers (DLs) .....</b>	<b>23</b>
2.4.1	Gaussian Beam ( $TEM_{00}$ ) .....	25
<b>2.5</b>	<b>Physical Phenomena in L-PBF .....</b>	<b>26</b>
2.5.1	Laser Absorptivity.....	27
2.5.2	Laser Power Density .....	29
2.5.3	Heat and Mass Transfer.....	30
2.5.4	Melt Pool Dynamics.....	31
2.5.5	An Insight into Melt Pool and Single-Track Formation .....	33
<b>2.6</b>	<b>Modelling Approaches in L-PBF.....</b>	<b>36</b>
2.6.1	Finite Element Method (FEM).....	39
2.6.2	Volume of Fluid (VoF) Method.....	40
<b>2.7</b>	<b>Surface Roughness .....</b>	<b>43</b>
<b>2.8</b>	<b>Residual Stress.....</b>	<b>43</b>
2.8.1	Characteristics and Origins of Residual Stresses.....	44
2.8.2	Characterising Residual Stresses in L-PBF.....	45
2.8.3	L-PBF Process Parameters and their Effects .....	47
2.8.4	Residual Stress Measurements .....	48
<b>2.9</b>	<b>X-Ray Diffraction of Ti6Al4V .....</b>	<b>52</b>
<b>2.10</b>	<b>Thermography .....</b>	<b>53</b>
<b>2.11</b>	<b>Ti6Al4V .....</b>	<b>55</b>
2.11.1	AM of Ti6Al4V.....	56
2.11.2	Microstructure and Cooling Rate in PBF of Ti6Al4V .....	57

2.12	Conclusions.....	59
2.13	Research Aims and Objective.....	60
<b>3</b>	<b><i>Chapter 3: Experimental Methodology</i></b> .....	<b>62</b>
<b>3.1</b>	<b>DAM System</b> .....	<b>62</b>
3.1.1	Initial Setup .....	63
3.1.2	Build Chamber .....	64
3.1.3	Laser Fibre Array .....	66
3.1.4	Diode Laser.....	68
3.1.5	CTP Laser Head.....	69
3.1.6	Modifications to the DAM Rig.....	70
<b>3.2</b>	<b>A Typical DAM Process Workflow</b> .....	<b>73</b>
<b>3.3</b>	<b>Beam Profiling</b> .....	<b>73</b>
<b>3.4</b>	<b>Optimisation of Parameters</b> .....	<b>75</b>
<b>3.5</b>	<b>In Situ Temperature Measurement</b> .....	<b>75</b>
3.5.1	Thermal Camera Setup .....	76
3.5.2	Thermographic Data .....	77
<b>3.6</b>	<b>Material Properties</b> .....	<b>79</b>
3.6.1	Titanium Alloy Powder .....	79
3.6.2	Absorptivity Measurement for Ti6Al4V.....	80
<b>3.7</b>	<b>Thermophysical Properties</b> .....	<b>81</b>
3.7.1	Analytical: Thermophysical Properties.....	81
3.7.2	FEM and VoF: Thermophysical Properties.....	81
<b>3.8</b>	<b>Characterisation</b> .....	<b>83</b>
3.8.1	Sample Preparation .....	83
3.8.2	Optical Microscope.....	84
3.8.3	Scanning Electron Microscope (SEM).....	84

3.8.4	Surface Roughness .....	85
3.8.5	X-Ray Diffraction (Phase) Analysis.....	85
3.8.6	Residual Stress Measurement by XRD.....	85
3.8.7	EBSD.....	88
<b>3.9</b>	<b>Conclusions.....</b>	<b>88</b>
<b>4</b>	<b><i>Chapter 4: Modelling Methodology.....</i></b>	<b>89</b>
4.1.1	Selected Literature for Model Validation .....	89
<b>4.2</b>	<b>Analytical Modelling Methodology .....</b>	<b>92</b>
4.2.1	Initial Conditions .....	92
4.2.2	Heat Source.....	92
4.2.3	Validation of Thermal Modelling .....	94
<b>4.3</b>	<b>FEM Methodology.....</b>	<b>98</b>
4.3.1	Initial Conditions .....	98
4.3.2	Heat Source.....	99
4.3.3	Validation of Thermal Modelling .....	100
<b>4.4</b>	<b>VoF Methodology.....</b>	<b>105</b>
4.4.1	DEM Simulation of Powder Bed Structure .....	105
4.4.2	Heat Source and Numerical Model .....	106
4.4.3	Nature of Results.....	108
4.4.4	Validation of Thermal Modelling .....	109
<b>4.5</b>	<b>Discussions .....</b>	<b>112</b>
<b>4.6</b>	<b>Conclusions.....</b>	<b>115</b>
<b>5</b>	<b><i>Chapter 5: Modelling of Ti6Al4V during DAM .....</i></b>	<b>118</b>
<b>5.1</b>	<b>Modelling approaches.....</b>	<b>118</b>
5.1.1	Analytical Model.....	118
5.1.2	FEM Model.....	119

<b>5.2</b>	<b>Experimental Methodology .....</b>	<b>120</b>
5.2.1	DAM Beam Profiles.....	120
5.2.2	Layer Thickness and Single Tracks.....	120
<b>5.3</b>	<b>Results and Discussion .....</b>	<b>122</b>
5.3.1	Melt Pool Surface Temperature.....	122
5.3.2	Melt Pool Width .....	128
5.3.3	Melt Pool Depth .....	130
5.3.4	Cooling Rate and Solidification Behaviour.....	134
<b>5.4</b>	<b>Conclusions.....</b>	<b>142</b>
<b>6</b>	<b><i>Chapter 6: Residual Stress in DAM of Ti6Al4V .....</i></b>	<b><i>144</i></b>
<b>6.1</b>	<b>Introduction.....</b>	<b>144</b>
6.1.1	DAM Characteristics .....	144
6.1.2	Scope of This Work.....	145
<b>6.2</b>	<b>Residual Stress in L-PBF of Ti6Al4V.....</b>	<b>145</b>
<b>6.3</b>	<b>Experimental Methodology .....</b>	<b>148</b>
6.3.1	DAM Samples .....	148
6.3.2	Thermal Model.....	150
6.3.3	Peak Analysis Using XRD .....	150
6.3.4	Residual Stress Through XRD .....	151
<b>6.4</b>	<b>Results.....</b>	<b>156</b>
6.4.1	Single Line Scanning .....	156
6.4.2	Surface Roughness in DAM.....	159
6.4.3	Melt Pool Temperature Predicted by FE Models.....	161
6.4.4	Cooling Rates Predicted by FE Models .....	161
6.4.5	XRD Analysis.....	163
6.4.6	Residual Stress.....	167
6.4.7	Microstructure Characteristics During DAM of Ti6Al4V.....	170



6.5	Discussions .....	178
6.6	Conclusions.....	181
<b>7</b>	<b><i>Chapter 7: Conclusions and Future Work .....</i></b>	<b><i>183</i></b>
7.1	Conclusions.....	183
7.2	Key Findings and Recommended Future Work .....	184
7.3	Summary .....	186
	<b><i>References .....</i></b>	<b><i>188</i></b>
	<b><i>Appendix A: ANSYS ADPL Code.....</i></b>	<b><i>201</i></b>
	<b><i>Appendix B: Ti6Al4V Powder Data .....</i></b>	<b><i>202</i></b>
	<b><i>Appendix C: COSHH assessment form for Ti6Al4V.....</i></b>	<b><i>203</i></b>

## List of Figures

Figure 1.1: Methodology flow of the current research.....	6
Figure 2.1: A schematic diagram of the L-PBF Process [14].....	11
Figure 2.2: Depicting key 'Process Variables' influencing the outcome of an L-PBF process.....	12
Figure 2.3: Schematic illustrating the foundational Diode Area Melting concept, depicting individually adjustable emitters within a mobile diode laser bar, selectively activated/deactivated to define shapes across the powder bed [26]. .....	19
Figure 2.4: A typical scanning path used in the DAM process [26]......	20
Figure 2.5: System layout of multi-laser array-based AM developed at GE global research [29]......	23
Figure 2.6: An example of a simple diode laser (a). Schematic of necessary parts required for the operation of a DL (b). Spatial characteristics of laser elements (c) and an illustration of a typical Current vs Power curve for a DL (d) [31]. ....	24
Figure 2.7: Illustrates laser beam spatial profile at different locations (a), power density distribution of a fibre laser with a focal spot diameter of 80 $\mu\text{m}$ (b), and a Gaussian beam diameter definition (c) [1]. ....	26
Figure 2.8: Illustrates the absorption of Ti6Al4V, AlSi12 and Cu within the wavelength ranges between 400 to 1100nm [38]. ....	28
Figure 2.9: Illustrates the difference of varying power density resulting in the workpiece [39]......	29
Figure 2.10: Illustrating Marangoni convection driven by the surface tension gradient [22]......	32
Figure 2.11: A typical cross section of a melt track formed during L-PBF [50].	34

Figure 2.12: The figure shows a sequence of composite schlieren images captured at the specified times following the initial exposure of the powder to the laser during a single-track scan [51].	35
Figure 2.13: Figure displaying five tracks deposited at the same energy density, with increasing laser power and scan speed from top to bottom [52].	35
Figure 2.14: An AM process optimisation model adapted from Ref [53].	36
Figure 2.15: This figure illustrates the transformation of 316L stainless steel powder particles as they undergo state transitions and topological changes while a laser heat source moves across the domain. The magenta line in the sub-figures marks the boundary between solid and fluid regions, while the white lines indicate the separation between metallic and shielding gas phases [57].	38
Figure 2.16: A representation of various mathematical models, including the Gaussian beam, as employed in a typical mesoscopic simulation using the Volume of Fluid (VoF) method.	41
Figure 2.17: Process window for L-PBF [85].	43
Figure 2.18: Illustrating residual stress categorised according to the length scale [1].	44
Figure 2.19: Illustrating the mechanisms of residual stress formation in PBF [87].	46
Figure 2.20: Definition of parameters used in X-ray measurements [93].	50
Figure 2.21: An example illustrating a pole figure (a) and the diffraction vector of an X-ray irradiation of the $\sin^2\psi$ method corresponding to ( $\varphi = 0$ and $\psi = 45^\circ$ ) [93].	51
Figure 2.22: X-Ray diffraction pattern for Ti6Al4V alloy obtained in the L-PBF (a), EB-PBF(b) and heat-treated and annealed sheet (c) [94].	53
Figure 2.23: Titanium $\alpha$ (left) and $\beta$ (right) crystal structure [97].	55

Figure 2.24: Illustration of a typical Ti6Al4V $\alpha + \beta$ Basket-weave microstructure [97].	56
Figure 2.25: Figure illustrating the variations in microstructure, tensile strength, and elongation of Ti-6Al-4V fabricated through different Additive Manufacturing (AM) methodologies [14].	57
Figure 3.1: Schematic of DAM.	62
Figure 3.2: The DAM 2 equipment used for this research.	63
Figure 3.3: Illustration of the build chamber in the DAM setup.	65
Figure 3.4: Build chamber showing the build area and the knife edge arrangement for a continuous gas flow.	65
Figure 3.5: Illustrating the fabrication of Inconel 718 within the DAM system.	66
Figure 3.6: Arrangement of the fibre array utilising 50 X 2 fibres: Fibre cables in the array (a), the adaptor which connects to the CTP head (b), and the schematic of the fibre array assembly unit; all dimensions in mm otherwise specified (c).	67
Figure 3.7: Illustrating the dimensions (in mm) of the diode laser top view (a) and side view (b).	68
Figure 3.8: The P/I curve of the DL measured using Thorlabs PM400 power meter.	69
Figure 3.9: The CTP laser head assembly with a beam profiler attached at one end.	70
Figure 3.10: The cooling system with the temperature controller (a) and the heat sink housing 6 diode lasers (b).	71
Figure 3.11: Illustrating the cooling arrangement with the help of TEC.	71
Figure 3.12: The diode laser drive unit consisting of nine DPS3005 modules.	72

Figure 3.13: The diagram illustrating the configuration for beam profile measurement using a NanoScan2sPryo/9/5 scanning slit beam profiler.....	74
Figure 3.14: Data illustrating the beam profile when two adjusant lasers within a single row are activated. ....	74
Figure 3.15: Representation of the multi-laser arrangement configuration, with (a) displaying six lasers in a single row, and (b) showcasing up to ten lasers arranged in two rows. All dimensions given in this illustration are in mm.....	75
Figure 3.16: Hamamatsu C13440 camera, filter and lens assembly used in the experiments.....	76
Figure 3.17: Radiance calibration curve and uncertainty of measured temperature showing the digital level from 0 – 16000. The blue dot represents the blackbody temperature mapped over the calibrated temperature, plotted in black colour. ....	77
Figure 3.18: An example of an image from the thermal camera, Hamamatsu c11440 captured whilst processing the beam profile with four lasers.....	78
Figure 3.19: Illustrating the Hamamatsu C13440 camera set up employed for in-situ spatter investigation. ....	79
Figure 3.20: particle size distribution of Ti6Al4V powder (a) and powder morphology (b).....	80
Figure 3.22: PANalytical XPert3 Powder machine used for residual stress studies. ....	86
Figure 4.1: The width of the molten pool versus scanning speed.....	91
Figure 4.2: The depth of the molten pool versus scanning speed.....	91
Figure 4.3: Analytical results showing the temperature colour map for 20 W laser power at 300 mm/s scanning speed. ....	94

Figure 4.4: Ref-[110] and Analytical model predicted melt pool width comparison.....	96
Figure 4.5: Analytical results showing the cooling rate in the form of a colour map for 20 W laser power at 300 mm/s scanning speed.....	97
Figure 4.6: The cooling rate derived for the analytical calculations for the 20, 30 and 50 W laser power at 100, 200 and 300 mm/s scanning speed. ....	98
Figure 4.7: Computational domain used for the ANSYS simulation.....	99
Figure 4.8: ANSYS simulated result of a melt pool with 20 W laser power and 300 mm/s scanning speed.....	100
Figure 4.9: Ref-[110] and ANSYS model predicted melt pool width comparison. ....	101
Figure 4.10: ANSYS simulated result of a melt pool depth with 20 W laser power and 300 mm/s scanning speed.....	101
Figure 4.11: Ref-[110] and ANSYS model predicted melt pool depth comparison. ....	102
Figure 4.12: The temperature-time data from the ANSYS simulation for the laser power 20, 30 and 50 W at a scanning speed of 300 mm/s. ....	103
Figure 4.13: The ANSYS predicted cooling time from $\beta$ -transus temperature (1267 K) to martensitic transformation temperature (847 K).....	104
Figure 4.14: The cooling rate derived for ANSYS simulations for the 20, 30 and 50 W laser power at 100, 200 and 300 mm/s scanning speed.....	104
Figure 4.15: Key process steps involved in a Flow 3D simulation.....	105
Figure 4.16: Packing density in a powder layer with 50 $\mu\text{m}$ thickness.....	106
Figure 4.17: Melt pool formation during VoF simulation of Ti6Al4V with a single laser at 100 W laser power and 1000 mm/s scanning speed.....	108

Figure 4.18: The cross-section of a melt track showing the liquid melt pool and solid region in a Flow 3D simulation with a single laser at 100 W laser power and 1000 mm/s scanning speed. ....	109
Figure 4.19: Ref-[110] and Flow 3D model predicted melt pool width comparison. ....	110
Figure 4.20: Ref-[110] and Flow 3D model predicted melt pool width comparison. ....	111
Figure 4.21: Temperature evolution during a Flow 3D simulation with 20W laser power at 300 mm/s scanning speed. ....	111
Figure 4.22: The cooling rate derived for Flow 3D simulations for the 20, 30 and 50 W laser power at 100, 200 and 300 mm/s scanning speed. ....	112
Figure 4.23: Time taken to complete ANSYS simulations. ....	113
Figure 4.24: Simulation time each model for Flow 3D for a fixed duration of 0.002s. ....	114
Figure 5.1: Illustrates the computational domain used for FEM simulation in ANSYS showing six laser beams. ....	119
Figure 5.2: An example of melt tracks created for this work. Each melt track is 5 cm long, has 120 $\mu\text{m}$ hatch spacing, and produces a total area of 5 $\text{cm}^2$ . ....	122
Figure 5.3: Calculated temperature for each cell within the melt pool for the beam profile with a single laser (a) and six lasers (b). ....	124
Figure 5.4: Temperature colour map of the melt pool for the beam profile with a single laser (a) and six lasers (b). ....	125
Figure 5.5: Temperature colour map produced by FEM simulation for a single laser beam surface (a) and cross section (b) ....	126
Figure 5.6: Temperature colour map produced by FEM simulation for a beam profile with .....	127

Figure 5.7: Compares average temperatures derived from the analytical and FEM solutions with the melt pool temperature from the thermal camera data for all six beam profiles.....	128
Figure 5.8: The SEM images depict the tracks produced using: (a) two lasers, (b) three lasers, (c) four lasers, (d) five lasers, and (e) six lasers.....	129
Figure 5.9: A comparison of the $1/e^2$ beam width with the corresponding resultant melt pool width.....	129
Figure 5.10: Figure illustrating a comparison between the empirical melt pool widths and as predicted by both analytical methods and FEM across all six beam profiles.....	130
Figure 5.11: Schematic of scanning strategy.....	131
Figure 5.12: A cross-section representation perpendicular to the laser traverse direction of a melted track produced with 5 lasers: Scanning speed 100 mm/min and 200 $\mu\text{m}$ hatch spacing.....	131
Figure 5.13: Cross section of a melt pool created by the beam profile with 6 lasers. ....	132
Figure 5.14: A schematic representation of a melt pool formed during L-PBF. ....	133
Figure 5.15: Figure illustrating a comparison between the empirical melt pool depths and as predicted by FEM across all six beam profiles.....	134
Figure 5.16: Measured transient temperature from the thermal camera for the beam profiles (a) single laser, (b) two lasers, (c) four lasers and (d) six lasers. Cooling rate determined from 1267 K to 847 K. ....	136
Figure 5.17: Depiction of an area plot illustrating the cooling rates achieved in DAM as each laser is activated, ranging from one to six.....	137



Figure 5.18: Depicts the anticipated cooling rates as extrapolated from the analytical model for the beam profiles employing two lasers (a) and six lasers (b). .....	138
Figure 5.19: A graphical representation of the temperature-time data procured from the ANSYS simulation. (a) delineates the results for the beam profile utilising a single laser and (b) illustrates the data corresponding to a configuration with six lasers. Each curve provides insight into the temperature variations over a specified duration under the influence of the respective laser configurations. ....	140
Figure 5.20: A comparison of the cooling rate predicted from the analytical and FE model for all six beam profiles with the cooling rate derived from the thermal camera data. ....	141
Figure 6.1: Scanning strategy and sample dimensions. ....	146
Figure 6.2: Depicting the D-spacing and the Interplay of X-ray Beams with Atom. .....	151
Figure 6.3: Definition of parameters used in X-ray stress measurement using $\sin^2 \psi$ method. ....	153
Figure 6.4: Illustrating a representative linear regression plot of $\sin^2 \psi$ against d for the $\sin^2 \psi$ residual stress methodology. This graph was generated using Origin Pro software. ....	155
Figure 6.5: SEM images of the samples produced using five laser beams at (a) 250 mm/min, (b) 200 mm/min, (c) 150 mm/min, (d) 100 mm/min and (e) 50 mm/min. ....	156
Figure 6.6: SEM images of samples produced using five laser beams at (a) 250 mm/min and (b) 50 mm/min. Both images are contributed to by 5 overlapping melt pools using the parallel scanning method. ....	157

Figure 6.7: A figure depicting the melt pool depth, as determined through SEM, across different beam profiles involving 3, 4, and 5 laser beams, with scanning speeds varying from 50 to 250 mm/min. ....	158
Figure 6.8: Surface roughness for different speeds and profiles, with corresponding r.m.s roughness $R_a$ . ....	159
Figure 6.9: The average temperature, as determined from simulations involving laser configurations with 3, 4, and 5 lasers, while varying the scanning speed from 50 to 250 mm/min. ....	161
Figure 6.10: The cooling rates, as determined from simulations involving laser configurations with 3, 4, and 5 lasers, while varying the scanning speed from 50 to 250 mm/min. ....	163
Figure 6.11: XRD phase analysis for the beam configuration with 5 Lasers illustrating for the scanning speed 250 mm/min; BP1 (a), 200 mm/min; BP2 (b), 150 mm/min; BP3 (c), 100 mm/min; BP4 (d), and 50 mm/min; BP5 (e). ....	165
Figure 6.12: XRD phase analysis for the beam configuration with 4 Lasers illustrating for the scanning speed 250 mm/min; BP6 (a), 200 mm/min; BP7 (b), 150 mm/min; BP8 (c), and 100 mm/min; BP9 (d). ....	166
Figure 6.13: XRD phase analysis for the beam configuration with 3 Lasers illustrating for the scanning speed 250 mm/min; BP11 (a), 200 mm/min; BP12 (b), 150 mm/min; BP13 (c), 100 mm/min; BP14 (d), and 50 mm/min; BP15 (e). ....	167
Figure 6.14: Depicting the $d$ (21.3) versus $\sin^2\psi$ plot for two distinct configurations: BP1 (comprising 5 lasers with a scanning speed of 250 mm/min) along the X axis. ....	168

Figure 6.15: Figure 6.14: Depicting the $d(21.3)$ versus $\sin^2\psi$ plot for two distinct configurations: BP1 (comprising 5 lasers with a scanning speed of 250 mm/min) along the Y axis. ....	169
Figure 6.16: The residual stress in XX and YY directions, as determined from the samples using XRD technique involving laser configurations with 3, 4, and 5 lasers, while varying the scanning speed from 50 to 250 mm/min. ....	170
Figure 6.17: The IPF map as determined from the samples using EBSD technique involving laser configurations with 3, 4, and 5 lasers, while varying the scanning speed from 50 to 250 mm/min. The crystallographic orientation direction in relation to the colour map: Ti - Alpha is $\alpha$ phase and Ti - Beta corresponds to $\beta$ phase.....	172
Figure 6.18: The pole figure as determined from the samples using EBSD technique involving laser configurations with 5 lasers, while varying the scanning speed from 250 mm/min (a), 200 mm/min (b), 150 mm/min (c), 100 mm/min (d) and 50 mm/min (e). ....	174
Figure 6.19: The pole figure as determined from the samples using EBSD technique involving laser configurations with 4 lasers, while varying the scanning speed from 250 mm/min (a), 200 mm/min (b), 150 mm/min (c), and 100 mm/min (d). ....	175
Figure 6.20: The pole figure as determined from the samples using EBSD technique involving laser configurations with 3 lasers, while varying the scanning speed from 250 mm/min (a), 200 mm/min (b), 150 mm/min (c), 100 mm/min (d) and 50 mm/min (e). ....	176
Figure 6.21: The phase map as determined from the samples using EBSD technique involving laser configurations with 3, 4, and 5 lasers, while varying the scanning speed from 50 to 250 mm/min. ....	177

Figure 6.22: The intensity of XRD diffraction at the $\beta$ phase at a $2\theta$ angle of $39^\circ$ , as determined from the samples involving laser configurations with 3, 4, and 5 lasers, while varying the scanning speed from 50 to 250 mm/min. ....	180
Figure 6.23: Compares the residual stress in XX and YY direction at various scanning speeds (50 – 250 mm/min) with the cooling rate obtained from FEA analysis.....	182

## List of Tables

Table 2.1: ASTM classified AM processes, brief description of technology involved and its strengths and weaknesses.....	8
Table 2.2: Key challenges in L-PBF and their cause.....	14
Table 2.3: Comparison between CO <sub>2</sub> , Yb-fibre and diode lasers. ....	17
Table 2.4: A summary of the key developments in L-PBF using diode lasers.....	18
Table 2.5: Comparison of the fundamental distinctions between DAM and L-PBF processes. ....	21
Table 2.6: Comparison of modelling methodologies employed in AM. ....	42
Table 3.1: Composition of Ti6Al4V .....	79
Table 3.2: Processing parameters and material properties used for Analytical modelling [109].....	81
Table 3.3: Recommended values for thermophysical properties of Ti6Al4V [109]. .....	83
Table 3.4: PANalytical XPert3 Powder equipment setup parameters used for residual stress experiments. ....	87
Table 4.1: The process parameters (Power and Scanning Velocity) chosen for the study. ....	90
Table 4.2: The table displays the accuracy of the three methodologies (analytical, FEM and VoF) in replicating various modelled effects, benchmarked against the original experimental data.....	116
<i>Table 5.1: Processing parameters and material properties.....</i>	119
Table 5.2: Specification of laser beam profiles used in this study. ....	120
Table 6.1: This table presents the published residual stress values of Ti6Al4V measured using XRD method during the L-PBF process, with a specific focus on the residual stress levels in the top layer, considering variations along the laser	

traverse directions. All the work mentioned here are carried out without substrate pre-heating. ....	148
Table 6.2: The average residual stress measurements for Ti6Al4V during L-PBF with the aid of powder bed pre-heating configurations.....	148
Table 6.3: The study illustrates the combination of parameters utilised, showcasing the number of lasers, total laser power, and the scanning speed.	149
Table 6.4: The $1/e^2$ beam diameter and the cumulative beam overlap generated with a 200 $\mu\text{m}$ hatch spacing. ....	157
Table 6.5: The percentage of changes in cooling rates, as determined from simulations involving laser configurations with 3, 4, and 5 lasers, while varying the scanning speed from 50 to 250 mm/min. The beam profile with 3 lasers at a scanning speed of 250 mm/min has the highest cooling rate of 8400 K/s. The rate of change is calculated from this highest value. ....	179
Table 7.1: The key findings of the current research and suggested areas for future work to advance DAM development. ....	186

## List of Abbreviations

AM	Additive Manufacturing
ASTM	American Society for Testing and Materials
BCC	Body-Centered Cubic
BJT	Binder Jetting
CFD	Computational Fluid Dynamics
CT	Computer Tomography
CTP	Computer to Plate
CNC	Computer Numerical Control
DAM	Diode Area Melting
DED	Direct Energy Deposition
DEM	Discrete Element Method
DL	Diode Laser
DMD	Direct Metal Deposition
DMLS	Direct Metal Laser Sintering
DT	Digital Thread
EB-PBF	Electron Beam Melting
EBSD	Electron Backscattered Diffraction
ED	Energy Density
FEM	Finite Element Method
FWHM	Full Width Half Maxima
HCP	Hexagonal Close Packed
HPDL	High Power Diode Laser
IP	Intellectual Property
L-PBF	Laser Powder Bed Fusion
MEX	Metal Extrusion
MJT	Material Jetting
NDT	Non-Destructive Test
PD	Power Density
PBF	Powder Bed Fusion
RAW	Radiation Absorption Material
SEM	Scanning Electron Microscope
SHL	Sheet Lamination
TEC	Thermo-Electric Coolers

TGM	Temperature Gradient Mechanism
VoF	Volume of Fluid
VPP	VAT Photopolymerization
WAAM	Wire Arc Additive Manufacturing
XRD	X-Ray Diffraction
2D	Two Dimensional
3D	Three Dimensional



## List of Symbols

A	Absorption (%)
$A_\lambda$ (I)	Intensity and wavelength dependent absorption coefficient
c	Heat Capacity
$c_v$	Heat capacity for constant volume
d	Lattice spacing of crystal planes
$\epsilon$	Strain in the material
f	Focal length (mm)
h	Hatch spacing (mm, $\mu\text{m}$ )
I	Power intensity ( $\text{W}/\text{mm}^2$ )
$I_{\text{abs}}$	Absorbed intensity of the laser radiation
$I_\lambda$	Space and time-dependent intensity at the wavelength $\lambda$
k	Thermal conductivity ( $\text{W}/\text{m}\cdot\text{K}$ )
$M^2$	Beam quality factor
P	Laser power (W)
$\rho$	Density
r	Radius (mm, $\mu\text{m}$ )
$r_B$	Laser beam radius (mm, $\mu\text{m}$ )
R	Reflection (%)
$t_L$	Layer thickness (mm, $\mu\text{m}$ )
T	Temperature ( $^\circ\text{C}$ , K)
$v$	beam traversing velocity/Scanning speed (mm/s, mm/min)
$v_P$	Velocity of the workpiece (mm/s)
N	Integer denoting the order of diffraction
$\eta$	Absorptivity (%)

$\lambda$	Wavelength (nm)
$\omega$	Absorbed energy per volume
$\theta$	Diffraction angle
$\Phi$	Tilt angle in XRD
$\Psi$	Tilt angle in XRD
$\Sigma$	Stress in the material

## 1 Chapter 1: Introduction

Laser Powder Bed Fusion (L-PBF) has become a leading technology in the field of Additive Manufacturing (AM), representing the most widely used and extensively researched technique for the production of metallic components. The process generally employs fibre lasers with a wavelength of 1070 nm, providing power outputs that range from 100 to 1000 watts. Through the years, enhancements in L-PBF technology have incorporated the addition of multiple lasers, increased laser power, and larger build volumes. To overcome the inherent productivity challenges of L-PBF, manufacturers such as Renishaw, EOS, and SLM Solutions have initiated the development of systems equipped with multiple high-power fibre lasers, typically with a quad 500 - 1000 watt laser arrangement. Notably, one model from SLM Solutions, the NXG XII 600, incorporates up to twelve lasers and achieves an actual build rate of up to 1000 cm<sup>3</sup>/h, a substantial increase from the earlier systems that achieved build rate of only 25 cm<sup>3</sup>/h using a single 400 W laser. These enhancements have resulted in increased build speeds, but they also entail significant rises in hardware costs, energy consumption, and the overall size of the systems [1].

Despite these advancements, L-PBF continues to be constrained by significant intrinsic challenges such as high residual stresses and warpage. Moreover, the throughput of L-PBF systems has not yet attained a level that is viable for mass production. Additionally, the high acquisition and operational costs associated with these systems further hinder the widespread adoption of this technology across various industries. For instance, integrating each additional laser into an L-PBF system results in a cost increase of several hundred thousand. These challenges have motivated the exploration of alternative technologies within this sector, aiming to reduce these barriers and enhance the applicability of AM processes.

In response to these challenges associated with L-PBF, researchers at the University of Sheffield have developed Diode Area Melting (DAM), a novel approach that represents a shift from conventional L-PBF techniques. Unlike traditional methods that rely on galvo scanning mirror-deflected fibre lasers, DAM utilises an array of low-powered diode lasers, each with a power output of less than 5 watts. This new method varies significantly from traditional L-PBF as

it operates at considerably slower speeds of 1 to 10 mm/s using a gantry system, in contrast to the 300 to 3000 mm/s speeds typical in standard L-PBF systems. Preliminary outcomes with Ti6Al4V alloy indicate that the current DAM equipment has the theoretical capability to achieve a build rate of 1000 cm<sup>3</sup>/h, using an assembly of ~4000 individual diode lasers arranged in a singular row. The cost per diode laser in DAM is estimated to be less than £30, and an entire laser system comprising 4000 lasers and its lens assembly can be obtained for a sum below £200K. This stands in contrast to the high purchase costs associated with L-PBF machinery, which may escalate by ~£175K with the addition of each laser, with a proportional increase in energy consumption. Moreover, the higher residual stresses and the increased surface roughness characteristic of L-PBF parts require additional post-processing, which in turn increases the overall cost of the final component.

The DAM development is set to overcome some of the principal challenges inherent in existing L-PBF technologies, including the high residual stresses and substantial costs associated with L-PBF. This advancement is anticipated to not only improve the quality of manufactured components but also to potentially decrease both the cost per part and the overall cost of ownership for the machinery. Nonetheless, the DAM approach presents its own set of challenges, particularly the increased complexity caused by the integration of multiple lasers. Furthermore, the effectiveness of low-powered diode lasers in processing metals and alloys with high melting points and densities remains to be demonstrated. These aspects requires further research to fully determine the capabilities and boundaries of the DAM methodology.

### **1.1 Novelty Statement**

The mirror galvanometers controlled single fibre laser in the L-PBF system has limitations in scalability due to beam quality deterioration with distance, restricting its operational area and causing difficulties in maintaining consistent performance. This is a major factor limiting the use of the L-PBF process, particularly for higher-volume manufacturing or when serial production is required. Multi-laser-based L-PBF systems are employed to solve this problem by using individual galvo-mirrors for each laser to ensure consistent beam quality across a larger work area, but this also increases the cost and complexity

of the system. The direct use of fibre-coupled multiple laser diode sources on a gantry system could solve this issue, which has not been explored before. The diode lasers are cost-effective, and a gantry system would provide reachability for the laser source to process a wider area without losing beam quality, forming the basis of the DAM process.

This work presents modelling, testing, and investigating DAM methodology for processing of Ti6Al4V powder using a multi-laser array. While L-PBF models have been extensively explored, a significant gap remains in modelling processes like DAM. Additionally, understanding residual stress formation in the context of DAM's unique laser array requires further study. We expect a cooling rate lower than L-PBF for DAM, making it crucial to quantify residual stress—a topic that has not been addressed before. Such research can provide insights into the specific dynamics of DAM, leading to better control and optimisation of the process. In essence, this research seeks to model and understand the specific dynamics of DAM, addressing critical gaps in modelling, process optimisation and residual stress formation.

Ti6Al4V is one of the most widely used titanium alloys, especially popular for its high specific strength, light weight, and outstanding corrosion resistance. Its versatility and excellent mechanical properties make it a preferred material in a diverse array of industries. The widespread L-PBF technique has been noted to induce the formation of undesirable  $\alpha'$ -martensite phases within Ti6Al4V alloys, a direct consequence of the rapid cooling of the melt pool [2]. This phase reduces ductility, often resulting in a product that falls short of the minimum percentage elongation specified by ASTM standards (examples: ASTM F136-13 and ASTM F1108-14) [3]. The optimal microstructural configuration for Ti6Al4V is an  $\alpha+\beta$  basket-weave microstructure. Interestingly, preliminary experiments conducted by Zavala-Arredondo *et al.* have suggested that the DAM process inherently produces a slower cooling rate for Stainless Steel, estimated at  $10^3$  K/s, significantly lower than the  $10^5$  to  $10^6$  K/s cooling rate typical of L-PBF [4], [5]. Validating this finding, our initial experiments with DAM have yielded promising results, demonstrating the formation of the desirable  $\alpha+\beta$  phase composition in Ti6Al4V due to the lower cooling rate, as documented by Alsaddah *et al* [6]. However, their study on the DAM processing of Ti6Al4V is incomplete, lacking in areas such as modelling and realising the residual stress within the samples, as

well as calculating or finding the cooling rate for various laser configurations employed in DAM. This has motivated me to explore Ti6Al4V further, aiming to close the gaps left by the previous study.

## **1.2 Thesis Overview and Structure**

A concise overview of each chapter is provided in the following section. In practice, multiple steps were conducted simultaneously; however, for clarity, they are presented sequentially in a flow diagram in *Figure 1.1*.

### **Chapter 2**

This chapter examines the current state of L-PBF technology, focusing on its efficiency, productivity, and scalability, as well as the limitations of this technology. It explores the use of diode lasers within the L-PBF sector and assesses the benefits and drawbacks of their use. The chapter then delves into the modelling of the L-PBF process, discussing both its state-of-the-art developments and inherent limitations. It concludes by investigating the formation of residual stresses during L-PBF and the measurement techniques used to assess them.

### **Chapter 3:**

This chapter details the methodology and setup of the research study. It describes the DAM setup, which features a multiple diode laser arrangement consisting of a 2D array, CTP head assembly, and outlines all developments carried out to the system. Additionally, this chapter provides an overview of the characterisation techniques employed to analyse the mechanical and microstructural properties including residual stress of the produced samples.

### **Chapter 4:**

This chapter develops and validates analytical, Finite Element Modelling (FEM), and Volume of Fluid (VoF) models by comparing them against a well-documented L-PBF study on the processing of Ti6Al4V. It provides an opportunity to develop and benchmark these three models, exploring their benefits and limitations. This evaluation sets the stage for potentially adopting useful models to simulate the DAM process. This benchmarking serves as a

foundational reference for the modelling work in DAM, where currently very limited models are available. Particularly for the fibre-coupled laser array used in this research, there are no existing models available.

### **Chapter 5:**

This chapter builds on the analytical and FEM frameworks developed in Chapter 4, applying these models to various multi-laser configurations in the DAM process, involving up to six lasers in a row. It examines the melt pool width and depth resulting from single line scanning and validates these findings against the models. Additionally, the average melt pool temperature and cooling rates deduced from the models are validated using thermal camera data.

### **Chapter 6:**

This chapter examines the formation of residual stress in samples produced by different laser configurations, activated by each diode laser, and at various scanning speeds. The X-ray Diffraction (XRD) method is used to quantify the residual stresses, and the chapter outlines this methodology. It also discusses how residual stress formation correlates with the cooling rates predicted by FEM models. Additionally, the chapter covers the use of XRD and Electron Backscatter Diffraction (EBSD) for characterising the samples, providing insights into their microstructural properties.

### **Chapter 7:**

This chapter presents the conclusions of this research and details the recommendations for future work.

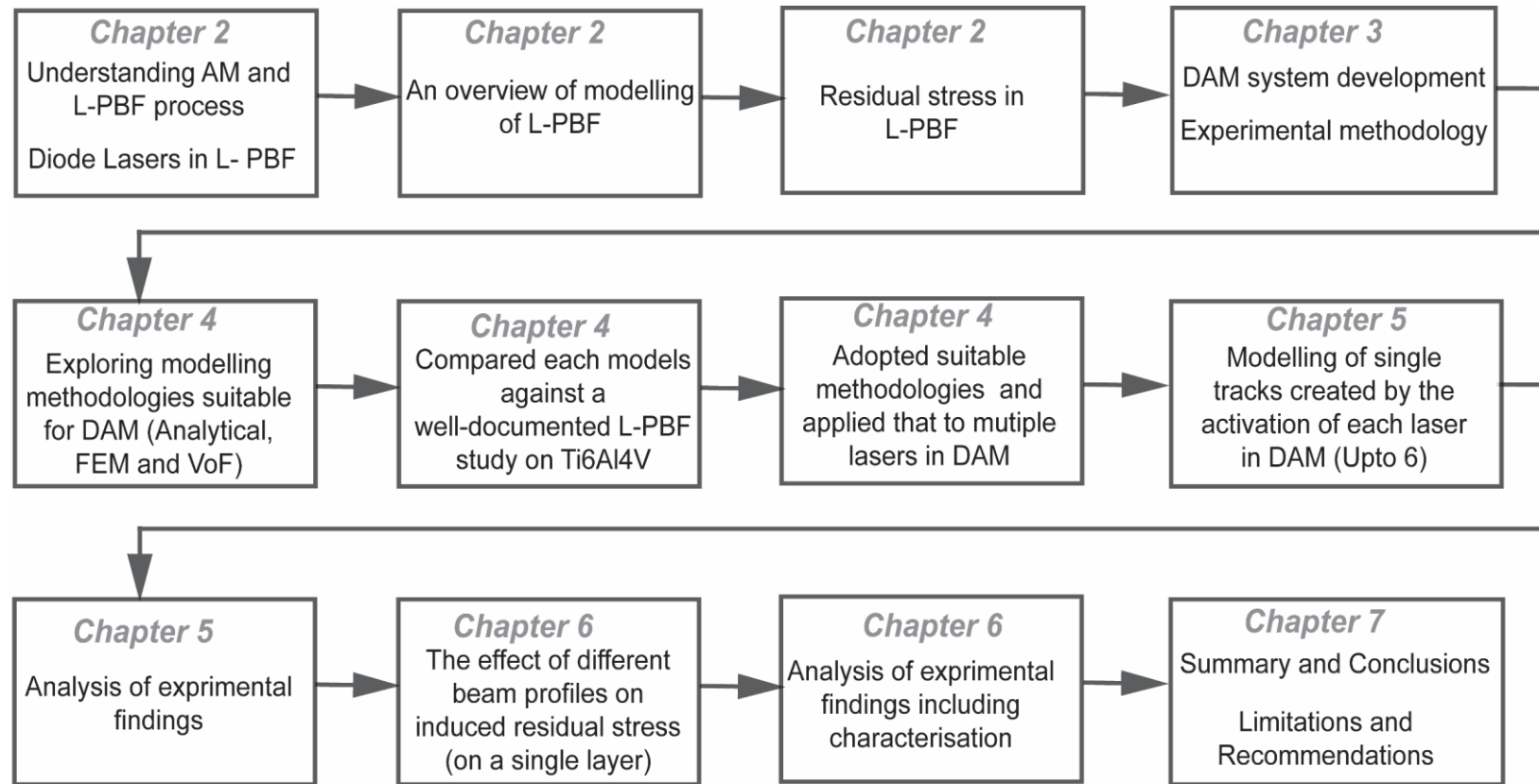


*Figure 1.1: Methodology flow of the current research.*



## 2 Chapter 2: Literature Review

### 2.1 Additive Manufacturing (AM)

Since the Industrial Revolution, there have been several disruptive changes to the landscape of manufacturing technology [7]. Over recent decades, the computerisation of traditional mechanical machinery has set the stage for more sophisticated Computer Numerical Controlled (CNC) machines, which can communicate within a digitally controlled environment. Similarly, a growing process in the field of rapid manufacturing and product prototyping is Additive Manufacturing (AM). AM holds the promise to revolutionise current conventional manufacturing towards a data-driven and on-demand Digital Thread (DT) technology [8], [9]. More widely recognised as three-dimensional (3D) printing, AM constructs parts layer by layer, drawing from digitally interpreted 3D model data in which components are fabricated by consecutively layering cross-sectional slices. To initiate this process, a solid model is designed in CAD or is translated into a digital CAD representation. Once established, the design is partitioned into layers using build preparation software, the precision of which is determined by the inherent resolution of the chosen method. Following this, each material layer is strategically placed and processed to form a final 3D geometry [10].

Various processes qualify as AM when considering the standard of digital layered production. Nevertheless, the American Society for Testing and Materials (ASTM) has classified AM techniques into seven distinct categories, as described in the ISO/ASTM52900:2021 standard [11]. The establishment of these seven categories is imperative, given the diverse requirements in materials, processes, geometry, surface finishes, and costs associated with this emerging technology. ASTM categorised these AM processes as Binder Jetting (BJT), Directed Energy Deposition (DED), Material Extrusion (MEX), Material Jetting (MJT), Powder Bed Fusion (PBF), Sheet Lamination (SHL), and VAT Photopolymerization (VPP). A brief description of each AM process, its strength and weaknesses are shown in *Table 2.1*.

AM Process	Technology	Strengths/Weaknesses
<b>Binder Jetting (BJT)</b>	Liquid bonding agent is selectively deposited to join powder materials.	<ul style="list-style-type: none"> <li>• Full-colour object printing and wider material selection.</li> <li>• Post-processing needed for fully dense metal parts and high porosities.</li> </ul>
<b>Directed Energy Deposition (DED)</b>	Focused thermal energy is used to fuse materials by melting as they are being deposited.	<ul style="list-style-type: none"> <li>• High deposition rate and repair of damaged parts possible.</li> <li>• Low resolution and requires machining to get high geometrical accuracy.</li> </ul>
<b>Material Extrusion (MEX)</b>	Material is selectively deposited through a nozzle or orifice.	<ul style="list-style-type: none"> <li>• Relatively Inexpensive machines and multi-material printing.</li> <li>• Limited part resolution and poor surface finish.</li> </ul>
<b>Material Jetting (MJT)</b>	Droplets of build material are selectively deposited, materials include photopolymers, resins and waxes.	<ul style="list-style-type: none"> <li>• Multi-material printing, high deposition rate and high surface finish.</li> <li>• Low-strength materials</li> </ul>
<b>Powder Bed Fusion (PBF)</b>	Thermal energy selectively fuses regions of a powder bed.	<ul style="list-style-type: none"> <li>• High accuracy and details, fully dense parts and high strength.</li> <li>• High machine cost, expensive raw material (powder) and health and safety concerns due to powder handling.</li> </ul>
<b>Sheet Lamination (SHL)</b>	Sheet of materials are bonded to form an object.	<ul style="list-style-type: none"> <li>• High surface finish and lower machine cost.</li> <li>• Complex shapes are difficult make.</li> </ul>
<b>VAT Photopolymerization (VPP)</b>	Liquid photopolymer in a vat is selectively cured by light-activated polymerization.	<ul style="list-style-type: none"> <li>• High build rate and high resolution.</li> <li>• Not suitable for metals &amp; alloys.</li> </ul>

*Table 2.1: ASTM classified AM processes, brief description of technology involved and its strengths and weaknesses.*

In AM, constructing parts layer by layer offers several advantages over conventional manufacturing processes such as casting, forging, machining, and injection moulding. Firstly, it facilitates the production of highly complex parts layer by layer, which is often not feasible with conventional methods, and this can be achieved without the need for specialised tooling such as moulds, jigs, and fixtures. This lack of tooling also significantly reduces the design cycle time,

allowing for quicker production of parts, which in turn reduces the overall product development cycle. Secondly, compared to subtractive processes, only a small amount of material is required to build these intricate shapes, and any leftover materials can be recycled. Finally, many parts can be consolidated into a single part using AM processes, which can reduce the product cost and also improve the function and quality of the final part. This layer-by-layer approach not only enhances design flexibility but also contributes to material efficiency and waste reduction in the manufacturing process [12].

Despite its numerous advantages, AM also has several limitations. One significant drawback is the relatively slow production speed compared to traditional manufacturing methods, making it less suitable for mass production. The initial cost of AM equipment and materials can be high, which may be prohibitive for small businesses or individual users. Additionally, the range of materials available for AM is more limited than for conventional processes, potentially restricting the types of products that can be manufactured. AM parts can also have lower strength and durability compared to those produced by traditional methods, due to issues such as porosity and anisotropic mechanical properties. Furthermore, the surface finish of AM parts often requires post-processing to achieve the desired smoothness and accuracy, adding time and cost to the production process. Finally, there are also concerns regarding the reproducibility and consistency of AM parts, particularly for critical applications in industries such as aerospace and healthcare [12].

In AM, creating intricate geometrical designs is most often as straightforward as producing simple shapes, which can provide a cost advantage over traditional methods where complex components are challenging and costly to manufacture. This capability has attracted significant attention and led major industries, such as aerospace, automotive, and healthcare, to invest heavily in AM technology. This has increased the demand for metal AM processes and equipment. Among the various AM techniques, PBF is the most widespread process for metal industries and has been in high demand in recent years.

## **2.2 Powder Bed Fusion (PBF) Process**

In PBF techniques, a fine layer of powder material is selectively fused using a targeted energy source. This process involves laying down a thin layer of

powder, which is then selectively melted and bonded to the previously fused layer. The process repeats layer by layer until the desired structure is complete. Among PBF techniques, Laser Powder Bed Fusion (L-PBF) and Electron Beam Melting (EB-PBF) are prominent, particularly in processing metals and alloys. L-PBF employs lasers, whereas EB-PBF uses electron beams as their respective energy sources.

L-PBF offers distinct advantages over other AM processes, particularly when working with metals and alloys. It achieves higher resolution and superior detail due to its use of finely powdered material (15 - 45  $\mu\text{m}$ ) coupled with a small laser beam. This combination enables the production of complex geometries that are challenging or even impossible to fabricate with other AM techniques. The process stands out for its material efficiency compared to methods like DED or MJT. It selectively melts only the powder required to build the part, significantly reducing waste. Additionally, unused powder can typically be recycled and reused, lowering material costs and minimising environmental impact. Parts produced through this method also exhibit superior mechanical properties, such as enhanced strength. Moreover, it is versatile in terms of the materials it can process, capable of handling a wide range of substances, including metals, polymers, ceramics, and composites.

The work in this research predominantly investigates a laser-based additive manufacturing process similar to L-PBF. To establish a foundational understanding of this technology, a brief review is undertaken. The review covers the essential principles of L-PBF, including the laser energy source used, its limitations, and the potential of alternative diode lasers in such processes. This review aims to build upon the established knowledge and explore advancements in laser-based additive manufacturing techniques.

### **2.2.1 Laser Powder Bed Fusion (L-PBF)**

L-PBF has dominated the PBF field largely because of its adaptability and capacity to handle an extensive array of materials, including Aluminium, Maraging Steel, Stainless Steel, Copper, Titanium, Cobalt Chrome, Nickel Superalloys, and precious metals. Furthermore, L-PBF has been more widely adopted compared to EB-PBF within high-value manufacturing such as aerospace, automotive and medical sectors [13].

In L-PBF, the base material is in the form of spherical powders with an approximate diameter of 15 - 45  $\mu\text{m}$ . Ideally, these powder particles should exhibit a homogenous composition and be spherically shaped, ensuring optimal morphological attributes. An optimal powder morphology aids in creating consistent melt pools, thereby facilitating superior build quality. To initiate the build process, the metal powder is deposited onto a build plate with the aid of a powder coater, which delivers a powder layer with a thickness ranging from approximately 30 to 100  $\mu\text{m}$ . Once settled, a laser scans the powder layer using a galvanometer mirror and f-theta lens to selectively melt specific regions of the powder bed, crafting a 2D shape based on the cross-sectional data of the design. The build plate lowers each time to produce a new layer, and the melting process repeats until the desired 3D shape is realised [14]. A schematic diagram of the process is shown in *Figure 2.1*.



*Figure 2.1: A schematic diagram of the L-PBF Process [14]*

The processing conditions applied during L-PBF create molten pools with high temperatures and steep temperature gradients during the formation of each layer. Most often, L-PBF promotes the generation of finer microstructures leading to higher strength and reduced ductility compared to the same materials produced using conventional methods [2]. L-PBF can produce parts with excellent mechanical properties and demonstrates promising results in achievable density and mechanical properties within the produced parts [15].

The laser used in L-PBF predominantly influences the output of the process, and requires careful tailoring of a range of parameters called process variables,

some of which are grouped in Figure 2.2. Due to the broad spectrum of L-PBF machines available from various OEMs, there are thought to be in the range of 150 different process parameters available across commercial machines [16]. The most investigated process variables are laser power or energy density, layer thickness, hatch distance and scanning strategy [17]. These studies generally indicate that in L-PBF, certain metallurgical conditions—like rapid solidification, directional heat flux, and temperature gradients—can be adjusted by tweaking process variables [18]. However, minor alterations in the process can introduce metallurgical flaws such as gas entrapment porosities, oxide layers, and residual unmelted materials, which compromise the performance of the final components. Thus, comprehending the physical phenomena inherent to laser processing and the impact of these process variables is important for pioneering a new process centered around the laser energy source. The ultimate aim in AM is the cost-effective creation of components that are both fully dense and free from defects.

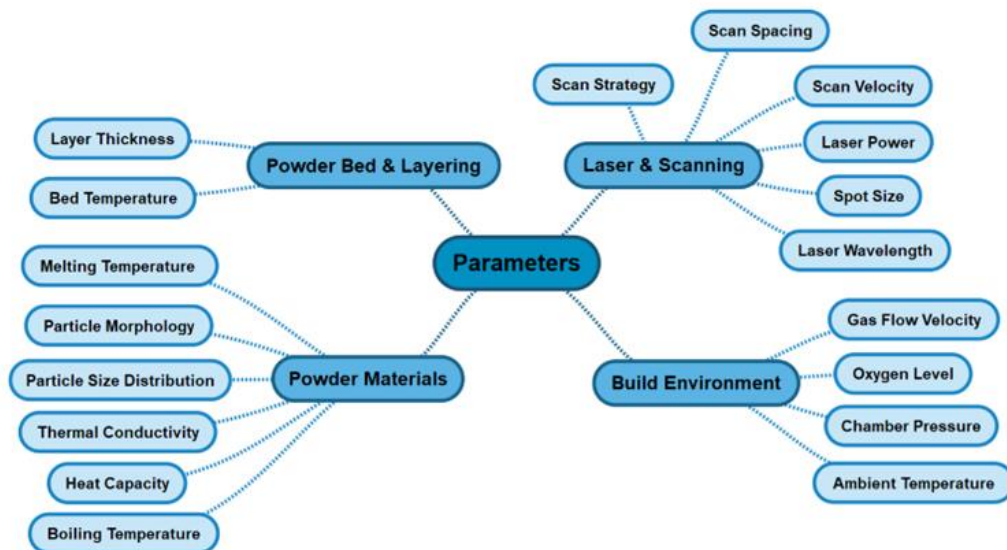


Figure 2.2: Depicting key 'Process Variables' influencing the outcome of an L-PBF process.

### 2.2.2 Challenges in L-PBF

In L-PBF, high power lasers (100 – 1kW) travelling at speeds of approximately 300 – 3000 mm/s fuse powder materials into molten pools with high temperatures, rapid cooling rates, and steep temperature gradients, which are crucial in shaping the microstructure, grain size, and mechanical properties of the final parts. These uninterrupted melt tracks formed by the moving high-energy laser beam create grooves of melt pools, potentially leading to the

vaporisation of alloying elements, particularly in cases like Ti6Al4V where excessive laser energy density (over  $126 \text{ J/mm}^3$ ) can cause significant vaporisation loss of Al ( $> 0.15\%$ ), altering the composition of the part and resulting in variable microstructures and degraded mechanical properties [19]. Conversely, lower energy densities can lead to defects such as balling effects and lack of fusion, highlighting the challenges in controlling the localised temperature of the melt pool during the L-PBF process.

L-PBF parts are particularly susceptible to high residual stresses and distortion due to the significant thermal gradients and rapid heating and cooling involved in the process. Residual stresses tend to accumulate with each added layer, with the highest stress values often occurring at or near the surface of the final layer. These tensile stresses near the surface critically affect the fatigue strength of the component, serving as precursors for micro-crack initiation and propagation under cyclic loading conditions typical in fatigue scenarios. Surface imperfections, such as voids or inclusions, coupled with tensile stress, act as stress concentrators, lowering the fatigue threshold. Additionally, the near-surface region is more exposed to operational conditions like corrosion, wear, and high contact stresses. Residual tensile stress in this area can interact with these environmental factors, further accelerating fatigue crack initiation and propagation. Consequently, the tensile stresses remaining near the surface after the process not only compromise the immediate mechanical integrity of the component but also significantly degrade its long-term fatigue performance [20], [21], [22], [23]. The magnitudes of this stress are influenced by an array of factors, some of which are discussed in detail in *Section 2.8*. Some of the key challenges associated with the L-PBF process and the issues they cause are summarised in Table 2.2.

<b>Challenge</b>	<b>Description/Issue</b>	<b>Cause</b>
<b>Porosity and balling effect</b>	<ul style="list-style-type: none"> <li>• Porosity is the presence of small voids within the solidified materials.</li> <li>• Balling effect is the formation of metal spherical droplets on the surface of the melt instead of a smooth layer.</li> </ul>	<ul style="list-style-type: none"> <li>• Porosity is formed due to insufficient melting of powder, rapid cooling, or gas entrapment.</li> <li>• Balling effect occurs when high surface tension causes molten material to form spherical droplets instead of spreading evenly.</li> </ul>
<b>Warpage and buckling</b>	<ul style="list-style-type: none"> <li>• Warpage occurs when parts deform. Buckling happens when built structures collapse during the layering process.</li> </ul>	<ul style="list-style-type: none"> <li>• Warpage is caused by thermal gradients that lead to uneven cooling and residual stresses in the material. Buckling results from excessive compressive stresses that exceed the structural stability of the material during the build process.</li> </ul>
<b>Spattering and evaporation</b>	<ul style="list-style-type: none"> <li>• Spattering refers to the expulsion of molten particles away from the melt pool due to vapor pressure or gas release. Evaporation involves the vaporisation of some metal components under the intense laser heat.</li> </ul>	<ul style="list-style-type: none"> <li>• Spattering is caused by the rapid vaporisation of metal or trapped gases ejecting molten material from the melt pool. Evaporation occurs due to the high laser power, which can vaporise volatile components of the metal powder.</li> </ul>
<b>Processing Highly Reflective Materials</b>	<ul style="list-style-type: none"> <li>• In L-PBF, highly reflective materials include aluminium, copper, and gold tend to reflect a significant portion of the laser energy, complicating the melting process.</li> </ul>	<ul style="list-style-type: none"> <li>• The cause is their intrinsic property of reflecting a significant portion of the laser energy, which hinders effective melting and bonding of the powder particles.</li> </ul>
<b>Productivity</b>	<ul style="list-style-type: none"> <li>• L-PBF has a slow build rate. Additionally, the requirement for post-processing steps further impacts overall productivity.</li> </ul>	<ul style="list-style-type: none"> <li>• This is caused by the slow layer-by-layer build process, the precise and time-consuming laser scanning required, and the necessity for post-processing to achieve the desired final part quality.</li> </ul>
<b>Cost</b>	<ul style="list-style-type: none"> <li>• Acquisition of L-PBF technology is expensive. This includes the machinery, powder materials, operating expenses and training.</li> </ul>	<ul style="list-style-type: none"> <li>• Expensive due to the high costs of advanced laser systems, specialised metal powders, and extensive post-processing requirements.</li> </ul>

*Table 2.2: Key challenges in L-PBF and their cause.*



Several recent developments have significantly enhanced the capabilities and applications of L-PBF technology. These advancements are designed to improve the efficiency, quality, and diversity of materials that can be utilised, as well as addressing some of the inherent limitations of this technology. Notable areas of recent progress include the incorporation of multiple lasers in modern L-PBF machines, which accelerates build speeds and enhances productivity. These systems reduce production times by enabling the simultaneous melting of multiple sections of a layer. Moreover, the adoption of advanced laser technologies, such as blue lasers, has enhanced the absorption rates for highly reflective metals like aluminium, copper and gold, which are traditionally difficult to work with due to their lower absorptivity. This improvement has led to increased energy efficiency and better material utilisation. The application of different lasers in L-PBF will be further discussed in the subsequent sections.

### **2.2.3 Lasers in L-PBF**

Since their introduction in 1960, lasers have seen extensive research applications, leading to their widespread industrial use. Early production applications involved drilling hard materials such as diamond and sapphire, joining microelectronics components, and cutting steel sheets. The L-PBF technology was commercialised in 1992 using a CO<sub>2</sub> laser with a 10.6 µm wavelength. However, this wavelength struggled to melt metallic parts with sufficient density because metals have very low absorptivity at this wavelength, requiring higher laser power and making the process much more inefficient [1]. During the initial phases of L-PBF development, CO<sub>2</sub> lasers were widely employed. Today, CO<sub>2</sub> lasers are primarily used for processing polymers. Significant advancements in high-power fibre lasers, particularly fibre lasers with ~1 µm wavelength, have transformed their application, especially in melting metals and alloys. These fibre lasers are preferred for metals and alloys due to their higher absorptivity and efficiency [24].

In laser technology, two principal types are popular: Continuous Wave (CW) and Pulse lasers. CW lasers emit a consistent beam, suitable for applications that require continuous exposure, whereas Pulse lasers emit light in controlled bursts, perfect for precise energy delivery without overheating the material. The choice between them depends on the specific needs of their applications.

Parameters such as spot size, focal plane, and laser power can be adjusted in CW for re-melting applications, whereas pulse systems allow for adjustments in peak power, frequency, spot size, and pulse duration. Typically, CW lasers are employed in commercial L-PBF equipment.

A modern L-PBF system typically utilises fibre laser sources, each ranging from 400 W to 1000 W, capable of processing areas up to 800 x 400 mm<sup>2</sup>. The commonly used CW Ytterbium-doped fibre laser operates at 1070 nm, resembling the operational principle of an amplification unit in fibre-optic systems, where a doped silica fibre, excited by a diode laser source, generates lasing action. Continuous laser emission is maintained by two Bragg gratings that act as mirrors within the linear laser cavity. Laser characterisation is based on three critical elements: the active medium (gain), the pumping energy source, and the optical resonator, which collectively determine the efficiency and quality of the laser beam produced [25].

Diode Lasers (DLs) are increasingly being used in various industrial applications. These semiconductor lasers operate at various wavelengths, typically ranging from the visible to the infrared spectrum, making them highly versatile across different materials. DLs work by passing an electric current through a specially designed semiconductor material. This process generates light at specific wavelengths through the recombination of electrons and holes within the semiconductor, producing coherent and highly focused light that is suitable for precise applications. DL is discussed in *Section 2.4*. Furthermore, *Table 2.3* summarises the comparison between CO<sub>2</sub>, Ytterbium-doped fibre lasers and diode lasers highlighting the key differences in their wavelength, operation, efficiency and suitability for specific applications.

Parameter	CO <sub>2</sub> Lasers	Yb-fibre Lasers	Diode Lasers
Wavelength	10.6 $\mu\text{m}$	1.07 $\mu\text{m}$	300 – 3500 nm
Pump Source	Direct electrical source	Diode laser	Direct electrical source
Mode of Operation	CW and Pulse	CW and Pulse	CW and Pulse
Laser Power	Up to 25 kW	Up to 10 kW	Up to 100 W
Efficiency	15%	30%	65%
Applications	AM, Material processing, Welding and Cutting	AM, Welding and Cutting	Heat treatment, Pump source for other lasers, Medical and Soldering
Maintenance	2,000 h	20,000 h	200,000 h
Merits & Demerits	<ul style="list-style-type: none"> <li>• Not suitable for metallic applications.</li> <li>• High maintenance.</li> </ul>	<ul style="list-style-type: none"> <li>• Suitable for metals and alloys.</li> <li>• High cost to acquire.</li> </ul>	<ul style="list-style-type: none"> <li>• Suitable for metals and alloys.</li> <li>• Highly efficient.</li> <li>• Low cost.</li> <li>• Poor beam quality.</li> </ul>

Table 2.3: Comparison between CO<sub>2</sub>, Yb-fibre and diode lasers.

### 2.3 Enhancing L-PBF with Diode Laser Technology

The use of diode lasers in material processing applications has been increasing primarily due to their advantages such as energy efficiency, cost-effectiveness, low maintenance, and low wavelength suitability for many metals and alloys, compared to conventional CO<sub>2</sub> and fibre lasers. However, high divergence and low beam quality still limit the direct application of these lasers in L-PBF processes. Despite these challenges, there have been significant developments in the industry where High Power Diode Lasers (HPDLs) have been successfully used for AM. These advancements aim to mitigate the limitations of the L-PBF process, primarily arising from the use of fibre lasers, by improving beam quality and reducing divergence. HPDLs are becoming more suitable for precise applications in AM, demonstrating their potential to overcome the inherent drawbacks of diode lasers. Table 2.4 summarises these key developments in L-PBF using diode lasers, providing an overview of the technological progress made. Some of the latest developments in L-PBF technology involving diode lasers are commercially sensitive, resulting in limited

publicly available information. Nevertheless, the information that is available has been reviewed and is presented in this section.

Innovation	Description	Benefit
<b>Diode Area Melting (DAM)</b>	DAM methodology developed at the University of Sheffield uses an array of low power diode laser to selectively melt a larger area. A gantry system is used to traverse the laser array for selective scanning [4], [5], [6], [26].	<ul style="list-style-type: none"> <li>• Process larger area.</li> <li>• Low power diode lasers</li> <li>• Low spatter due to slower speed.</li> <li>• Low cooling rate and residual stress.</li> </ul>
<b>HPDL Enhanced L-PBF Process</b>	Fraunhofer ILT has developed a new HPDL-based multi-spot system that achieves 200 W power per melting spot, comparable to standard L-PBF systems. To reach this high power, multiple laser diode bars are stacked and combined, with several emitters multiplexed to form each 200 W laser spot. A gantry system is used to traverse this single beam to selectively scan the power bed [27], [28].	<ul style="list-style-type: none"> <li>• This low cost HPDL could replace the fibre lasers in L-PBF.</li> <li>• HPDLs can be stacked to achieve even higher power levels.</li> <li>• More efficient than L-PBF lasers.</li> <li>• Longer operational life span.</li> </ul>
<b>Area Melting with Multi-laser Array</b>	GE global research had developed a methodology utilising 16 edge-emitting HPDLs bars, each delivering 60 W at a wavelength of 976 nm for a total irradiation of 960 W. Connected via multimode fibres, the laser beams produced are about 100 $\mu\text{m}$ in diameter and spaced 127 $\mu\text{m}$ apart, focused using a relay lens for precise application [29].	<ul style="list-style-type: none"> <li>• Like DAM, it processes a larger area, specifically 2.01 mm.</li> <li>• Faster build rate than DAM but uses HPDLs.</li> <li>• More efficient than L-PBF lasers.</li> <li>• Longer operational life span.</li> </ul>
<b>Diode based Additive Manufacturing (DiAM)</b>	Developed at the Lawrence Livermore National Laboratory, the DiAM hybrid method employs four 1.25 kW stacked diode arrays, each comprising 60 individual bars, delivering a total of 4.8 kW power from a combined incoherent beam. An optically addressable photomask captures this incoherent light to selectively melt a larger area of using a $\sim 10$ mm wide hybrid laser beam that integrates these diode laser beams with Q-switched Nd: YAG laser pulses [30].	<ul style="list-style-type: none"> <li>• Processes larger area.</li> <li>• Allows scaling to increase productivity.</li> <li>• Potentially controls residual stress and microstructure.</li> <li>• Hybrid approach potentially provides benefit of both Fibre and HPDL lasers.</li> </ul>

Table 2.4: A summary of the key developments in L-PBF using diode lasers.

The Area Melting technique with multi-laser array, demonstrated using multiple lasers at GE Global Research, closely mirrors the DAM methodology. Both are elaborated upon in detail in the subsequent section.

### 2.3.1 The Diode Area Melting (DAM)

Diode Area Melting (DAM) is a novel L-PBF method conceptualised at the University of Sheffield. In principle, DAM can employ hundreds (or potentially thousands) of low-powered and undeflected diode emitters, as illustrated in *Figure 2.3*. These replaces the high-power laser and mirror galvanometer mechanism used in the L-PBF. DAM is a slower process due to the low power of the energy source but attains productivity through its use of multiple laser beams to simultaneously process a larger area. In the early development of DAM, Zavala-Arredondo *et al.* used an array of multiple undeflected 808 nm wavelength diode lasers (2.63 W each) with a total output power of up to 50 W to selectively melt the powder materials [26]. The DL array acted as a print head and consisted of 19 emitters with a 135  $\mu\text{m}$  beam diameter placed across a 500  $\mu\text{m}$  pitch producing a 10mm broad stripe of laser radiation before focusing. The linear stripe of laser radiation reduced to 4.5mm in length and 0.25 mm in width after focusing and produced enough energy density to melt BiZn<sub>2.7</sub> and Stainless Steel 17-4 powder materials. Unlike L-PBF, the wide stripe of laser radiation in DAM creates a layer with the help of a parallel scanning regime as shown in *Figure 2.4*.



*Figure 2.3: Schematic illustrating the foundational Diode Area Melting concept, depicting individually adjustable emitters within a mobile diode laser bar, selectively activated/deactivated to define shapes across the powder bed [26].*

The parallel scanning path of the DAM not only scans a broader area but also allows the activation of individual emitters in order to control the shape of the geometry. Furthermore, this arrangement can be scaled to process a much larger area. Zavala-Arredondo *et al.* argued that a theoretical build rate of  $>2.8 \text{ mm}^3/\text{s}$  could be achieved for Stainless Steel by scaling the DAM system by stacking up seven DL modules featuring 19 emitters each. This theoretical arrangement is potentially further scalable for processing even more extensive areas leading to considerable productivity improvements [4], [26]. Due to the anticipated low cooling rate, the DAM process could potentially reduce residual stress formation within the built parts. Furthermore, a mathematical model predicted DAM's temperature gradients and cooling rates to be comparable to optimised pre-heated L-PBF methods [5].



Figure 2.4: A typical scanning path used in the DAM process [26].

Though the initial DAM approach successfully demonstrated use of low-powered multiple-diode lasers as an alternative to galvanometer mirror-deflected high-power lasers in L-PBF, it had a number of limitations. Firstly, the lack of precise independent control of the 19 emitters of the diode laser bar constrained the use of multiple lasers. Secondly, the diode laser bar and its cooling system were positioned inside the build chamber, causing thermal management, and overheating issues, severely restricting the potential to scale the system to larger number of lasers. Finally, this work demonstrated the feasibility of using wavelength optimised lower power diode lasers to melt powders with temperatures exceeding  $1300 \text{ }^\circ\text{C}$ , but was insufficient to process engineering alloys such as Ti6Al4V. Table 2.5 compares the key differences between the DAM and L-PBF process.

DAM	L-PBF	DAM Advantages
<ul style="list-style-type: none"> <li>Independently controllable emitters.</li> </ul>	<ul style="list-style-type: none"> <li>Galvano mirror controlled single laser beam.</li> </ul>	<ul style="list-style-type: none"> <li>Diode laser and control units are relatively inexpensive than L-PBF laser systems.</li> <li>The non-deflected beam in the DAM provides a scanning regime where laser beams can be switched on and off to produce various geometries.</li> </ul>
<ul style="list-style-type: none"> <li>Laser arrangement is scalable to a larger scanning area.</li> </ul>	<ul style="list-style-type: none"> <li>The scalability is limited as the cost and complexity increase with the number of laser beams.</li> </ul>	<ul style="list-style-type: none"> <li>Multiple diode lasers can provide a much larger scanning area leading to faster build rate.</li> </ul>
<ul style="list-style-type: none"> <li>DL has high wall-plug efficiency.</li> <li>Tuneable and low wavelength.</li> </ul>	<ul style="list-style-type: none"> <li>Solid-state and fibre lasers used in L-PBF have 20-30% wall-plug efficiency.</li> <li>Due to a 1,060-10600nm wavelength, L-PBF lasers provide lower laser absorption.</li> </ul>	<ul style="list-style-type: none"> <li>Up to 60-80% wall-plug efficiency can be achieved with DLs.</li> <li>DLs are tuneable and available in wavelengths from 400 - 1060nm. The lower wavelength increases laser absorption for most metals.</li> </ul>
<ul style="list-style-type: none"> <li>Small beam diameter (135 <math>\mu\text{m}</math>). It is possible to reduce the beam diameter even further to 65 <math>\mu\text{m}</math>.</li> </ul>	<ul style="list-style-type: none"> <li>L-PBF lasers have a larger beam diameter compared to DLs.</li> </ul>	<ul style="list-style-type: none"> <li>Small beam diameter provides higher resolutions in the produced parts.</li> <li>Higher energy densities can be achieved at low laser power due to the small beam diameter.</li> </ul>
<ul style="list-style-type: none"> <li>Optical pre-heat</li> </ul>	<ul style="list-style-type: none"> <li>In some cases, substrate pre-heating is provided</li> </ul>	<ul style="list-style-type: none"> <li>DAM can provide accurate surface heating, which improves the material's laser absorptivity and reduces the thermal gradient.</li> </ul>

Table 2.5: Comparison of the fundamental distinctions between DAM and L-PBF processes.

### 2.3.2 Use of fibre-coupled lasers in DAM:

The initial scheme demonstrated by Zavala-Arredondo *et al.* was improved upon through the use of multiple individually addressable fibre-coupled DLs, which replaced the laser bar system initially used. This system evolution introduced a fibre head assembly consisting of a 2D array of 50 multimode fibre channels. Alsaddah *et al.* demonstrated this new setup by using up to ten laser beams with 808 nm wavelength to process Ti6Al4V powders and produced samples with more than 95% density. Those samples provided a hardness value

between 4 and 5 GPa and a modulus of elasticity up to 120 GPa. Experiments were conducted with two laser profiles, one with two rows, LP1 and the other with a single row, LP2, with scanning speeds between 75 - 300 mm/min. Both the LP1 and LP2 laser profiles produced samples with  $\alpha + \beta$  phase. Scanning speeds faster than 100 mm/min encouraged the growth of a finer  $\alpha + \beta$  Widmanstätten, whereas slower speeds produced a coarser phase. Though both laser profiles showed a similar temperature rise, the cooling rate of LP1 was 600 °C/s compared with 1086 °C/s for LP2. Moreover, the samples did not show any evidence of variations in aluminium and vanadium elements, indicating an insignificant amount of elemental evaporation during the process. Furthermore, the DAM process has demonstrated its potential to manipulate the microstructure formation by controlling the cooling rate from the  $\beta$  – transus (994 °C) temperature in the case of Ti6Al4V [6].

### 2.3.3 Area Melting with Multi-Laser Array

At GE Global Research, J. H. Karp and colleagues showcased a process utilising 16 edge-emitting High Power Diode Lasers (HPDLs) bars. Each operated at a 976 nm wavelength and provided 60 W power, culminating in a maximum irradiation of 960 W [29]. Every diode package combined numerous edge-emitting lasers, connected with a multimode fibre, resulting in approximately 100  $\mu\text{m}$  diameter laser beams. These beams, spaced 127  $\mu\text{m}$  apart, were focused using a relay lens, depicted in *Figure 2.5*. This configuration effectively processed the CoCr alloy, achieving a density of over 99%. The laser array described could fabricate components at 28  $\text{cm}^3/\text{h}$ , aided by a 2.01 mm radiation stripe. The lensing system has the potential to house a laser array spanning 30mm in width, which could enhance the building speed to a rate surpassing conventional single beam L-PBF systems by up to 20 times. Nevertheless, this raises the laser power close to 10 kW, which could pose thermal challenges. The study omitted details on microstructure, mechanical properties, and melt pool dynamics.





*Figure 2.5: System layout of multi-laser array-based AM developed at GE global research [29].*

Both DAM and Area Melting with multi-laser array have highlighted the potential of DLs for AM applications. These approaches have shown the feasibility of additively manufacturing engineering metals to a high density using energy-efficient and cost-effective DLs. However, claims of enhanced productivity compared to traditional L-PBF systems warrant deeper scrutiny. There is also a pressing need for in-depth analyses into melt pool dynamics, temperature gradient variations, microstructural development, mechanical characteristics, and the potential constraints of integrating DL based L-PBF in AM contexts.

## **2.4 Diode Lasers (DLs)**

Diode Lasers (DLs) operate differently to the CO<sub>2</sub> and fibre lasers, as shown in Figure 2.6 (a). The production of radiative energy transitions between distinct energy bands is achieved by processing a compound semiconductor material, such as Gallium Arsenide (GaAs), a direct bandgap material. This material is treated to form a doped junction, encompassing both n-doping (negative doping) and p-doping (positive doping). DLs are widely acknowledged for their superior efficiency compared to CO<sub>2</sub> or fiber lasers. Their operation is situated within an active region described by a p-n junction. In this context, the excited state is characterised by the presence of electrons occupying the conduction band, while the lower energy state corresponds to the absence of electrons, resulting in holes within the valence band. Upon the application of voltage, it instigates a flow of current, inducing electrons to transition from the conduction band to the valence band. During this process, they release energy equivalent to the disparity

between the Fermi levels of these two bands, manifesting as radiation. When an external pumping voltage is channelled in the conduction direction, lasing commences only after the current breaches a specific threshold value, as depicted in Figure 2.6 (d). The necessary ingredients for a DL (two mirrors and a gain medium) is as shown in Figure 2.6 (b). The special characteristics of laser elements that get superimposed for single mode operation is shown in Figure 2.6 (c). Increasingly, DLs are being recognised and favoured in direct material processing endeavours, notably in applications pertaining to surface heating and welding [31].

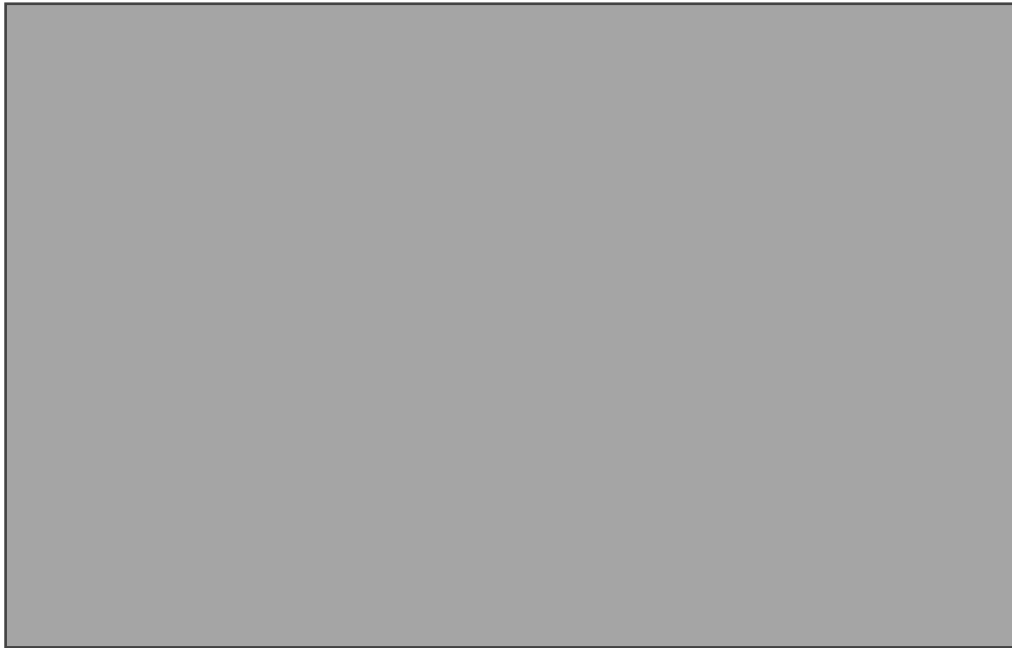


*Figure 2.6: An example of a simple diode laser (a). Schematic of necessary parts required for the operation of a DL (b). Spatial characteristics of laser elements (c) and an illustration of a typical Current vs Power curve for a DL (d) [31].*

A defining characteristic that differentiates DLs from their solid-state counterparts is their remarkable electrical to optical conversion efficiency, which typically ranges between 50-70%. This elevated efficiency stems from the DL's innate characteristic of direct operation, which removes the need for any intermediate energy-transferring stages commonly seen in other laser types. However, there exists an inherent limitation in DLs: the total volume of their active material is condensed to a span of a few millimetres. This spatial constraint effectively limits the output power of an individual DL to a handful of Watts. There is an accompanying thermal challenge; a significant amount of heat needs to be swiftly dissipated from this compact zone. In the absence of adequate thermal management, the consequences can be severe: heightened temperatures trigger the DL to increase its current uptake, which can be a precursor to an

accelerated failure [31]. In scenarios demanding elevated output power, a solution often adopted is the alignment and combination of several individual DLs, resulting in the formation of High-Power Diode Lasers (HPDLs). For context, a single-bar HPDL, dimensioned at 10 mm in width, 1 mm in resonator length, and 0.1 mm in thickness, can generate a laser power in the vicinity of 60 W when operating in a CW mode. These bars, when systematically arrayed in a vertical configuration and supplemented with active water cooling, are instrumental in orchestrating high-powered kW laser systems, greatly expanding the possibilities of laser applications [32], [33]. In the early stages of DAM development, a HPDL was initially employed. However, as the technology evolved, there was a transition to using multiple multi-mode DLs with lower power ratings, specifically around 5W each.

Due to the miniature scale of the resonator, emitter width and its subsequent diffraction, the divergence of the laser beam produced by DLs differ from that of other solid-state lasers. In some cases, up to  $60^\circ$  divergence angles in the vertical axis and  $7^\circ$  in the lateral direction are observed by each emitter on the bar. The beam divergence in the fast axis can be compensated by a collimating cylindrical lens which keeps the beam parallel while compensating at the slow axis [34]. Fibre coupling is another standard laser delivery method from the source to the processing area. However, beam collimation and focusing through microlenses or mirror plates are necessary to achieve enough power density for metal processing. The DLs used in this work are coupled to the fibres before collimating and focusing through a tailor-made Computer to Plate (CTP) mirror plate arrangement.

#### **2.4.1 Gaussian Beam ( $TEM_{00}$ )**

In conventional L-PBF processes, the employment of a single-mode fibre laser is widespread. Characterised by its Gaussian beam profile, when this laser is collimated, it generates a beam with an exceptionally high-quality output. As depicted in *Figure 2.7 (a)*, the complete power density distribution range of the beam within contour sections is illustrated via colour maps. Additionally, a three-dimensional representation showcases the power density at the focal point of the laser beam. Commonly, the diameter of the focal point is referred to as its Gaussian diameter. Specifically, this represents the diameter at which intensity

of the beam is equivalent to  $1/e^2 \times I_{MAX}$ , where  $I_{MAX}$  stands for the peak intensity of the laser beam, as illustrated in Figure 2.7 (c). A representation of a Gaussian beam with an 80  $\mu\text{m}$  diameter can be observed in Figure 2.7 (b).

An alternative method to ascertain the beam diameter is by measuring the beam width at the half-intensity point, termed Full Width Half Maxima (FWHM). This offers a more universal definition, encompassing any beam intensity profile, not merely the Gaussian. In the context of laser simulations, determining the exact power within a specific area is crucial and often employs the  $1/e^2$  value. To explain, when a circular Gaussian beam profile is integrated down to  $1/e^2$  of its peak value  $I_{MAX}$ , it encompasses 86% of the entire power [1].



*Figure 2.7: Illustrates laser beam spatial profile at different locations (a), power density distribution of a fibre laser with a focal spot diameter of 80  $\mu\text{m}$  (b), and a Gaussian beam diameter definition (c) [1].*

## 2.5 Physical Phenomena in L-PBF

In general, L-PBF process stability and outcome are driven by the temperature field in the melt pool. Hence, understanding the behaviour of the melt pool and its temperature evolution is vital in controlling the process outcome. In L-PBF, the small size of the melt pool and the transient temperature field make it challenging. Many efforts are undertaken to measure the temperature of the melt pool; however, only measurements of the readily accessible areas at the surface, not the interior locations, seem to be most successful [35]. The detailed understanding of the melt pool dynamics comes from the transient three-dimensional (3D) mathematical models. For example, Bartlett *et al.* combined a full-field infrared thermographic technique with a numerical tool and developed a helpful model to predict the defects during the L-

PBF of AlSi10Mg [36]. Although process modelling and thermographic analysis via various methods have been researched to understand L-PBF and EB-PBF processes, little attention has been given to the process modelling of DAM, which is one of the objectives of this research. However, before tackling process modelling, the physical phenomena associated with the laser interactions with the powder material must be explored first.

### 2.5.1 Laser Absorptivity

The physical phenomena in L-PBF are affected predominantly by the interaction between the laser beam and the material. A large proportion of the laser energy from electromagnetic radiation incident upon the material is reflected from the surface, leaving a fraction of photons interacting with the matter within it. The temperature process in L-PBF consists of heating, melting and resolidification, which is influenced by various physical phenomena such as absorption, reflection, radiation, heat transfer, phase transformation, fluid flow due to surface tension gradients and mass transformation. In the case of L-PBF, the absorption of the laser beam in the material depends on the wavelength-dependent material properties and morphological characteristics of the powder. The absorbed radiation causes heating, initiating a conduction process within a specific region. The conduction causes the material to melt. Shear stresses and surface forces drive this, and considering wavelength-dependent material properties, the temperature produced ( $T$ ) in the workpiece from the absorbed laser energy can be expressed as below in *equation 1* and *equation 2* [37].

$$T = T(I_{abs}, t_L, r_B, \vartheta p, k, c) \quad (1)$$

$$I_{abs} = A_\lambda(I) I_\lambda \quad (2)$$

Where the term  $I_{abs}$  is the absorbed intensity of laser irradiation,  $t_L$  is the layer thickness,  $r_B$  is the laser beam radius,  $\vartheta p$  is the velocity of the workpiece relative to the laser beam,  $k$  is the thermal conductivity,  $c$  is the heat capacity of the material,  $A_\lambda(I)$  is the intensity and wavelength-dependent absorption coefficient and  $I_\lambda$  is space and time-dependent intensity at the wavelength  $\lambda$ .

The power absorbed within the materials determines the result and the measure of this available power is known as absorptivity, which depends on many factors, such as the wavelength of the laser source, powder particle

morphology, layer thickness and temperature of the powder bed. Generally, the absorption increases with a decrease in the wavelength of laser irradiation. Ref [38] indicated a notable increase in the absorptivity of materials such as TiAl4V, AlSi12, and Cu when transitioning from the conventional 1064 nm wavelength of L-PBF fibre lasers to shorter wavelengths provided by DLs, spanning between 450 to 850 nm. Within the context of this research, the DAM uses DLs at an 808nm wavelength, which consequentially enhances the absorptivity, leading to an optimised optical efficiency throughout the process. Figure 2.8 illustrates the absorption of Ti6Al4V, AlSi12 and Cu within the wavelength ranges between 400 to 1100nm. It should be highlighted that the peak absorptivity for Ti6Al4V and Cu is observed at 450nm, after which it commences a decline [38].



*Figure 2.8: Illustrates the absorption of Ti6Al4V, AlSi12 and Cu within the wavelength ranges between 400 to 1100nm [38].*

The laser radiation absorbed by the material is primarily converted into thermal energy. This energy transition is non-uniform and is influenced by several factors, including the irregular thickness of the material layer, the morphology of powder particles, and the characteristics of the Gaussian beam, which result in temperature gradient-induced heat flux. At this stage, heat conduction becomes the predominant mechanism; therefore, understanding heat transfer is crucial. However, terminologies such as laser power density and energy density are frequently used in L-PBF during the parameter optimisation process to correlate laser power, scanning speed, and layer thickness with the process outcome.

### 2.5.2 Laser Power Density

In order to explain the effect of a stationary laser beam with a circular cross-section, the process variables beam power ( $P$ ) and beam radius ( $r_B$ ) are conveniently grouped to form a relationship known as power density, PD in equation 3.

$$PD = \frac{P}{\pi r_B^2} \quad (3)$$

PD is a principle process variable for laser processing as the behaviour of the process will be manipulated by varying it. For example, changing the power densities of a CO<sub>2</sub> laser in the order of 10, 100, 10000 W/mm<sup>2</sup> produces three different processes namely surface heating (3a), surface melting (3b) and surface vaporisation 3(c) respectively as shown in Figure 2.9 [39]. This variable has the most significant effect on the principle processing mechanisms. An example might be the way that very high PD could evaporate the material, whereas low PD may not produce fully dense parts due to lack of melting.

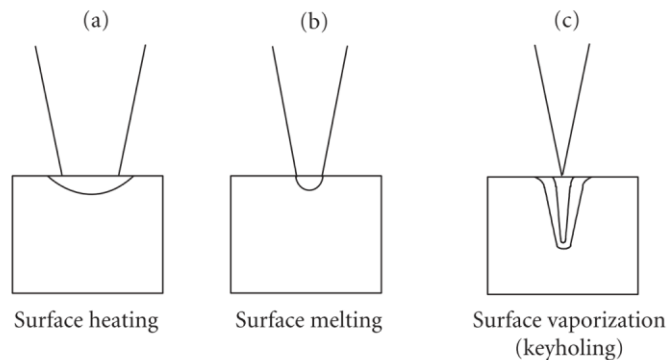


Figure 2.9: Illustrates the difference of varying power density resulting in the workpiece [39].

Considering the temporal effect of the process and the speed at which the laser beam traverses speed,  $v$  the heating time can be expressed as the beam interaction time. The product of power density and beam interaction time is the Energy Density (ED), which profoundly influences the L-PBF process. Researchers previously represented ED in various ways and correlated its influence on the process outcome. Ciurana *et al.* defined ED by combining laser power with the beam diameter, layer thickness and scanning speed to suggest 151 J/mm<sup>3</sup> as the optimum ED required to process CoCrMo efficiently [40]. This was done by comparing various single melt tracks formed by varying these parameters, whereas C. Y. Yap *et al.* combined laser power ( $P$ ), scanning speed

( $v_p$ ), hatch spacing ( $h$ ) and layer thickness ( $t_L$ ) to form volumetric energy density as shown in *equation 4* [41]. This study proposes a useful analytical model for predicting the energy input required to process different metals using L-PBF. However, in practice, the average energy supplied in the L-PBF process to achieve full density is about four times the calculated value. This may be due to the assumptions of made to arrive at this analytical model in which the melt track is assumed to be a semi-circular cross-section. Also, the heat losses to the surroundings are ignored in the model [41].

$$ED = \frac{P}{v_p h t_L} \quad (J/mm^3) \quad (4)$$

M. Zavala-Arredondo *et al.* compared the densification mechanism in AlSi10Mg using continuous and pulsed laser systems. This model introduced three different parameters, namely volumetric ( $J/mm^3$ ), areal ( $J/mm^2$ ) and linear ( $J/mm$ ) energy density as a power factor model [42]. Though it managed to characterise the melt pool dimensions against specific point energy, it fell short of accurately predicting it. U. Scipioni Bertoli *et al.* concluded that since ED is being a thermodynamic quantity, it is impossible to fully capture complex physics in laser melting, such as Marangoni flow, hydrodynamic instabilities and recoil pressure [43]. Given that the melt pool and its characterisation determine the final track morphology, process optimisation in L-PBF would be improved if this morphology could be forecast through mathematical modelling and simulation. In order to understand the modelling of the L-PBF process, it is essential to first understand the heat and mass transfer during the interaction between the laser and the powder materials.

### 2.5.3 Heat and Mass Transfer

The absorption of laser energy takes place in a thin layer at the surface of the powder bed. Incident electromagnetic radiation prompts the release of free electrons and induces lattice vibrations, yielding heat. The bulk of this heat is conveyed through a conduction method within the material. As the metal powder reaches its melting point, a melt pool is formed, which shifts the energy transfer to a convection mechanism within the melt pool. During laser material processing, the workpiece and the laser beam often move relative to each other. This relative motion makes heat conduction time-dependent, when viewed from



the perspective of the workpiece. However, from the laser beam's reference frame, it remains stationary, with an added conduction heat flow term. Consequently, the energy transport equation can be expressed as follows, where  $T$  is the temperature,  $\rho$  mass density,  $c$  specific heat,  $C_v$  heat capacity for constant volume,  $\omega$  absorbed energy per volume,  $\vec{v}$  velocity,  $\vec{q}$  heat flux density and  $K$  heat conductivity [37], [44].

$$\frac{\partial \rho c_{\vartheta} T}{\partial t} + \vec{v} \cdot (\rho c_{\vartheta} T \vec{v}) = - \vec{v} \cdot \vec{q} + \omega \quad (5)$$

$$\vec{q} = -k \vec{\nabla} T \quad (6)$$

For virtually incompressible fluids, the difference in  $C_v$  can often be overlooked. The heat conduction problem is solvable only if the right initial and boundary conditions are applied to *equation 5* and *equation 6*. At a specific time,  $t_0$ , the temperature must be defined throughout the entire area of interest. The heat conduction equation is quasi-linear since variables such as  $\rho$ ,  $c$ , and  $K$  can depend on temperature, but the highest derivative is linear. The velocity  $\vec{v}$  typically varies with space. When the material is molten, the heat conduction equation generally needs to be solved alongside the Navier-Stokes equation and the mass transport equation. Solving the linear problem for space-dependent flow velocity typically requires numerical methods. For precise results, one must solve the Navier-Stokes and mass transport equations in tandem with the conduction equation, considering suitable boundary conditions and temperature-dependent variables. This highlights the importance of numerical simulation in laser interactions [44].

#### 2.5.4 Melt Pool Dynamics

Single melt tracks are crucial for the L-PBF process, where repeated deposition of these tracks builds layers to form a 3D object. Studying single tracks is essential for optimising any new laser based processes. L-PBF resembles a welding process, where a moving laser creates fusion zones along its path. Energy transfer in the material occurs through heat conduction and convection within the melt pool. Incident laser radiation generates high temperatures in the powdered materials, spreading initially via thermal conduction. As the material heats, molten pools form along the path of the laser beam and solidify as the laser

moves away. Subsequent formation of adjacent melt tracks causes remelting of the earlier solidified tracks, a cycle that continues through the layering process. These melting, solidification, and remelting processes are critical to the L-PBF melting regime.

The result of absorption and heat conduction is the formation of a melt pool. A convection flow initiates within the melt pool induced by the temperature gradients from the intense laser radiation. For a Gaussian beam, the intensity distribution is at the centre of the laser beam. It manifests a temperature gradient in the radial direction since the temperature at the centre of the melt pool is higher than at the edges. A temperature gradient induces a surface tension gradient,  $\sigma$ , given that surface tension is temperature-dependent. The free surface on the melt pool and subsequent surface tension gradient caused by this temperature gradient result in a flow of molten metal from the centre to the edges of the melt pool, as shown in *Figure 2.10 (a)*, and the gradient of  $\sigma$  in the  $y$ -direction shown in *equation 7*. Shear stresses lead to material flow along the solid-liquid boundary at the edges of the melt pool, moving downwards. For metals and alloys, if  $\frac{d\sigma}{dT} < 0$  the material flow is generally from the centre to the edges, but in some cases even a positive gradient reverses the flow. Either way, the material flow causes deformation of the melt pool, as shown in *Figure 2.10 (b)*. This convection flow behaviour is known as Marangoni convection [22].

$$\frac{\partial \sigma}{\partial y} = \frac{\partial \sigma}{\partial T} \cdot \frac{\partial T}{\partial y} \quad (7)$$

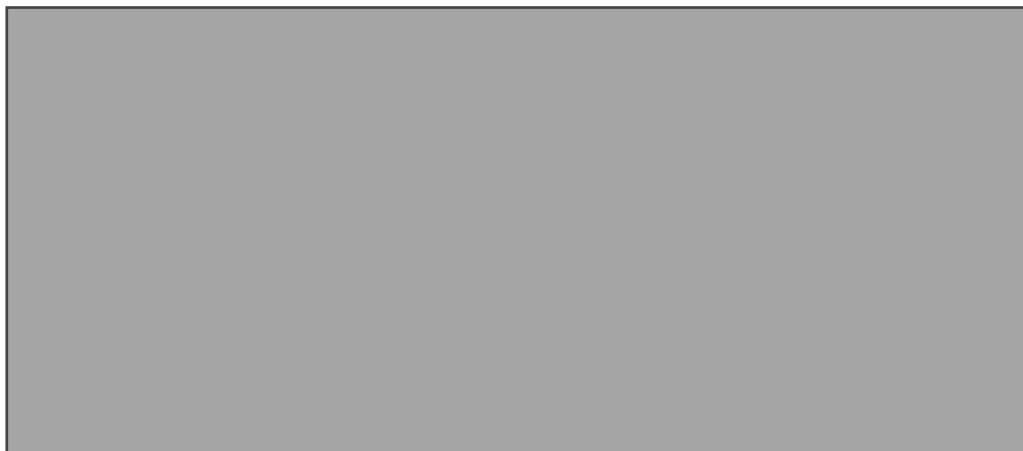


*Figure 2.10: Illustrating Marangoni convection driven by the surface tension gradient [22].*

Convection is a vital part of the heat and mass transfer mechanism of laser-based AM, as the magnitude and direction of the molten metal ultimately define

the fusion zone geometry. A study at the Lawrence Livermore National Laboratory demonstrated the importance of Marangoni convection in shaping the melt pool flow and its influence on the spattering and pore defects in the L-PBF [45]. Factors other than energy density influence the behaviour of Marangoni convection, as C. X. Zhao *et al.* pointed out that in laser welding, flow reversal in the melt pool was observed due to the dissolution of oxygen in the liquid metal [46]. This means that the surface tension and its temperature dependence are also determined by the alloying elements or the presence of oxidation agents.

A prerequisite for Marangoni convection is a free surface on the melt pool. The presence of a solid layer, often resulting from an oxide layer, inhibits the development of convective flow. Thus, shielding the melt pool is very important in this context. The alloying elements in the powder material and the oxide layer on the surface of the molten pool also dictate the convective flow along with the temperature gradient [44]. This phenomenon is significant for maintaining the shape, size and stability of the molten pool. Furthermore, Marangoni flows greatly enhance heat and mass transfer, influencing the solidification rate, microstructure and overall part properties [47].

### **2.5.5 An Insight into Melt Pool and Single-Track Formation**

A melt pool in L-PBF is a transient, minute feature formed when a concentrated laser beam melts powdered material. The size and stability of the melt pool are determined by factors such as the power and speed of the laser beam, as well as the thermal characteristics of the material. The edges of the melt pool, adjacent to the unmelted powder, constitute the heat-affected zone. Research indicates that, given a consistent thickness of the powder layer, the depth of the melt pool increases with laser power. Conversely, the width of the melt pool is strongly influenced by the diameter of the laser beam, the scanning speed, and the laser power, as referenced in studies [48] and [49]. The continuous formation of a melt pool results in the creation of a single track, with the development of this track progressing in accordance with the scanning direction of the laser beam.

The principal characteristics of single tracks include their width, penetration depth, and height. When the laser power and interaction time are increased, the

track width significantly exceeds the size of the laser spot. The depth of the track is affected by the laser power density, with higher power densities resulting in deeper melt tracks. Typically, a melt track possesses a semi-spherical shape in its cross-section, and the aspect ratio of depth to width of the melt pool generally does not exceed 1:2 [1]. For example, *Figure 2.11* illustrates a typical cross-section of a melt track formed during the L-PBF of SS grade 904L powder on a steel substrate [50].



*Figure 2.11: A typical cross section of a melt track formed during L-PBF [50].*

At a mesoscopic level, the interaction between the laser and powder material can yield more complex outcomes. Bidare *et al.* observed an intensive jet-like flow in the gas phase under different conditions, using Schlieren imaging to capture these dynamics. *Figure 2.12* displays images of the laser beam interacting with the powder. Throughout this process, the laser energy can overheat the material to the point of boiling, leading to intensive evaporation. This phenomenon significantly affects the stability and morphology of the melt pool, influencing the microstructural properties of the fabricated part. Additionally, this intense evaporation can lead to spattering, where molten particles are ejected from the melt pool, potentially causing defects in the build and affecting the overall quality and density of the final product [51].



*Figure 2.12: The figure shows a sequence of composite schlieren images captured at the specified times following the initial exposure of the powder to the laser during a single-track scan [51].*

To determine the optimal melt track parameters, an optimisation process is carried out tailored to the specific machine-material configuration. The ideal energy density, or process window, for achieving the optimal melt track is identified from the study. Bertoli *et al.* investigated the deposition of 316L stainless steel with varying parameters and found that increasing laser power or scan speed led to a degradation in track shape, ultimately progressing to the balling regime. These tracks were deposited at the same energy density ( $242 \text{ J/mm}^3$ ), but achieved different results with increased laser power and speed, demonstrating a transition from the continuous to the irregular and balling regimes, as illustrated in *Figure 2.13*. It is crucial to acknowledge that while energy density is a significant thermodynamic measure, it fails to fully represent the intricate physics involved, such as Marangoni flow, hydrodynamic instabilities, and recoil pressure. These dynamics are responsible for driving heat and mass transport throughout various sections of the melt pool and ultimately dictate the final track morphology [52].

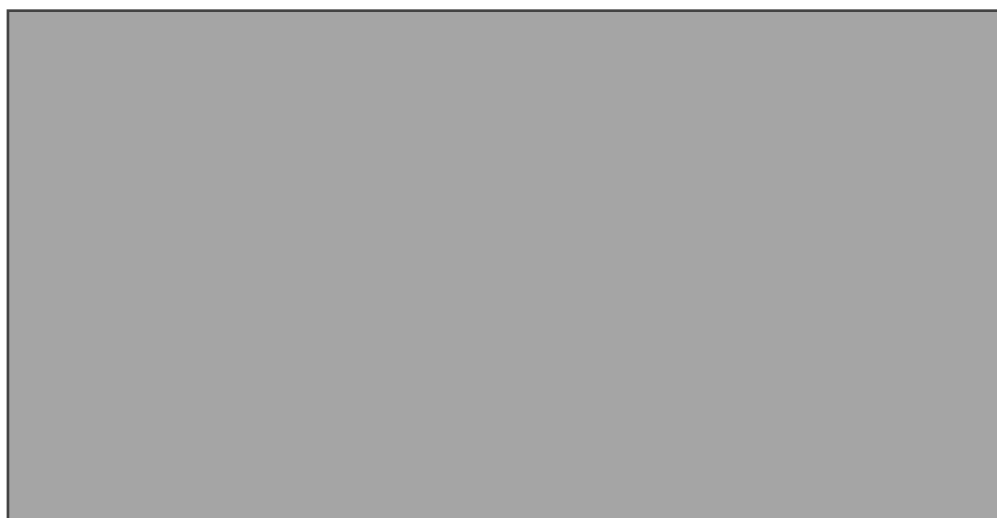


*Figure 2.13: Figure displaying five tracks deposited at the same energy density, with increasing laser power and scan speed from top to bottom [52].*

To better understand these complex interactions on a mesoscopic scale, process modelling is employed, focusing on capturing the thermophysical interactions between the laser and the powder materials. The subsequent section explores a range of modelling techniques used within AM, specifically addressing the interaction between laser energy and powder materials in processes such as L-PBF. These models are essential for comprehensively understanding the thermophysical and mechanical dynamics occurring during AM fabrication.

## 2.6 Modelling Approaches in L-PBF

Mesoscopic numerical simulations are part of the process required to understand the multi-physical interaction between the laser and powder particles. Insight into solidification and cooling rates, as well as the thermal history of the melt tracks, is gathered from these models. An example of a typical framework is illustrated in *Figure 2.14*. According to this framework, the L-PBF process cycle and modelling tools are seamlessly incorporated into the design phase. On a larger scale, build and residual stress simulations are executed at the part level. Coupled with in-situ and process monitoring data, this framework aids in refining and further optimising the process. Alongside design and process optimisation, numerical simulations have been pivotal in addressing L-PBF defects. This was evidenced at the Lawrence Livermore National Laboratory, where simulations predicted residual stresses in L-PBF-constructed parts. These findings, consistent with experiments, were instrumental in refining processing parameters for 316L parts [53].

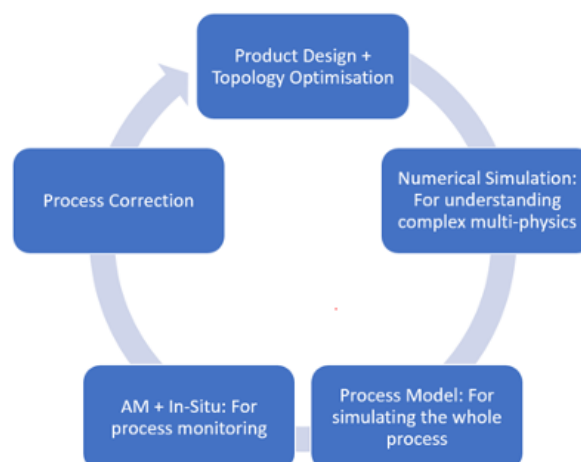


*Figure 2.14: An AM process optimisation model adapted from Ref [53].*

Raghavan *et al.* used a thoroughly tested analytical model of laser welding to calculate melt pool shapes and thermal cycles during the DED processing of Ti6Al4V alloy, and validated these calculations against thermographic data. The study highlights that thermography-based monitoring systems, which only capture the top surface geometry of the melt pool, do not provide sufficient data to accurately predict melt depth. For example, while the top surface dimensions of the molten pool might appear similar under different laser processing settings, significant variations can exist in the depth and volume of the molten pool. Furthermore, the analytical models used in this study failed to account for critical phenomena such as Marangoni flow and convection, which significantly impacted the melt pool depth parameters. Bridging this gap can be achieved by integrating thermography with numerical simulation data, thereby offering a more comprehensive solution that provides precise estimations of molten pool shapes, thermal cycles, and solidification parameters, and enhances the overall predictive capability beyond what analytical modelling alone can achieve [54].

V. Manvatkar *et al.* employed a three-dimensional heat transfer and material flow model to simulate the fabrication of stainless steel structures using the DED process and found that the build geometry, peak temperature and temperature profiles are in fair agreement with the experimental data [55]. In L-PBF, numerous simulation studies have reached a level of alignment that is deemed acceptable when compared to experimental data. An example of this is demonstrated by Mohamad Bayat *et al.*, who used a commercial Computational Fluid Dynamics (CFD) software, Flow-3D, for simulating the L-PBF process with Ti6Al4V material. Their simulation accurately predicted the influence of input power on factors such as thermal absorptivity, heat transfer, and the morphology of the molten pool, including the formation of porosity. Additionally, X-ray and CT scans were employed to visualise the pores generated during the L-PBF process, and these findings exhibited excellent agreements with the simulation results [56].

Simulating laser based process presents significant challenges due to the complexity of phenomena such as multi-reflection of laser beams from powder material and high computing resources that are required for these simulations. Flint *et al* developed advanced simulation tools employing a sophisticated ray-tracing algorithm to accurately trace these reflections and capture phenomena

like Marangoni flow and phase changes. This simulation also accounts for the dynamic changes in substrate topology under high-energy photonic sources, driven by hydrodynamic forces and state transitions from fusion to vaporisation. The integrated thermal-fluid-dynamics framework within this tool enhances predictive accuracy for L-PBF. The solver, named *LaserBeamFoam*, uses this framework alongside a Fresnel equation implementation to precisely calculate the absorptivity of laser rays based on their incidence angle, facilitating deeper insights into the thermal and physical behaviours during these processes. *Figure 2.15* illustrates the simulation of the 316L stainless steel powder particles using *LaserBeamFoam*, as the powders undergo state transitions and topological changes while a laser heat source moves across the domain. The magenta line in the sub-figures marks the boundary between solid and fluid regions, while the white lines indicate the separation between metallic and shielding gas phases. The multireflection of the laser beam is captured during the process and the progress of the melting process with respect to the time is shown in *Figure 2.15 (a), (b) and (c)* [57].

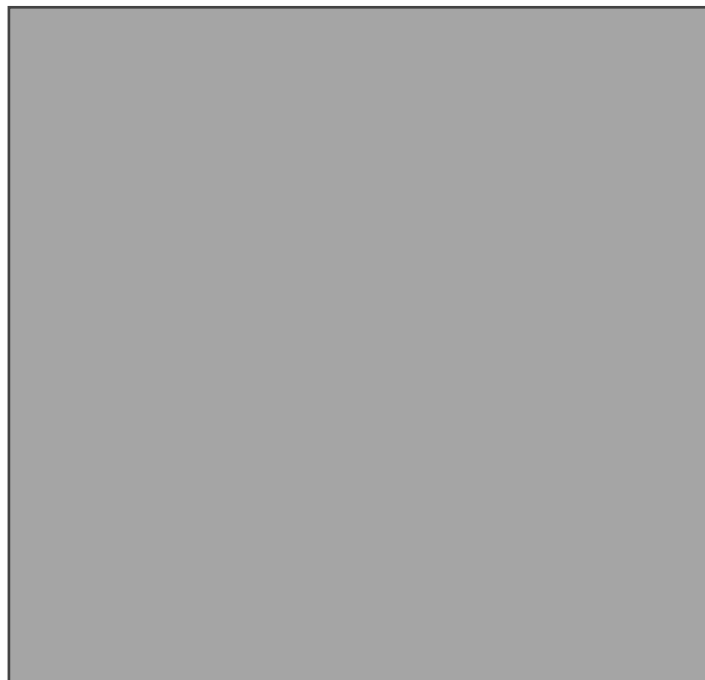


*Figure 2.15: This figure illustrates the transformation of 316L stainless steel powder particles as they undergo state transitions and topological changes while a laser heat source moves across the domain. The magenta line in the sub-figures marks the boundary between solid and fluid regions, while the white lines indicate the separation between metallic and shielding gas phases [57].*

Previously, there has been a limited endeavour to model the DAM process, and the appropriate methodology for such modelling remains to be identified. On



one hand, analytical modelling techniques present more straightforward solutions, serving as a more accessible approach for initial insight and understanding. These techniques often employ simplified assumptions and yield general solutions, making them useful for preliminary assessments or when dealing with problems where high precision is not the topmost priority. On the other hand, numerical techniques, although often more complex and computationally intensive, can provide a higher degree of accuracy and detail. Numerical methods, such as Finite Element Methods (FEM) and Computational Fluid Dynamics (CFD) are capable of handling complex geometries, boundary conditions, and non-linearities in material properties. They offer in-depth insights, making them invaluable when precision and detailed insight into process behaviour are important [58].

In the context of the DAM process, it is crucial to determine which of these methodologies, or potentially a combination of both, would be most appropriate. Given the novelty of DAM, a staged approach might be advantageous, starting with analytical models for a general understanding and then investigating deeper with numerical techniques for a more detailed understanding of the intricacies within the process. This will be undertaken in *Chapter 4: Modelling Methodology*. Numerical technique based on FEM and Volume of Fluid (VoF) technique based on CFD are briefly discussed in the following sections.

### **2.6.1 Finite Element Method (FEM)**

Numerical simulation techniques such as FEM can provide steady state or transient temperature distributions and melt pool dimensions. FEM is relatively easy to implement and computationally less demanding, and many existing software packages perform the simulation for L-PBF. Chiumenti *et al.* developed an FEA model to capture the thermal behaviour of multiple layers during L-PBF of Ti6Al4V and compared it with experimental results [59]. Song *et al.* demonstrated the use of ANSYS™, a commercial software capable of solving FEM problems and developed a models to predict the temperature distribution during L-PBF [60]. The main limitation of the FEM approach is that it does not consider the effects of the convective flow of liquid metal within the melt pool. In the FEM approach, the large workpiece model is broken into a mesh of smaller pieces. The material properties and process parameters are applied to each mesh, and the

governing equation is solved until the associated error function becomes eliminated or minimised [58]. This technique is thoroughly explained in *Chapter 4 Section 4.3*.

### 2.6.2 Volume of Fluid (VoF) Method

In a numerical simulation, free surfaces or boundaries cause difficulties when the solution region changes during the simulation. The changes in the solution region include changes in the size and shape of the boundary and, in some cases, losses or gains of free surfaces. For example, a L-PBF process is highly dynamic and involves phase changes and the loss of materials through evaporation. The VoF method can solve highly transient fluid flow problems involving free surfaces [61]. It is commonly used to mathematically model fluid dynamics, environmental engineering, hydrology, metal casting and laser-based manufacturing processes [62], [63]. This method can be applied in melt pool simulation to understand the heat transfer, fluid flow and phase transformation during the melting and solidification processes. M. Khorasani *et al.* applied this methodology to the L-PBF processing of Inconel 718 and accurately estimated the melt pool depth and bonding behaviour of the powder materials [64].

The complex physical phenomena involved in a L-PBF process occur at a mesoscopic scale, and the melting and remelting are complete within microseconds. Consequently, any real-time observation during experiments to obtain a comprehensive understanding becomes a challenge. Mesoscopic modelling could be used to simulate and comprehend the melting and remelting processes that happen within microseconds. By modelling these processes at the mesoscopic scale, one can gain detailed insight into how different physical variables, such as temperature or pressure, evolve over time. *Figure 2.16* illustrates several of the mathematical models needed for the development of a robust simulation tool adept at handling mesoscopic complexity. The mathematical models illustrated encompass a range of factors, not confined to but inclusive of heat transfer, the fluctuating behaviour of density and viscosity with respect to temperature, phase changes, the response to gravitational forces, surface tension dynamics, Marangoni flow, the process of solidification as well as the precise representation of the Gaussian heat source. The outputs derived from

such a simulation can confer a thorough understanding of the process, thereby bolstering the real-time observations accrued during experimental procedures.

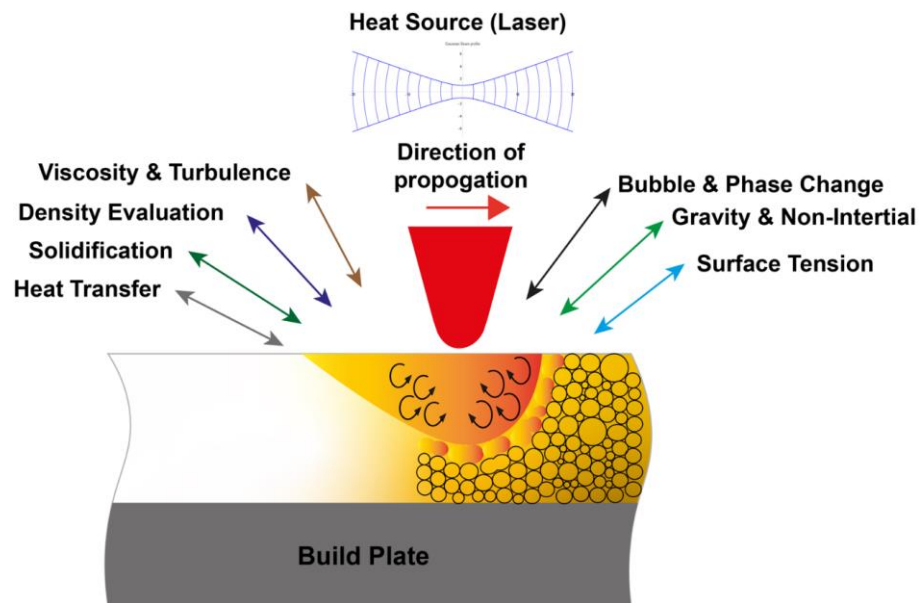


Figure 2.16: A representation of various mathematical models, including the Gaussian beam, as employed in a typical mesoscopic simulation using the Volume of Fluid (VoF) method.

In the context of L-PBF, it is well-recognised that the layer thickness and powder packing density exert an influence on the final quality of the manufactured parts [65][66]. Consequently, the accurate representation of powder particle distribution, layer thickness, and packing density emerges as an important component in any simulation aiming to replicate the L-PBF process [67]. VoF method has the capability to interpret phenomena such as powder spreading and compaction in relation to a range of variables, including but not limited to powder size distribution, material properties and the effects of cohesion. Furthermore, geometric influences, such as the motion and interaction of the roller or blade, can also be comprehended using these simulations [68].

A diverse range of methodologies exists for modelling AM processes, with some being more prevalent than others. *Table 2.6* presents a comparison of the commonly utilised methodologies for modelling the laser based AM processes.

Methodology	Description	References
<b>Analytical Method</b>	<ul style="list-style-type: none"> <li>Analytically solves basic heat conduction equation.</li> <li>Rosenthal Equation is one example.</li> <li>Outputs are temperature fields, melt pool dimension and cooling rates.</li> <li>Easy to use and less expensive.</li> <li>Uses constant thermophysical properties, ignores dominant heat transfer mechanisms and produces large errors.</li> </ul>	[41], [69], [70], [71], [72], [73], [74]
<b>Finite Element Method (FEM)</b>	<ul style="list-style-type: none"> <li>FEM solves the steady or transient state energy conservation equation.</li> <li>Predominantly solves the conduction problem and the convection within the molten fluid is ignored.</li> <li>Outputs are 3D temperature fields, melt pool dimensions and cooling rates.</li> <li>Requires computational resources and many existing software packages can be used.</li> <li>Overestimates the temperature and cooling rates due to the omission of convective flow in the model.</li> </ul>	[59], [75], [76], [77], [78], [79]
<b>Volume of Fluid (VoF)</b>	<ul style="list-style-type: none"> <li>Tracks the free surface of the molten pool.</li> <li>Mass conservation is maintained hence phase change can be calculated. The convective flow problem can be resolved.</li> <li>Outputs are 3D temperature fields, velocity vectors of the molten pool and cooling rate.</li> <li>Computationally intensive and may require high performance computing equipment.</li> </ul>	[56], [64], [68], [80]
<b>Finite Difference Method (FDM)</b>	<ul style="list-style-type: none"> <li>Solves 3D transient conservation equations of mass, momentum and energy.</li> <li>Outputs 3D temperature fields, melt pool dimensions velocity distribution and solidification parameters.</li> <li>Considers the effect of molten pool flow inside the melt pool.</li> </ul>	[75], [81], [82]
<b>Level Set Method (LSM)</b>	<ul style="list-style-type: none"> <li>Track the free surface of the molten pool.</li> <li>Outputs are 3D temperature fields and velocity distribution.</li> <li>Computationally intensive.</li> </ul>	[83], [84]

Table 2.6: Comparison of modelling methodologies employed in AM.

## 2.7 Surface Roughness

During the course of L-PBF, there is potential for molten metal to coalesce into bead-like structures. This phenomenon arises from inadequate wetting of the underlying materials, and is consequence of surface tension effects. This phenomenon is referred to as "balling" and can be attributed to insufficient energy input. Balling manifests as the creation of a roughened surface, impeding the seamless deposition of subsequent powder layers. Consequently, this gives rise to increased porosity and heightened surface roughness in the manufactured component [85]. In order to understand the process and so mitigate the phenomenon of balling, it is necessary to undertake process optimisation. *Figure 2.17* outlines an example of a process parameter window, wherein the requisite laser power and scanning velocity required to achieve a uniformly smooth surface have been established through empirical investigations.

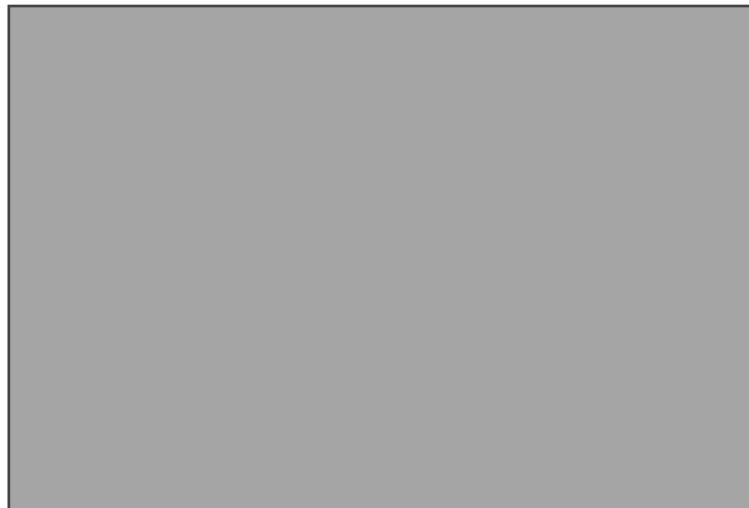


*Figure 2.17: Process window for L-PBF [85].*

## 2.8 Residual Stress

Residual stresses refer to the internal stresses that remain within a material even when there are no external forces applied. These stresses can arise from several sources during manufacture or processing of a material. For instance, when a force is applied and then removed, some stresses may not dissipate and will stay trapped within the material. Temperature differences within a material can also induce stresses, especially if one area cools or heats more quickly than another, leading to mismatches in contraction or expansion. Non-uniform plastic deformation can cause variations in stress levels across a material, with some

regions experiencing more deformation than others, resulting in stress imbalances. Furthermore, as materials cool, they contract, and if this contraction is uneven due to varied cooling rates, residual stresses can emerge. Lastly, phase transformations during manufacturing can introduce stresses, as materials transitioning from one phase to another might occupy different volumes or possess varied properties [20].

In essence, these stresses remain "locked" within the material even after the original cause (like the applied force or temperature gradient) has been eliminated. Over time, residual stresses can impact the performance, longevity, and structural integrity of the material, hence making their understanding is crucial in various engineering and design applications [86].

### 2.8.1 Characteristics and Origins of Residual Stresses

Residual stresses within materials can be categorised based on their scale of manifestation. As shown in *Figure 2.18*, macro residual stresses, or Type-I ( $\sigma^I$ ), are characterised by variations across dimensions significantly larger than individual grain sizes, primarily resulting from overarching component properties or external loading conditions. Conversely, micro residual stresses pertain to the intrinsic microstructure of the material, with Type-II ( $\sigma^{II}$ ) stresses emerging due to microstructural disparities spanning roughly the size of individual grains. The Type-III ( $\sigma^{III}$ ) stresses being localised within grains, predominantly attributable to crystalline irregularities such as dislocations. These distinctions, rooted in scale and origin, are pivotal for comprehensively interpreting material behaviour under diverse external conditions [23].

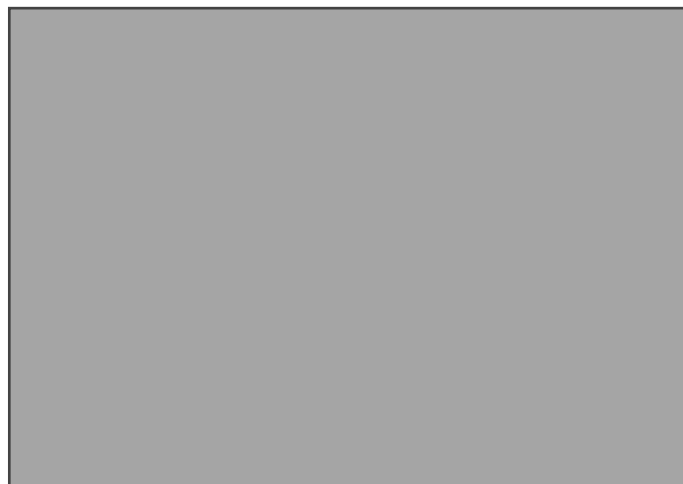


*Figure 2.18: Illustrating residual stress categorised according to the length scale [1]*

In material science, mechanically induced residual stresses emerge primarily from non-uniform plastic deformation inherent to the manufacturing procedures. Such stresses might naturally evolve as a by-product of specific processes or treatments. Alternatively, they can be intentionally engineered to achieve a desired stress profile within a component. Practices such as rod or wire drawing, welding, and precise machining methods, including turning and milling, frequently give rise to undesired surface tensile stresses. Conversely, methods like shot peening, autofrettage of pressure vessels, glass toughening, or cold expansion of apertures serve as techniques to introduce advantageous compressive residual stresses. Thermally induced macroscopic residual stresses arise due to disparities in heating or cooling regimes. On a more intricate microscopic scale, thermal residual stresses manifest from discrepancies in the coefficient of thermal expansion among distinct phases or constituents within a material. Additionally, chemically induced residual stresses materialise as a consequence of volumetric alterations linked with chemical reactions, precipitation, or phase metamorphoses. Notably, during chemical surface treatments and coatings, pronounced residual stress gradients may evolve within the superficial layers of components [23], [86]. Moreover, a tensile surface residual stress is generally unwelcome as it can precipitate issues such as fatigue failure, quench cracking, and stress-corrosion cracking. Nonetheless, in practical terms, no component is entirely devoid of residual stress, which inherently arises during the manufacturing process.

### **2.8.2 Characterising Residual Stresses in L-PBF**

Undesirable thermal stresses in L-PBF mainly arise from considerable temperature variations taking place over a short period. In the course of the L-PBF process, the laser beam heats and liquefies the material, consequently generating a temperature gradient in the solid material under irradiation. This results in the formation of the residual stresses as the material cools. If such stresses exceed acceptable levels, the fabricated components are at risk of cracking. The formation of residual stresses within components during L-PBF can be explained by two specific models: the Temperature Gradient Mechanism Model (TGM) and the Cool-Down Phase Model. According to the TGM model, the laser beam elevates the temperature of the solid material targeted during the L-

PBF process, causing it to expand, as depicted in *Figure 2.19 (a)*. This thermal expansion ( $\varepsilon_{th}$ ) is partially restrained by the surrounding cooler material, resulting in a compressive stress-strain scenario in the irradiated area. If the compressive stress surpasses the compressive yield stress ( $\sigma_{yield}$ ) of the material, the compressive strain will exhibit both elastic ( $\varepsilon_{el}$ ) and plastic ( $\varepsilon_{pl}$ ) characteristics, as illustrated in *Figure 2.19 (b)* [87][88].

In the Cool-Down Phase Model, the irradiated zone cools and subsequently contracts. This contraction is partially impeded by the plastic deformation that occurred during the heating stage, giving rise to a condition of residual stress in the irradiated area. As the process progresses, the layer most recently laid down contracts as it cools, its shrinkage being constrained by the preceding layer that was earlier deposited. This induces tensile stress ( $\sigma_{tens}$ ), in the latest-deposited layer, whilst imparting additional compressive stress into the prior-deposited layer or the material below the solidified melt pool as shown in *Figure 2.19 (c)*. During this stage, the plastic deformation ( $\varepsilon_{pl}$ ) partly restricts the contraction of the material within the irradiated zone, leading to the accumulation of residual tensile stress ( $\sigma_{tens}$ ), as illustrated in *Figure 2.19 (d)* [87].



*Figure 2.19: Illustrating the mechanisms of residual stress formation in PBF [87].*



### **2.8.3 L-PBF Process Parameters and their Effects**

Within the L-PBF process, several process parameters impact the formation of residual stress within the components produced. The subsequent sections explore some of these parameters and their effect on residual stress.

#### **2.8.3.1 Layer Morphology**

According to Ref [89], the experimental data revealed that the highest tensile residual stress value was observed in the uppermost layer of the model, irrespective of the scanning speed.

#### **2.8.3.2 Hatch Spacing and Scanning Strategies**

In L-PBF, the cooling and solidification processes initiate when the laser beam moves away from the irradiated zone. The contraction rates of material areas are not uniform during this phase, potentially leading to non-uniform deformation along the tracks and inter-layers. Hence, the residual stresses and subsequent deformations are contingent upon the scanning direction. Ref [22] reported that the magnitudes of residual stress observed along the laser scanning direction were approximately double those observed in the direction perpendicular to the laser traversing laser. Furthermore, re-scanning with the laser leads to a reduction in tensile stress by approximately 55% [89].

#### **2.8.3.3 Energy Density and Cooling Rate**

Ref [21] explained that through the modulation of energy density, achieved by varying the laser power and exposure duration, one can reduce the cooling rate. This adjustment subsequently results in a reduction of residual stress, from 78 MPa to 55 MPa. It is suggested that reduced cooling rates inherently contribute to reduced residual stresses.

#### **2.8.3.4 Pre-Heated Powder Bed**

The average principal residual stress in the longitudinal direction for Ti6Al4V produced via L-PBF was documented as 214 MPa in Ref [90]. Introduction of a powder bed pre-heating temperature of 370 °C led to a notable reduction in this stress, bringing it down to 61 MPa. When the pre-heat temperature was increased to 470 °C, the residual stress further diminished to 25 MPa, and an even

more pronounced reduction was observed at 570 °C, where the stress was measured at a mere 1 MPa.

### **2.8.3.5 Post-Processes**

As per Ref [89], heat treatment at temperatures of 600°C and 700°C for a duration of one hour effectively mitigated the residual stress by approximately 70% in the standard chrome molybdenum steel produced via L-PBF. Conventional heat treatment techniques possess the ability to mitigate the enduring stresses present in components fabricated through L-PBF. Nonetheless, when L-PBF-generated parts exhibit a non-equilibrium martensitic microstructure, as seen in materials like Ti6Al4V, the effectiveness of standard thermal treatment approaches becomes insufficient in achieving the desired results.

### **2.8.4 Residual Stress Measurements**

There are two primary categories of residual stress measurements: destructive and non-destructive. In the destructive method, the strain within the material is measured to assess the internal stress distribution based on the principles of the generalised Hooke's Law. Commonly employed destructive measurements include the hole drilling method, contour method, curvature, and peeling method. On the other hand, non-destructive techniques employ X-ray, neutron diffraction, ultrasomic waves, and magnetic methods to measure the lattice strain and consequently calculate the residual stress within the material [20].

The hole drilling method stands as one of the common techniques used in L-PBF samples wherein strain gauges are utilised to quantify the strain consequential to stress relaxation following material extraction from a specimen. Within this technique, a small hole is drilled at the centre of a strain gauge rosette affixed to the surface of the component. The hole drilling eases the encapsulated stresses, precipitating a change in the strain state. This modification can be determined using the strain gauge. However, when dealing with a small specimen, this method poses challenges owing to the practicalities associated with affixing the strain gauges on to the specimen [23].

X-ray diffraction (XRD) emerges as a more cost-effective, faster, accessible, and commonly employed non-destructive technique for measuring residual stress [20]. Owing to the limited penetration capability of X-rays in metals, XRD is conventionally utilised for the assessment of surface and near-surface stress levels in standard laboratory apparatus. Such an approach aligns well with the present requisites for DAM. The principal aim is to inspect the residual stress levels instigated by the interaction of multiple diode lasers with the powder material. Notably, the specimens fabricated using the DAM prototype machine are of a relatively smaller size, rendering the hole drilling method largely impracticable.

#### 2.8.4.1 X-Ray Diffraction Method

Residual stress can lead to minor alterations in the spacing of a material's crystal lattice. These changes can be detected through the use of X-ray diffraction (XRD) technique. When X-rays are directed at a material, the X-rays are diffracted, or scattered, by the atoms in the material. The manner in which the X-rays are diffracted depends on the arrangement of the atoms, and thus, the diffraction pattern can provide information about the crystal structure. The induced residual stresses can cause small amount of distortions in the crystal lattice of the material especially changes in the spacing between the atoms, which can be detected using XRD methods. The diffraction occurs at an angle,  $2\theta$  defined by Bragg's law as shown in *equation 8* [20]. Any changes in the lattice spacing,  $d$ , result in a corresponding shift in the diffraction angle  $2\theta$ .

$$n\lambda = 2d \sin\theta \quad (8)$$

Where  $n$  is an integer denoting the order of diffraction,  $\lambda$  is the x-ray wavelength,  $d$  is the lattice spacing of crystal planes, and  $\theta$  is the diffraction angle.

The existence of tensile stress within the sample leads to a contraction governed by Poisson's ratio, thereby diminishing the lattice spacing and incrementally elevating the diffraction angle,  $2\theta$ . Upon rotating the sample through a specified angle  $\psi$ , the surface tensile stress induces an expansion in lattice spacing relative to the stress-free condition, subsequently reducing  $2\theta$ . By quantifying the shift in the angular position of the diffraction peak for a minimum of two orientations, as determined by angle  $\psi$ , one can compute the stress extant

within the sample surface. This surface resides in the diffraction plane, which encompasses both the incident and diffracted X-ray beams. The residual stress ascertained through X-ray diffraction represents the arithmetic mean stress within the region defined by the dimensions of the X-ray beam. One of the method employed for this process is called  $\text{Sin}^2\psi$  Technique.

#### 2.8.4.2 The $\text{Sin}^2\psi$ Technique

The  $\text{sin}^2\psi$  method is a commonly used XRD technique for residual stress evaluation. In this method, the sample is oriented at various tilt angles ( $\varphi$ ,  $\psi$ ), relative to the incident X-ray beam, and the resulting diffraction angles are measured. The lattice spacing  $d$  is calculated for each ( $\varphi$ ,  $\psi$ ), angle, and the strain  $\epsilon_n$  in the material is then determined. This strain data is often plotted against  $\text{sin}^2\psi$ , and a linear fit to the data points is used to determine the residual stress in the material. The stress,  $\sigma_\theta$  is calculated using the slope of the best fit line and the elastic constant (Young's modulus and Poisson's ratio) of the material. This method allows for the accurate determination of uniaxial or biaxial residual stresses within thin films or surfaces [91], [92].

The unit diffraction vector  $n$  is characterised by two angular parameters,  $\varphi$  and  $\psi$ , as illustrated in *Figure 2.20*. Here,  $\varphi$  represents the rotational angle of the diffraction vector about the  $S_3$  axis, while  $\psi$  defines the tilt angle of the diffraction vector relative to the  $S_3$  axis. The strain as gauged through X-ray measurements can be articulated utilising the elements of the strain tensor, in accordance with *Equation 9* [93].

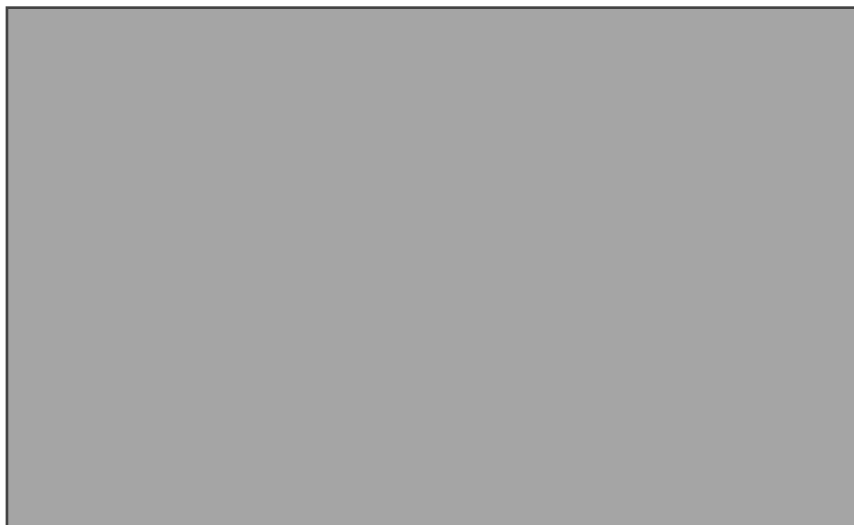


*Figure 2.20: Definition of parameters used in X-ray measurements [93].*

$$\varepsilon_{\varphi\psi} = \varepsilon_{11} \cos^2 \varphi \sin^2 \psi + \varepsilon_{22} \sin^2 \varphi \sin^2 \psi + \varepsilon_{33} \cos^2 \psi + \varepsilon_{12} \sin(2\varphi) \sin^2 \psi + \varepsilon_{13} \cos\varphi \sin(2\psi) + \varepsilon_{23} \sin\varphi \sin(2\psi) \quad (9)$$

The diffraction vector  $\mathbf{n}$  can be described using  $\varphi$  and  $\psi$  as

$$\mathbf{n} = \begin{pmatrix} n_1 \\ n_2 \\ n_3 \end{pmatrix} = \begin{pmatrix} \sin\psi \cos\varphi \\ \sin\psi \sin\varphi \\ \cos\psi \end{pmatrix} \quad (10)$$

Substituting *equation 10* in *equation 9* becomes

$$\varepsilon_{\mathbf{n}} = n_1^2 \varepsilon_{11} + n_2^2 \varepsilon_{22} + n_3^2 \varepsilon_{33} + 2n_1 n_2 \varepsilon_{12} + 2n_1 n_3 \varepsilon_{13} + 2n_2 n_3 \varepsilon_{23} \quad (11)$$

*Equation 11* is the fundamental equation in the diffraction vector representation. Should the diffraction vector be characterised by two angular coordinates ( $\varphi$ ,  $\psi$ ), a pole figure may be generated, as depicted in *Figure 2.21 (a)*. The diffraction vector of an X-ray irradiation of the  $\sin^2\psi$  method corresponding to  $\varphi = 0$  and  $\psi = 45^\circ$  is shown in *Figure 2.21 (b)*. It is important to observe that multiple radiations and detections are needed for the identification of the peak position within the diffraction ring when utilising a two-angular-coordinate approach. Conversely, XRD instruments equipped with an area detector demand one X-ray radiation and detection for the determination of the peak position pertinent to resolving  $\sin^2\psi$  for the sinular angle  $\psi$ .



*Figure 2.21: An example illustrating a pole figure (a) and the diffraction vector of an X-ray irradiation of the  $\sin^2\psi$  method corresponding to ( $\varphi = 0$  and  $\psi = 45^\circ$ ) [93].*

The  $\sin^2\psi$  method with single angular coordinate is applied in all work undertaken in this research. In this approach, the sample remains fixed in one orientation, and only the tilt angle ( $\psi$ ) is varied to obtain different measurements of lattice spacing. The limitation here is that this approach only captures the residual stress component along a specific direction. Therefore, to fully characterise the state of biaxial stress, the sample would have to be re-oriented manually and the experiment repeated along different axes.

In XRD, the positions and intensities of the diffracted X-ray peaks provide a 'fingerprint' of the material. The positions of the peaks are related to the distances between the atomic planes in the crystal lattice (as per Bragg's law), and the intensities of the peaks give information about the type and arrangement of atoms in the crystal lattice. When residual stresses alter the crystal lattice spacing, this changes the angle at which X-rays are diffracted by the material, leading to a shift in the positions of the diffraction peaks. The stress-induced changes in lattice spacing are generally very small, but XRD can detect these changes with a high degree of sensitivity. Therefore, XRD is a very powerful technique for measuring residual stresses in crystalline materials. It is also worth noting that the type of stress (tensile or compressive) can cause different shifts in the diffraction peaks. Tensile stresses increase the lattice spacing and cause a shift to lower angles, while compressive stresses decrease the lattice spacing and cause a shift to higher angles. By analysing the shift in the XRD peaks, it is possible to determine not only the magnitude of the residual stress, but also its nature.

The lattice spacing,  $d_{\psi}$  is a linear function of  $\sin^2\psi$ . Consequently, stress can be ascertained by measuring lattice spacings at various  $\psi$  angles. A linear relationship between lattice spacing and  $\sin^2\psi$  is established through the application of least squares regression. The stress,  $\sigma_{\phi}$  is then calculated from the slope of the best-fitting line, utilising *equation 12* for this purpose.

$$\sigma_{\phi} = \left( \frac{E}{1+\nu} \right)_{(hkl)} \frac{1}{d_{\phi 0}} \left( \frac{\partial d_{\phi \psi}}{\partial \sin^2\psi} \right) \quad (12)$$

## 2.9 X-Ray Diffraction of Ti6Al4V

In the titanium alloy Ti-6Al-4V, two principal crystalline phases are present: the alpha ( $\alpha$ ) and beta ( $\beta$ ) phases. The former,  $\alpha$ -Ti, is characterised by a hexagonal close-packed (HCP) lattice structure, whereas the latter,  $\beta$ -Ti, manifests as a body-centred cubic (BCC) lattice. Typically, Ti-6Al-4V specimens consist of a microstructure in which approximately 90% are  $\alpha$  laths, enveloped by grains of the  $\beta$  phase. Upon examination through X-ray diffraction, each phase reveals its own set of unique diffraction peaks.

Ref [94] has reported that in both EB-PBF and conventionally fabricated samples of Ti6Al4V, the Bragg peaks identified in XRD scans corresponded to hcp  $\alpha$ -Ti and bcc  $\beta$ -Ti structures. Interestingly, L-PBF processed Ti6Al4V samples

deviated from this norm, showing an absence of peaks attributable to  $\beta$ -Ti in their XRD patterns. *Figure 2.22* serves to illustrate these distinctions by presenting the diffraction peaks of Ti-6Al-4V alloy processed through various techniques: *L-PBF (a)*, *EB-PBF (b)*, and *conventional heat treatment and annealing (c)*. This contrast in peak profiles, particularly between L-PBF-processed samples and their counterparts, signifies the potential influence of fabrication techniques on phase composition.



*Figure 2.22: X-Ray diffraction pattern for Ti6Al4V alloy obtained in the L-PBF (a), EB-PBF(b) and heat-treated and annealed sheet (c) [94].*

The positional coordinates, amplitude, and breadth of the peaks discerned from XRD data offer invaluable insights into the material under analysis. Specifically, the locational attributes of each peak serve as an indicator of lattice parameters and, by extrapolation, furnish information regarding existing strains within the material. The amplitude or intensity of said peaks could potentially explain aspects such as the relative proportion of distinct phases, granular dimensions, and the tendency for specific grain orientations, commonly referred to as texture. Furthermore, the breadth (FWHM) of these peaks might be employed as a metric for ascertaining defect densities as well as the dimensions of domains that scatter coherently.

## **2.10 Thermography**

Common issues within the L-PBF process include gas entrapment, incomplete powder melting, fusion inconsistencies, and spattering, which all

culminate in porosity of the final construct. Traditional approaches for identifying these defects are often costly and time consuming. For post-production quality checks of AM components, Non-Destructive Testing (NDT) methods, such as X-ray Computer Tomography (CT) and ultrasonic scanning, are routinely utilised. *In-situ* process monitoring presents the benefit of sequential data acquisition for every layer, deploying a diverse range of sophisticated sensors. These sensors, used both in-situ and in-line, range from pyrometers to high-definition cameras and acoustic emission detectors. Monitoring melt pool dynamics in the L-PBF process amplifies the complexities of *in-situ* observation. However, with the advent of advanced thermographic methods, it has become feasible to undertake such monitoring, particularly with the aid of devices such as infrared thermal cameras. These methods not only offer real-time perspectives on melt pool activity but also facilitate immediate modifications, ensuring the best conditions for the process and enhancing the quality of the resulting component [95].

Khanzadeh *et al.* presented an *in-situ* method to predict porosity in Ti6Al4V components during DED. They linked porosity to the size and thermal distribution of the laser-induced melt pool. Thermal images of the melt pool were converted into bi-harmonic data clusters, which were compared to highlight anomalies and validated against NDT results. This approach reduced data processing by transforming imagery into bi-harmonic 3D data. While melt pool data is insightful, it does not fully capture the complex thermal dynamics. However, the research did associate the thermal history of layers with their microstructure [96].

In this research, a high-precision imaging setup is employed, consisting of a 16-bit Hamamatsu C13440 camera, paired with a Tamron 180 mm prime lens. This combination is specifically chosen for its capability to capture detailed thermal images with high resolution and clarity. The 16-bit Hamamatsu C13440 camera is known for its excellent dynamic range and sensitivity, which are crucial for accurately detecting and recording the subtle temperature variations and thermal phenomena occurring during the DAM process.



## 2.11 Ti6Al4V

In the titanium alloy Ti6Al4V, aluminium constitutes 6% by weight whilst vanadium comprises 4% by weight. The primary attributes of titanium alloys, notably their high specific strength and superior corrosion resistance, have contributed to their widespread recognition and adoption within the aerospace, chemical, medical, and leisure industries. In comparison to titanium alloys, only carbon fibre reinforced plastics exhibit a superior specific strength, although this advantage is retained only below 300°C. Titanium alloys maintain their utility at temperatures reaching just above 500°C; beyond this threshold, their application becomes constrained due to their oxidation behaviour. Moreover, titanium is distinguished as the ninth most abundant element and the fourth most prevalent structural metal in the Earth's crust, surpassed only by aluminium, iron, and magnesium [97].

Titanium exhibits polymorphism, crystallising in distinct crystal structures that are stable within specific temperature ranges. At lower temperatures, Ti6Al4V assumes a hexagonal close-packed (HCP) structure, referred to as  $\alpha$ -titanium. Conversely, at elevated temperatures, it adopts a body-centred cubic structure (BCC), termed  $\beta$ -titanium, as illustrated in *Figure 2.23*. This allotropic transformation occurs at the  $\beta$ -transus temperature of approximately 882°C. The presence of these two distinct crystal structures, along with the associated allotropic transformation temperature, is of paramount significance. This is because they underpin the extensive range of properties that can be realised in titanium alloys [97].

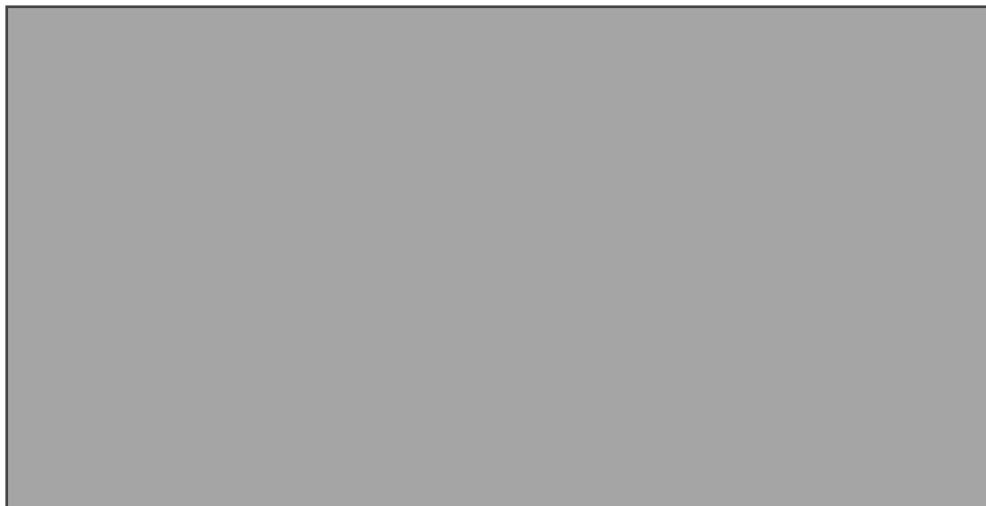


*Figure 2.23: Titanium  $\alpha$  (left) and  $\beta$  (right) crystal structure [97].*

When Ti6Al4V is cooled from the  $\beta$  phase field, the  $\{110\}$  planes of the BCC  $\beta$  phase, being the most densely packed, transform to the basal planes  $\{0001\}$  of the hexagonal  $\alpha$  phase. This results in the formation of a characteristic lamellar microstructure, often referred to as a basket-weave structure, as depicted in *Figure 2.24*. The mechanical properties of the two phases differ significantly: the  $\beta$  phase exhibits greater ductility but possesses lower strength compared to the  $\alpha$  phase. Below the  $\beta$ -transus temperature, diffusion processes that are dependent on time and temperature become markedly slower. As a result, the cooling rate from  $\beta$ -transus temperature plays a crucial role in determining the resultant microstructure of this alloy.



*Figure 2.24: Illustration of a typical Ti6Al4V  $\alpha + \beta$  Basket-weave microstructure [97].*

When Ti6Al4V is cooled slowly from temperatures exceeding the  $\beta$ -transus, the  $\beta$  phase predominantly transforms into globular  $\alpha$ . Conversely, with rapid cooling from temperatures surpassing the martensite start temperature, the BCC  $\beta$  undergoes a complete transformation to  $\alpha$  via a diffusionless transformation process resulting in a metastable, fine plate-like or acicular hcp  $\alpha'$  martensitic microstructure [98]. The suggested cooling rate for the martensitic transformation is approximately  $410^\circ\text{C/s}$ , transitioning from the  $\beta$ -transus to the martensitic transformation temperature [99]. Furthermore, during quenching from temperatures below approximately  $900^\circ\text{C}$ , a second type of martensite  $\alpha''$ , characterised by an orthorhombic structure, is observed [100].

### **2.11.1 AM of Ti6Al4V**

In the laser-based fabrication of Ti6Al4V, the rapid cooling mechanism gives rise to the formation of  $\alpha'$ -martensite. This consequently produces materials with

enhanced tensile strength, although at the expense of reduced ductility. *Figure 2.25* presents the differences in microstructures, tensile strength, and elongation of the Ti-6Al-4V alloy as produced through various AM methods, in addition to the traditional wrought and cast procedures.

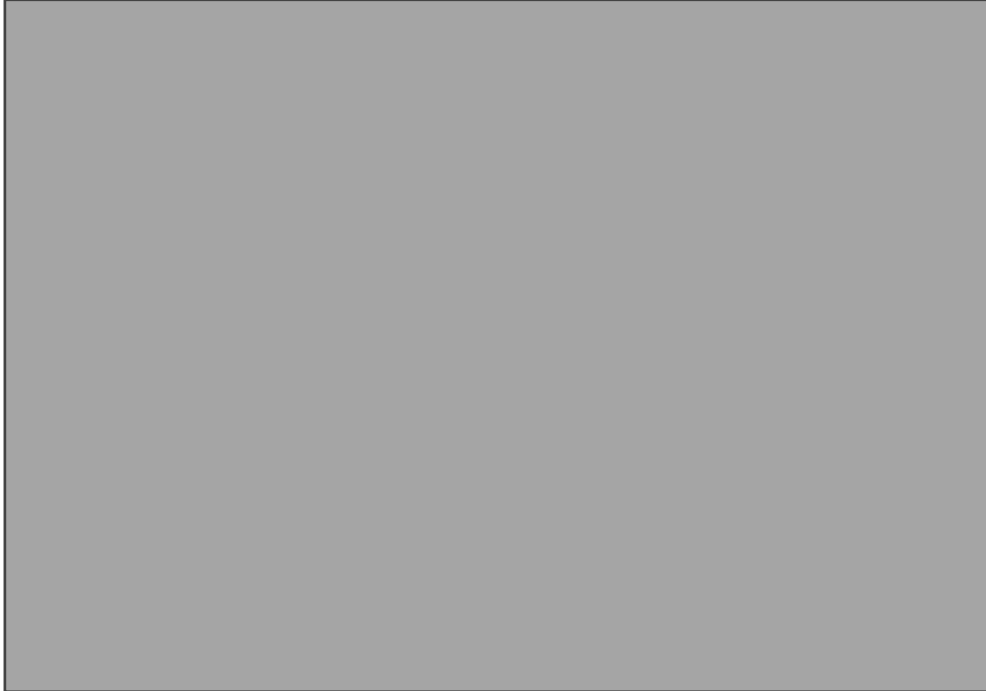


*Figure 2.25: Figure illustrating the variations in microstructure, tensile strength, and elongation of Ti-6Al-4V fabricated through different Additive Manufacturing (AM) methodologies [14].*

Materials processed via the EB-PBF display an  $\alpha + \beta$  microstructure, a consequence of the moderated cooling rate in a vacuum environment coupled with a heated substrate. This invariably leads to a reduction in tensile strength and an increase in ductility than Direct Metal Laser Sintering (DMLS), another acronym for L-PBF. The microstructure of cast materials is notably more granular, whilst that of wrought materials yields an equiaxed  $\alpha + \beta$  configuration. Notably, the Wire Arc Additive Manufacturing (WAAM) technique produces a microstructural pattern akin to that of cast materials, although on a more refined length scale. Furthermore, Direct Metal Deposition (DMD), provides more deposition rate than L-PBF and produces similar properties. In general, the elongation properties of Ti6Al4V tend to be reduced in the additively manufactured processes.

### **2.11.2 Microstructure and Cooling Rate in PBF of Ti6Al4V**

In the PBF process, the microstructure of metals and alloys is significantly influenced by the rapid heating and cooling cycles inherent to the technique. This

results in fine microstructures with unique grain orientations and distributions, often leading to enhanced mechanical properties compared to traditional manufacturing methods. The high cooling rates can produce a cellular or dendritic structure, while the layer-by-layer construction can introduce anisotropy in the material properties.

L-PBF and EB-PBF produce similar average melt pool temperatures. However, the thermal behaviour of the EB-PBF built parts is different due to the requirement for pre-heating and the maintenance of a high build chamber temperature of  $\sim 973$  K, which reduces the cooling rate compared to L-PBF [102]. The cooling rate reported for typical EB-PBF processing is in the range  $10^3 - 10^5$  K/s, whereas that for L-PBF is in the range  $10^5 - 10^6$  K/s [2]. In both cases, the intense heating and cooling cycles encourage martensitic phase transformation in Ti6Al4V, occurring in the cooling phase of the manufacturing process. The prior- $\beta$  grains transform to form a fine lamellar  $\alpha'$  or  $\alpha$  morphology, which again depends on the cooling rate of the molten pool.

In the case of EB-PBF production, the bulk of the microstructure is made up of columnar prior- $\beta$  grains surrounded by the  $\alpha$  grain boundaries. Furthermore, a transformed  $\alpha + \beta$  phase with both a colony and Widmanstätten morphology is seen within the columnar prior- $\beta$  grains, which make up the bulk of the materials [103]. In some cases, the presence of a transitional martensitic region is observed in EB-PBF and believed to be formed due to the regional high cooling rate from above the martensite start temperature ( $M_s$ ), which results in the formation of  $\alpha'$  [101]. However, the EB-PBF process can control the cooling cycle better than L-PBF through build chamber temperature controls, reducing  $\alpha'$  formation in general. A previous study demonstrated that in Ti6Al4V, a cooling rate above  $410^0$  C/s results in the formation of martensitic  $\alpha'$  microstructure, and as the cooling rate reduced below  $410^0$  C/s, the volume fraction of a secondary  $\alpha$  morphology increased to form a Widmanstätten  $\alpha$  formation [99]. This behaviour of Ti6Al4V was observed during the heating and cooling cycles of a circumferentially insulated quench bar in a lab environment.

The new grains created during solidification of the melt pool nucleate at a previously solidified polycrystalline layer and derive their crystallographic orientation from their surroundings, producing epitaxial nucleation and cellular

or dendritic crystallisation. In the case of Ti6Al4V, the nucleation, growth, subsequent transformation, size, and the location of prior- $\beta$  grains are essential in determining the mechanical properties of the produced parts. The grain refinement of prior- $\beta$  has been shown to improve the corrosion fatigue resistance of Ti6Al4V in surgical implants and the resistance of pure Ti against acid solutions [104]. Kobryn and Semisatin compared the microstructures of metal-mould-cast Ti6Al4V against the DED process and demonstrated that the grain size tends to decrease with an increasing cooling rate. The metal-mould-cast produced an equiaxed prior- $\beta$  grain morphology with grain sizes between 1750 – 3850  $\mu\text{m}$ . The laser-based DED process produced a columnar morphology with a grain size between 120 – 750  $\mu\text{m}$  [105].

## 2.12 Conclusions

The literature review indicates that the L-PBF process has been evolving to meet diverse industrial demands by incorporating multi-laser systems and employing green lasers with lower wavelengths. Despite these advancements, L-PBF faces significant challenges, as detailed in Section 2.2.2. Various efforts, including the use of diode lasers, are underway to address these issues. However, a viable alternative that could overcome these challenges comprehensively is still lacking. Furthermore, the current L-PBF systems are costly both to acquire and operate. A cost-effective solution that reduces the operational expenses of L-PBF would enable a broader range of industries to adopt this technology. In this context, DAM has shown potential as a cost-effective alternative. Initial capabilities of DAM have been demonstrated using Stainless Steel and Ti6Al4V, with a fibre-coupled multiple array system successfully processing Ti6Al4V. This suggests that DAM could provide a feasible solution to some of the challenges faced by L-PBF.

However, there is limited information available in the literature regarding technologies like DAM and the existing literature primarily focuses on parameter optimisation through experiments. There is a noticeable lack of detailed studies on further advancements or comprehensive modelling approaches, especially for systems that utilise a fibre-coupled diode laser array. In contrast, the literature on L-PBF is plentiful with information on modelling techniques, none of which are currently applied to DAM. According to the various modelling methodologies

reviewed for AM in *Table 2.6*, some could potentially be adapted to enhance the understanding of DAM.

Furthermore, induced residual stress remains a significant challenge in L-PBF. Various researchers have proposed different strategies for reducing residual stress, but the outcomes vary between studies, even when similar strategies are employed. Although some strategies are claimed to be more effective than others, the combined effect of these stress reduction approaches has not been widely accepted commercially. Therefore, stress-relieving through post-processing is still commonly employed for L-PBF parts. It is also noted that the DAM process intrinsically reduces residual stress due to the lower cooling rates associated with its slower processing speed. However, the extent of residual stress reduction during the DAM process has not been experimentally established.

### **2.13 Research Aims and Objective**

The limitations of the current L-PBF systems are discussed in *Section 2.2.2*. These systems use galvanometer mirror deflection mechanisms coupled with fibre lasers, which also hinder scalability and reachability. Additionally, the current L-PBF process generates high residual stresses within materials, due to the rapid cooling rates inherent in the process and worsened by the high scanning speeds and laser powers used. Furthermore, the lasers typically used in L-PBF have a wall-plug efficiency of only 20-30%, as discussed in *Section 2.2.3*, necessitating higher powers for processing materials with high reflectivity due to their operation at a 1070 nm wavelength.

In response to these challenges, DLs have emerged as a promising alternative, offering potential enhancements in efficiency and effectiveness within L-PBF systems. This development, outlined in *Section 2.3*, has been corroborated by recent research exploring the use of multiple laser spots from diode lasers to process larger areas and mitigate the limitations of conventional L-PBF, as highlighted in *Table 2.4*. Despite these advancements, the direct application of fibre-coupled laser diode sources remains underexplored.

This research aims to develop and evaluate a novel methodology using fibre-coupled multiple diode lasers operating at an 808 nm wavelength. This approach

employs an array configuration to facilitate processing over larger areas at reduced scanning speeds. Initial findings from this innovative approach were demonstrated by Alsaddah *et al.* in processing Ti6Al4V, as detailed in *Section 2.3.2*. However, their study did not extend to modelling the process or quantifying the residual stress formation within the samples. Moreover, the original equipment developed required modifications for effective material processing, which were not completed. This research seeks to address these gaps by further developing the equipment and methodologies to improve the understanding and application of fibre-coupled diode lasers in L-PBF systems.

1. Develop and enhance the DAM system to facilitate experimental research.
2. Explore and develop mathematical models capable of predicting melt pool morphology and temperature evolution within the DAM process and validate with experimental findings.
3. Capture, measure, and validate the melt pool temperature during the process using a high-resolution thermal camera.
4. Investigate the impact of using multiple lasers on the residual stress formation during DAM of Ti6Al4V.
5. Evaluate the DAM processes and propose recommendations for advancing this novel technique.

### 3 Chapter 3: Experimental Methodology

#### 3.1 DAM System

The Diode Area Melting (DAM) system, custom-designed and built at the University of Sheffield, was developed to support this experimental research. This system features a fully enclosed powder deposition setup equipped with a silicon blade for the precise deposition of powder layers. Laser power is delivered from the laser control unit via an optical fibre assembly to the laser head. The laser head, part of a Computer to Plate (CTP) unit as illustrated in *Figure 3.1*, incorporates a telescopic lens arrangement that collimates and focuses the beams passing through it. The fibre array in the laser system consists of a 2D array with 100 Diode Lasers (DLs) arranged in two rows (2D linear array of 2 x 50), which can create a 3.5 mm stripe of laser when all beams in a row are activated. Selective scanning is achieved by moving the laser head in the X-Y directions using a gantry system.

The original DAM system constructed for the research showed certain deficiencies that needed addressing prior to advancing with this study. The following section outlines the initial setup and the limitations thereof. It then explains the modifications implemented to enable the system to process powder materials by activating individual laser beams as required.

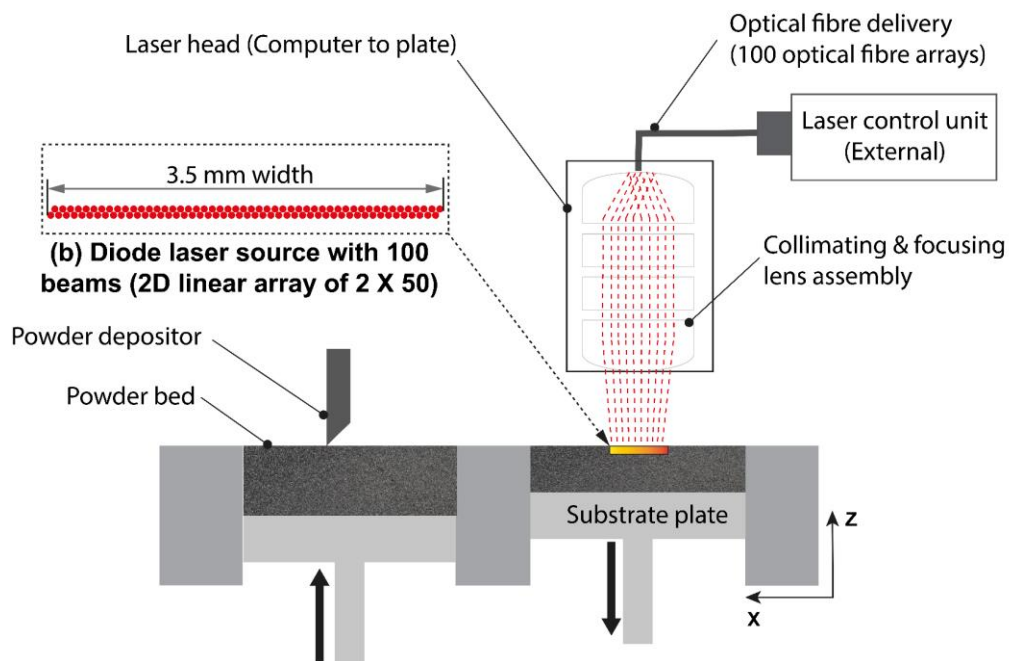


*Figure 3.1: Schematic of DAM.*



### 3.1.1 Initial Setup

The DAM system is divided into two main sections: one dedicated to the control of the laser system, including laser power and the cooling system management and the other focused on gantry system and build chamber management. At the outset of the research, the DAM system was equipped with a fully operational powder delivery system and an Argon knife edge for flow control. Additionally, a gantry system was in place and managed by a computer that controlled the movement of the laser head (CTP) along the X and Y axes, as well as the Z-axis positioning of the powder bed, using G-codes. This setup is controlled by four stepper motors that manage the mechanical movements of the wiper, powder bed, powder container, and laser head as depicted in *Figure 3.2*.

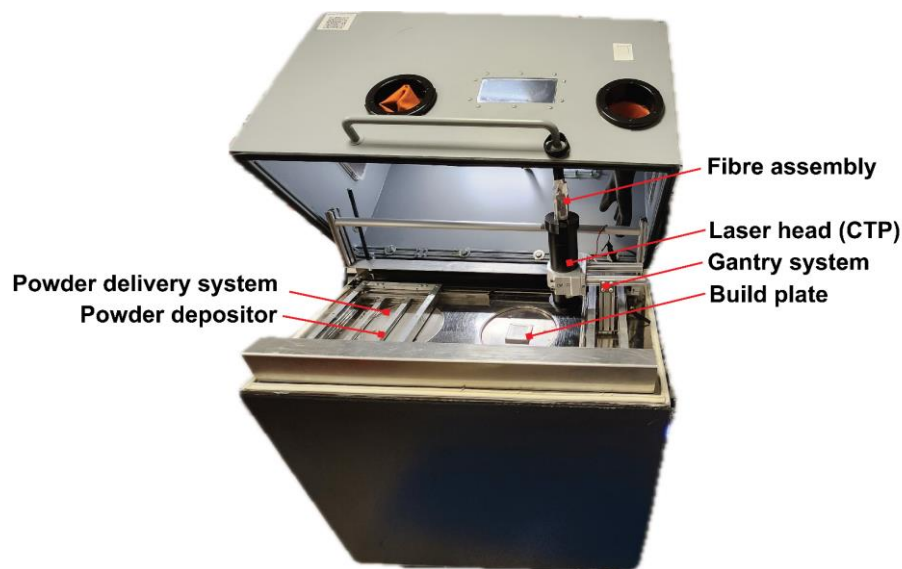


*Figure 3.2: The DAM 2 equipment used for this research.*

The first section manages critical functions such as adjusting laser power and maintaining an optimal operating temperature for the DLs. These functions are essential for sustaining optimal laser performance and preventing overheating, thereby ensuring precise control over laser characteristics, which significantly affect the quality and properties of the manufactured parts. This system, crucial for effective operations, was initially unavailable but was later developed for this research.

The second section addresses the gantry system and its role in managing the overall operation of the build chamber. This includes controlling the movement of the optical assembly, which is essential for directing the laser along the XY axes. The gantry's movements are enabled by a motor-driven pulley system,

facilitating precise placement within the build area, thus ensuring smooth and efficient operation critical for Powder Bed Fusion (PBF) processes. Additionally, the laser head assembly can traverse the powder bed in the XY plane at speeds up to 1500 mm/min. The CTP head can accelerate up to  $0.1 \text{ m/s}^2$ , with a constant speed maintained via G code.

### 3.1.1.1 Areas Requiring Enhancements

DLs are directly pumped by electric current and tend to overdraw current when operating at higher temperatures, particularly above  $25 \text{ }^\circ\text{C}$ . This can reduce the lifespan of the diode laser or may cause permanent damage. Therefore, a cooling system is crucial for optimal operation and efficiency of the diode laser system. This development is elaborated upon in *Section 3.1.6.1*.

Furthermore, DLs require a constant current for stable operation, and any current overdraw can damage the laser. Each DL needs a dedicated control circuit responsible for managing its operation. This circuit is crucial as it not only switches the laser on and off but also adjusts the power output as required during the process. Such precise control is essential to prevent damage due to overcurrent and to ensure the laser operates efficiently under varying conditions. This development is elaborated upon in *Section 3.1.6.2*.

### 3.1.2 Build Chamber

The build chamber of the DAM system is comprised of two sections: one for the CTP laser head and the other for the actual build process, as depicted in *Figure 3.3*. Initially, the system included a heating provision for the build area, but this feature was later removed as a health and safety precaution. The CTP laser head was affixed to rails within the gantry system, allowing it to move along the XY axis. This movement was facilitated by a pulley system driven by two motors.

In order to maintain an optimal atmosphere within the chamber, it is filled with argon gas. A provision for Argon gas flow (inlet and outlet) is integrated into the side of the chassis. Additionally, argon gas is directed over the build area to protect the build surface during the manufacturing process. Due to the high risk of oxide layer formation associated with the PBF process, the chamber is fully enclosed. During the operation, oxygen is pumped out using a vacuum pump and then the processing area is purged with argon gas to establish a controlled

environment. This process typically lasts about 1 to 2 hours and guarantees a completely inert atmosphere.

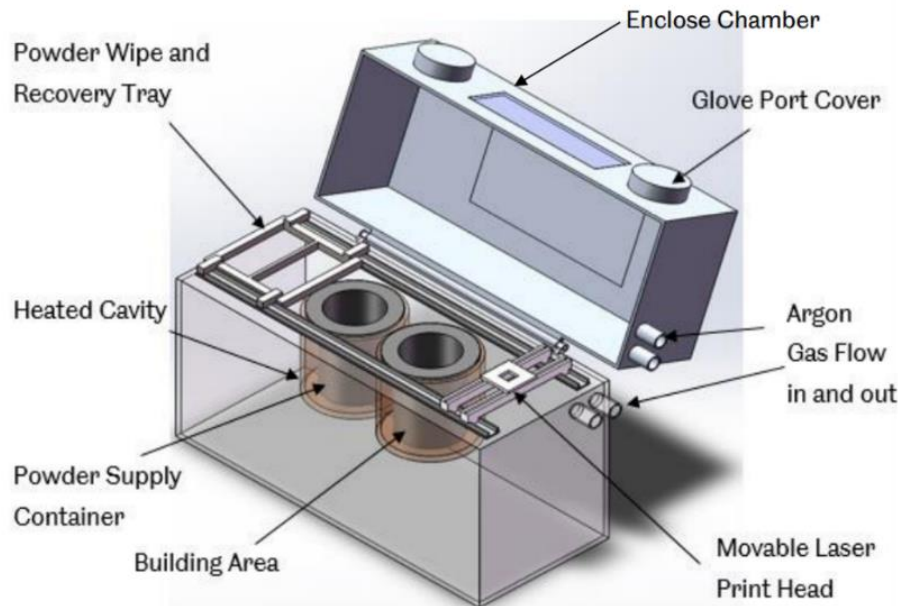


Figure 3.3: Illustration of the build chamber in the DAM setup.

### 3.1.2.1 Inert Gas Environment

The argon gas cylinder is directly connected to the gas flow inlet of the machine (shown in *Figure 3.3*), allowing argon to be continuously released into the machine. The gas flows inside the build chamber through an inlet valve located on the side of the machine and exits through a knife edge placed inside the chamber as shown in *Figure 3.4*. This knife edge provides a continuous flow of gas just above the melting surface/build plate, which not only removes any excessive spatter from the process but also maintains a conducive environment that helps to reduce oxidation during the process.

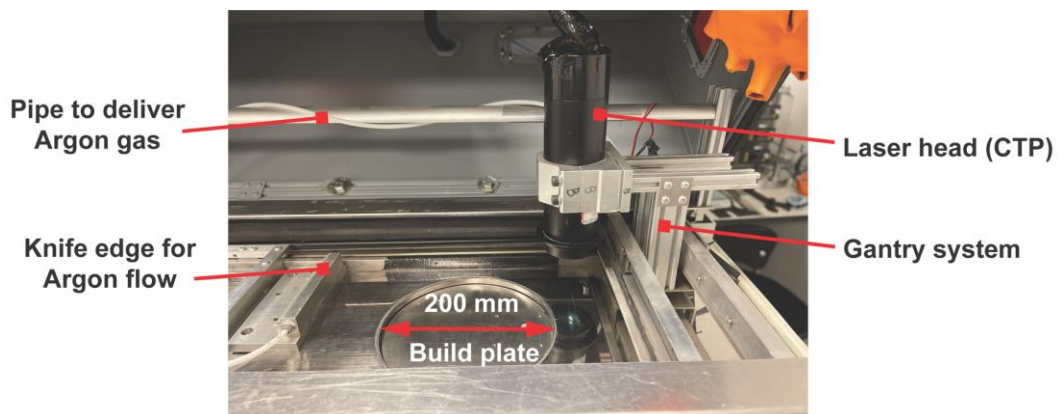
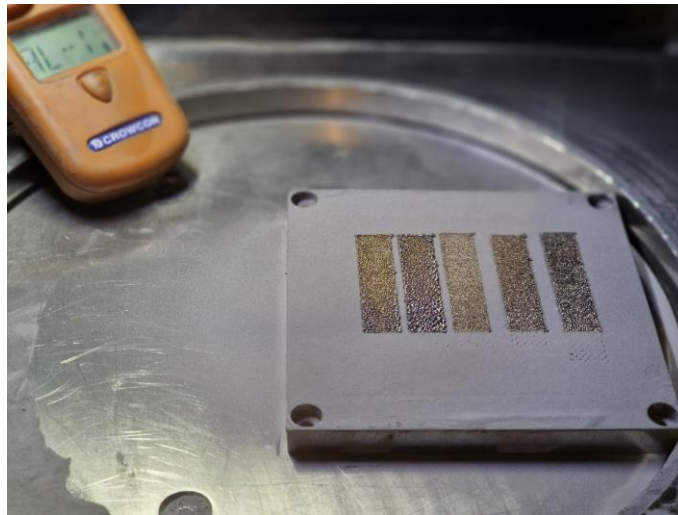


Figure 3.4: Build chamber showing the build area and the knife edge arrangement for a continuous gas flow.

The oxygen levels within the chamber are continuously monitored and maintained at no more than 0.1% during the fabrication process to ensure optimal conditions. Additionally, two glove ports have been integrated into the design. These ports provide operators with the ability to access tools within the evacuated chamber or to perform necessary interventions during the building process without compromising the controlled environment. A Crowcon T4 (manufactured by Crowcon Detection Instruments Ltd) gas monitor was used to monitor the oxygen content within the chamber. *Figure 3.5* shows an example of parts fabricated within the DAM system whilst calibrating for the oxygen content using a Crowcon gas monitor during the initial start up phase of an experiment. The experiment commences once the oxygen content reaches 0.1% by volume.



*Figure 3.5: Illustrating the fabrication of Inconel 718 within the DAM system.*

### 3.1.3 Laser Fibre Array

The delivery of laser beams from the DLs is achieved using coupled optical fiber cables, as illustrated in *Figure 3.6 (a)*. Each fiber cable is connected to one end of each DL, and the other end is brought to an adapter (incorporating a v-groove fibre array), as shown in *Figure 3.6 (b)*. The overall length of this fibre cable assembly from end to end is 1.2 meters, allowing for the placement of all the DLs, their controllers, and cooling systems outside the build area. The laser array is organized into two rows, with 50 fibers in each row, creating a 50 x 2 array as depicted in *Figure 3.6 (c)*.

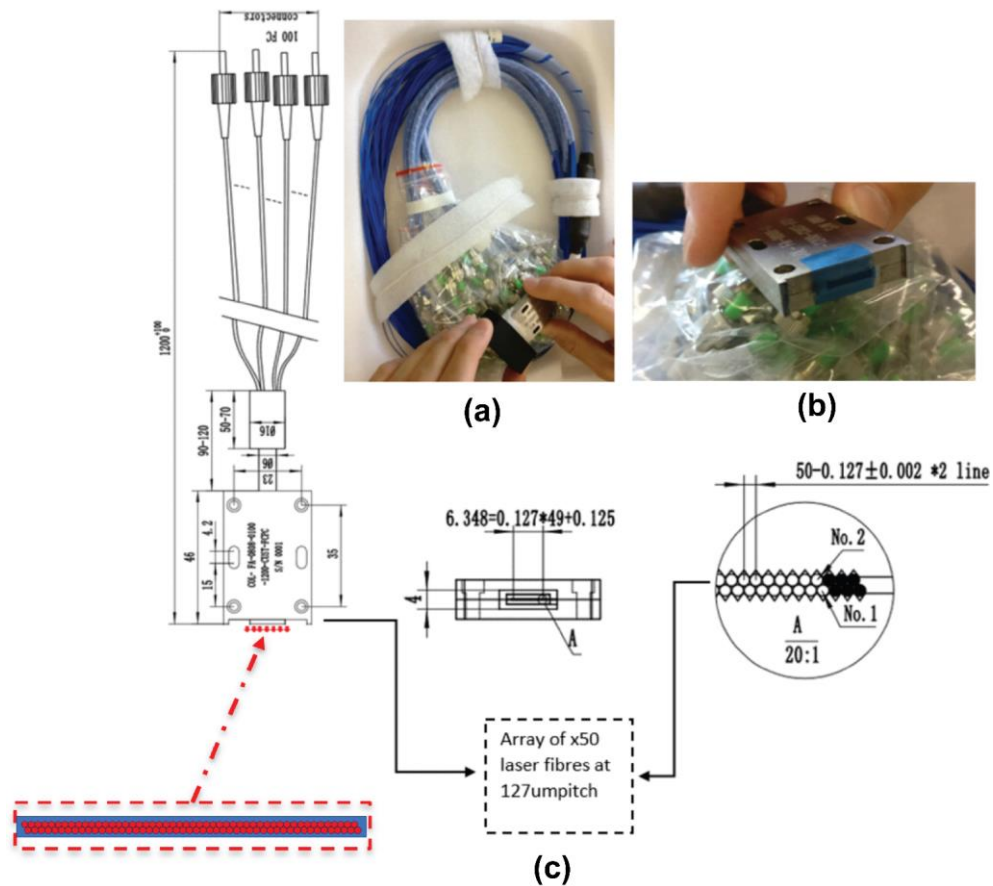
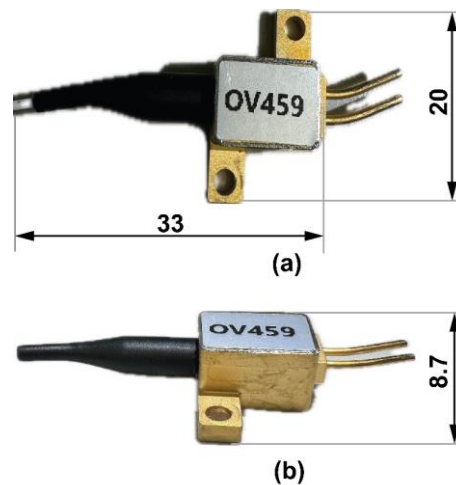


Figure 3.6: Arrangement of the fibre array utilising 50 X 2 fibres: Fibre cables in the array (a), the adaptor which connects to the CTP head (b), and the schematic of the fibre array assembly unit; all dimensions in mm otherwise specified (c).

For the experiments conducted in this research, a single row of this array was used. The fiber-coupled DL modules are linked to a specially manufactured 2-D fiber array head (2D-FAH). This 2D-FAH comprises a 2D array of v-groove lines. Each linear array contains 50 multimode fiber channels, each having a 105  $\mu\text{m}$  core diameter and a numerical aperture of 0.22 NA. To ensure the necessary overlap of adjacent melt pools for achieving high part density, the fibers were precisely positioned with a center-to-center spacing of 127  $\mu\text{m}$ , resulting in a total width of 6.35 mm before collimating and focusing the beams. Each diode laser connected to the fiber array emits laser light at a wavelength of 808 nm and a maximum optical output power of 4.5W. The optical assembly generates a Gaussian laser beam with a  $1/e^2$  diameter of 65  $\mu\text{m}$ . This configuration yields a laser radiation stripe that is 3.5 mm wide (after focusing), employing a total of 50 diode lasers in a row, resulting in a combined laser power output of 225 W. The dual-row configuration of this particular laser array enables the use of a maximum of 100 DLs. The width and energy density of the laser stripe can be precisely controlled by activating the necessary number of lasers.

### 3.1.4 Diode Laser

The 808nm wavelength fiber-coupled DL was procured from a supplier based in China, and *Figure 3.7* illustrates its key dimensions in both the top view (a) and side view (b). A fiber cable with a core diameter of  $105\ \mu\text{m}$  is employed for DL coupling, and this cable will be linked to the CTP laser head assembly. To regulate each individual DL, a commercially available power supply, DPS3005 is employed, providing a consistent current to the DL. The length of the fibre cable attached to the DL is 800 mm.



*Figure 3.7: Illustrating the dimensions (in mm) of the diode laser top view (a) and side view (b).*

The performance of the DL is sensitive to the operating temperature of the device. The ideal operational temperature range falls within  $15$  to  $25\ ^\circ\text{C}$ . To manage the temperature during operation, a cooling system is employed, featuring a thermoelectric cooler (TEC) fastened on top of a copper plate and an aluminum heatsink as described in *Section 3.1.6.1*. This setup effectively dissipates heat from the DL. To assess the output power of the DL, experiments were conducted using a Thorlabs PM400 power meter, and the power-current (P/I) curve is illustrated in *Figure 3.8*. It is notable that the DLs were consistently maintained at an operating temperature below  $20\ ^\circ\text{C}$  throughout the experiments. The power output was set at  $4\ \text{W}$ , and the current required to achieve this  $4\ \text{W}$  laser power was measured to be  $4.5\ \text{A}$ .

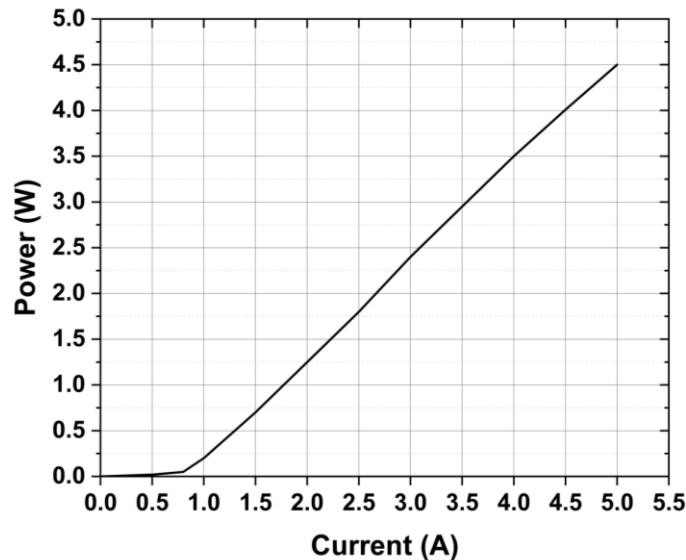


Figure 3.8: The P/I curve of the DL measured using Thorlabs PM400 power meter.

### 3.1.5 CTP Laser Head

Due to the wide divergence of the laser beam emitted from each fibre in the array, collimation and focusing are necessary. This crucial function is accomplished through a custom-manufactured (supplied by EASTCOM Optical Technology Inc., China) Computer to Plate (CTP) head assembly, as illustrated in Figure 3.9. The CTP assembly is designed as a telescopic lens arrangement, with the adapter of the fiber array connecting to one end of it. Since this assembly is a bespoke design and manufactured by a third party, specific technical details and the technologies employed in its construction remain undisclosed.

The working distance of the CTP head is set at 60 mm, and this distance is maintained consistently throughout the experiments. This distance is deemed sufficient to prevent any spattered or powder particles from reaching the lens while effectively melting the layer. The CTP uses imaging lenses that have been integrated to capture and transmit the emitted light from the v-groove array, effectively concentrating it onto the powder bed. The relay optics perform the tasks of collimation and focusing for each beam emanating from the 2D-FAH, with a magnification factor of  $\times 0.6$ .

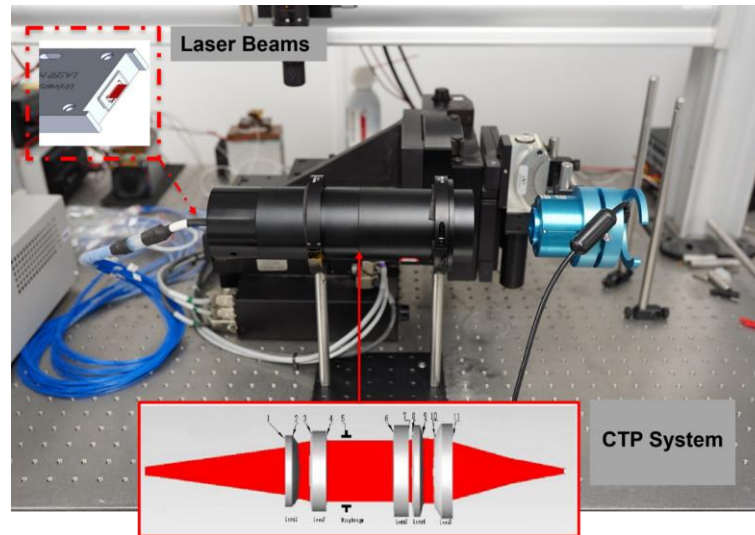


Figure 3.9: The CTP laser head assembly with a beam profiler attached at one end.

### 3.1.6 Modifications to the DAM Rig

Modifications to the rig were carried out after receiving the lasers and CTP head from the supplier. The gantry system was adjusted to fit the CTP head, and laser profiling was completed. Subsequently, the cooling system was designed and tested, followed by the implementation of the laser control system. The development of both systems is detailed further in the sections below.

#### 3.1.6.1 Cooling System

After initial testing, it became clear that the air cooling solution, comprising just a heat sink and fan, was inadequate for the DLs. Consequently, a solution was required to consistently maintain the temperature below 20 °C range. Given that the surface area of the DL is only 10 mm<sup>2</sup>, effective heat removal from such a compact area can be achieved by directly attaching the heat removal device to the DL. Air cooling is insufficient for such a confined space, as the limited surface area restricts the volume of air that can contact the surface, thereby reducing the efficiency of heat dissipation.

Figure 3.10 (a) illustrates the cooling system setup, which includes a unit capable of cooling six DLs simultaneously. It comprises a heat sink, fan, and temperature controller for six DLs. This system is scalable; Figure 3.10 (b) shows the internal structure consisting of an aluminium heat sink block, to which a large fan is attached at the end to remove heat from the entire block. Each DL is mounted on a copper plate that includes a thermoelectric cooler (TEC) and a thermistor among other components in the system.



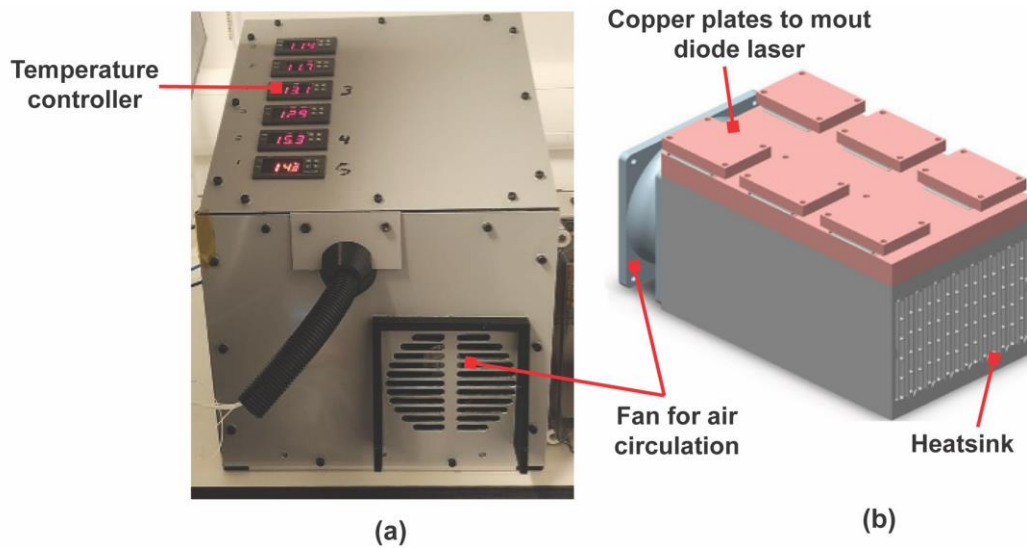


Figure 3.10: The cooling system with the temperature controller (a) and the heat sink housing 6 diode lasers (b).

In this setup, each TEC is attached to a copper plate, as illustrated in *Figure 3.11*, with the DL positioned on top of the TEC. The TEC operates based on the Peltier effect, where passing an electric current through the device creates a temperature gradient. This gradient moves heat from the cold junction, in direct contact with the DL, to the hot junction attached to the copper plate. The copper plate acts as a heat sink, effectively dissipating the transferred heat into the environment.

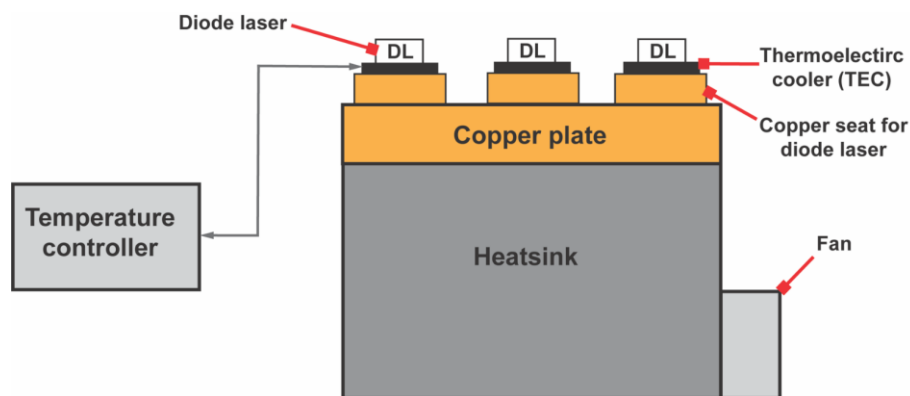


Figure 3.11: Illustrating the cooling arrangement with the help of TEC.

Additionally, a thermistor is attached to the DL to monitor its temperature. If the temperature exceeds a predefined limit, the thermistor signals the temperature controller to adjust the TEC. This adjustment modifies the current flow, enhancing the cooling efficiency to maintain the DL within its optimal operating temperature range (below 20 °C). This direct and efficient method of temperature regulation is essential for maintaining system stability and

performance, making thermoelectric cooling a critical component in managing the thermal dynamics of DL systems.

### 3.1.6.2 Laser Power Controller

The characteristics of the laser beam, including output power, wavelength, and the heat generated by the laser module, are heavily influenced by the electrical power supplied to the laser. DLs are both current-driven and current-sensitive, meaning fluctuations in the drive current can significantly affect the output power and wavelength. Such instability in the drive current, arising from noise or drift, can adversely impact the performance and longevity of the laser diode. Furthermore, fluctuations in the current also directly affect the temperature, causing variations in the output characteristics. To ensure the stability of the DL, an ideal power source would be a constant current source that is linear, noiseless, and accurate, delivering precisely the current needed for specific applications.

In this research, a DPS3005 constant voltage current step-down power supply was employed to provide a stable current to the diode lasers. Nine laser drivers were housed in a single compact box as shown in *Figure 3.12*, each initially set to 2A and 3V. During operation, the current could be manually or remotely controlled via Bluetooth, aiming for a constant output power of 4 W. To verify the stability of the laser output in the designed system, power-voltage-current characteristics were tested after a continuous 12 hour laser run, during which power was measured with a laser power meter. This system was used throughout the project to control the DLs.

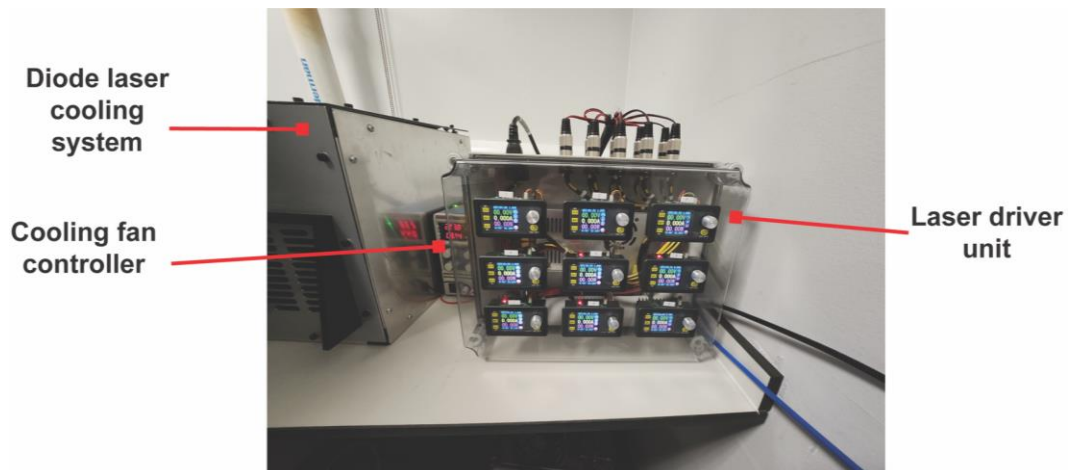


*Figure 3.12: The diode laser drive unit consisting of nine DPS3005 modules.*

### 3.2 A Typical DAM Process Workflow

1. Define key processing parameters such as laser power, scanning speed, and hatch distance based on experimental design.
2. Use LightBurn software to generate G-code to control the laser driver, cooling system, and gantry (X-Y) movements.
3. Upload the G-code to the machine's microcontroller, which configures the motors for building preparation.
4. Instruct the laser driver to regulate the electrical current to the DLs, ensuring it provides a constant power at 4 W.
5. Thermistors to monitor the temperature of each DL, controlled by a TEC to keep temperatures below 20 °C.
6. After the fabrication, carefully remove and hot-mount the parts.
7. Characterise the final parts to assess the effects of processing parameters such as beam profiles, laser power, scanning speed, and hatch distance.

### 3.3 Beam Profiling

The CTP laser head projects the array of laser beam, which emerges from the fiber array, onto the powder bed surface after the processes of collimation and focusing. The activation of each DL results in the generation of a beam or beams with distinct characteristics. It is crucial to understand these beam attributes before employing them for the selective melting of powder particles. To achieve this understanding, a NanoScan2sPryo/9/5 scanning slit beam profiler is employed for the characterisation of each beam profile. The NanoScan profiler is securely attached to the end of the CTP head at a fixed distance of 60mm as shown in *Figure 3.13*. This distance is chosen because it corresponds to the point where laser beams achieve their maximum intensity focus. Each individual DL operates at a maximum power of 4 W and produces a beam with a 65  $\mu\text{m}$   $1/e^2$  diameter when focused. The beam radius was measured as a function of the Z-axis position, with incremental increases of 10  $\mu\text{m}$ , until reaching the distance specified in ISO standard 11146-1.

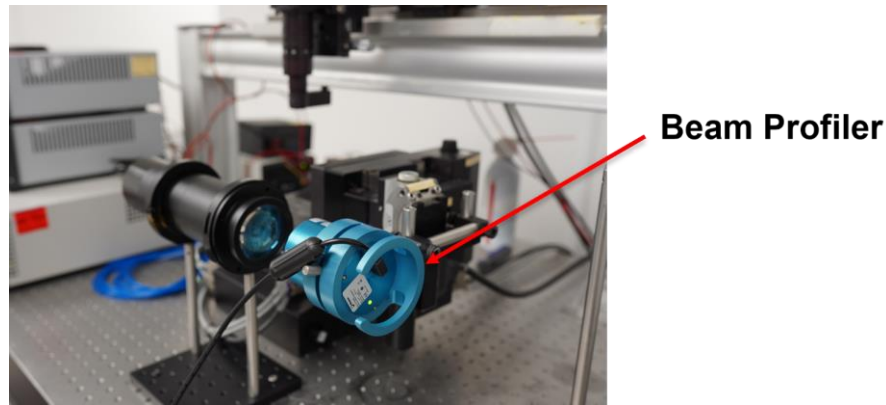


Figure 3.13: The diagram illustrating the configuration for beam profile measurement using a NanoScan2sPryo/9/5 scanning slit beam profiler.

Figure 3.14 presents an example of beam profile data obtained from the NanoScan profiler using their proprietary software, NanoScan V2. This data reflects the configuration when two adjacent lasers from a single row were examined. In this configuration, a beam length of  $65\ \mu\text{m}$  is measured on the X-axis, corresponding to  $1/e^2$  of the maximum intensity. Simultaneously, the beam width is indicated as  $141\ \mu\text{m}$  on the Y axis. As each individual DL is activated, the total length of the beam extends. For instance, when six beams are simultaneously activated, the resulting beam length measures  $446\ \mu\text{m}$  as shown in Figure 3.15 (a).

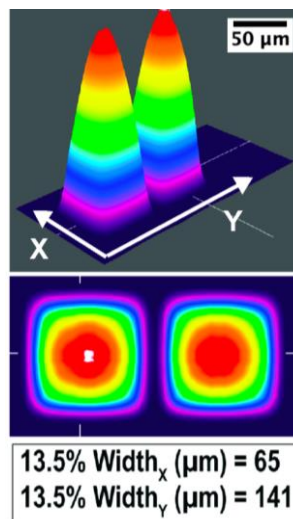


Figure 3.14: Data illustrating the beam profile when two adjacent lasers within a single row are activated.

The second row within the array generates a distinct beam profile configuration compared to the laser arrangement of the first row. For instance, the activation of each laser in either row results in a beam profile with a length of  $103\ \mu\text{m}$ . Figure 3.15 (b) illustrates the beam configuration of the two-row arrangement, displaying up to ten lasers.

The DAM process is primarily distinguished by its slower scanning speed compared to L-PBF. Its productivity, however, is achieved by processing a larger area, facilitated by a long stripe of laser beam. This is where the single-row arrangement in the fiber array plays a crucial role, making it a priority for investigation in this study. Moreover, Alsaddah *et al.* conducted an investigation that encompassed both single-row and two-row arrangements. Their findings presented only minor differences between the single-row and double-row configurations [6].

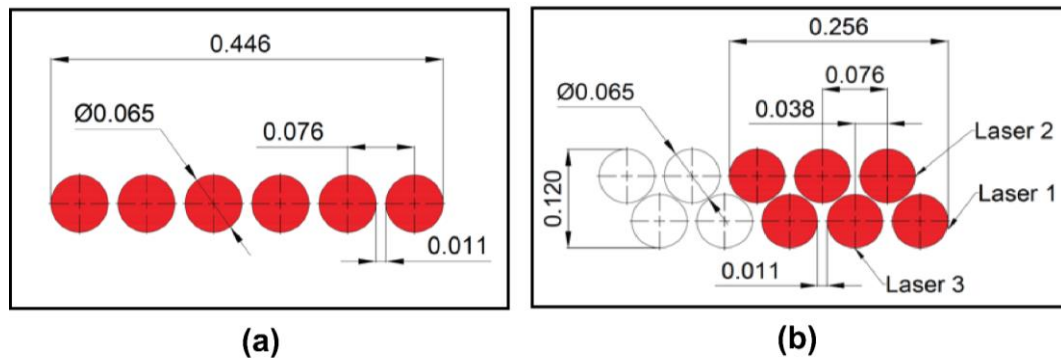


Figure 3.15: Representation of the multi-laser arrangement configuration, with (a) displaying six lasers in a single row, and (b) showcasing up to ten lasers arranged in two rows. All dimensions given in this illustration are in mm.

### 3.4 Optimisation of Parameters

In a prior investigation, ref [6] conducted comprehensive experiments using Ti6Al4V and optimised parameters for both single and double row configurations within the fibre array. The findings of this study suggest that the optimal scanning speed is 100 mm/min, and the recommended individual laser power for successful fabrication of Ti6Al4V parts falls within the range of 4 to 4.5 W.

### 3.5 In Situ Temperature Measurement

To gain insight into the evolution of melt pools and their thermal characteristics during the process, precise temperature measurements at various locations are crucial. However, this can be particularly challenging for the interior regions of the melt pool. *In-situ* temperature monitoring for AM processes is typically achieved using high-resolution thermal imaging cameras and pyrometers. In this research, a thermal camera is employed to record the surface temperature during the multi-laser interaction with the powder material.

### 3.5.1 Thermal Camera Setup

A 16-bit Hamamatsu c13440 camera with a Tamron 180 mm prime lens as shown in *Figure 3.16* was used to record thermal images during processing. Thorlabs RG 850 long-pass filters were used to remove any interference from scattered 808 nm emission from the diode lasers. Thorlabs FESH1000 filters were also used to restrict the sensitivity between 850 nm – 1000 nm. A neutral density (ND) filter with OD 1.0 was used to optimise the dynamic range and match the interested temperature range in this work.



*Figure 3.16: Hamamatsu C13440 camera, filter and lens assembly used in the experiments.*

The calibration process relies on Planck's Law. A total of 100 images were acquired and then averaged at each temperature point, using a blackbody furnace with a high emissivity of approximately 0.99. The temperature range covered in this calibration spanned from 900 °C to 1500 °C. It is important to note that the furnace had a maximum temperature capability of 1500 °C, hence the measurements were taken up to that temperature limit. Temperatures above 1500 °C were extrapolated based on Planck's Law. The dark offset was determined by averaging 100 images with the lens covered. The temperature calibration curve is plotted in *Figure 3.17*. It is found that the uncertainty of InGaAs is limited, which is under 5 °C within the temperature range 900 °C to 1500 °C. The absorptivity of the sample material Ti6Al4V was measured as 0.65, and the emissivity can be calculated as 0.35. An additional transmission loss through the observation window was measured as 5%. After correcting for emissivity and transmission, the effective temperature measurement range is 800 °C to 2094 °C.

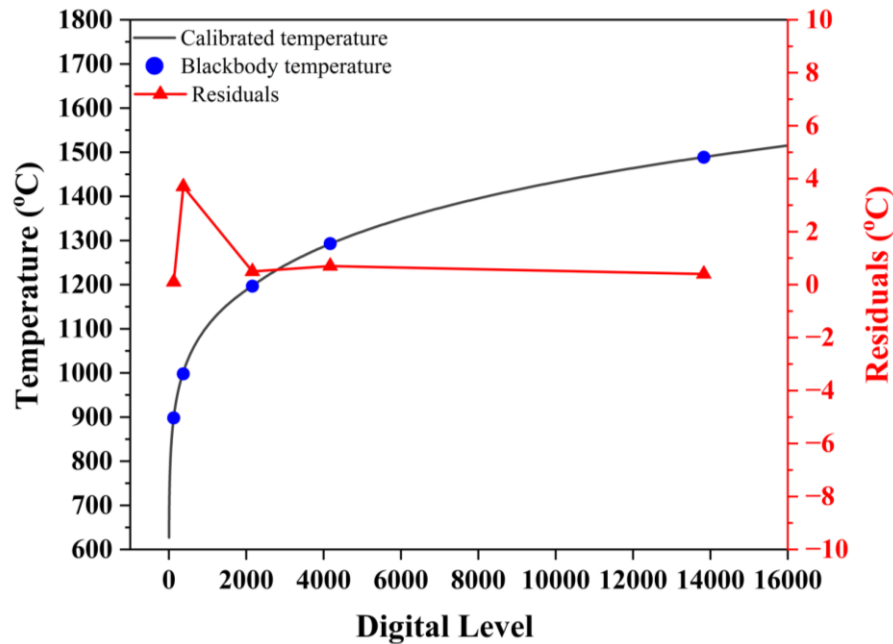


Figure 3.17: Radiance calibration curve and uncertainty of measured temperature showing the digital level from 0 – 16000. The blue dot represents the blackbody temperature mapped over the calibrated temperature, plotted in black colour.

### 3.5.2 Thermographic Data

Thermal images were recorded using a Hamamatsu C13440 thermal camera in its high-speed mode, with a resolution of  $2048 \times 1024$ . The camera produces images at two hundred frames per second in this mode. During the DAM process, images were streamed to a PC where they were saved as TIFF files for post-processing. Cropping of images and conversion to thermal images was performed in MATLAB. The look-up table produced during the camera calibration process was used for converting TIFF files into thermal images. The sequence of TIFF images, captured by the thermal camera, was processed using the ImageJ software. Figure 3.18 demonstrates the temperature of the melt pool at a point in time as the laser array is traversed across the powder bed. This is from the TIFF images taken using the thermal camera, showing the temperature at each respective pixel location within the image. To ascertain the temperature-time data, a specific point (probe) was chosen on the top surface of the melt pool. The temperature at this designated location was then monitored over a period of time, providing a detailed temperature-time profile for that particular point.

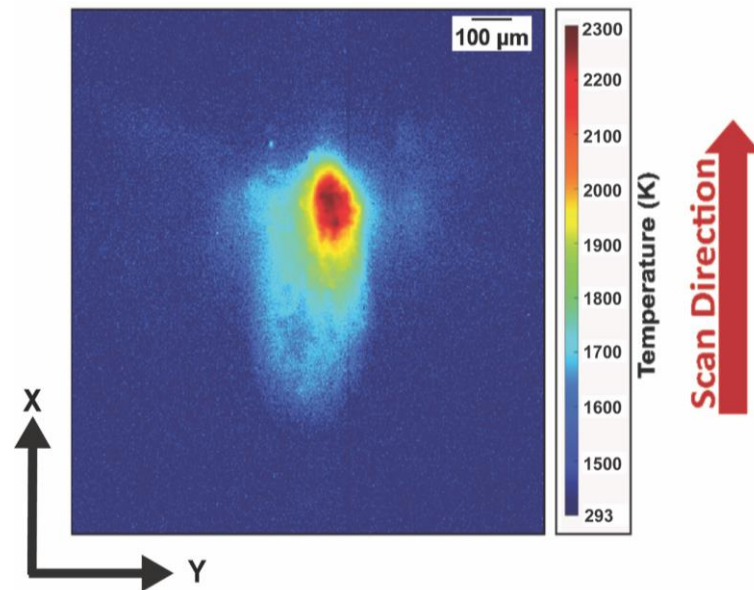


Figure 3.18: An example of an image from the thermal camera, Hamamatsu c11440 captured whilst processing the beam profile with four lasers.

### 3.5.2.1 Placement of Thermal Camera

The field of view (FOV) was measured as 20 mm x 20 mm in a complete camera sensor with a working distance of 40 cm. The camera sensor was cropped into 2048 x 1024 to capture the images at 200 frames per second (fps). The Hamamatsu camera was positioned at a 45° angle in front of the DAM setup, as illustrated in *Figure 3.19*. In this configuration, the camera captured information through the viewing windows, allowing observation and recording of the laser-material interaction during the process. This angle provided a strategic perspective to effectively capture the melt pool within the material interaction zone.



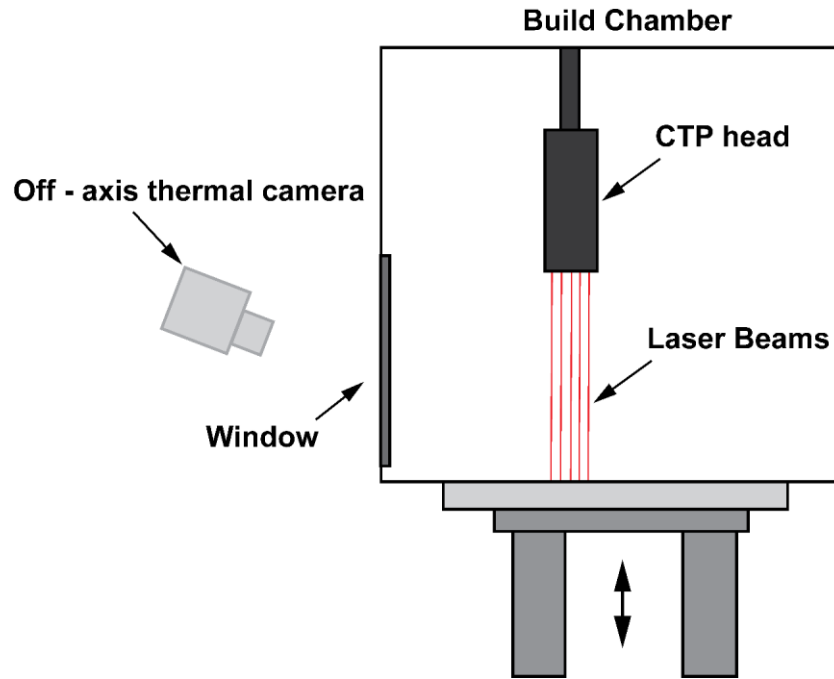


Figure 3.19: Illustrating the Hamamatsu C13440 camera set up employed for in-situ spatter investigation.

### 3.6 Material Properties

#### 3.6.1 Titanium Alloy Powder

Pre-alloyed and gas atomised Ti6Al4V powder used in this study was supplied by Carpenter Additive with the material composition in nominal weight % as shown in *Table 3.1*.

<i>Element</i>	<i>Al</i>	<i>V</i>	<i>Fe</i>	<i>O</i>	<i>C</i>	<i>N</i>	<i>H</i>	<i>Ti</i>
<i>UNIT (Weight %)</i>	5.8	3.8	0.3	0.15	0.02	0.05	0.03	Balance

*Table 3.1: Composition of Ti6Al4V*

The powder material is analysed using the Malvern Mastersizer (Malvern Mastersizer 3000 PSA) to determine the particle size distribution. The size distribution measured is shown in *Figure 3.20 (a)*, indicating  $d_{10}$ : 23.4  $\mu\text{m}$ ,  $d_{50}$ : 33.3  $\mu\text{m}$ , and  $d_{90}$ : 47.3  $\mu\text{m}$ . The SEM image depicting the shape and sphericity of the powder is shown in *Figure 3.20 (b)* indicating that most particles appear to be spherical. More information regarding the analysis conducted in Malvern Mastersizer is available in *Appendix B: Ti6Al4V Powder Data*.

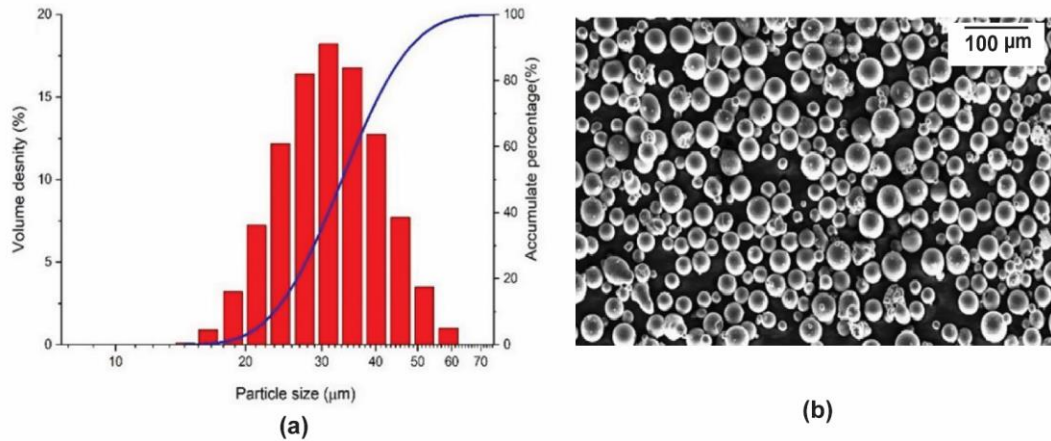


Figure 3.20: particle size distribution of Ti6Al4V powder (a) and powder morphology (b).

### 3.6.2 Absorptivity Measurement for Ti6Al4V

The absorptivity measurement was conducted using an Ocean HDX Vis NIR spectrophotometer. Metallic powders were compacted into a diminutive cup, measuring 10 mm in diameter and 5 mm in depth. Subsequently, the surface was levelled using a glass microscope slide to ensure uniformity. The absorptivity of Ti6Al4V powder was assessed and contrasted with that of copper and AlSi12 powders, using spectralon as a perfectly reflective reference material. This measurement took place at ambient temperature, spanning the 380–1100 nm wavelength range. Absorptivity was calculated as a function of wavelength by employing the formula  $\text{Absorptivity} = 1 - \text{Reflectivity}$ . This calculation was based on the average of 10 separate measurements, ensuring no transmission had occurred.

The results from this experiment show that the absorptivity of powders significantly varies with the laser wavelength. For instance, the absorptivity of Ti6Al4V increases by 6% and 14% when a 808nm and 450 nm laser source is employed respectively compared to a 1064 nm fibre laser. Highly reflective and conductive materials such as copper and AlSi12 also demonstrate substantial increases in absorption. Specifically, copper's absorption rises from 9% at 1064 nm to 26% at 808 nm, an approximate increase of 189%. At 450 nm, copper's absorption reaches 88%, marking a significant 878% increase compared to the 1064 nm fibre laser. Similarly, AlSi12 exhibits increased absorption at shorter wavelengths: 19% at 1064 nm, 26% at 808 nm, and 48% at 450 nm. These results indicate a clear trend of increasing absorption with decreasing wavelength across all tested materials.

### 3.7 Thermophysical Properties

The thermophysical properties of metals refer to the characteristics that describe how materials behave in relation to temperature and heat. Depending on the specific property being examined, these properties can exhibit linear or non-linear behaviour. The use of linear or non-linear thermophysical properties in L-PBF modelling depends on the nature of the problem being investigated. Analytical methods often use linear properties, which are simpler to work with mathematically, as they exhibit a consistent relationship between variables. In its simplest form, a constant value for each thermophysical property can be used for analytical-based calculations [107]. Temperature-dependent thermophysical properties are required for numerical methods to attain the highest accuracy during simulations [108]. In the numerical method, the computational domain is subdivided into many small volumes, and thermophysical properties are assigned to each volume for calculating the required outputs.

#### 3.7.1 Analytical: Thermophysical Properties

In this investigation, the thermophysical characteristics of Ti6Al4V are held constant for analytical modelling in accordance with the Rosenthal equation. The constant thermophysical properties of Ti6Al4V utilised for the analytical models are presented in *Table 3.2*.

<b><i>Parameter and Properties</i></b>	<b><i>Values</i></b>	<b><i>Units</i></b>
<i>Solidus temperature</i>	<i>1878</i>	<i>K</i>
<i>Liquidus temperature</i>	<i>1923</i>	<i>K</i>
<i>Initial temperature (<math>T_0</math>)</i>	<i>293</i>	<i>K</i>
<i>Density</i>	<i>4375</i>	<i>kg/m<sup>3</sup></i>
<i>Thermal conductivity</i>	<i>7</i>	<i>W/m K</i>
<i>Thermal diffusivity (<math>10^6 a</math>)</i>	<i>2.9</i>	<i>m<sup>2</sup>/s</i>

*Table 3.2: Processing parameters and material properties used for Analytical modelling [109].*

#### 3.7.2 FEM and VoF: Thermophysical Properties

The transient thermal analysis of an LPBF process requires inclusion of temperature-dependent physical properties such as density, specific heat, thermal conductivity, viscosity, surface tension and solid fraction. *Table 3.3*

presents some of the thermo-physical properties used in both FEM and VoF modelling for this study.

<b>STATE</b>	<b>TEMPERATURE (K)</b>	<b>DENSITY (kg/m<sup>3</sup>)</b>	<b>SPECIFIC HEAT (J/kg/K)</b>	<b>THERMAL CONDUCTIVITY (W/m/K)</b>
<b>SOLID</b>	298	4420	546	7
	373	4406	562	7.45
	473	4395	584	8.75
	573	4381	606	10.15
	673	4366	629	11.35
	773	4350	651	12.6
	873	4336	673	14.2
	973	4324	694	15.5
	1073	4309	714	17.8
	1173	4294	734	20.2
	1268	4282	753	22.7
<b>β TRANSUS</b>	1268	4282	641	19.3
	1373	4267	660	21.0
	1473	4252	678	22.9
	1573	4240	696	23.7
	1673	4225	714	24.6
	1773	4205	732	25.8
	1873	4198	750	27.0
	1923	4189	759	28.4
<b>LIQUID</b>	1923	3920	831	33.4
	1973	3886	831	34.6
	2073	3818	831	-
	2173	3750	831	-
	<i>Uncertainty</i>	±3%	±3%	±10%

Table 3.3: Recommended values for thermophysical properties of Ti6Al4V [109].

## 3.8 Characterisation

### 3.8.1 Sample Preparation

The methodology adopted to prepare Ti6Al4V samples for microstructure analysis comprised several steps, as outlined below. Due to laboratory restrictions, the typical etching chemicals were not used in this preparation process. Initially, the parameters for sample preparation were selected based on

recommendations from Buehler for Ti6Al4V. However, modifications were necessary due to the samples being very thin and the prohibition of acids in the laboratory. Consequently, the procedure was further adjusted based on recommendations from Buehler UK Ltd and also slightly refined based on our previous experience with similar samples.

**(a) Sectioning:** The process began with sectioning using a diamond saw machine (Sectom - 50, Struers UK Ltd) at 3000 RPM speed and a feed rate of 0.02 mm/s.

**(b) Hot-Mounting:** Subsequently, hot-mounting was performed. The sample was immersed in a conductive thermoset polymer using a SimpliMet Machine (Buehler UK Ltd, London, UK) at 600°C and 7 bar pressure.

**(c) Grinding:** The samples underwent grinding using a Buehler Automet Grinder-Polisher with P600, P1200, and P2500 grit papers. A force of 27 N was applied for 1 minute, with a plate speed of 150 rpm and a head speed of 60 rpm, with a complimentary head rotation direction.

**(d) Polishing:** After grinding, the samples were polished with diamond suspensions, specifically 6 µm, 3 µm, and 1 µm diamond grits, until a mirror-like finish was achieved.

**(e) Etching:** To reveal the microstructure of Ti6Al4V, a mixture of colloidal silica (OP-S) and hydrogen peroxide (30%) was applied for 10 minutes. A force of 15 N was employed, with a plate speed of 150 rpm and a head speed of 60 rpm.

Lastly, the samples were cleaned with a ChemoMet polishing cloth using water for 10 minutes and stored in a desiccator, with the surface protected by a metallographic cap.

### 3.8.2 Optical Microscope

Melt pools were observed initially using a Nikon LV150NL Upright Materials Microscope followed with a detailed analysis using SEM.

### 3.8.3 Scanning Electron Microscope (SEM)

Surface morphology and microstructural analyses were carried out utilising a scanning electron microscope (SEM), specifically the Tescan VEGA3 model.

Surface morphology images were captured at a beam intensity of 15 kV to achieve high-resolution visuals. These images were acquired at a distance of 15 mm and at various magnifications, including x100, x200, x500, and x1000.

#### **3.8.4 Surface Roughness**

Surface roughness measurements were conducted utilising the Alicona Infinite Focus SL instrument, known for its variable focus measurement capabilities. To assess the surface roughness of Ti6Al4V samples with densities exceeding 90%, a 10 mm × 10 mm area was scrutinized using a 10× magnification lens. Within this region, three measurements, separated by 4 mm intervals on the top surface, were taken, and the average roughness (Ra) was determined for each. These Ra values were then correlated with relevant processing parameters.

#### **3.8.5 X-Ray Diffraction (Phase) Analysis**

The phase was conducted utilising a PANalytical XPert<sup>3</sup> Powder XRD equipment, which was supplied by Malvern Panalytical. In the reflective configuration, the phase analysis was executed utilising a power setting of 45 kV and 40 nA. Default divergence and anti-scatter slits were employed to optimise the analytical conditions.

#### **3.8.6 Residual Stress Measurement by XRD**

The PANalytical XPert<sup>3</sup> Powder X-ray diffractometer as shown in *Figure 3.21* is a sophisticated instrument, composed of several key components which include an incident beam optics assembly, a sample stage equipped with a reflection/transmission spinner, and a diffracted beam optics assembly. The incident beam optics assembly is equipped with a programmable divergence slits (PDS), Soller slits, and a beta nickel filter, which are instrumental in fine-tuning the beam for precise analysis. Conversely, the diffracted beam optics assembly comprises programmable anti-scatter slits (PASS), Soller slits, and a beta nickel filter. These components contribute to enhance the accuracy and reliability of the diffraction data acquired during the residual stress analysis.



Figure 3.21: PANalytical X'Pert3 Powder machine used for residual stress studies.

### 3.8.6.1 The Parameters Used for Residual Stress Investigation

The PDS in the diffractometer regulates the divergence and helps to alter the width of the incident X-ray beam. The programmability (using slits) of PDS allows for the optimisation of the beam's divergence based on the specific requirements of the analysis, such as the type of sample being analysed and the desired resolution. The beta nickel filter acts as a monochromator, selectively filtering out unwanted X-ray wavelength such as the  $K\beta$  radiation. The PASS slits are adjustable and can be programmed to control the width of the diffracted X-ray beam that reaches the detector, by mitigating the effects of scatter and unwanted radiation.

The residual stress assessed through X-ray diffraction represents the arithmetic average stress within a designated volume of material, delineated by the irradiated area. This area oscillates in size, extending from square centimetres to square millimetres, dictated by the depth of the X-ray beam penetration. The PDS and PASS slits play a crucial role in defining the dimensions of this irradiated area for the experiment. Specific parameters were used in this study as outlined in *Table 3.4*:



<b>PARAMETER (UNIT)</b>	<b>VALUES</b>
<i>X-ray Wavelength <math>K\alpha</math> (Å)</i>	<i>1.541874</i>
<i>X-ray Wavelength <math>K\beta</math> (Å)</i>	<i>1.392250</i>
<i>Beta-filter</i>	<i>Nickel</i>
<i>Filter thickness (mm)</i>	<i>0.020</i>
<i>Soller slit (rad)</i>	<i>0.04</i>
<i>PDS slit angle (°)</i>	<i>0.5</i>
<i>PASS slit angle (°)</i>	<i>1</i>
<i>X-Ray beam radius (mm)</i>	<i>240</i>
<i>Scan axis</i>	<i>2Theta - Omega</i>
<i>Scan angle (°)</i>	<i>138.5510 - 143.4486</i>
<i>Tilt angle (°)</i>	<i>0 - 51</i>

*Table 3.4: PANalytical XPert3 Powder equipment setup parameters used for residual stress experiments.*

The depth of X-ray penetration was rather superficial, approximately 0.005 - 0.01 mm, thereby facilitating the evaluation of both macro and microscopic residual stresses. This methodology offers a depth resolution that is approximately 10 to 100 times more precise than to alternative techniques, enabling a more comprehensive and nuanced determination of residual stresses within the examined material [20].

### **3.8.6.2 Determination of The Lattice Strain**

In theory, any interplanar spacing could be employed to gauge strain in the crystal lattice, but the practicality of this approach is constrained by the limited wavelengths yielded by commercial X-ray tubes, narrowing the selection to a few viable planes. Generally, precision is enhanced as the diffraction angle increases. Practical methodologies typically necessitate diffraction angles where  $2\theta$  exceeds  $120^\circ$ . Specifically, for the Ti6Al4V alloy and the lattice plane (hkl) of 21.3, a  $2\theta$  angle of  $141.7^\circ$  is recommended, aligning with established norms and optimising measurement accuracy within the constraints of available X-ray wavelengths and instrumental capabilities [20]. The PANalytical XPert<sup>3</sup> Powder is programmed at performing scans within a range of  $138.5510$  to  $143.4486^\circ$ , enabling the precise determination of peak positions at each scanned angle based on the acquired data. The shift in peak positions obtained from this experiment

fundamentally characterises lattice strain, which is intrinsic for the accurate determination of residual stresses within the material.

### 3.8.7 EBSD

Electron backscattered diffraction (EBSD) was employed to investigate grain size, phase identification, and crystallographic orientation. This analysis was conducted using an Oxford Instruments® C-NANO EBSD detector, operated at 20 kV. To strike a balance between resolution and scanning time, the step size was set at 0.1  $\mu\text{m}$ , with a magnification of 650x, which was defined based on the scanning area.

Subsequently, the acquired EBSD data was subjected to analysis using Aztec Crystal software from Oxford Instruments. Prior to the EBSD analysis, a standard data clean-up procedure was executed. This involved the replacement of incorrectly indexed isolated points and unindexed points, ensuring that they were filled with a minimum of four indexed pixels surrounding them. This process was accomplished using level 5 of the Zero Solution Removal function. To distinguish grain boundaries, a threshold of  $15^\circ$  was applied. Further exploration of grain morphology and sizes was carried out through calculations of grain aspect ratios and the determination of average grain size.

## 3.9 Conclusions

In this chapter, the DAM mechanism and its system are described, highlighting its multi-laser array technology. Different beam configurations are characterised to investigate effects on melting area dimension, beam shape (line or multi-spot), and spot-spacing, with an eye on process optimisation through various optical configurations. The chapter also delves into the methodology and experimental setup of the study. This involves the use of multiple fibre-coupled diode lasers with 808 nm wavelengths and low power (less than 5 W) for efficient parallel processing. It covers the characterisation of laser systems, including single diode modules and the multi-laser head (CTP), detailing the specific modifications and equipment characteristics required for DAM processing. Finally, the chapter provides an overview of the characterisation techniques used to analyse the microstructural properties and residual stress of the build.

## 4 Chapter 4: Modelling Methodology

From the literature review conducted in Chapter 2, *Section 2.6*, it was shown that specific literature on modelling the Diode Area Melting (DAM) process using systems that use a fibre-coupled Diode Laser (DL) array is not available. Despite the availability of various established methodologies and models for the Laser Powder Bed Fusion (L-PBF) process, comparable models for DAM are not readily accessible. However, given the similarities in laser and powder material interactions between L-PBF and DAM, it is feasible to adapt L-PBF models for DAM. These models could be adopted and validated using experimental data to ensure their applicability before employing them in DAM simulations.

This chapter details the development and subsequent validation of one analytical and two numerical models designed for simulating the DAM process. It begins with the construction of an analytical model based on the Rosenthal equation, followed by the development of numerical models using the Finite Element Method (FEM) and Volume of Fluid (VoF) method. These models were initially validated against experimental measurements of melt pool dimensions from L-PBF of Ti6Al4V, as documented in the literature. This validation process established a solid foundation for the applicability of these models. Following validation, the models that best suited will be selected and adapted for detailed DAM process simulations. The aim is to use these models to predict and understand the melt pool morphology and associated thermal characteristics in DAM, leveraging the insights gained from the initial L-PBF-based validations.

### 4.1.1 Selected Literature for Model Validation

Yadroitsev *et al.* studied the distribution of surface temperature and size of the melt pool formed during L-PBF of Ti6Al4V [110]. In this study, a CCD camera was used to determine the surface temperature of the melt pool formed due to various processing parameters, which are shown in *Table 4.1*. The 20, 30 and 50 W laser power and 300, 200 and 100 mm/s scanning velocities selected here are relatively low power compared to the process parameters used in a typical L-PBF machine for commercial applications. The relatively low power used shares similarities with the laser power employed in DAM. Hence, this study was selected to validate the models developed for DAM. Although a single DL used in

DAM provides only 4 W optical power, a laser profile with multiple lasers could easily reach similar power levels ( 4 – 50 W). The fibre array in DAM is uniquely engineered to operate a multitude of laser beams, as many as a hundred, each of which can be individually regulated.

	20 W	30 W	50 W
300 mm/s	•	•	•
200 mm/s	•	•	•
100 mm/s	•	•	•

Table 4.1: The process parameters (Power and Scanning Velocity) chosen for the study.

Yadroitsev *et al.* conducted experiments using a TEM<sub>00</sub> Gaussian beam with a diameter of 70µm, operating at a wavelength of 1075 nm. A series on melt tracks were created for each set of process parameters, each 10 mm long. For the theoretical calculations, the Carslaw and Jaeger heat conduction equation was used for the Gaussian heat source [73], [111]. The geometry of the resulting melt pool was then compared against the calculated results.

#### 4.1.1.1 Experimental Results

Figure 4.1 demonstrates the melt pool width, calculated using the Carslaw and Jaeger heat conduction equation, alongside data from experiments plotted with varying scanning speeds and laser powers. Conversely, Figure 4.2 presents the data relating to the melt pool depth. The experimental data suggests an increase in both the width and depth of the melt pool in relation to energy input. Yadroitsev *et al.* assert that the primary influences on the geometric characteristics of single tracks are the laser power density and interaction time, as defined in equation 13 and equation 14.

$$\text{Interaction time} = \frac{\text{Laser beam diameter}}{\text{Scanning speed}} \quad (13)$$

$$\text{Laser power density} = \frac{\text{Laser power}}{\text{Spot area}} \quad (14)$$

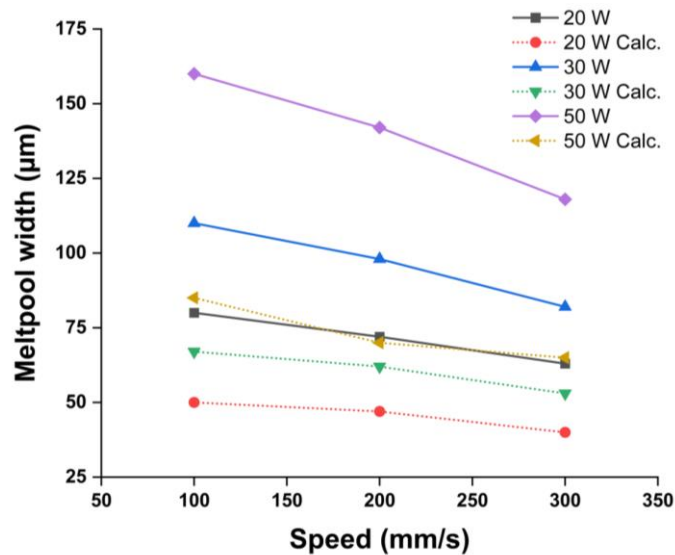


Figure 4.1: The width of the molten pool versus scanning speed.

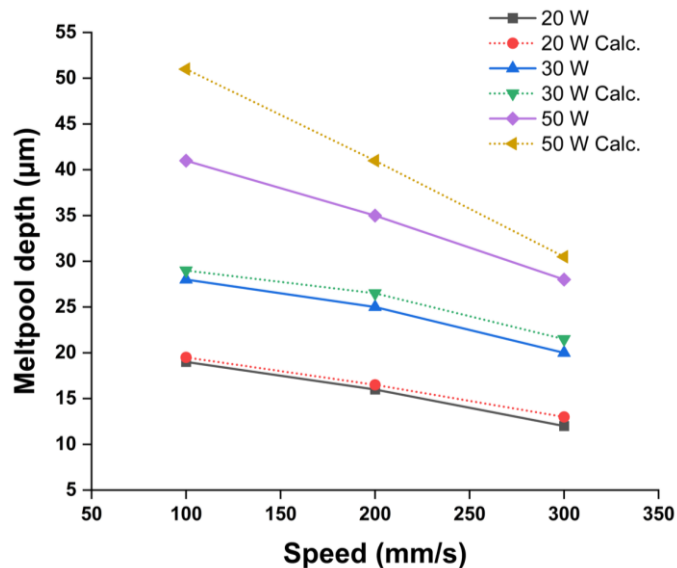


Figure 4.2: The depth of the molten pool versus scanning speed.

The work presented by here shows that the melt pool depth does not exceed a depth-to-width aspect ratio of 1:2. This means that the width of the melt pool is at least twice the depth, illustrating a shallow, wider melt pool rather than a deep, narrow one. The theoretical values obtained from the Carslaw and Jaeger model show a degree of correlation with the experimental data. However, notable differences also exist with the melt pool width and depth data. While the mean depth-to-width ratio of the melt pool is calculated to be 1:2.4, it exhibits a range from 1:1.7 to 1:3.1. This suggests that in some instances, the melt pool is deeper relative to its width. Yadroitsev *et al.* argues that these inconsistencies between theoretical calculations and actual experimental outcomes might stem from omitting the influence of Marangoni flow within the melt pool. The effect of

Marangoni flow and its influence within the melt pool are very important and well studied [47], [64].

The data from this experimental study will be used to validate the models developed in this chapter. Key parameters considered include the melt pool width, depth, temperature, and cooling rate.

## 4.2 Analytical Modelling Methodology

Researchers employ simpler analytical models for L-PBF since numerical-based approaches are computationally intensive and expensive. Moreover, the two-dimensional (2D) analytical calculations are simple and easily traceable [12]. The Rosenthal equation and Green's function methods are two popular analytical modelling techniques that can be used to solve heat conduction problems [112][69][73]. The Rosenthal equation, initially formulated for the purpose of laser welding, has subsequently been adapted for use within AM process modelling. This equation has come to serve as a tool for modelling of L-PBF process. For example, Plotkowski *et al.* constructed a transient semi-analytical model, using the Rosenthal equation, to determine the effects of heat transfer and compared them with the experimental results on AlSi10Mg created by both L-PBF and EB-PBF processes [113].

### 4.2.1 Initial Conditions

In the analytical model, internal heat generation is disregarded, and so the internal heat energy is represented as  $q_s = 0$ . In laser applications, the heat source comes from an external entity in the form of laser radiation, and in this particular case, any exothermic reaction is neglected. The workpiece was assigned an initial temperature condition of 293 K. The heat source, represented by the Rosenthal equation, is subsequently introduced to the initial boundary condition.

### 4.2.2 Heat Source

In the analytical model, the governing equation for the heat flow is predominantly driven by the heat conduction behaviour of the workpiece or material and is considered as being adiabatic for simplification. The assumption is that heat conduction within the workpiece typically surpasses any heat exchange with the environment via natural convection or radiation. Also, the

processed material is presumed to be uniform and isotropic, and there is no heat loss or gain by either natural convection or radiation. Hence, the heat exchange through natural convection (gas flow within the build chamber) and radiation of the surrounding area is ignored as the conduction heat exchange greatly exceeds the other two, which leads to the governing equation for heat flow as in *equation 15*. In order to make the problem more analytically traceable, the physical material properties are linearised, and the internal energy,  $q_s$ , is neglected to form *equation 16* [107], where  $\lambda$  is the thermal conductivity (W/mm K),  $C_p$  specific heat (J/kg K),  $t$  is the time (s), and  $T$  is the temperature (K).

$$\rho C_p \frac{dT}{dt} = \frac{\partial}{\partial x} \left( \lambda \frac{dT}{dt} \right) + \frac{\partial}{\partial y} \left( \lambda \frac{dT}{dt} \right) + \frac{\partial}{\partial z} \left( \lambda \frac{dT}{dt} \right) + q_s \quad (15)$$

$$\rho C_p \frac{dT}{dt} = \nabla \cdot (\lambda \nabla T) \quad (16)$$

The differential equation 15 is conveniently expressed in *equation 17* at a quasi-stationary state. This equation is popularly known as the Rosenthal equation [114]. The heat source used here is a moving point along the x-axis. The 2D spatial temperature distribution solved with the Rosenthal equation is commonly represented as isotherms drawn around the instantaneous heat source position in the x-y plane.

$$T = T_0 + \frac{q}{2\pi\lambda h} \exp\left[-\frac{U_x x_1}{2\alpha}\right] K_0\left[\frac{U_x r}{2\alpha}\right] \quad (17)$$

Where  $T$  is the peak temperature (K),  $T_0$  is the preheat temperature (K),  $q$  is the net-power input available (W),  $\lambda$  is the thermal conductivity (W/mm<sup>2</sup>),  $h$  is the plate thickness (m),  $U_x$  is the traverse velocity (m/s),  $x_1$  is the distance along the beam (m), and  $K_0$  is the zeroth order of Bessel's function of the second kind.  $r$  is the radial distance away from the beam (m), and  $\alpha$  is the thermal diffusivity (mm<sup>2</sup>/s),  $\rho$  is the density in (kg/m<sup>3</sup>).

$$r = \sqrt{x_1^2 + y_1^2} \text{ and } \alpha = \frac{k}{\rho C_p} \quad (18)$$

Differentiating *equation 17* provides the cooling rate at any given position. The highest cooling rate occurs along the laser traverse line, and due to the coordinate system attached to the heat source, the temperature does not change with time with respect to the coordinate system. Hence, the temperature change rate equation is expressed as *equation 19* [114].

$$\frac{dT}{dt} = -2\pi k\rho C_p \left(\frac{U_x h}{q}\right)^2 (T - T_0)^3 \quad (19)$$

To calculate the temperature distribution and the width of the melt pool, the Rosenthal equation is applied to multiple locations ( $r_1, r_2 \dots r_n$ ) around the centre of the laser beam. The values of the calculated thermal distribution and the respective cooling rate can be visually represented using a colour scheme. This work is done in a Microsoft Excel™ spreadsheet. The calculated temperature values at each location are presented in each spreadsheet cell.

### 4.2.3 Validation of Thermal Modelling

#### 4.2.3.1 Temperature Distribution and Melt Pool Width

The Rosenthal equation-based analytical model often treats the heat source as a point, line, or ellipsoid. In the current study, the heat source in the Rosenthal equation is implemented as a point energy source and performed as a steady-state analysis in a Microsoft Excel™ spreadsheet. This approach can calculate the heat transfer through the material and display it as a spatial temperature distribution. For each beam profile, the surface temperature of the melt pool is spatially derived within each cell of the spreadsheet. *Figure 4.3* illustrates a temperature colour map created using the analytical model, displaying the temperature distribution (a).

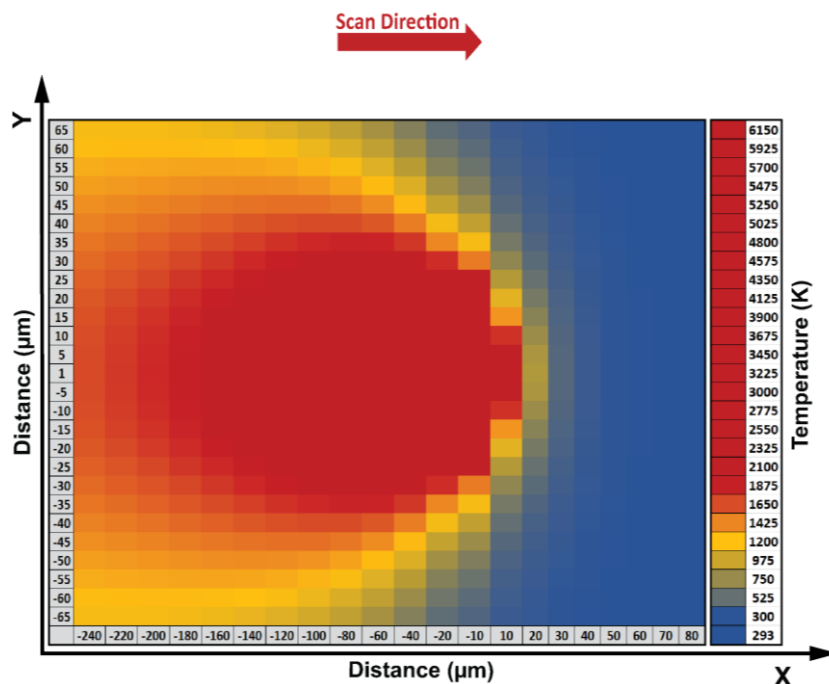


Figure 4.3: Analytical results showing the temperature colour map for 20 W laser power at 300 mm/s scanning speed.



The maximum temperature computed from the analytical solution reaches 6128 K for the processing parameters using 20 W laser power at a scanning speed of 300 mm/s. This is significantly higher than the actual maximum temperature of 1955 K observed in the molten pool during experiments. Nonetheless, the average temperature of the molten pool surface is calculated to be 2550 K (ranging from 1878 K to 6128 K), which is comparable to that recorded using a thermal camera in the experiments. The average temperature is determined by selecting the temperature of each cell that exceeds the solidus temperature of Ti6Al4V. The analytical solution overestimates the peak temperature due to several simplifying assumptions. These include considering the Gaussian beam as a point heat source, assuming no heat loss through convection or radiation, disregarding internal heat generation, and presuming a steady-state calculation. Furthermore, the temperature prediction is too high at the center for a Gaussian point heat source in the Rosenthal equation because the Gaussian distribution assumes maximum laser intensity at the center, with intensity decreasing radially outward. This results in a high concentration of energy at the center, leading to an overestimation of the peak temperature in that area.

After extracting the melt pool width from the temperature colour map, we can compare the calculated temperature with the experimental results. The melt pool width is calculated by measuring the width across the scanning direction on the temperature color map, using the regions where the melt pool temperature exceeds the solidus temperature of Ti6Al4V. *Figure 4.4* displays a comparison between the calculated melt pool dimensions from analytical models and the experimental data from the study by Yadroitsev *et al.* When using the Rosenthal equation to calculate the melt pool width, there is an average accuracy of 16% (with variations between 6% and 31%) relative to the experimental data. The Carslaw and Jaeger model, in the Yadroitsev *et al.*'s study, underestimated the computed width by an average of 40% compared to the empirical data.

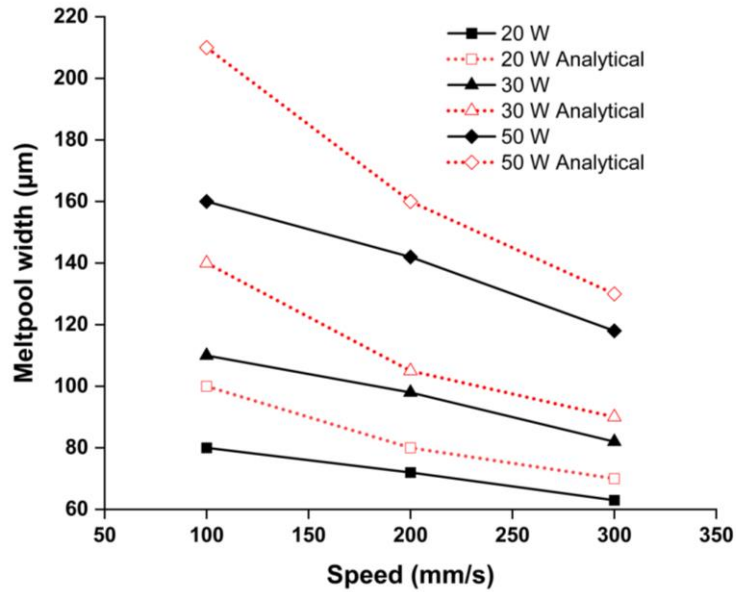


Figure 4.4: Ref-[110] and Analytical model predicted melt pool width comparison.

#### 4.2.3.2 Cooling Rate

In the analytical modelling of L-PBF, the cooling rate is derived using *equation 19* and is visually represented as a color map in *Figure 4.5*. The average cooling rate for the melt pool is then calculated by applying *equation 19* to the average temperature of the melt pool obtained from the color map in *Figure 4.3*. The average cooling rate corresponding to each process parameter, across varying laser powers and scanning speeds is illustrated in *Figure 4.6*. The computed cooling rate for the L-PBF laser, operating at 20 W and moving at a speed of 300 mm/s, peaks at  $1.8 \times 10^6$  K/s. An increase in laser power led to a reduction in the cooling rate, with values of  $1 \times 10^6$  K/s observed at 30 W and further dropping to  $6.2 \times 10^5$  K/s at 50 W laser power. Likewise, a reduction in laser scanning speed led to a decrease in the cooling rate. The lowest value was recorded at  $8.2 \times 10^4$  K/s under the processing conditions of 50W laser power and a scanning speed of 100 mm/s.

The relationship between cooling rate, laser power, and scanning speed is well-established in the context of laser welding processes [114]. It is interesting to observe similar trends within L-PBF. In laser welding, the laser power and scanning speed play significant roles in determining the cooling rate, which in turn influences the microstructure and mechanical properties of the welded joint. Generally, as the laser power increases, the cooling rate decreases. This is because higher laser power results in greater heat input, raising the overall

temperature and hence extending the time it takes for the material to cool. Conversely, an increase in scanning speed reduces the amount of time the material is exposed to the heat source, leading to a faster cooling rate.

Similar to laser welding, the cooling rate in L-PBF is affected by the laser power and scanning speed. As demonstrated in ref-[110] and the analytical modelling in this work, an increase in laser power or a decrease in scanning speed reduces the cooling rate. This can be attributed to the same fundamental principles of heat transfer and thermodynamics that apply to laser welding. The cooling rate can affect the microstructural evolution and phase transformation of the material, which in turn influences the residual stress, mechanical properties, microstructure, and quality of the manufactured component. By understanding and controlling the cooling rate, it is possible to optimise the L-PBF process for different applications and materials.

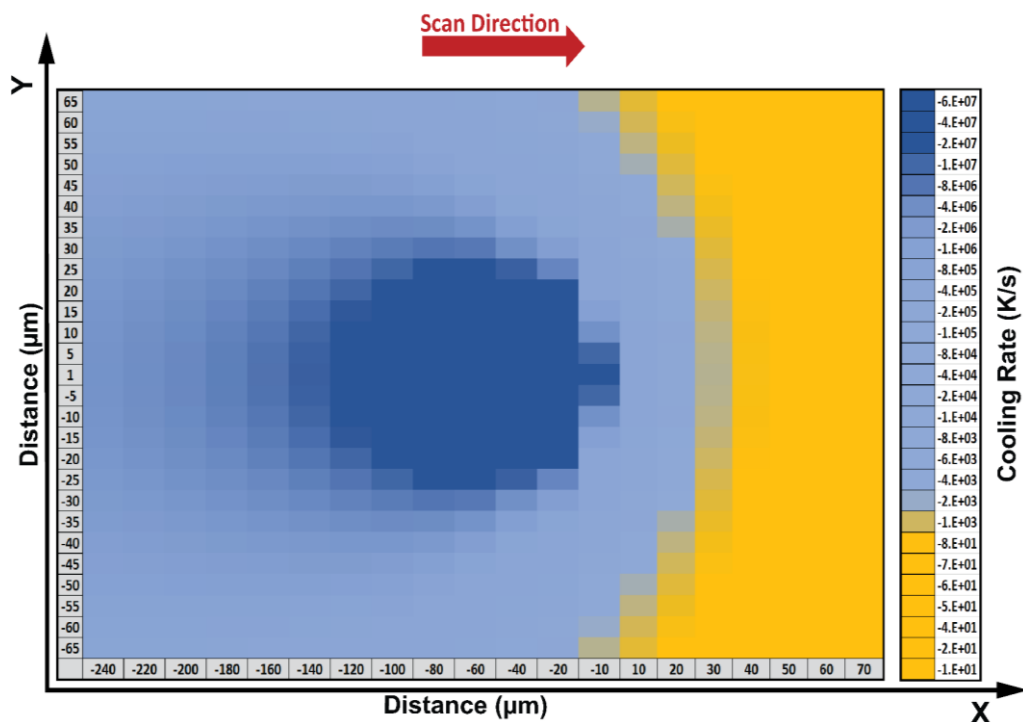


Figure 4.5: Analytical results showing the cooling rate in the form of a colour map for 20 W laser power at 300 mm/s scanning speed.

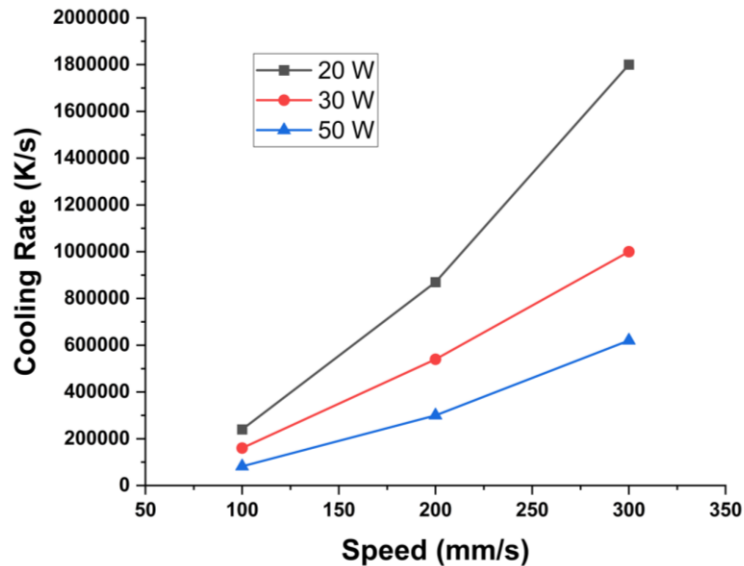


Figure 4.6: The cooling rate derived for the analytical calculations for the 20, 30 and 50 W laser power at 100, 200 and 300 mm/s scanning speed.

### 4.3 FEM Methodology

#### 4.3.1 Initial Conditions

Numerical calculations for the FEM approach were performed with the finite element analysis code in ANSYS 2021 R2™. A 2 x 1x 0.5 mm volume was modelled with a body mesh size of 15 x 15 x 15  $\mu\text{m}$ , as shown in *Figure 4.7*. A mesh-independence study was conducted to select a mesh size that would not affect the calculated values. The optimum mesh size was 15  $\mu\text{m}$ . Smaller mesh sizes would have impacted the computational time without significantly improving accuracy. The below boundary conditions were then applied to this model.

- Ambient room temperature was maintained for the substrate, implying that there was no additional heating applied to the substrate.
- Radiation on the top surface of the powder bed is permitted.
- Convective flow to the four side walls representing the shield gas.
- All the applied thermophysical values are temperature-dependent.

During the L-PBF process, most of the heat dissipates through conduction to the substrate and adjacent regions. Additionally, heat loss during the process is also attributed to convection and radiation from the top surface. In this study, convective heat losses from the top surface, resulting from the flow of inert gas in the chamber, were modelled by establishing natural convection as a surface

film interaction on the exposed surfaces. A convective heat transfer coefficient of  $10 \text{ W}/(\text{m}^2\text{K})$  was utilised for this purpose.

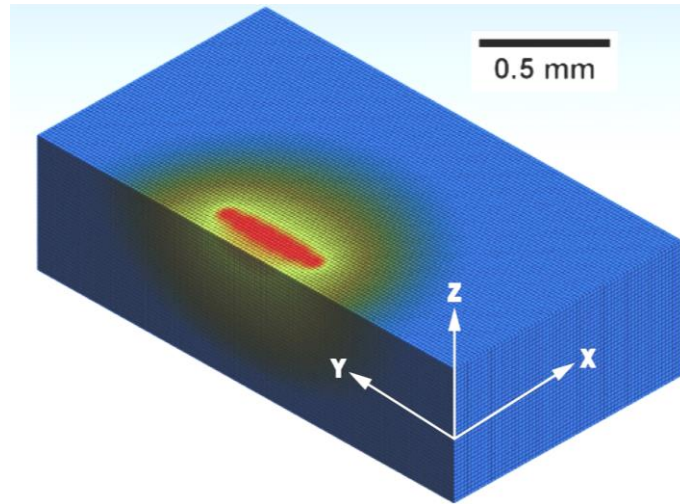


Figure 4.7: Computational domain used for the ANSYS simulation.

### 4.3.2 Heat Source

The laser beam radius and the power density distribution are important parameters for modelling the heat source in laser processing. The 1070 nm laser beam exiting the fibre laser in L-PBF is Gaussian ( $\text{TEM}_{00}$ ) in nature. For a Gaussian distributed energy source, the intensity of the laser beam drops by  $1/e^2$  as a function of distance from the centre of the beam. The  $1/e^2$  width is the diameter of the beam where the power per unit area drops to  $1/e^2$  (or approximately 13.5%) of its maximum value. This is another common method of measuring laser beam width and is often preferred in many applications because it provides a more complete picture of the beam's spatial extent. Mazumder *et al.* used a mathematical expression to define a moving Gaussian heat source and developed a three-dimensional heat transfer model for laser material processing [115]. This study employs a similar approach, and *equation 20* defines the moving Gaussian laser heat source.

$$Q_{xy} = \frac{2Q\alpha}{\pi r_b^2} \exp\left(\frac{-2r^2}{r_b^2}\right) \quad (20)$$

The Ansys Parametric Design Language (APDL) script was used to apply the heat source *equation 20* within the ANSYS platform.  $Q$  is the laser power in  $W$ ,  $\alpha$  is the absorption coefficient of the material for 1075 nm wavelength, and  $r_b$  is the  $1/e^2$  of the beam radius in  $m$ .  $Q_{xy}$  is the heat flux in  $W/m^2$  and defines the two-dimensional distribution of the heat source. The radial distance of any point from the axis of the heat source is represented as  $r$ , where  $r^2 = (x^2 + y^2)$ .

### 4.3.3 Validation of Thermal Modelling

#### 4.3.3.1 Melt pool Width and Depth

Figure 4.8 illustrates an example of the melt pool temperature extracted from the ANSYS simulation using a 20 W laser power and a scanning speed of 300 mm/s. The transient FEM simulation of the melt pool provides temperature data, from which the melt pool width can subsequently be determined. The melt pool width are derived from the FEM models by extracting the solid-liquid interface of the melt pool perpendicular to the laser traverse direction.

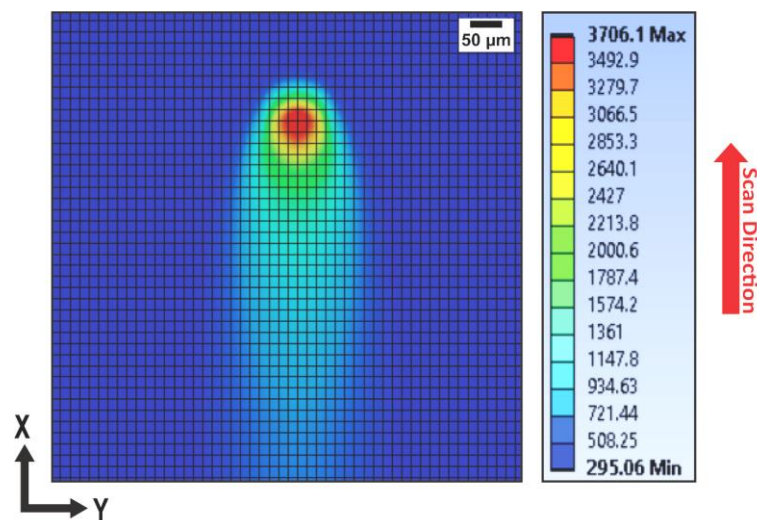


Figure 4.8: ANSYS simulated result of a melt pool with 20 W laser power and 300 mm/s scanning speed.

Figure 4.9 presents a comparison of the measured melt pool width with the width predicted by the FEM model. For all the simulated conditions, the widths predicted by the FEM model are within the range of 1 – 9 % of the values obtained from the experiments. This suggests that in terms of melt pool width, the FEM model demonstrates a closer alignment with the experimental results than the analytical results, which exhibited an average accuracy within 6%.

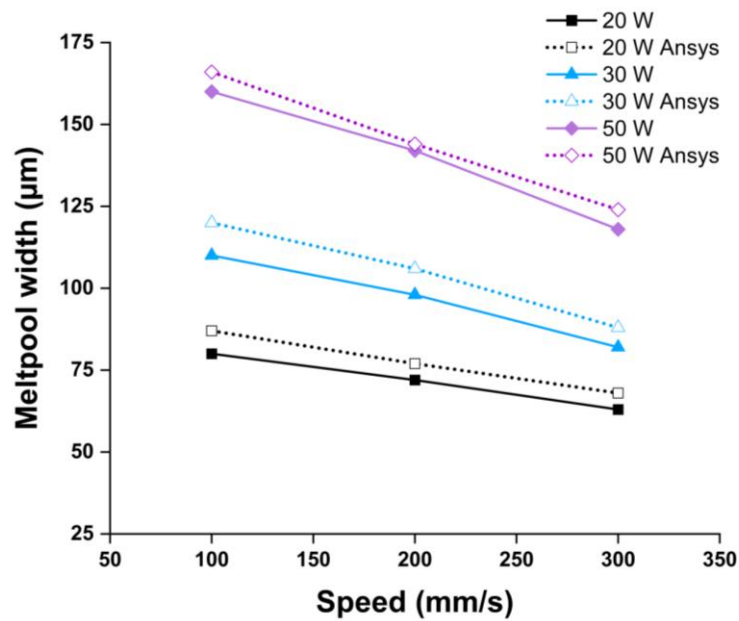


Figure 4.9: Ref-[110] and ANSYS model predicted melt pool width comparison.

Figure 4.10 illustrates an example of the melt pool depth data extracted from the ANSYS simulation using a 20 W laser power and a scanning speed of 300 mm/s.

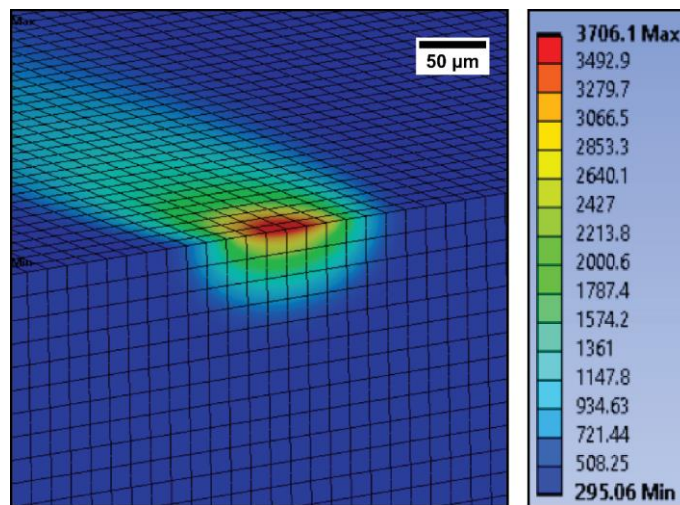
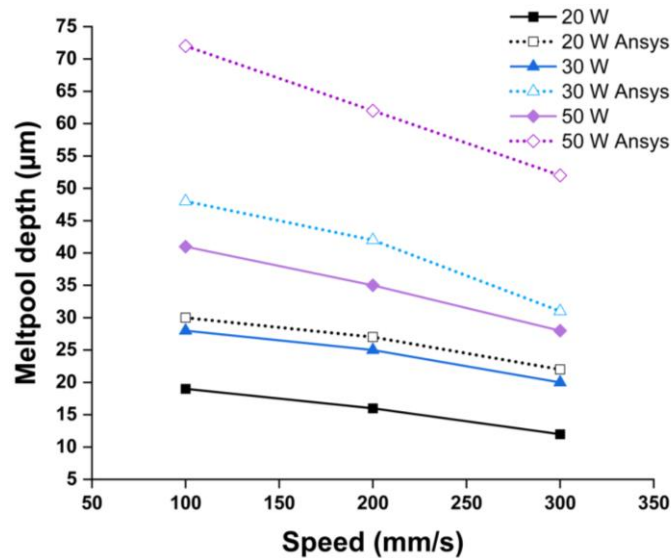


Figure 4.10: ANSYS simulated result of a melt pool depth with 20 W laser power and 300 mm/s scanning speed.

Similar to the analysis of the melt pool width, Figure 4.11 illustrates a comparative study between the melt pool depth predicted by the FEM models and the experimental results. It emerges that the FEM models have a propensity to overestimate the melt pool depth by approximately 70%. However, this degree of accuracy is not consistent, fluctuating within a 50 to 80% range. The mean width-to-depth ratio anticipated by the FEM models was 2.6 (with variations between 2.3 to 3.1), suggestive of a relatively shallow melt pool. The Carslaw and Jaeger model, mentioned in reference [7], generated a more precise prediction of

the computed melt pool depth (*Figure 4.2*) compared to the FEM approach. However, Carslaw and Jaeger's model failed to calculate melt pool width (*Figure 4.1*) accurately and resulted in underestimated values.



*Figure 4.11: Ref-[110] and ANSYS model predicted melt pool depth comparison.*

The overestimation by the FEM models, specifically regarding the depth of the melt pool, may be attributed to several factors. A primary cause could be the omission of Marangoni convection within the model. By not accounting for the Marangoni effect in the model, the FEM simulations might not fully capture the real-world dynamics of the melt pool, leading to an overestimation of its depth. Therefore, to improve the accuracy of the model, it would be beneficial to consider the influence of Marangoni convection. It is important to highlight that the accuracy of predicting the melt pool depth appears to degrade with increasing laser power. This is discussed in more detail in *Section 4.6*.

Neglecting Marangoni flow in simulations primarily impacts the depth rather than the width of the melt pool due to the directional nature of this surface tension-driven flow. The Marangoni effect, which arises from temperature gradient-induced variations in surface tension, predominantly influences fluid movement from the surface towards the bottom of the melt pool or *vice versa*. This flow significantly affects the distribution of heat and material along the direction perpendicular to the surface flow affecting the depth of the melt pool. Additionally, the surface tension gradients that drive the Marangoni effect are more impactful in the vertical direction, leading to deeper heat penetration and consequently affecting the depth of the melt pool.



### 4.3.3.2 Melt pool Temperature Evolution

Temperature transients were determined by selecting a point (probe) at the top surface of the melt pool and obtaining the temperature *versus* time data at this specific location. The temperature-time data for 20, 30 and 50 W laser power at a scanning speed of 300 mm/s is plotted in *Figure 4.12*. The simulated data shows that at a scanning speed of 300 mm/s, a 20 W laser required 0.0006 s to reach the melting point of Ti6Al4V. When the laser power was increased to 30 W, this duration dropped to 0.00025 s and further decreased to 0.0002 s with the use of a 50 W laser.

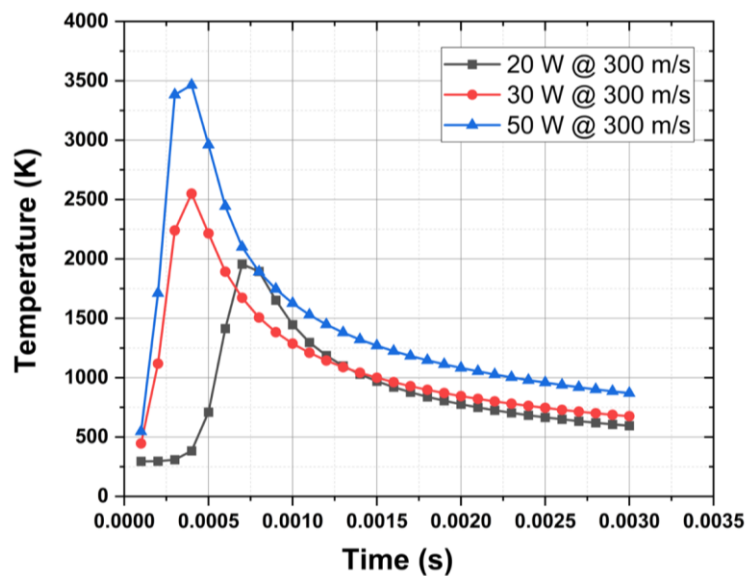


*Figure 4.12: The temperature-time data from the ANSYS simulation for the laser power 20, 30 and 50 W at a scanning speed of 300 mm/s.*

The cooling duration was calculated as the time taken for temperature to fall from the beta transus temperature (1267 K) to the martensitic transformation temperature (847 K), employing data obtained from the probe. This cooling duration is presented in *Figure 4.13* as a function of processing speed. In observing the relationship between cooling time, power input, and scanning speed, it was found that the cooling duration correlates positively with power input and inversely with scanning speed. More specifically, at a constant scanning speed of 100 mm/s, a rise in laser power from 20 W to 50 W resulted in an elongation of the cooling time from 0.002 s to 0.0054s. Additionally, for a fixed laser power of 20 W, an increase in scanning speed from 100 mm/s to 300 mm/s led to a reduction in cooling time, dropping sharply from 0.002s to 0.0007s.

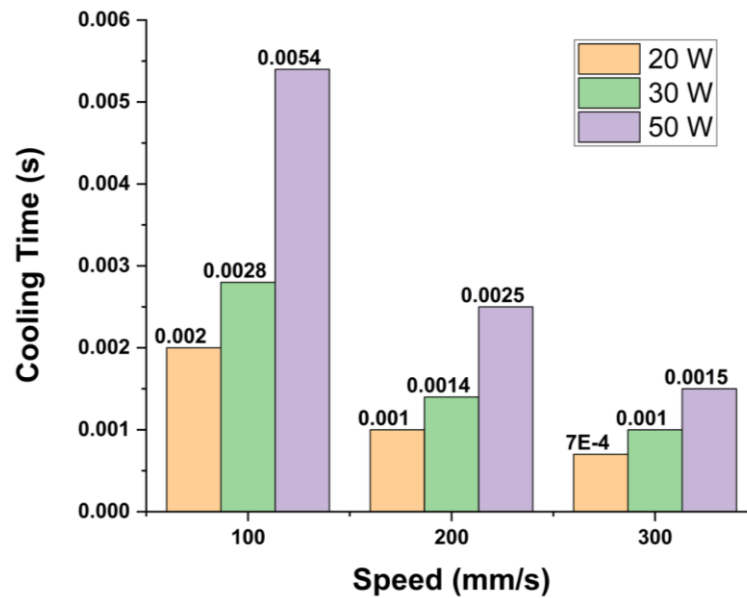


Figure 4.13: The ANSYS predicted cooling time from  $\beta$ -transus temperature (1267 K) to martensitic transformation temperature (847 K).

#### 4.3.3.3 Cooling Rate

Figure 4.14, on the other hand, demonstrates the cooling rates attained in each individual simulation. Echoing the discussion detailed in Section 4.3.3.2, the cooling rate demonstrates a comparable pattern to the cooling duration, whereby a surge in laser power or a decrease in scanning speed precipitates a reduction in the cooling rate. At a scanning speed of 300 mm/s, an increase in laser power from 20 W to 50 W saw a reduction in the cooling rate from  $6 \times 10^5$  K/s to  $2.8 \times 10^5$  K/s. The lowest value was recorded at  $7.9 \times 10^4$  K/s under the processing conditions of 50W laser power and a scanning speed of 100 mm/s.

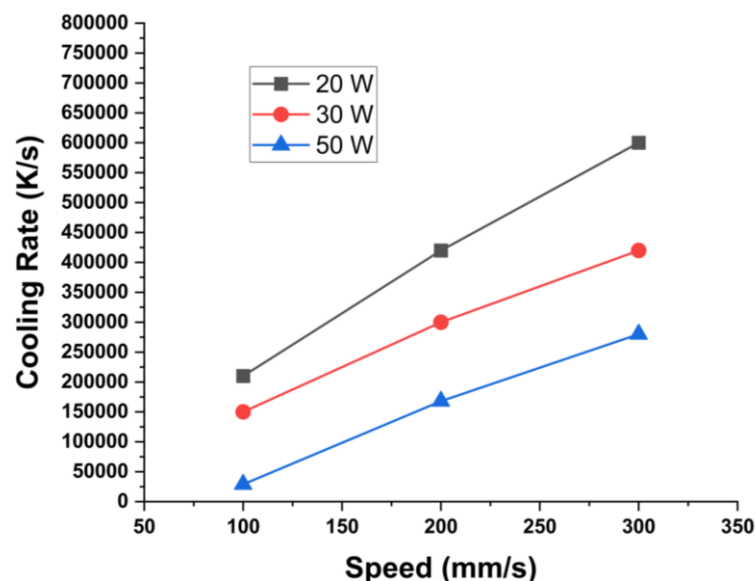
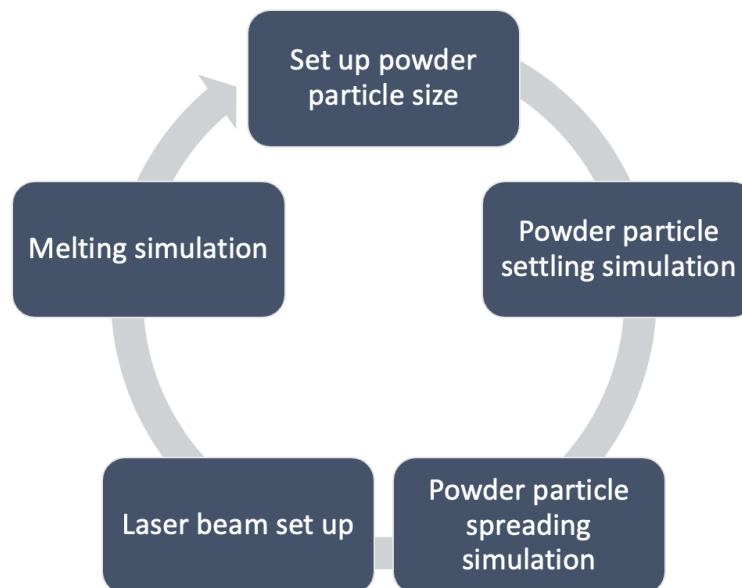


Figure 4.14: The cooling rate derived for ANSYS simulations for the 20, 30 and 50 W laser power at 100, 200 and 300 mm/s scanning speed.

#### 4.4 VoF Methodology

The mesoscopic simulation detailed in this section is performed by using a commercial CFD software Flow 3D™, developed by FlowScience Inc. Flow 3D is a CFD software package based on VoF method. *Figure 4.15* illustrates the distinct stages summarised within a Flow 3D simulation process. Starting with a Discrete Element Method (DEM) oriented simulation, the settlement of powder particles a fundamental operation within L-PBF, is carefully replicated. This is followed by a simulation modelling the spreading of powder particles, reflecting the powder spreading process that is intrinsic to L-PBF. The final stage in the simulation procedure introduces a Gaussian laser beam to instigate a melting simulation, replicating the laser melting event observed in real L-PBF operations.



*Figure 4.15: Key process steps involved in a Flow 3D simulation.*

##### 4.4.1 DEM Simulation of Powder Bed Structure

DEM is an effective computational model, specifically used for examination of the consequential dynamics of numerous solid elements. It is useful in analysing the impact motion of many solid elements and can be applied in combination with flow analysis. Using DEM, the powder layer can be depicted as an assembly of spheres with different sizes and population densities. This method allows users to track the evolution of the particle distribution, thereby facilitating an understanding of the ultimate deposition of the particle population. The various physical phenomena at play are interconnected, implying that alterations in one aspect could provoke changes in others. For

instance, diverse powder recoating mechanisms may engender contrasting powder packing conditions, which in turn can influence the heat dissipation capacity of the powder bed. This subsequently impacts the local thermal behaviour, microstructure, and conditions within the melt zone. In accordance with the ref-[110], the spherical powder particles exhibit a volume-weighted sieve diameter distribution with the 10<sup>th</sup>, 50<sup>th</sup>, and 90<sup>th</sup> percentiles recorded as  $d_{10} = 8.5 \mu\text{m}$ ,  $d_{50} = 16.6 \mu\text{m}$ , and  $d_{90} = 24.7 \mu\text{m}$ , respectively. These particles are initially introduced, following the outlined specifications, and later permitted to settle onto the powder bed. Subsequently, a spreading simulation is performed, where a blade traverses the powder bed to generate a consistent and uniform layer of powder. *Figure 4.18* illustrates output of the formed powder layer after performing DEM simulation in Flow 3D, a commercial software package capable of performing VoF simulation.

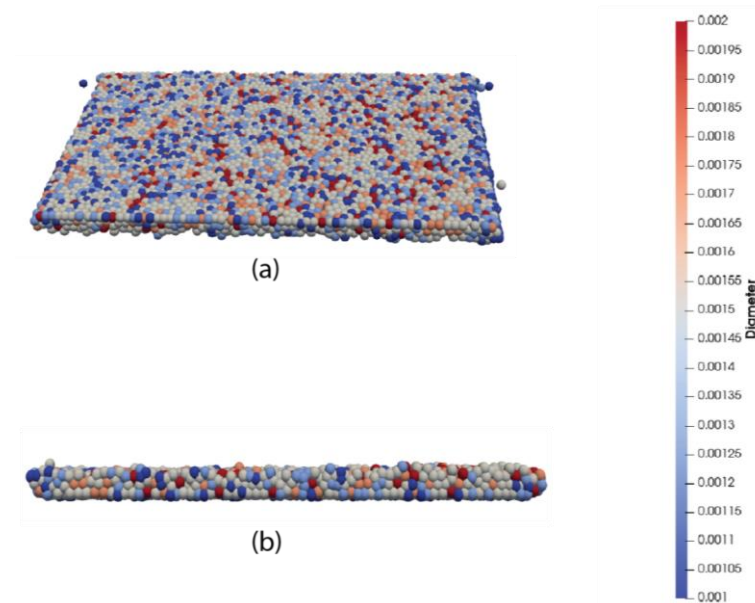


*Figure 4.16: Packing density in a powder layer with 50  $\mu\text{m}$  thickness*

#### 4.4.2 Heat Source and Numerical Model

The laser beam in L-PBF can be conceptualised as a moveable heat flux ( $Q_f$ ), exhibiting a Gaussian distribution in accordance with the specifications defined in *equation 21*.

$$Q_f = \frac{Q\alpha}{\pi r_b^2} \exp\left\{-\left(\frac{r_0}{r_b}\right)^2\right\} \quad (21)$$

Where  $Q$  is the laser power in W,  $\alpha$  is the absorption coefficient of the material for 1075 nm wavelength, and  $r_b$  is the  $1/e^2$  of the beam radius in m.  $Q_{xy}$

is the heat flux in W/m<sup>2</sup> and defines the two-dimensional distribution of the heat source. The radial distance of any point from the axis of the heat source is represented as  $r_0$ , where  $r^2 = (x^2 + y^2)$ .

Flow 3D is primarily a Computational Fluid Dynamics (CFD) code, and the VoF method is a technique employed within the CFD framework. The VoF method is utilised to track and simulate the behaviour of fluid interfaces, such as free surfaces or phase boundaries. In the CFD-based numerical simulation of an L-PBF process, the melt pool is assumed to be an incompressible, laminar, and Newtonian fluid. The governing equations for mass, momentum, and energy conservation, which are solved in the CFD simulation, are presented below:

$$\text{Mass:} \quad \nabla \cdot \vec{v} = 0 \quad (22)$$

$$\text{Momentum:} \quad \frac{\partial \vec{v}}{\partial t} + (\vec{v} \cdot \nabla) \vec{v} = -\frac{1}{\rho} \nabla P + \mu \nabla^2 \vec{v} + \vec{g} + F_b \quad (23)$$

$$\text{Energy:} \quad \frac{\partial h}{\partial t} + (\vec{v} \cdot \nabla) h = -\frac{1}{\rho} (\nabla \cdot k \nabla T) + \dot{q} \quad (24)$$

Where  $t$  is the time,  $\vec{v}$  is the velocity of melted material,  $P$  is the pressure,  $\rho$  is the mass density,  $\mu$  is the kinetic viscosity,  $g$  is gravity,  $F_b$  is the body force in the system,  $h$  is enthalpy,  $k$  is material thermal conductivity,  $T$  is temperature, and  $\dot{q}$  is heat source term.

The VoF method was introduced to track the instant free surface evolution of the melt pool and the equation is described as below.

$$\frac{\partial F}{\partial t} + \nabla \cdot (\vec{v}F) = 0 \quad (25)$$

Where  $F$  is the fluid volume fraction ( $0 \leq F \leq 1$ ). A void cell without any fluid is defined as  $F = 0$ , whereas a cell completely filled with fluid is defined as  $F = 1$ . Anything in between is defined as  $0 < F < 1$ .

The Marangoni effect, which arises from variations in surface tension, significantly influences the surface morphology and convective heat transfer within the melt pool. Therefore, a surface tension term is incorporated into the model to accurately represent the primary driving forces of fluid flow in the melt pool. The surface tension force, which depends on temperature, can be expressed as follows:

$$\gamma(T) = \gamma_m + \frac{d\gamma}{dT} (T - T_m) \quad (26)$$

Where  $\gamma$  is the surface tension at temperature  $T$ ,  $\gamma_m$  is the surface tension at melting temperature  $T_m$  and  $\frac{d\gamma}{dt}$  is the temperature coefficient of material surface tension.

#### 4.4.3 Nature of Results

Upon successful generation of the powder bed through Flow 3D's DEM simulation, the resulting configuration is extracted as an STL file. The subsequent stage involves simulation of the laser melting process using CFD techniques. At the end of the simulation, the model captures the intricate interaction between the laser beam and the powder bed. *Figure 4.17* illustrates the progression of this process by depicting the sequential interaction of the laser at intervals of 50 microseconds during a Flow 3D simulation of L-PBF of Ti6Al4V. The simulation parameters include the utilisation of a single laser with a power of 100 W and a scanning speed of 1000 mm/s over a duration of 0.0005s. The figure provides a visual representation of the evolution of the characteristics and dynamics of laser-melted material during the L-PBF process. Completion of this simulation required a total duration of 2 hours and 30 minutes.

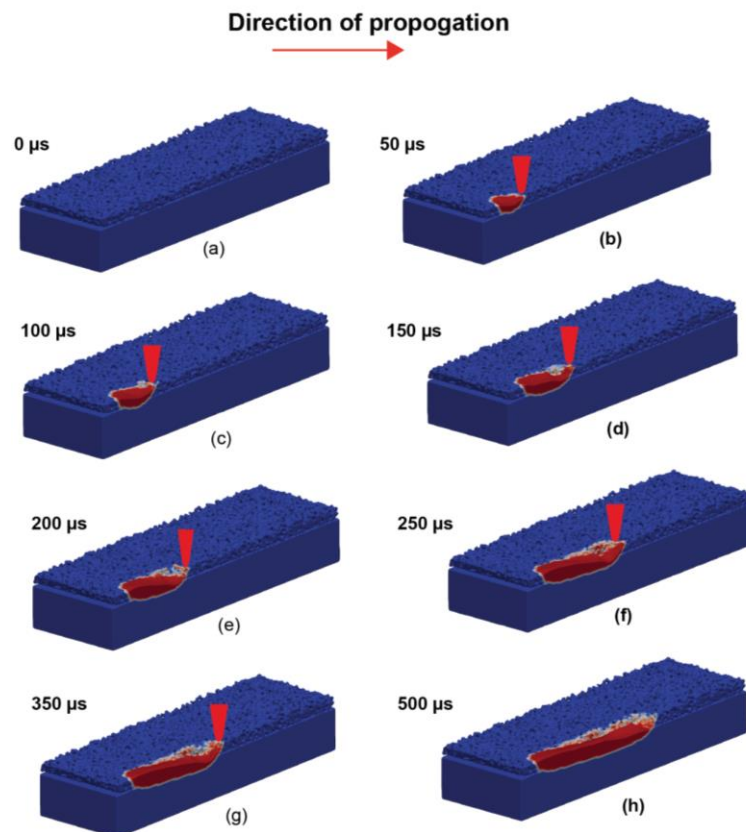


*Figure 4.17: Melt pool formation during VoF simulation of Ti6Al4V with a single laser at 100 W laser power and 1000 mm/s scanning speed.*

#### 4.4.4 Validation of Thermal Modelling

##### 4.4.4.1 Melt pool Width and Depth

The result of each simulation is then post-processed using FlowSight™. The width of the melt pool is established via direct measurement perpendicular to the trajectory of the traversing laser. The melt pool depth is measured by taking a lateral cross-section using the upper surface of the molten pool to the maximum depth of the melt region as reference points. *Figure 4.18* provides an illustration of a typical cross-sectional view of a melt track, clearly displaying the geometry of the melt pool highlighting the liquid melt pool and solid powder region. The melt pool dimensions can be extracted from this simulation data.

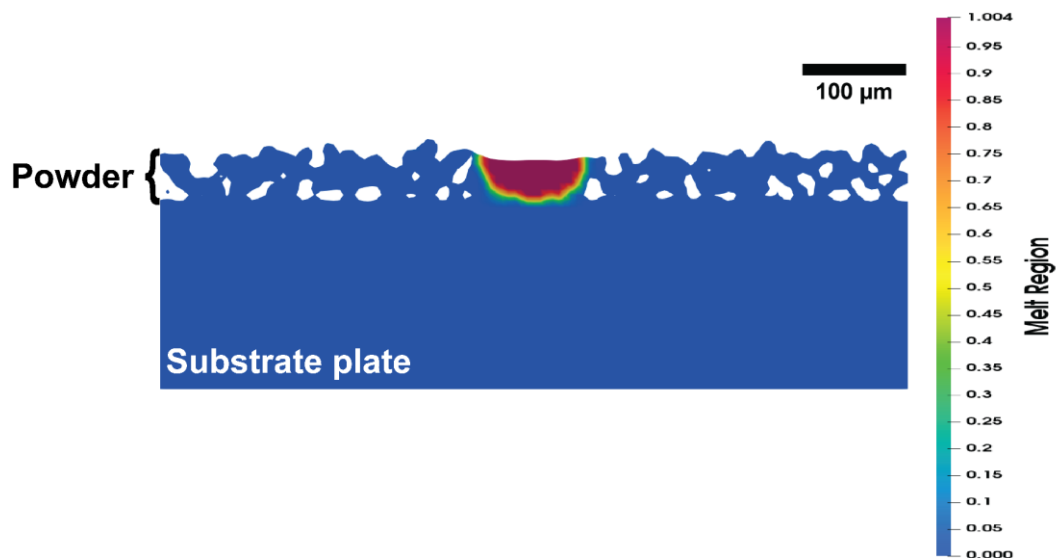


*Figure 4.18: The cross-section of a melt track showing the liquid melt pool and solid region in a Flow 3D simulation with a single laser at 100 W laser power and 1000 mm/s scanning speed.*

*Figure 4.19* illustrates a comparative analysis between the melt pool width as predicted by the Flow 3D model and the empirical width obtained from Yadroitsev *et al.*'s study. For each simulated model, the predicted melt pool width generated by the Flow 3D model deviated by no more than 5% from the experimentally measured values. The average accuracy of the Flow 3D model in predicting the melt pool width is around 2%, although this varies within a range of 1% to 5%. This data suggests that the Flow 3D model exhibits a higher degree of convergence of melt pool width with empirical findings as compared to the analytical and FEM models.

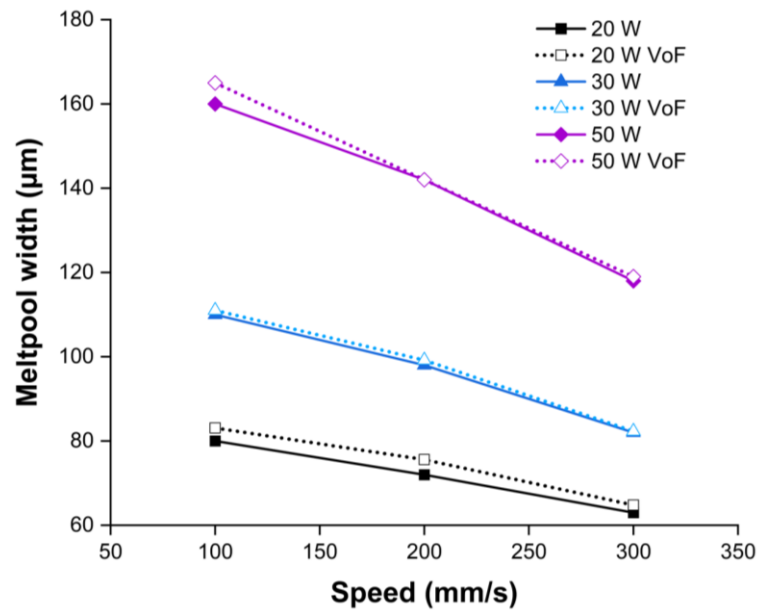


Figure 4.19: Ref-[110] and Flow 3D model predicted melt pool width comparison.

Similar to the FEM forecasts, the accuracy of the melt pool depth predictions made using the Flow 3D models does not quite align with the level of accuracy achieved for the width predictions as shown in *Figure 4.20*. The average accuracy of the Flow 3D model's predictions for the melt pool depth is approximately 56%, with a range extending from 26% to 79%. This signifies a notably lower level of accuracy in the depth estimations as compared to the predictions for the width. Nonetheless, the depth prediction produced by Flow 3D betters that offered by ANSYS using its FEM. The improvements in the accuracy of Flow 3D models can be attributed to the incorporation of Marangoni flow and phase change effects. These factors could influence the behaviour of fluids in numerous real-world situations. By factoring them in, simulations become more realistic, thereby enhancing their accuracy compared to more basic FEM, which does not consider Marangoni flow and phase change effects.



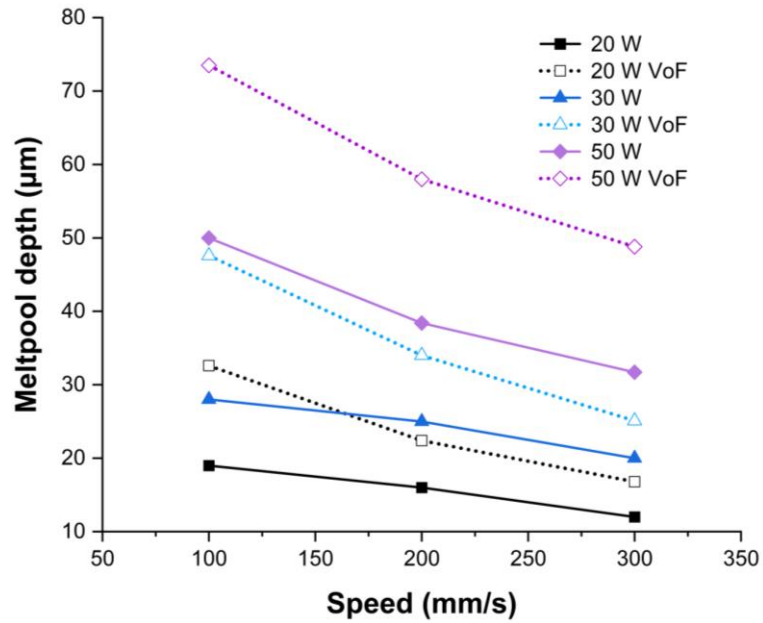


Figure 4.20: Ref-[110] and Flow 3D model predicted melt pool width comparison.

#### 4.4.4.2 Melt pool Temperature Evolution

Similar to the FEM methodology, temperature *versus* time data was gathered by choosing a location, specifically a point (referred to as a probe) at the top centre of the laser spot, and retrieving the temperature-time information from this exact position. Figure 4.21 illustrates a sample of the temperature-time data obtained from the Flow 3D simulation, which was run using a 20 W laser power at a scanning speed of 300 mm/s. During this simulation, the peak melt pool temperature at the probe's location climbed up to 2200 K.

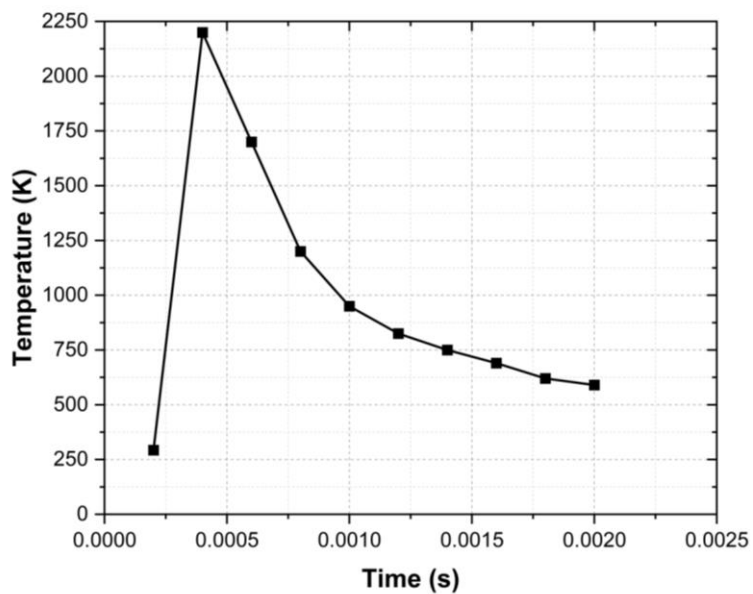


Figure 4.21: Temperature evolution during a Flow 3D simulation with 20W laser power at 300 mm/s scanning speed.

#### 4.4.4.3 Cooling Rate

Figure 4.22, demonstrates the cooling rates attained from each individual Flow 3D simulations for the 20, 30 and 50 W laser power at 100, 200 and 300 mm/s scanning speed. The employment of VoF methodology within the framework of Flow 3D simulation exhibits parallels with the cooling rates observed in analytical and FEM based simulations. Within the simulation, a link between the cooling rate and duration is evident. This connection becomes clearer when laser power is increased or scanning speed is reduced, both actions leading to a slower cooling rate. At a scanning speed of 300 mm/s, the cooling rate decreased from  $1.05 \times 10^6$  K/s to  $6.5 \times 10^5$  K/s when the laser power was raised from 20 W to 50 W. The smallest observed cooling rate was  $5.3 \times 10^5$  K/s, which occurred under processing conditions of a 50W laser power and a scanning speed of 100 mm/s.

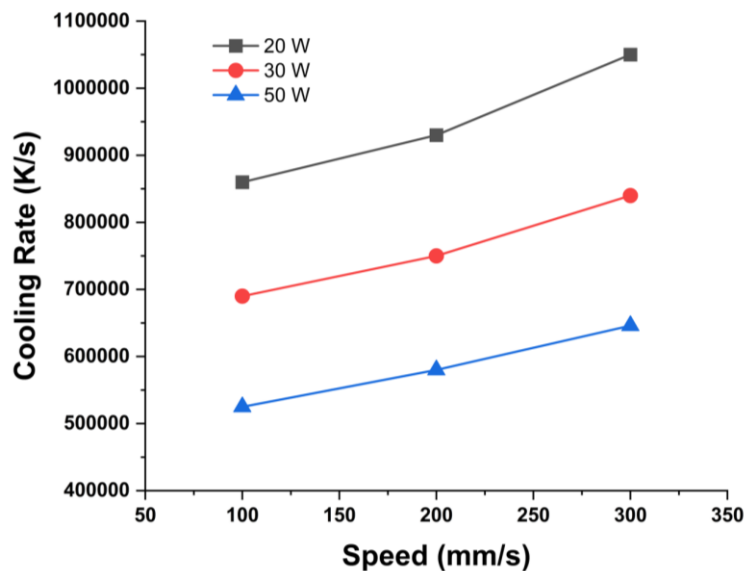


Figure 4.22: The cooling rate derived for Flow 3D simulations for the 20, 30 and 50 W laser power at 100, 200 and 300 mm/s scanning speed.

#### 4.5 Discussions

The analytical solution illustrated in this chapter demonstrates proficiency in predicting parameters such as the width of the melt pool, the surface temperature of the melt pool, and the corresponding cooling rate. The precision of these characteristics, while usable, does not quite reach the level of accuracy observed in methodologies such as FEM and VoF. Numerical techniques such as FEM and VoF innately display a superior capability when compared to analytical

methods. Their inherent strength lies in managing complex geometries and intricate boundary conditions. Their capacity to address non-linearities and transient conditions is another advantage, providing iterative solutions that analytical methods typically find challenging. While numerical methods may introduce some degree of approximation error, they still maintain a high level of accuracy, providing localised results for intricate systems that are typically inaccessible using analytical methods. However, their advanced proficiency requires a trade-off with more significant computational resources and careful error and convergence considerations. Hence, while they are suited for high-precision simulations, analytical methods remain valuable for elementary understanding and quick calculations.

Using the FEM-oriented ANSYS software, numerical simulations were performed. These findings demonstrate a direct relationship between the time needed to complete each simulation and the temporal span represented within the simulated scenario. *Figure 4.23* presents a comparison of the ANSYS simulation times. It is notable that the most prolonged duration required for a simulation, operating under conditions of 50 W laser power at a speed of 100 mm/s, amounted to 2 hours and 30 minutes. The total duration represented within the simulation was 0.00925s, sufficient to capture adequate data, including the cooling rate during solidification.

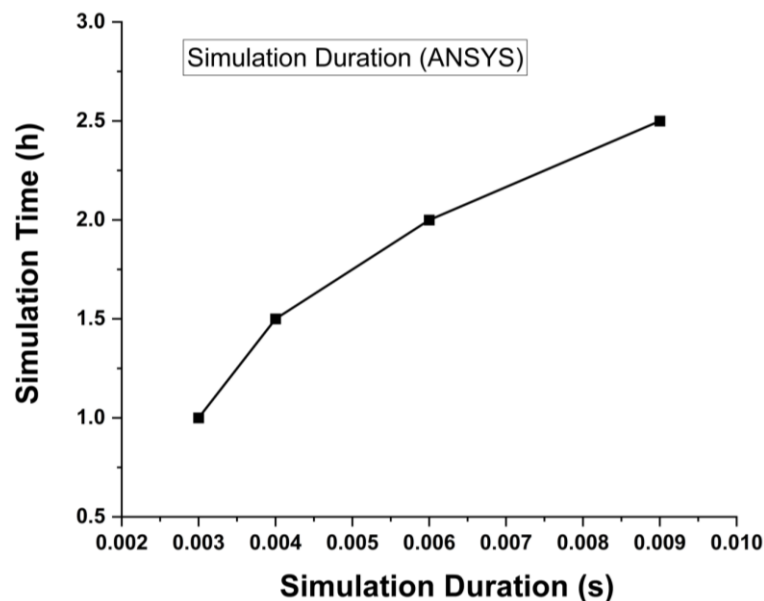


*Figure 4.23: Time taken to complete ANSYS simulations.*

Whilst the VoF method affords detailed outputs such as three-dimensional temperature and velocity distributions of the deposit with free curved surfaces,

and tracks the free surface of the molten pool, inclusive of surface tension-enabled flow within the molten pool, it is important that this method is computationally intensive. *Figure 4.24* presents a comparative analysis of the duration required for each VoF simulation executed in Flow 3D. In contrast to the FEM simulation, the duration of the Flow 3D simulations exhibited a correlation with both the laser power and the scanning speed. For a simulation running for a total duration of 0.002 seconds, there was, on average, a notable 60% increase in simulation time when the laser power was elevated from 20W to 30W and subsequently to 50W. In parallel, a reduction in scanning speed led to a marked escalation in simulation time, on average increasing by a factor of 2.5 times.

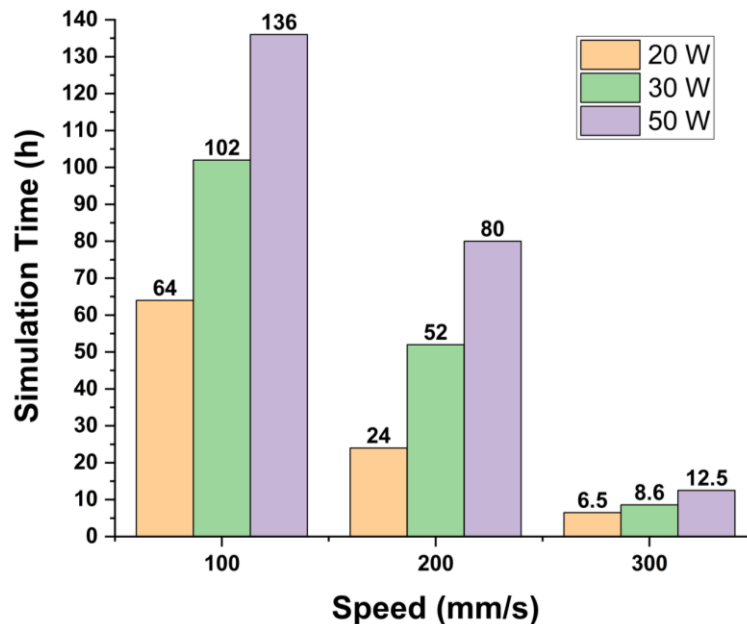


*Figure 4.24: Simulation time each model for Flow 3D for a fixed duration of 0.002s.*

The optimal scanning speed for a typical DAM process for Ti6Al4V is identified to be 1.6 mm/s. Due to this slower scanning speed, the time required for simulation would predictably increase, as it becomes crucial to capture the cooling rate during solidification. The solidification period for Ti6Al4V, extending from the beta transus phase to the martensitic transformation temperature, is estimated to be approximately 1 second. This time span introduces a significant challenge for a mesoscopic simulation in terms of the resultant elongation of simulation time. At present, for a L-PBF simulation employing a 50W laser at its slowest speed of 100 mm/s, as presented in this chapter, the lengthiest duration recorded is 136 hours. The simulation duration decreases to 64 hours when utilising a 20W laser at the same speed. However, it is worth noting that the DAM

process, deploying five diode lasers each with a 4W laser power, can readily accumulate a total power of 20W. Furthermore, any DAM simulation at a speed of 1.6 mm/s necessitates a minimum simulation duration of 1 second to obtain any significant insights regarding the solidification and cooling rates. This condition implies that the 64-hour simulation period may experience an exponential increase, potentially reaching an unsustainable level during the DAM simulation process.

Consequently, while VoF simulations at a mesoscopic scale can provide comprehensive data regarding the melt pool, including aspects such as the Marangoni flow and other convective flows, they may not be entirely suitable for DAM simulations due to the intensive computational resources and time required. A FEM based approach could represent a balanced compromise, providing valuable insights while managing computational resources more effectively. Furthermore, the FEM approach holds an advantage over analytical methods as it furnishes more accurate and comprehensive information. This includes data pertaining to the depth of the melt pool, the correlation between temperature and time, as well as the cooling rate of the melt pool.

#### **4.6 Conclusions**

*Table 4.2* presents the accuracy of predicted melt pool width, depth, and temperature using analytical, FEM, and VoF methods, compared against experimental results. Additionally, the table includes data on the cooling rate and computational time from each simulation. The accuracy of melt pool width predictions is significantly better with FEM and VoF compared to the analytical method. This improvement is primarily attributed to the numerical nature of these methods, which allows for the incorporation of thermophysical properties, enhancing the precision of the simulations. Similarly, the accuracy of melt pool temperature has improved in FEM and VoF in comparison to the analytical method. However, the FEM method has overestimated the temperature when the energy density increased. This is attributed to the fact that FEM is a conduction-driven process where convective flow, including Marangoni convection, is omitted; hence, when the laser power increases, it produces more error. Furthermore, the accuracy of melt pool depth prediction is notably enhanced in the VoF method due to the incorporation of Marangoni flow, which allows for a

more detailed simulation of fluid dynamics within the melt pool. This inclusion helps to better capture the real-world behaviors and interactions that affect melt pool characteristics.

The key benefit of the analytical solution is its simplicity and the minimal computational time required, typically around 10 seconds. However, both FEM and VoF require high-performance computers to run the simulations due to their complex numerical nature. This complexity allows for enhanced accuracy in predicting melt pool characteristics but at the cost of increased computational resources and time. Hence, the analytical solution could be used as a first stage in the modelling process to get an initial idea of the results, and then proceed with more advanced simulations when necessary. This approach allows for a preliminary assessment before committing significant computational resources to more detailed analyses.

Parameter	Analytical	FEM	VoF
<b>Melt Pool Width</b>	6 – 31%	1 – 9 %	1 – 5 %
<b>Melt Pool Depth</b>	Not possible	50 – 80%	26 – 79 %
<b>Average Melt Pool Temperature</b>	14 – 40 %	2 – 40 %	6 – 11 %
<b>Cooling Rate (Minimum and Maximum)</b>	Min: $7.9 \times 10^4$ K/s Max: $6.5 \times 10^5$ K/s	Min: $7.9 \times 10^4$ K/s Max: $6 \times 10^5$ K/s -	Min: $5.3 \times 10^5$ K/s Max: $1.05 \times 10^6$ K/s
<b>Simulation Time</b>	10s	2.5 h	6.5 to 136 h

*Table 4.2: The table displays the accuracy of the three methodologies (analytical, FEM and VoF) in replicating various modelled effects, benchmarked against the original experimental data.*

Using ANSYS for FEM simulations revealed a direct correlation between simulation time and the temporal scope of the scenario. For example, a simulation with a 50W laser at 100 mm/s speed took 2 hours and 30 minutes, adequately capturing data like the cooling rate during solidification. In contrast, VoF simulations, performed in Flow 3D, showed that simulation duration is affected by both laser power and scanning speed, with notable increases in time when altering these parameters. The scanning speed for a DAM process using Ti6Al4V was determined to be 1.6 mm/s, significantly impacting simulation time due to the need to capture detailed solidification rates. The longest recorded simulation for a L-PBF process was 136 hours, which could potentially increase

exponentially (estimated to be 130 days) for DAM simulations due to their slower speeds and more detailed requirements such as multiple laser arrangements.

This suggests that while VoF simulations offer comprehensive data, including convective flows like Marangoni flow, they may not be the most feasible for DAM due to the heavy computational demands. An FEM-based approach, in contrast, offers a more balanced solution, providing data while efficiently managing computational resources. It offers advantages over analytical methods by delivering more accurate information on aspects such as melt pool morphology (width and depth) and temperature-time correlation making it a preferable choice for DAM in comparison to the analytical and VoF methods.

## 5 Chapter 5: Modelling of Ti6Al4V during DAM

Various process modelling and thermographic analysis methods have been studied in order to understand L-PBF and EB-PBF processes [74], [116], [117], [118]. However, little attention has yet been paid to the modelling of Diode Area Melting (DAM). The work in this chapter presents an analytical model based on the Rosenthal equation and a numerical model based on the Finite Element Method (FEM) to investigate the temperature distribution, temperature evolution, melt pool dimensions and cooling rates of Ti6Al4V during DAM. It should be noted that the Analytical and FEM models elaborated upon here build upon a prior models specific to L-PBF, which were developed, validated and delineated in *Chapter 4*. The surface temperature of the molten pool formed using multiple diode lasers is captured using a charged coupled device (CCD) thermal camera. The calculated melt pool dimensions, molten pool temperature and cooling rate are then compared against the empirical results. In the study presented, the mathematical models endeavour to provide a comprehensive interpretation of the melt pool dimensions, temperature fields and the subsequent cooling rates induced by an array of laser beams in a range of configurations. The primary ambition of these investigative models is to offer a mechanism through which one might determine the optimal processing window and assist with the selection of process parameters for DAM processing of different materials.

### 5.1 Modelling approaches

#### 5.1.1 Analytical Model

The analytical model employed in this study is detailed in Chapter 4, specifically in *Section 4.2*, where it has been validated for the processing of Ti6Al4V within the context of L-PBF. As with the previous approach, the Rosenthal equation is applied to multiple locations ( $r_1, r_2 \dots r_n$ ) around the centre of the laser beam in order to calculate the temperature distribution and width of the melt pool. The resultant values of the calculated thermal distribution and the respective cooling rates can be visually represented using a colour contour plot. This work is done in a Microsoft Excel™ spreadsheet. The calculated values of temperature at each location are presented in each cell of the spreadsheet and



the width of the melt pool is extracted from the spreadsheet and presented. The physical properties of Ti6Al4V are kept constant, and Table 5.1 presents the thermo-physical properties of Ti6Al4V used for the analytical model [109].

*Table 5.1: Processing parameters and material properties.*

<b>Parameter and Properties</b>	<b>Values (Unites)</b>
Scanning speed	100 (mm/min)
Beam diameter	65 ( $\mu\text{m}$ )
Solidus temperature	1878 (K)
Liquidus temperature	1923 (K)
Absorptivity at 808nm wavelength	0.65
Density	4375 (kg/m <sup>3</sup> )
Thermal conductivity	7 (W/m K)
Thermal diffusivity ( $10^6 a$ )	2.9 (m <sup>2</sup> /s)

### 5.1.2 FEM Model

Numerical computations utilising the FEM were executed using the finite element analysis software ANSYS 2021 R2™. A volume dimension of 2 x 1 x 0.5 mm was modelled, incorporating a body mesh dimension of 15 x 15 x 15  $\mu\text{m}$ , as depicted in *Figure 5.1*. In the interest of ensuring computational robustness, a mesh-independence study was undertaken to identify a mesh size that would not unduly influence the resultant values. The optimal mesh dimension was determined to be 15  $\mu\text{m}$ . Employing finer mesh dimensions would have overly elongated the computational dura

tion without yielding a notable enhancement in accuracy. The initial conditions, boundary conditions, and the heat source are consistent with those detailed in Chapter 4.

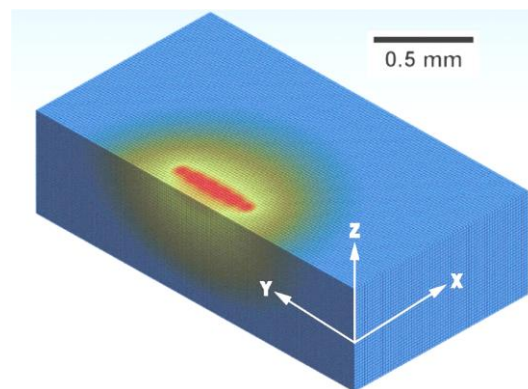


*Figure 5.1: Illustrates the computational domain used for FEM simulation in ANSYS showing six laser beams.*

## 5.2 Experimental Methodology

### 5.2.1 DAM Beam Profiles

The experimental setup used in this work employed a laser assembly comprising a linear array of multiple individually addressable laser beams (as described in Chapter 3, *section 3.1.3*), which were traversed across the powder bed using a gantry system. The primary aim of this investigation is to gain an understanding of the temperature distribution and resultant cooling rate generated using various laser profiles produced through the activation of different numbers of lasers in the array. A total number of six laser arrays are selected to understand the effect of multiple diode laser beams; these are referred to as beam profiles (BP). Although the system can currently accommodate up to fifty lasers simultaneously in a single row, only six lasers will be utilised in this study in order to maintain sensible computational times. The small-scale multi-laser interactions and their effects on the melt pool provided by the six lasers can be used for subsequent scaling of the DAM process.

The beam profiles are characterised using a scanning slit beam profiler (NanoScan2sPryo/9/5) as described in *Section 3.3*. *Table 5.2* provides a comprehensive breakdown of the total power and the  $1/e^2$  width of each laser profile in the Y direction. Additionally, the table incorporates a schematic representation of the configuration of each laser beam profile.

*Table 5.2: Specification of laser beam profiles used in this study.*

<i>Beam profile (BP.)</i>	<i>No. of lasers</i>	<i>Total power (W)</i>	<i>1/e<sup>2</sup> Beam Width (μm)</i>	<i>BP Schematic</i>
1	1	4	65	●
2	2	8	141	●●
3	3	12	217	●●●
4	4	16	294	●●●●
5	5	20	370	●●●●●
6	6	24	446	●●●●●●

### 5.2.2 Layer Thickness and Single Tracks

The layer thickness of the powder was kept at 1mm for all experiments. The objective of this study is to investigate the morphology of the melt pool formed during the activation of BPs. Due to the fragility and small size of the tracks formed, a layer thickness of 1 mm was chosen to ensure sufficient powder

support beneath the solidified melt pool for the individual tracks. Layers between 30 to 50  $\mu\text{m}$  were deemed unsuitable as they could not be effectively removed from the powder bed owing to their smaller size. Furthermore, multiple tracks were created in close proximity to one another, ensuring that the tracks were held together by the heat affected zone. This arrangement was crucial for maintaining the structural integrity of the formed tracks.

The scanning speed was set at 100 mm/min, which was demonstrated as the optimum processing speed for Ti6Al4V during DAM [6]. Pre-alloyed and gas atomised Ti6Al4V powder used in this study was supplied by Carpenter Additive. The material composition and the particle size distribution of the powder is described in *Section 3.6.1*. The build chamber was purged with Argon to avoid oxidation during the process. This process is described in *Section 3.1.2*.

A single layer with an area of 5  $\text{cm}^2$  consisting of multiple melt tracks, as shown in *Figure 5.2*, was created with each beam profile. Multiple melt tracks were distinctly segregated by using a hatch spacing that was sufficiently large enough to avoid coalescence of tracks. The melt pool width was subsequently determined by taking an average of measurements made at various positions along these melt tracks. Samples resulting from these experiments were hot-mounted and prepared for high-resolution imaging using a scanning electron microscope (Tescan Vega 3).

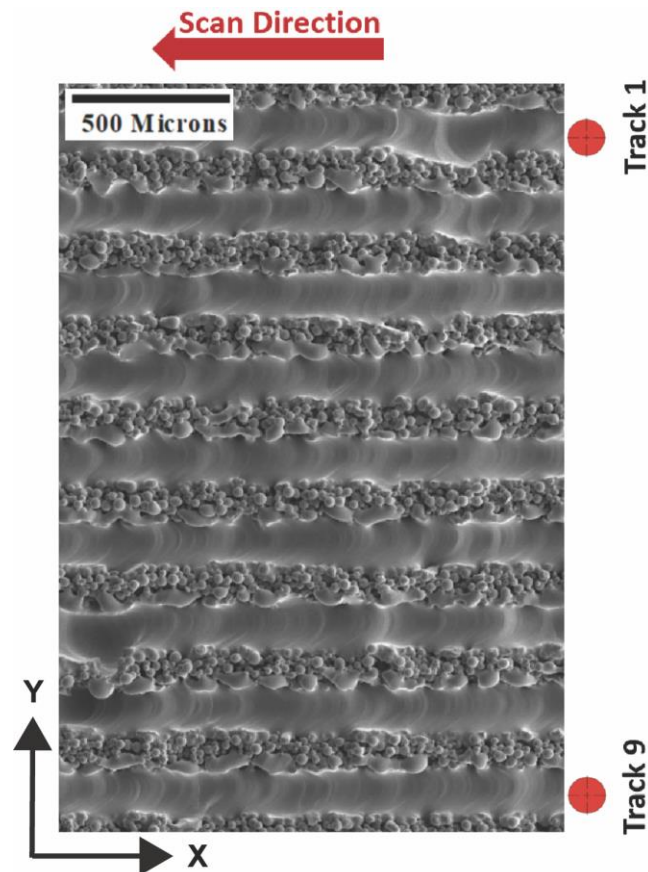


Figure 5.2: An example of melt tracks created for this work. Each melt track is 5 cm long, has 120  $\mu\text{m}$  hatch spacing, and produces a total area of 5 cm<sup>2</sup>.

In order to transfer the formed melt pool tracks, each sample, covering an area of 5 cm<sup>2</sup>, was carefully removed along with the underlying powder. Due to the heat affected zone, the powder between each track was sintered and bonded together, enabling safe transfer to a sample box. Subsequently, each sample was hot-mounted and sectioned to measure the depth of the melt pool.

## 5.3 Results and Discussion

### 5.3.1 Melt Pool Surface Temperature

#### 5.3.1.1 Temperature colour map from the analytical model

In the analytical model based on the Rosenthal equation, the heat source is often considered as a point, line, or ellipsoid type. Plotkowski *et al.* developed a transient semi-analytical model based on the Rosenthal equation to calculate the heat transfer effects and compare with the experimental results of AlSi10Mg produced by both L-PBF and EB-PBF processes [113]. Analytical-based solutions require significantly lower computing power compared to numerical techniques. However, consideration of complex boundary conditions, non-linear material

properties, and most notably, the ability to solve transient conditions are unfeasible with this approach.

In this work, the heat source in the Rosenthal Equation is applied as a point energy source and executed as a steady-state analysis in a Microsoft Excel™ spreadsheet. This method is capable of calculating the heat flow through the material and present it in the form of a spatial temperature distribution. For each beam profile the temperature on the surface of the melt pool is then derived spatially within each cell of the spreadsheet as shown in *Figure 5.3*. *Figure 5.3 (a)* illustrates the calculated melt pool temperature for a beam configuration with a single laser. In contrast, *Figure 5.3 (b)* displays the same for a configuration employing six lasers. The observed differences in the scale bar across the X and Y axes between these figures are due to the increase in the number of lasers, which leads to an growth of the melt pool size. To adequately show the enlarged melt pool, adjustments in the scale parameters are made. The melt pools generated by multiple laser beams overlap and effectively creating a single melt track due to the close proximity of each beam. The *Figure 5.4* shows a corresponding temperature colour map showing the temperature distribution for the beam profile with a single laser (a) and six lasers (b). The average temperature across the melt pool (perpendicular to the beam traverse direction) is calculated as 2060 K and 2369 K for the single beam and the six lasers beam profiles respectively. The melt pool width is then extracted from the temperature colour map. The following sections compare the average surface temperature of the melt pool extracted from the analytical and FEM models with those determined from the thermal camera data for each beam profile.

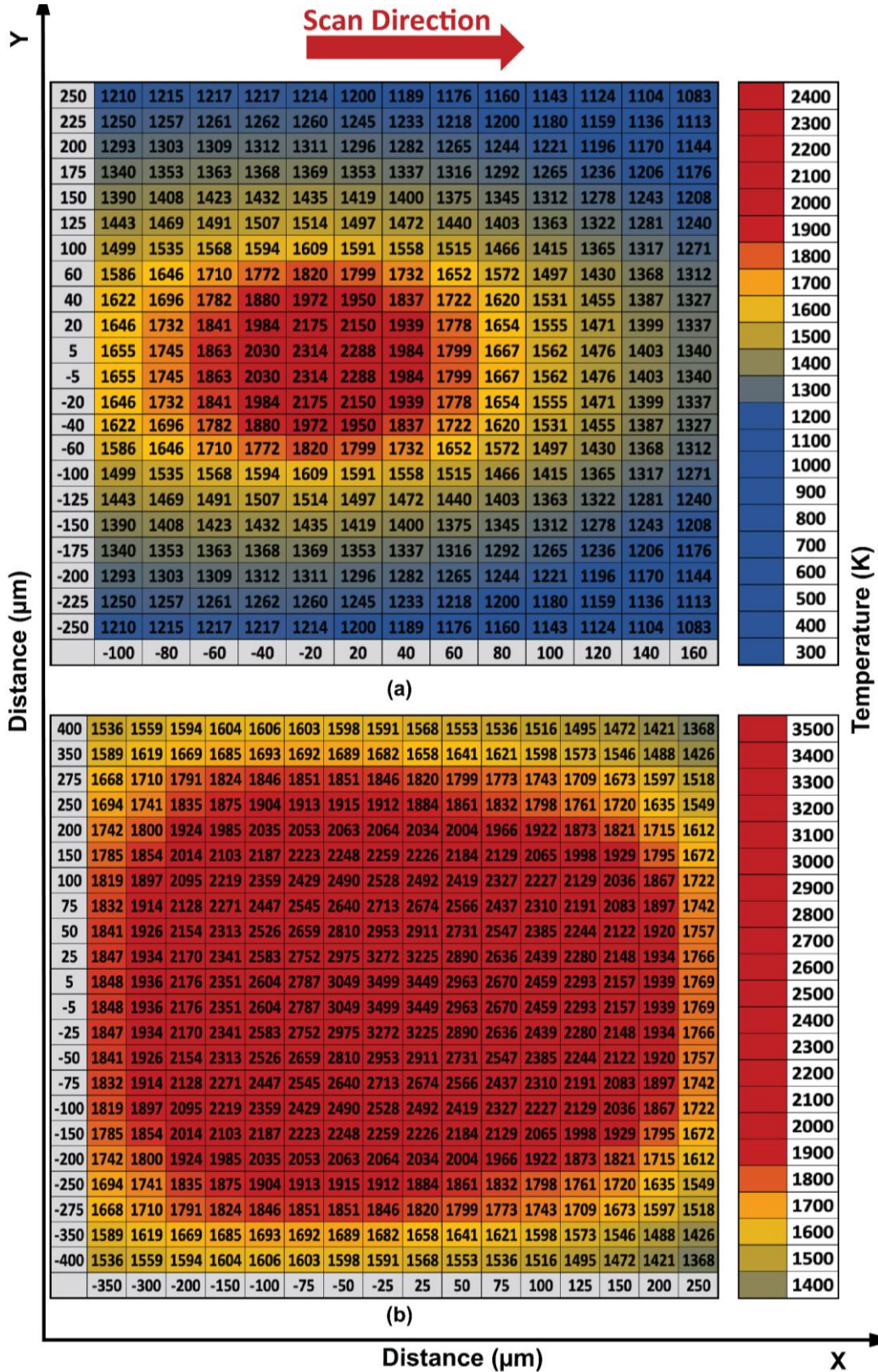


Figure 5.3: Calculated temperature for each cell within the melt pool for the beam profile with a single laser (a) and six lasers (b).

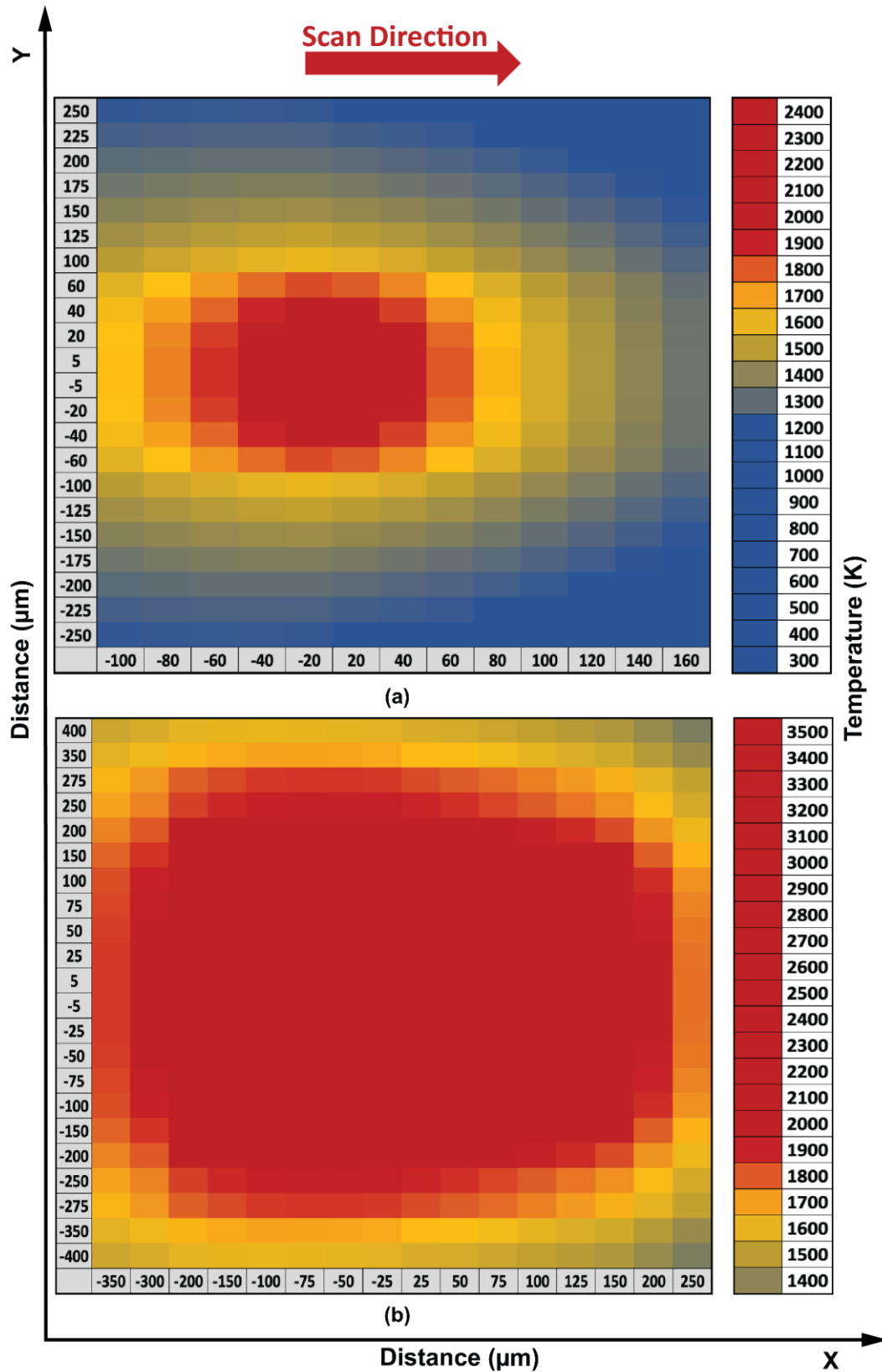
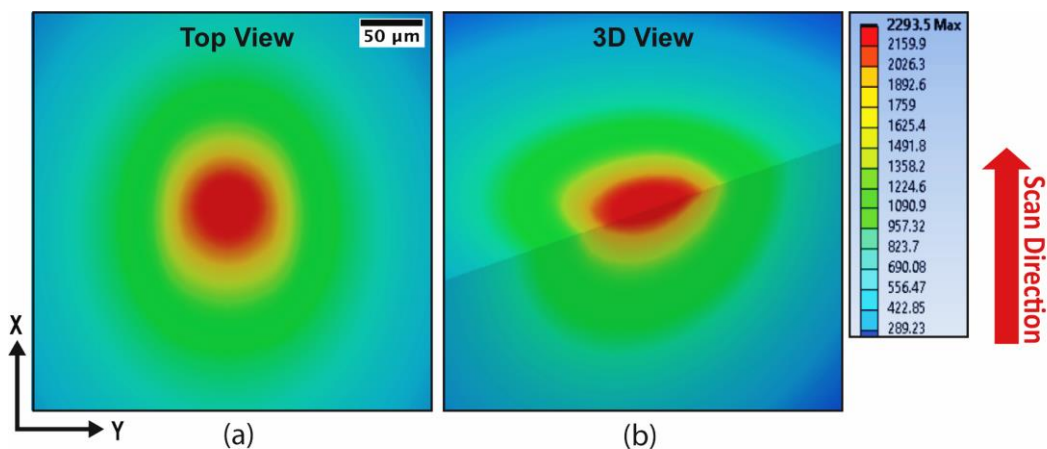


Figure 5.4: Temperature colour map of the melt pool for the beam profile with a single laser (a) and six lasers (b).

### 5.3.1.2 Temperature colour map from the FEM model

FEM models numerically solve the transient energy conservation equation with convective and radiative boundary conditions within the environment yielding the temperature distribution in 3D, from which both melt pool width and depth can be determined. The principal forces responsible for flow in the molten pool are surface tension and buoyancy forces. The continuity equation for mass conservation and the Navier-Stokes equations for fluid motion must be solved for fluid flow and penetration depth to resolve the melt pool depth. The Rosenthal equation and FEM model do not consider the effects of the convective flow of liquid metal inside the molten pool necessary for calculating the temperature field. In addition, the omission of Marangoni convective phenomena further restricts the prediction of melt pool depth information, including temperature distribution below the surface layer [12]. The temperature distribution in the form of a colour map and melt pool boundary, as obtained from the FEM model for the beam profile with a single laser (melt pool width (a) and depth (b)) is shown in *Figure 5.5*. Similarly, *Figure 5.6* illustrates the corresponding temperature colour maps produced by FEM simulation for a beam profile with six lasers, showing width (a) and cross section (b). The surface temperature of the melt pool increases with addition of each laser. The calculated average melt pool temperature (perpendicular to the beam traverse direction) is 1985 K and 2310 K for the beam profile with a single and six lasers respectively.



*Figure 5.5: Temperature colour map produced by FEM simulation for a single laser beam surface (a) and cross section (b)*



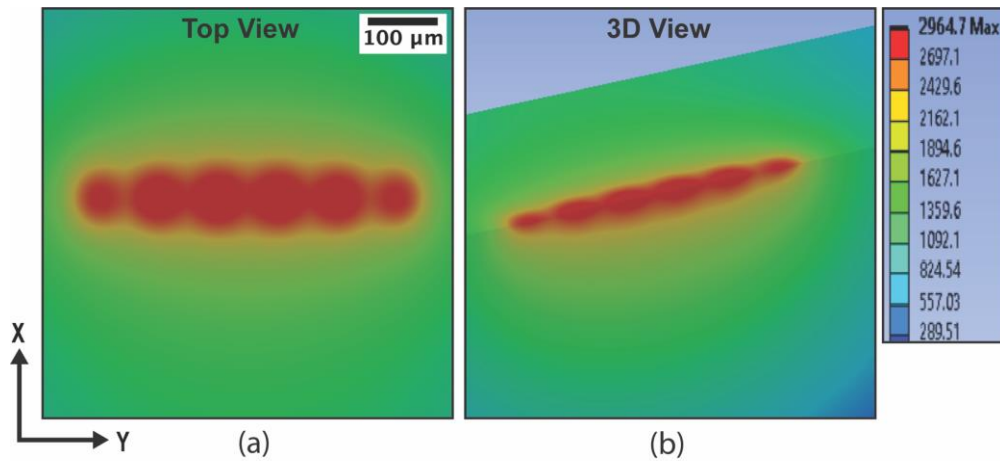


Figure 5.6: Temperature colour map produced by FEM simulation for a beam profile with six lasers width (a) and cross section (b).

### 5.3.1.3 Temperature from the Thermal Camera

The resulting images from the thermal camera is described in *Section 3.5*, with each pixel value representing a temperature in Kelvin. The average melt pool temperature (perpendicular to the beam traverse direction) and cooling rate of the melt pool are extracted from the thermal images. The melt pool temperature for a single laser beam was measured to be at 1946 K. This increased to 2258 K for the beam profile with six lasers.

The average temperature of the melt pool derived from the temperature colour maps of the mathematical models are compared with the thermal camera data in *Figure 5.7*. The melt pool temperature increases with the addition of each laser. The melt pool temperatures obtained using the FEM model were within 2% of those recorded using the thermal camera. The calculated temperature of the analytical method was within 6% of the thermal camera data. Though both methods were able to calculate the melt pool temperature to within 6% of the thermal camera, the lower accuracy of the analytical solution can be attributed to the omission of natural convective and radiative heat flows in the model. Also, the FEM model is a numerical-based simulation method making it more accurate than the analytical model. Furthermore, the Rosenthal approach considers the heat source as a stationary point source, not a moving Gaussian beam; hence the calculated heat intensity is identical across the beam diameter, resulting in the observed overestimation of the surface temperature. Promopattum *et al.* modelled the L-PBF process using a similar approach and demonstrated an overestimation of the surface temperature using the Rosenthal approach. The

improved fit with the FEM model was attributed to the accuracy of the numerical method and the inclusion of natural convection and radiation effects [71].

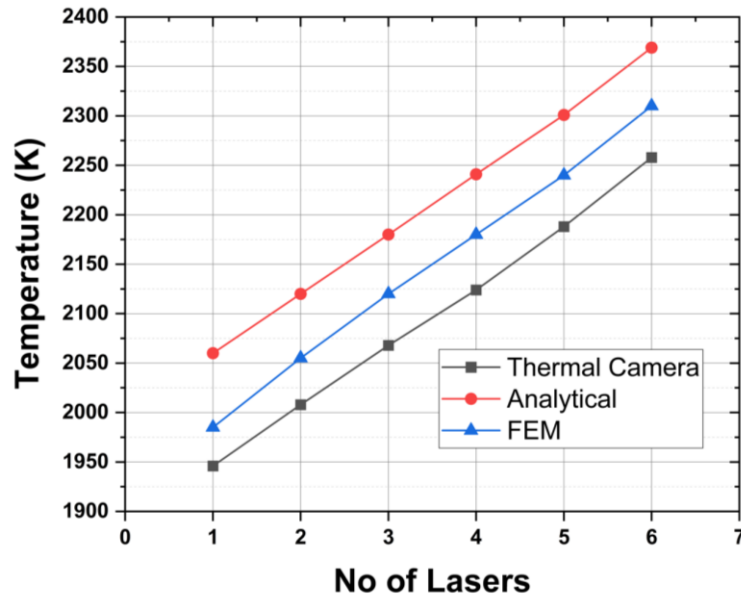


Figure 5.7: Compares average temperatures derived from the analytical and FEM solutions with the melt pool temperature from the thermal camera data for all six beam profiles.

### 5.3.2 Melt Pool Width

Alsaddah *et al.* demonstrated that in DAM, the morphology of the melt pool can be adeptly altered by modulating the laser power, adjusting the scanning speed, or through the utilisation of diode lasers with varied wavelengths to manipulate absorptivity [6], [38]. In their study, each beam profile yielded a singular melt pool trajectory. Figure 5.8 shows scanning electron micrographs of adjacent tracks, generated using two (a), three (b), four (c), five (d), and six (e) lasers. The addition of each laser amplifies the  $1/e^2$  width of the beam, effectively broadening the melt pool formed by each beam profile. A beam profile using a single laser yields a  $1/e^2$  beam width of  $65\ \mu\text{m}$  and results in a melt pool width of  $72\ \mu\text{m}$  (measured perpendicular to the laser traverse direction). In contrast, the beam profile with six lasers creates the widest melt pool, measuring  $480\ \mu\text{m}$  across. This is illustrated in Figure 5.9, which plots the  $1/e^2$  width of the laser array as a function of the number of lasers in the array, ranging from 1 to 6, and correlates it with the resulting melt pool width. As each beam is incorporated into the laser configuration, the melt pool width increases accordingly. On average, the breadth of the melt pools (measured perpendicular to the laser

traverse direction) from each beam profile is within 10% (Ranging from 8% to 11%) of the  $1/e^2$  width of the laser beam.

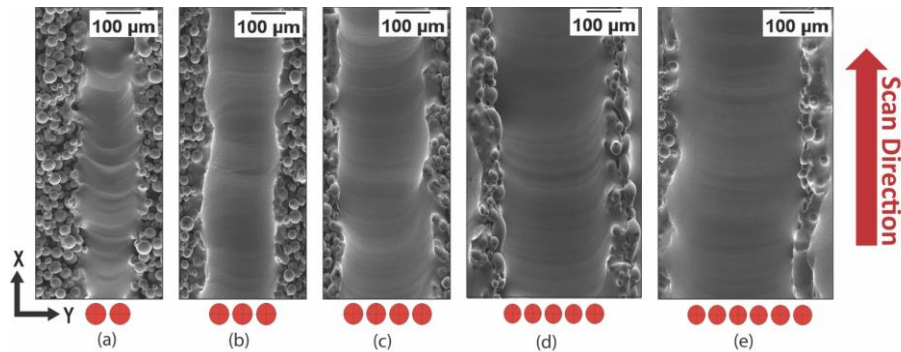


Figure 5.8: The SEM images depict the tracks produced using: (a) two lasers, (b) three lasers, (c) four lasers, (d) five lasers, and (e) six lasers.

The observed relationship between the melt pool width and the  $1/e^2$  width is important for enhancing predictability within DAM. This correlation facilitates a more accurate prediction of the melt pool width based on the number of lasers active at a particular moment. Furthermore, this relationship serves as a dependable reference for fine-tuning parameters, including laser power, traverse speed, and focus. Should the melt pool width diverge from anticipated measurements, it may indicate discrepancies in the laser system or inherent inconsistencies in the material. Additionally, researchers attempting to craft computational models of laser-material interactions find this correlation invaluable in ensuring that their simulations fit accurately with empirical observations. It is recommended to establish this relationship for each material early on during parameter optimisation in DAM.

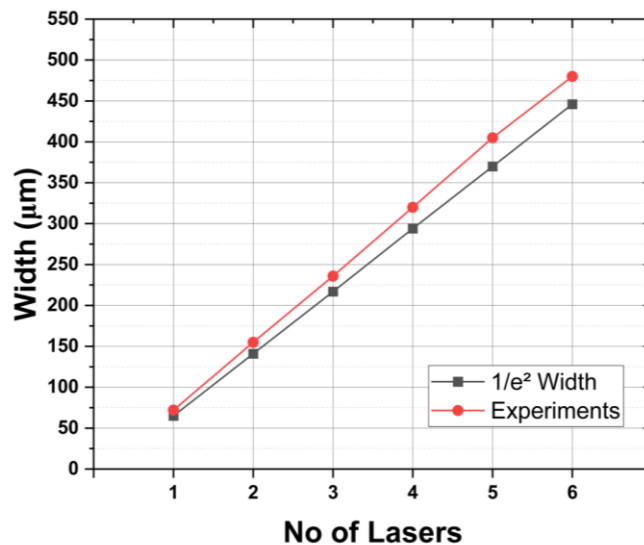
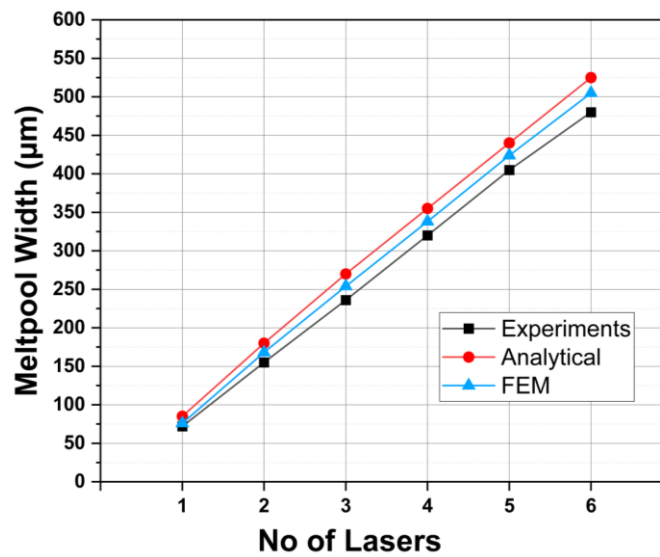


Figure 5.9: A comparison of the  $1/e^2$  beam width with the corresponding resultant melt pool width.

The melt pool widths determined experimentally are compared with those predicted by the analytical and FEM models in *Figure 5.10*, with both models following the same trend as the experimental data. The Rosenthal approach calculated the melt pool width to be higher than the experimental results but with calculation and experiment falling within an acceptable average variance of 13% (Ranging from 9% to 13%). In contrast, the melt pool width predicted using the FEM model is in closer agreement with the experimental data, consistently matching the measured widths to within 6% (Ranging from 5% to 8%) across all six beam profiles.



*Figure 5.10: Figure illustrating a comparison between the empirical melt pool widths and as predicted by both analytical methods and FEM across all six beam profiles.*

The FEM model demonstrates a higher degree of accuracy in comparison to the analytical model. This heightened accuracy can primarily be attributed to the FEM model's meticulous consideration of temperature-dependent thermo-physical properties. In addition, the employment of numerical calculations within the FEM framework allows for a more detailed representation of the phenomena under study. Contrastingly, the analytical model discussed in this context conducts a steady-state analysis, leveraging uniform thermo-physical material property values for its computations.

### 5.3.3 Melt Pool Depth

#### 5.3.3.1 Scanning Strategy

In the DAM system, X-Y translations of the laser head are facilitated through the deployment of a gantry mechanism. Typically, a parallel scanning

methodology is adopted. The determination of hatch spacing between adjacent tracks is conditional upon the quantity of lasers activated within the laser head. As depicted in *Figure 5.11*, the parallel scanning approach is explained in the context of a configuration comprising five lasers. The  $1/e^2$  beam width of this five-laser configuration is  $370\ \mu\text{m}$ . A hatch spacing of  $200\ \mu\text{m}$  result in an approximate overlap of 50% during the processing phase. A prior study indicated that a hatch spacing overlap ranging from 30% to 50% ensures consistent melting and affords the melted layer adequate density [6].

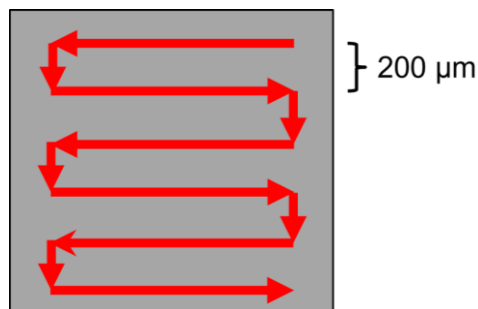


*Figure 5.11: Schematic of scanning strategy.*

In *Figure 5.12*, a cross-sectional representation perpendicular to the laser traverse direction (observed by SEM) of a melted track is presented, which has been produced utilising five lasers. The parameters under which this was achieved include a scanning speed of  $100\ \text{mm}/\text{min}$  and a hatch spacing of  $200\ \mu\text{m}$  produced a thickness of  $118\ \mu\text{m}$ . The consistency in the thickness of this single layer can be attributed to the 50% overlap of the hatch spacing.

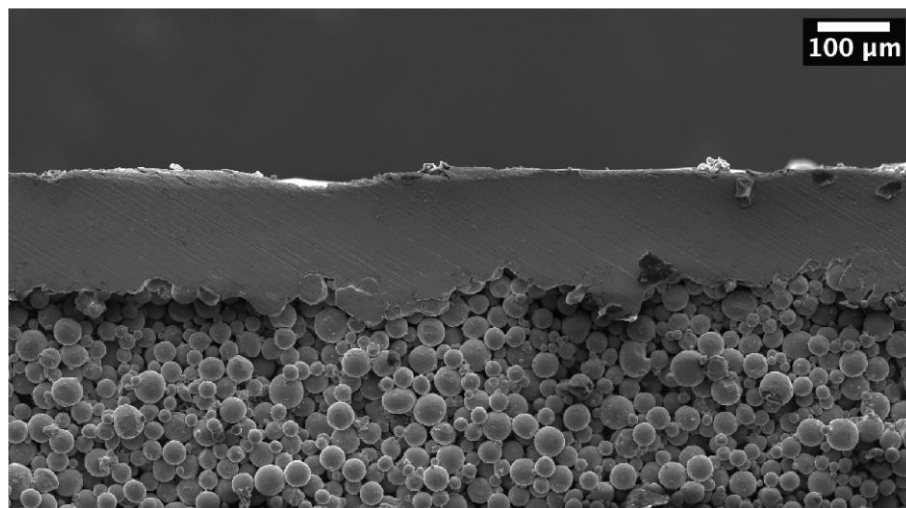


*Figure 5.12: A cross-section representation perpendicular to the laser traverse direction of a melted track produced with 5 lasers: Scanning speed  $100\ \text{mm}/\text{min}$  and  $200\ \mu\text{m}$  hatch spacing.*

In *Figure 5.13*, a comparative analysis between the experimentally measured melt pool width dimensions and their simulated counterparts is illustrated.

Figure 5.13 (a) shows a cross-sectional view across the track, demonstrating the melt pool depth within a single layer generated using six laser beams. Figure 5.13 (b) provides an illustration of the melt pool dimensions derived from the FEM model, utilising six laser beams. Within this study, the analytical model predicated upon the Rosenthal equation proves ineffectual in determining the melt pool depth information. Nevertheless, it enables a rapid approximation of the melt pool width, alongside the generation of a temperature colour map of the surface.

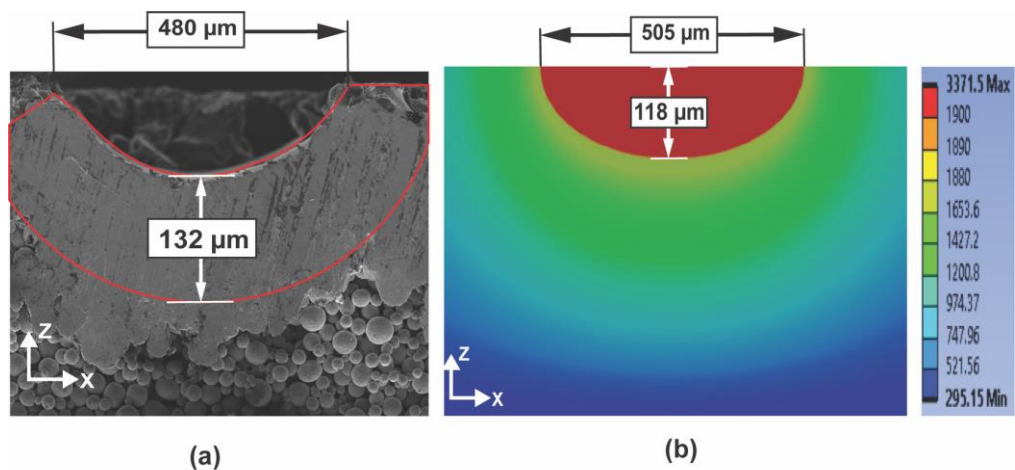


Figure 5.13: Cross section of a melt pool created by the beam profile with 6 lasers.

In DAM, melt pools commonly exhibit a crescent shape, as also reported by Caglar et al. in their study of a hybrid system that combines DAM with a fibre laser system [119]. This characteristic crescent shape is primarily due to Marangoni flow and recoil pressure. Marangoni flow, driven by surface tension differences resulting from temperature variations, pulls the molten material towards the hotter centre, as depicted in Figure 5.14. Additionally, the melt pool adjacent to the first laser experiences heat transfer towards the cooler powder bed and the substrate beneath, while the melt pool at the bottom of the fifth laser, surrounded by higher temperatures, mainly transfers heat towards the cooler substrate. Recoil pressure further influences the melt pool dynamics by pushing molten metal downwards, which can obstruct heat dissipation near the centre where the pressure is highest. These dynamics collectively concentrate heat at the centre and accentuate the curvature at the edges, reinforcing the crescent shape of the melt pool.

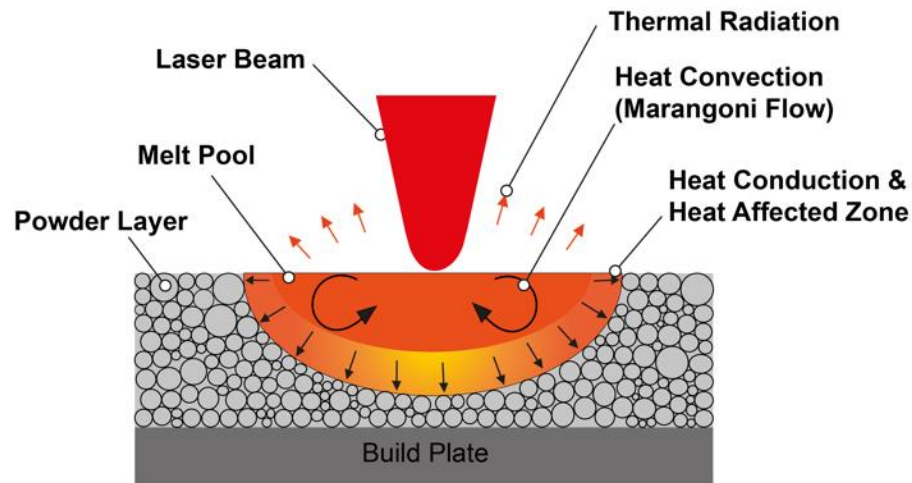


Figure 5.14: A schematic representation of a melt pool formed during L-PBF.

The FEM calculated melt pool depth information corresponding to each laser configuration is plotted in *Figure 5.15* together with the empirical melt pool depths across all six beam profiles. On average, the depths projected by the models were 14% (with a range from 11% to 19%) less than the empirical data obtained. In comparison, referencing *Chapter 4*, specifically *Sections 4.4.3.1 and 4.5.4.1*, both the FEM and VoF approaches considerably overestimated the melt pool depth whilst modelling Ti6Al4V using the L-PBF process. As discussed in *Chapter 4, Section 4.6*, the FEA model is predominantly a conduction-driven numerical model. When the energy density increased, the error in the model also increased, primarily due to the omission of Marangoni convection flow. This omission led to an increased temperature at the centre of the melt pool, thereby contributing to the overestimation of the melt pool depth in L-PBF simulations. However, in DAM, the multiple laser array is powered by low-power lasers (4W), and the total laser power of the beam profile is spread across a wider area, which mitigates the error that caused the overestimation in L-PBF simulations. The inclusion of Marangoni flow would improve the accuracy of melt pool depth prediction in the simulation. This enhancement is due to the more realistic modeling of fluid dynamics within the melt pool, capturing the effects of thermal gradients on the flow patterns.

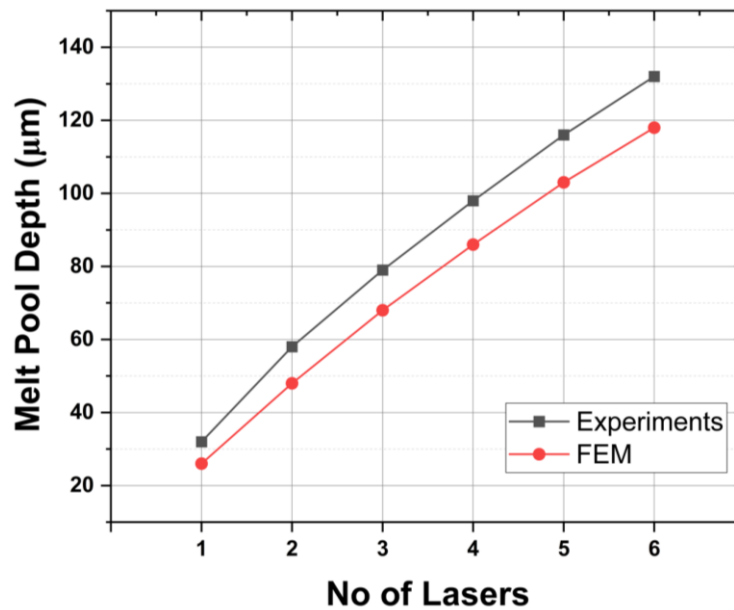


Figure 5.15: Figure illustrating a comparison between the empirical melt pool depths and as predicted by FEM across all six beam profiles.

### 5.3.4 Cooling Rate and Solidification Behaviour

#### 5.3.4.1 Solidification Dynamics and Cooling Rates in L-PBF Process

In DAM, microstructure and the grain morphology are controlled by varying the laser power or scanning velocity. Alsadah *et al.* demonstrated that above 100 mm/min scanning speed, DAM produced a fine  $\alpha + \beta$  Widmanstätten, whereas below 100 mm/min a coarser microstructure was produced consisting of  $\alpha + \beta$  Widmanstätten [6]. Furthermore, the effect of beam profile on coarseness of the grain size was more pronounced than the scanning speed. A laser profile with an interleaved second array (providing an effective pitch of 38 $\mu\text{m}$ ) maintained the temperature above the  $\beta$  transus for a more extended period than the single laser array (pitch of 72 $\mu\text{m}$ ), leading to a coarser microstructure. Furthermore, the second array increased the input power causing a further reduction in cooling rate in comparison to the single array. In general, as the number of lasers increased, the cooling rate decreased, causing the crystal to grow.

#### 5.3.4.2 Cooling Rates Determined Using Thermal Camera

##### Measurements

This study collected temperature data for each beam profile. Figure 5.16 plots the temporal temperature evolution captured using the thermal camera for single (a), two (b), four (c), and six (d) lasers. In the analysis of the Ti6Al4V alloy,



the cooling duration was determined as the time taken for the temperature to fall from the beta transus temperature, of 1267 K, to the martensitic transformation temperature at 847 K. It should be noted that the thermal camera experiences sensor saturation when recording temperatures below 916 K. This limitation arises from the sensor's inability to reliably capture temperatures beneath this threshold. Consequently, this results in a degree of noise in the acquired data. To account for this limitation and to ensure the integrity of the assessment, the data was extrapolated from 916 K down to the 847 K mark. This methodology was adopted to provide a robust and accurate representation of the cooling timeline.

Within the context of DAM, empirical observation using the thermal camera confirms that the beam profile with a single laser necessitates 0.54 seconds to complete a transition to the martensitic transformation commencing from the  $\beta$ -transus. As the number of lasers in the array is increased, the time taken for the temperature to fall to the solidification temperature also increased: exactly 1 second when utilising two lasers, 1.8 seconds for four lasers, and 2.2 seconds when activating all six lasers. The rate of cooling was ascertained based on the solidification duration. Notably, the application of a single laser yielded a cooling rate of 778 K/s. However, when six lasers were utilised, this rate decreased significantly to 191 K/s. This is consistent with previous work on DAM [5], [6], where the cooling rate decreases with the addition of lasers and is  $10^4$  orders of magnitude slower than conventional L-PBF. During processes like cylindrical casting and float-zone DS casting of Ti6Al4V, the cooling rate can range from 1 to 200 K/s [105], [120]. The cooling rate in DAM is therefore comparable to that of some of the casting processes.

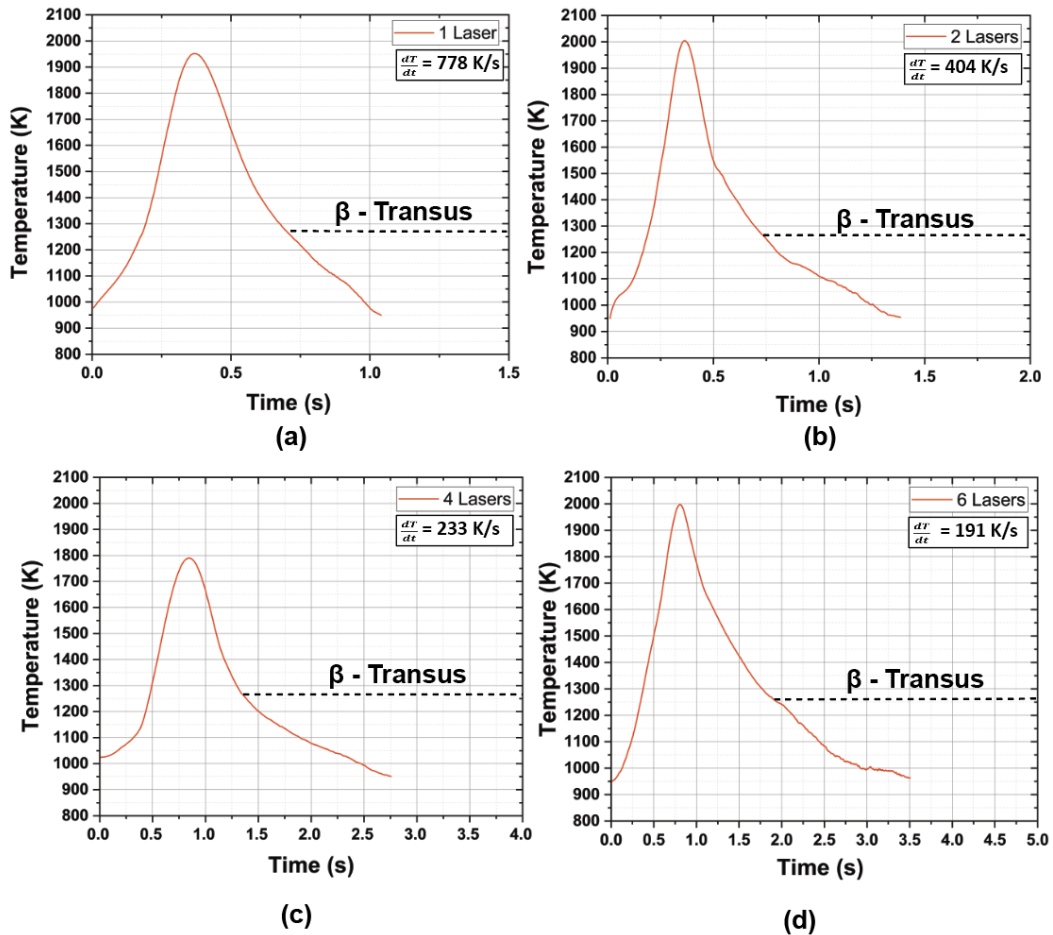


Figure 5.16: Measured transient temperature from the thermal camera for the beam profiles (a) single laser, (b) two lasers, (c) four lasers and (d) six lasers. Cooling rate determined from 1267 K to 847 K.

Cooling rate extracted from Figure 5.16 are plotted in Figure 5.17 as a function of the number of lasers in the array to highlight how the cooling rate observed in DAM decreases with the sequential activation of lasers, spanning from one to six. There is a pronounced reduction in the cooling rate from initially utilising a singular laser. However, the fractional decrease in cooling rate decreases as the number of lasers is increased, with minimal advantage gained beyond implementation of a beam profile comprising five lasers. Such a trend can be explained by considering that the cooling rate is computed in relation to a specific locus within the melt pool. Consequently, the integration of additional lasers beyond a certain count within the beam profile, which are distanced from this central reference, mitigates their influence on the subsequent cooling rates. It follows, therefore, that the incorporation of several more rows of lasers within the established beam profile might precipitate a further reduction in the cooling rates. Such a modulation is anticipated to influence the solidification rate, particularly in the direction orthogonal to the laser's traverse direction. This is

especially relevant where the additional rows of lasers are positioned. However, it should be cautiously noted that the advantages derived from the incorporation of additional rows might reach a saturation point upon achieving a specific number of rows.

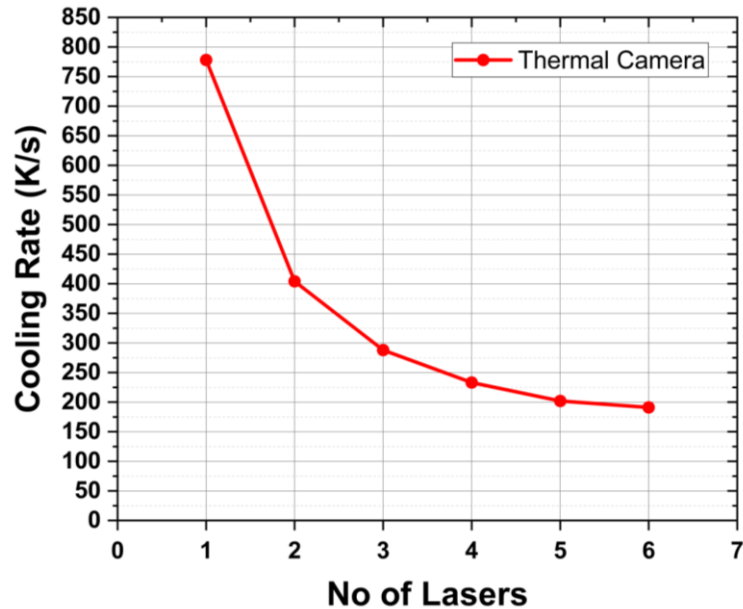


Figure 5.17: Depiction of an area plot illustrating the cooling rates achieved in DAM as each laser is activated, ranging from one to six.

#### 5.3.4.3 Cooling Rates as Predicted by Analytical Models

The cooling rate associated with each beam profile is calculated using the analytical models, described in *Chapter 4, Section 4.4*. The cooling rates calculated using this model are presented in *Figure 5.18* for beam profiles comprising two lasers (a) and six lasers (b).

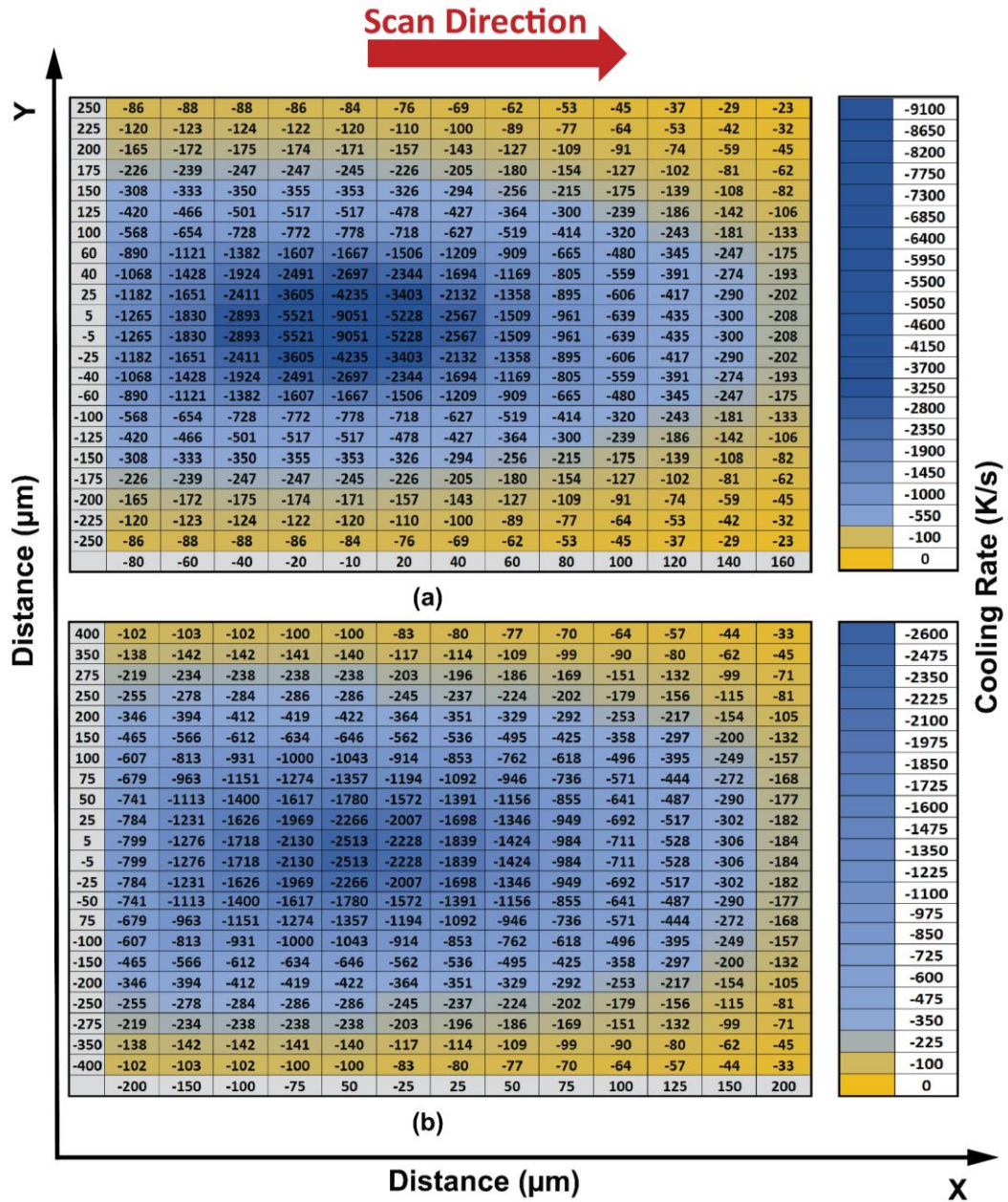


Figure 5.18: Depicts the anticipated cooling rates as extrapolated from the analytical model for the beam profiles employing two lasers (a) and six lasers (b).

The mean cooling rates stand at 4482 K/s and 592 K/s for the beam configurations with two and six lasers, respectively. Notably, the peak cooling rate is located at the melt pool's epicentre and diminishes progressively as one moves radially outwards from this point. The underlying rationale for this observation can be attributed to the characteristics inherent in the Rosenthal model. Within this framework, the heat source is conceptualised as a singular point source. Consequently, the thermal gradient is significantly higher at the epicentre compared to its periphery, indicating a more pronounced cooling rate in the central region. To counteract the implications of such pronounced central

cooling rates, one might consider adopting an approach that takes into account the average cooling rate values spread across the entirety of the melt pool.

#### **5.3.4.4 Cooling Rates as Predicted by FEM Models**

Temperature-time data were ascertained by selecting a specific point, referred to as the probe, situated atop the melt pool's surface. Utilising the data sourced from this probe, the cooling duration was gauged, spanning from the beta transus temperature (1267 K) to the martensitic transformation temperature (847 K). The requisite timeframe associated with the cooling transition from the  $\beta$ -transus to the onset of martensitic transformation is demonstrated in *Figure 5.19*, which plots the modelled transient temperature for a single laser (a) and six lasers (b). For the beam profile employing a single laser, the solidification duration stands at 0.05 seconds. Contrastingly, this timeframe increases to 0.2 seconds when the configuration is expanded to encompass six lasers.

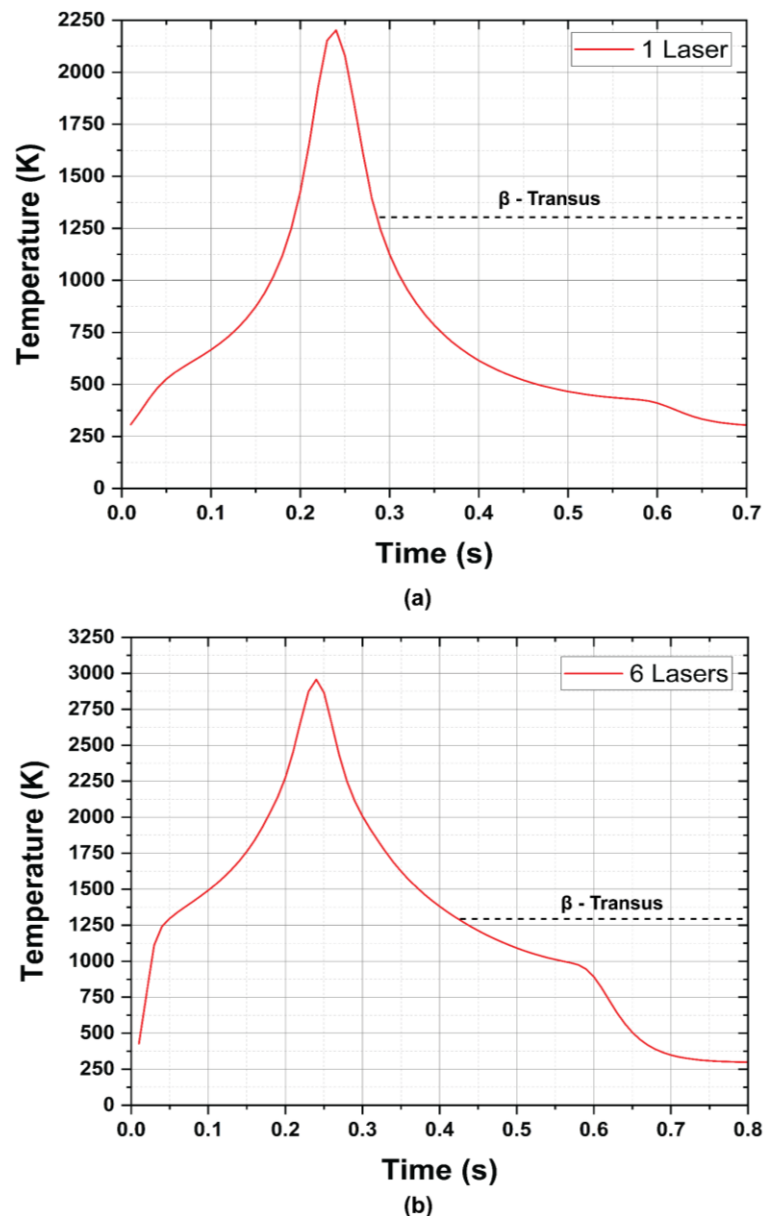


Figure 5.19: A graphical representation of the temperature-time data procured from the ANSYS simulation. (a) delineates the results for the beam profile utilising a single laser and (b) illustrates the data corresponding to a configuration with six lasers. Each curve provides insight into the temperature variations over a specified duration under the influence of the respective laser configurations.

#### 5.3.4.5 Comparative Analysis of Cooling Rates in DAM

The cooling rate extracted from thermal camera measurements is compared with those determined using both the Analytical and FEM models in *Figure 5.20*. A comparison between the cooling rates ascertained through both the FEM and the analytical approach with data captured by the thermal camera reveals a pronounced overestimation by both theoretical approaches. Specifically, the FEM model's estimate surpasses the cooling rate derived from the thermal camera by a factor of ten. In comparison, the analytical method's deviation is somewhat lower, being approximately fivefold. To illustrate, the FEM's prediction for the

cooling rate with a single laser is 8400 K/s, while the analytical approach forecasts a rate of 4482 K/s. However, in stark contrast, the thermal camera's measured cooling rate is considerably lower at 778 K/s.

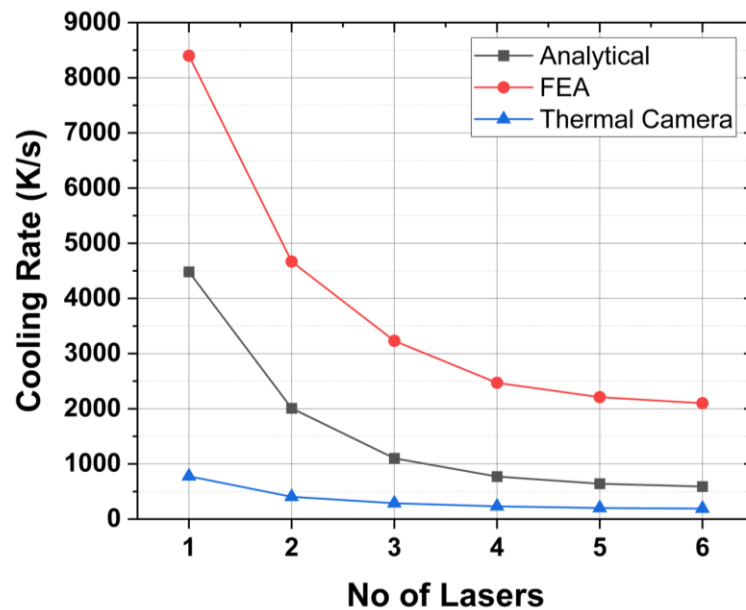


Figure 5.20: A comparison of the cooling rate predicted from the analytical and FE model for all six beam profiles with the cooling rate derived from the thermal camera data.

While both modelling methodologies indeed overestimate the cooling rate, it is noteworthy to mention that they exhibited similar trends in response to the activation of each individual laser. The data derived from the thermal camera, FEM, and analytical models all exhibit comparable variations (from one laser beam to the other) in cooling rates. Notably, this correlation becomes increasingly pronounced when five or more lasers are utilised. While the mathematical models may not precisely mirror the cooling rates as indicated by the thermal camera, the salient correlation underscores their utility in drawing meaningful conclusions. The overestimation factors manifest with reasonable consistency, suggesting the potential applicability of these models in future research, provided they are adjusted by an appropriate factorial variable.

The analytical model solves Rosenthal's heat equation and provides the temperature fields, melt pool width and cooling rates. It is computationally less expensive, and straightforward to use but ignores the dominant mechanism of heat transfer and is known to produce some errors. Furthermore, the analytical model provides an initial approximation to the DAM problem, which can be further improved with the help of other modelling techniques when necessary. The analytical modelling can be performed either through hand calculation or in

any software package that enables mathematical calculations. The FEM model solves the steady state or transient energy conservation equation with convective (gas flow) and radiative boundary conditions. The outputs are in the form of 3D transient temperature distributions and the shape of the melt pool can be derived from the 3D model. The FEM model based on numerical calculations provides greater consistency and accuracy than the analytical model. Many existing software packages can perform FEM numerical calculations. The FEM simulation is more complex to set up in comparison to the analytical modelling process.

Convective flow of the molten metal plays an important role in heat transfer during a L-PBF process. The convective flow mixes molten metal from the surrounding area helping to distribute the heat more evenly within the molten pool. The convective flow of molten fluid has been shown to reduce the thermal gradient within the melt pool [121]. Manvatkar *et al.* argued that by ignoring convection in the liquid pool in modelling, modelled cooling rates would be twice as fast as those observed experimentally [122]. The over estimation of the cooling rate is mainly due to the higher thermal gradient in the modelling due to the omission of convective flow calculations. As demonstrated in *Chapter 4*, the simulation of convective heat transfer is a difficult and computationally intensive task due to the complex physical processes involved in the L-PBF process. In general, both analytical and FEM models provide a simplified solution for calculating the melt pool surface temperature, melt pool width and the cooling rate for the DAM process and can be used for quick estimations to support process optimisations. This study is the first attempt carried out to model the DAM process involving multiple individually addressable diode laser beams.

## 5.4 Conclusions

DAM uses an array of low-powered (< 5W each) diode lasers for melting larger areas with slower scanning velocities (1 - 20 mm/s) compared to L-PBF, which uses single or multiple fibre lasers with high power (> 200W) and speed (~ 1000 mm/s) for melting metallic powdered feedstocks. Furthermore, DAM intrinsically produces lower temperatures and reduced thermal gradients due to the slow processing speed combined with low power laser sources. It produces very low cooling rates, which should consequently incorporate lower residual



stress within the produced parts. In general, L-PBF process stability and outcome are driven by the temperature field in the melt pool. As such, it is vital that we understand the behaviour of the melt pool and its temperature evolution.

The influence of laser number on melt pool size and cooling rate during DAM has been analysed for a linear array of diode lasers. FEM and analytical methods were extended to apply to our scheme with up to 6 lasers simultaneously irradiating a Ti6Al4V powder bed. Simulated results were compared with those measured using a thermal camera. Both models could predict the temperature distribution and cooling rate in the surface of the single layer melt pool of Ti6Al4V, however the FEM approach predicted the melt pool width and temperature more accurately than the analytical method. For any number of lasers in the array, the cooling rate for Ti6Al4V from the  $\beta$ -transus to the martensitic transformation temperature was observed to be substantially lower than for reported L-PBF and EB-PBF processes. The beam profile with the single laser produced a cooling rate of 778 K/s whereas the cooling rate reduced to 191 K/s for the one with six lasers. The cooling rate achieved in DAM is  $10^4$  orders of magnitude slower than conventional L-PBF and comparable to that of some casting processes, offering a clear advantage over more established L-PBF processes.

## 6 Chapter 6: Residual Stress in DAM of Ti6Al4V

### 6.1 Introduction

In the DAM process, a notable decrease in the cooling rate is evident with the utilisation of each consecutive laser beam within the specified array. *Chapter 5* describes investigations that affirm a proportional relationship wherein an increase in the number of active lasers in the array is directly related to a reduction in the cooling rate, a trend that stabilises upon the activation of up to five laser beams in a single row. The incorporation of an extra row of lasers incites a further reduction in the cooling rate of Ti6Al4V [6]. However, it remains critical to recognise the significant role that scanning speed/velocity plays in influencing the cooling rate in the DAM process. This chapter examines the effect that varying scanning velocity has on residual stress and microstructural formation when employing either 3, 4 or 5 lasers. The FEM model detailed in *Chapter 5* enables simulation of the dynamics of the thermal process and successive cooling rates.

#### 6.1.1 DAM Characteristics

In the previous study reported in ref [6], the processing of Ti6Al4V through DAM resulted in the generation of a  $\beta$  phase, a phenomenon that was consistently observed across all experimental samples. However, it is important to note that this phenomenon has not yet been thoroughly examined or studied in depth. The  $\beta$  phase presence in the samples is influenced by the inherent slow cooling rate of DAM, which is substantially slower than cooling rates in L-PBF. The cooling rate in DAM is influenced by the number of lasers incorporated within the beam profile, and the scanning speed of the laser array. This, sequentially, may induce alterations in the microstructure of the material. Moreover, the slow cooling rate may exhibit favourable characteristics in DAM, potentially reducing the formation of residual stress within the samples. The formation of residual stress within samples fabricated utilising DAM has not been studied previously; therefore, quantifying such stress formation is an important next step in understanding the advantages of the DAM process.

### 6.1.2 Scope of This Work

As previously noted, there is a need for a comprehensive quantification of residual stress and the extent of  $\beta$  phase presence in these specific instances. Within this chapter, attention will be focused on analysis of the lattice spacing of the  $\beta$  phase using X-ray diffraction (XRD). Also, a detailed discussion on the  $\beta$  phase emanating from each distinct processing environment will be presented using the results from Electron Backscatter Diffraction (EBSD) measurements. Subsequently, analysis of residual stress will be undertaken, leveraging the XRD technique. In *Chapter 2, Section 3*, a detailed literature review was conducted on residual stress accumulation in materials during the L-PBF process. During L-PBF, a reduction in the scan speed has been shown to lower the temperature gradients and cooling rates, leading to a decrease in residual stresses and reduced deformation [123][124]. The DAM process inherently operates with a notably slower laser speed when compared to the L-PBF process. Consequently, it is expected that the formation of residual stress in parts produced by DAM would be lower than that observed in their L-PBF processed counterparts. This anticipated difference will be subject to evaluation and discussion.

### 6.2 Residual Stress in L-PBF of Ti6Al4V

Most often, L-PBF induces tensile residual stress within the parts produced, the magnitude of which differs in different directions. Refs [90], [125] observed that in a single layer the residual stress is greater in the laser traverse direction (denoted as X direction) than in the direction perpendicular to the laser propagation (denoted as Y direction) during layer formation. In L-PBF, directional stress is markedly influenced by the scanning strategies employed; nevertheless, the highest levels of residual stress have been observed in the X-direction during line scanning [126]. Employing an alternative strategy of 90° rotational line scanning has been noted to encourage a reduction in residual stress in comparison to unidirectional line scanning. Presently, the DAM process utilises unidirectional line scanning with its multibeam technology, wherein both the beam width and hatch spacing can be controlled through the optical system design (e.g fibre pitch and lens magnification). The scanning strategy employed in this work is depicted in *Figure 6.1*. The laser traverse direction is designated

as the X-axis, the direction perpendicular to the laser traverse direction is the Y-axis and the build direction is the Z axis. Once baseline values for residual stress are determined using unidirectional scanning in DAM, there is potential for further reducing residual stress. This can be achieved by implementing a 90° rotational line scanning strategy, a method that has shown effectiveness in reducing residual stress in L-PBF[126].

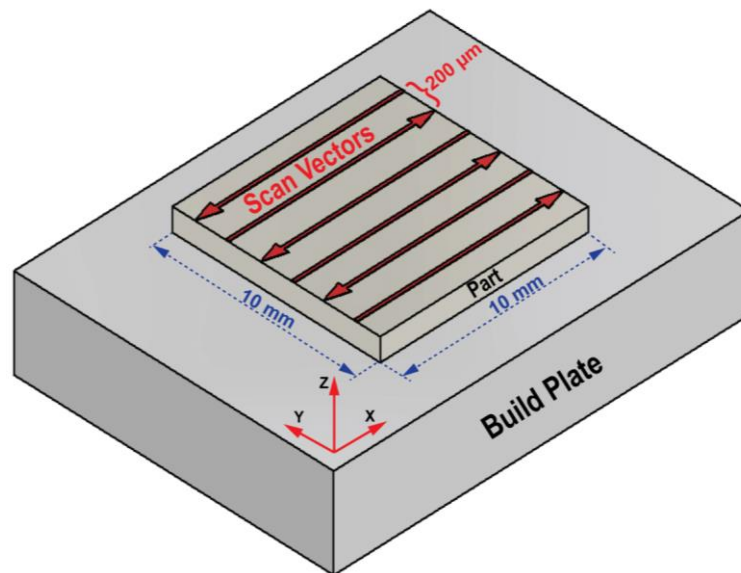


Figure 6.1: Scanning strategy and sample dimensions.

It has been documented that increasing the layer thickness may result in a reduction in residual stress, this being attributable to a corresponding decrease in the cooling rate [127]. Nonetheless, the reduction in residual stress attributable to an increase in layer thickness is perceived to provide limited practicality, especially given the confines imposed on the maximum thickness of a layer within the framework of L-PBF. This restriction originates from the intrinsic attributes of the L-PBF process, including the need to maintain effective laser-material interaction and powder bed stability. Therefore, such a constraint limits the viability of increasing layer thickness as a robust strategy for attainment of a significantly lower residual stress, thereby necessitating the exploration of alternative methodologies for the mitigation of stress.

Furthermore, it is often observed that the top layers formed during L-PBF exhibit higher residual stresses compared to the bottom layers [128]. This discrepancy can be attributed to a range of contributing factors, including differing thermal gradients—where the top layers cool rapidly due to their exposure to the shielding gas, the presence of support structures anchoring the

lower layers that induce compressive stresses, distinct thermal histories for individual layers, and the gradual accumulation of material during the build process. The actual distribution of residual stress, however, hinges on multiple variables, encompassing scanning strategies, layer thickness, and the specific process parameters employed. Consequently, while higher residual stresses in top layers are common, the precise distribution within an L-PBF-produced part is reliant on the combination of a number of influencing factors, the specific conditions of the L-PBF process and the materials utilised.

The existing DAM configuration is limited in its capability to fabricate intricate three-dimensional objects, owing to current restrictions in the control system, which is still undergoing development. Accordingly, this study is principally concentrated on analysing single layer components leaving the exploration of multi-layer complex geometries for subsequent research. The inference drawn from this limitation is that the residual stress generated in the present top layer is anticipated to be slightly higher than that in subsequent layers of a multi-layered part. Nevertheless, acquiring an understanding of the residual stress incorporated within the DAM process, stemming from the interaction of multiple laser beams at varying scanning speeds, is considered to present an important next step in gaining a comprehensive understanding of the full process capabilities of this method. Comparison of residual stress between L-PBF and DAM in this work will specifically concentrate on the uppermost layer, ensuring a like-for-like comparison.

The development of residual stress in L-PBF is a well-researched area, and the values of residual stress for Ti6Al4V on the top surface (without any substrate heating arrangements) and in the laser traverse direction ( $\sigma_{xx}$ ) are presented in Table 6.1. This also sheds light on the methods and process parameters employed for measuring residual stress within the samples produced by the L-PBF process. Table 6.2 offers additional insights into the alleviation of residual stresses in the L-PBF process for Ti6Al4V, highlighting the use of powder bed pre-heating as an effective mitigation strategy. The table presents data on the average residual stress in the build direction ( $\sigma_{zz}$ ) and demonstrates its reduction as the pre-heat temperature increases. In general, the average stress along the build direction is expected to be lower than that reported for the laser traverse direction in the top layer. Additionally, the

residual stress observed at a powder bed pre-heat temperature of 100°C is documented as 214 MPa.

<i>Features</i>	<i>Residual Stress (<math>\sigma_{xx}</math>), MPa</i>	<i>Refs</i>
<ul style="list-style-type: none"> <li>• <i>Laser power: 150 W</i></li> <li>• <i>Scanning Speed: 1200 mm/s</i></li> <li>• <i>Layer thickness: 30 <math>\mu\text{m}</math></i></li> </ul>	510	[129]
<ul style="list-style-type: none"> <li>• <i>Laser power: 200 W</i></li> <li>• <i>Scanning Speed: 200 mm/s</i></li> <li>• <i>Layer thickness: 50 <math>\mu\text{m}</math></i></li> </ul>	425	[130]
<ul style="list-style-type: none"> <li>• <i>Laser power: 200 W</i></li> <li>• <i>Scanning Speed: 800 mm/s</i></li> <li>• <i>Layer thickness: 50 <math>\mu\text{m}</math></i></li> </ul>	450 - 650	[131]

*Table 6.1: This table presents the published residual stress values of Ti6Al4V measured using XRD method during the L-PBF process, with a specific focus on the residual stress levels in the top layer, considering variations along the laser traverse directions. All the work mentioned here are carried out without substrate pre-heating.*

<i>Experimental Methodology</i>	<i>Features</i>	<i>Minimum Residual Stress (<math>\sigma</math>), MPa</i>	<b>Refs</b>
<i>Hole Drilling Method</i>	<ul style="list-style-type: none"> <li>• <i>Laser power: 200 W</i></li> <li>• <i>Scanning Speed: 500 mm/s</i></li> <li>• <i>Layer thickness: 50 <math>\mu\text{m}</math></i></li> <li>• <i>Pre-heat temperature: 100° C</i></li> </ul>	214	[132]
	<ul style="list-style-type: none"> <li>• <i>Pre-heat temperature: 370° C</i></li> </ul>	61	
	<ul style="list-style-type: none"> <li>• <i>Pre-heat temperature: 470° C</i></li> </ul>	25	
	<ul style="list-style-type: none"> <li>• <i>Pre-heat temperature: 570° C</i></li> </ul>	1	

*Table 6.2: The average residual stress measurements for Ti6Al4V during L-PBF with the aid of powder bed pre-heating configurations.*

## 6.3 Experimental Methodology

### 6.3.1 DAM Samples

The alloy powder of Ti6Al4V, that is used for the fabrication of the samples, was procured from Carpenter Additive, UK, with the specification as described in 3.6.1. To prevent oxidation during processing, the DAM machine's build chamber was purged with argon gas. The laser head was operated with activated beam

profiles incorporating three, four, and five beams, traversing over the powder bed along the X-Y axes at scanning velocities varying from 50 mm/min to a peak of 250 mm/min. A consistent hatch spacing of 200  $\mu\text{m}$  was maintained for all beam profiles, facilitating the production of samples of 10 x 10 mm in size. The build plate position and scanning strategy are as shown in *Figure 6.1*. Furthermore, This investigation was expressly focused on the fabrication and examination of a single layer rather than building a complex 3D geometry.

### 6.3.1.1 Process Parameters

Ref [6] suggested that the optimal scanning speed for Ti6Al4V during DAM is 100 mm/min. However, scanning speeds ranging from 50 to 250 mm/min yielded samples with reasonable density; therefore, this range was chosen for the scanning speed in this study. The findings in *Chapter 5* indicate that beyond the usage of five lasers in a single row, no further reduction in the cooling rate is observed from the  $\beta$  - transus temperature to the martensitic transformation temperature for Ti6Al4V. Consequently, beam profile configurations incorporating three, four, and five lasers have been selected for this study. The combination of process parameters used here is illustrated in Table 6.3, which outlines the number of lasers, the total laser power per beam profile, and the traverse speed. The combination of these process parameters is anticipated to yield the necessary output for determining the optimal process windows for Ti6Al4V, enabling the study of residual stress formation within this range. The sample BP10 incurred damage during processing, and subsequent attempts to create another BP10 were postponed due to a machine breakdown.

Number of Lasers 5 4 3	BP1	BP2	BP3	BP4	BP5	Total Laser Power (W) 20 16 12
	BP6	BP7	BP8	BP9	<del>BP10</del>	
	BP11	BP12	BP13	BP14	BP15	
	250	200	150	100	50	
	Scanning Speed (mm/min)					

Table 6.3: The study illustrates the combination of parameters utilised, showcasing the number of lasers, total laser power, and the scanning speed.

### 6.3.2 Thermal Model

*Chapter 5* detailed the development and validation of a numerical model using FEM for configuring multiple lasers in the DAM process. Simulations were initially performed for laser configurations ranging from 1 to 6, with a consistent scanning speed of 100 mm/min. This model was subsequently extended in this chapter to include multiple simulations at scanning speeds varying from 50 to 250 mm/min, specifically for laser configurations of 3, 4, and 5. The choice to utilise the FEM model for calculating cooling rates was driven primarily by the unavailability of high-resolution cameras and support technicians. The camera generated 30 GB of data for each 30-second interval of process capture, which also demanded considerable computational time to cover all the laser configurations required for this study. FEM models provide a convenient solution that requires significantly less time to simulate the necessary data, hence their use in this study. The rate of change of the cooling rate for each laser configuration and scanning speed can be conveniently obtained from FEM simulations. This data can be correlated with the residual stress to establish the relationship between changes in the cooling rate and the induced residual stress during the DAM process

#### 6.3.2.1 Cooling Rates

The temperature-time data required for the cooling rate calculation was obtained by selecting a specific point (probe) at the top surface of the melt pool in the thermal model created in ANSYS. The temperature-time data for this particular location was extracted. The cooling duration was calculated using data acquired from the probe, spanning from the beta transus temperature (1267 K) to the martensitic transformation temperature (847 K).

### 6.3.3 Peak Analysis Using XRD

The distinctive diffraction pattern observed in X-ray diffraction (XRD) is generated when incident X-rays interact with the well-ordered three-dimensional atomic arrangement within a crystal. This interaction results in an interference effect that enhances the X-ray beam at specific directions, thereby yielding the characteristic diffraction peaks. The occurrence of the diffraction peak is dependent upon the inter-atomic spacing, a relationship explained by



Bragg's law, as illustrated in Figure 6.2. The determination of lattice spacing can subsequently be carried out using equation 27 [20].

$$n\lambda = 2d \sin\theta \quad (27)$$

Where  $n$  is an integer denoting the order of diffraction,  $\lambda$  is the X-ray wavelength,  $d$  is the lattice spacing of crystal planes, and  $\theta$  is the diffraction angle.

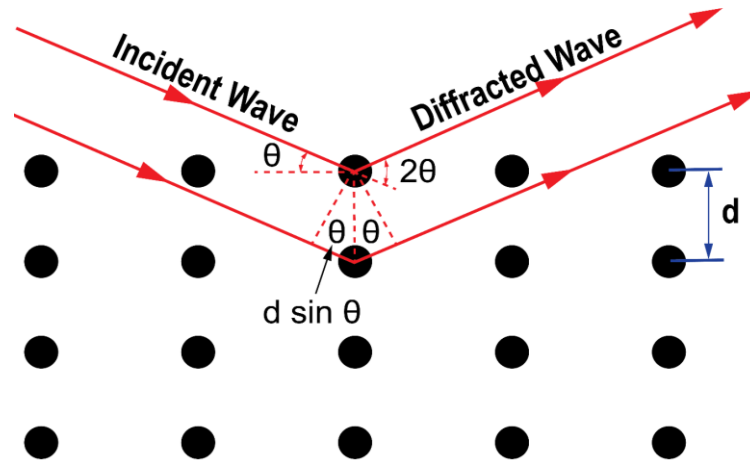


Figure 6.2: Depicting the D-spacing and the Interplay of X-ray Beams with Atom.

#### 6.3.4 Residual Stress Through XRD

Diffraction techniques for ascertaining residual stress evaluate the angles at which peak diffracted intensity occurs upon irradiating a crystalline specimen with X-rays. From these angles, the spacings of the diffracting lattice planes are subsequently derived using Bragg's Law, as described in *equation 27*. Should the material be subject to residual stress, these lattice spacings will diverge from those of the unstressed planes, with the discrepancy being proportional to the stress exerted upon said planes. Employing elastic theory allows for the calculation of the residual stress,  $\sigma_{\theta\psi}$  acting on these lattice planes. The details of which are discussed in *Chapter 2, Section 2.7.4*.

The positioning of the fabricated Ti6Al4V component created for this study is depicted in Figure 6.3. The illustration also details the different parameters used in the XRD based residual stress measurement process. The potential residual stresses, denoted as  $\sigma_{XX}$  and  $\sigma_{YY}$ , occur within the samples;  $\sigma_{XX}$  aligns parallel to the laser traverse direction, while  $\sigma_{YY}$  is perpendicular to it, both situated on the surface plane of the specimens. This investigation is restricted to analysis of the stresses present on the surface of the components, thereby

excluding the stresses manifested in the build direction,  $\sigma_{ZZ}$ . The strain,  $\epsilon_{\phi\psi}$  in the direction defined by the angles  $\phi$  and  $\psi$  is:

$$\epsilon_{\phi\psi} = \left[ \frac{1+\nu}{E} (\sigma_{XX} \delta_1^2 + \sigma_{YY} \delta_2^2) \right] - \left[ \frac{\nu}{E} (\sigma_{XX} + \sigma_{YY}) \right] \quad (28)$$

Where E is the modulus of elasticity,  $\nu$  is the Poisson's ratio, and  $\delta_1$  and  $\delta_2$  are the angle cosines of the strain vector:

$$\delta_1 = \cos\phi \sin\psi \quad (29)$$

$$\delta_2 = \sin\phi \sin\psi \quad (30)$$

Substituting for the angle of cosines in *equation 29 & 30* transform *equation 28* as below:

$$\epsilon_{\phi\psi} = \left[ \frac{1+\nu}{E} (\sigma_{XX} \cos^2\phi + \sigma_{YY} \sin^2\phi) \sin^2\psi \right] - \left[ \frac{\nu}{E} (\sigma_{XX} + \sigma_{YY}) \right] \quad (31)$$

Assuming the angle  $\psi$  to be  $90^\circ$ , the strain vector lies in the plane of the surface and the surface stress component,  $\sigma_\phi$ :

$$\sigma_\phi = (\sigma_{XX} \cos^2\phi) + \sigma_{YY} \sin^2\phi \quad (32)$$

Substituting *equation 32* into *equation 31*:

$$\epsilon_{\phi\psi} = \left[ \frac{1+\nu}{E} \sigma_\phi \sin\psi \right] - \left[ \frac{\nu}{E} (\sigma_{XX} + \sigma_{YY}) \right] \quad (33)$$

*Equation 33* establishes the relationship between the surface stress, denoted as  $\sigma_\phi$ , and the strain represented as  $\epsilon$ , in any direction stipulated by the angle  $\psi$ . This is correlated to the strain occurring in the directions defined by  $\phi$  and  $\psi$  as well as the principal stresses present on the surface. The strain is determined through variations in the crystal lattice's linear dimensions, with  $d_{\phi\psi}$  representing the distance separating the lattice planes as determined by the directions  $\phi$  and  $\psi$ :

$$\epsilon_{\phi\psi} = \frac{\Delta d}{d_0} = \frac{d_{\phi\psi} - d_0}{d_0} \quad (34)$$

Where  $d_0$  is the stress-free lattice spacing. The elastic constants are not the bulk values but are the values for the crystallographic direction normal to the lattice planes in which the strain is measured as specified by the Miller indices  $(hkl)$ . Substituting *equation 34* in *equation 33* gives:

$$d_{\phi\psi} = \left[ \left[ \frac{1+\nu}{E} \right]_{(hkl)} \sigma_\phi d_0 \sin\psi \right] - \left[ \left[ \frac{\nu}{E} \right]_{(hkl)} d_0 (\sigma_{XX} + \sigma_{YY}) + d_0 \right] \quad (35)$$

Equation 35 is the fundamental relationship between lattice spacing and the biaxial stresses in the surface of the sample [20].

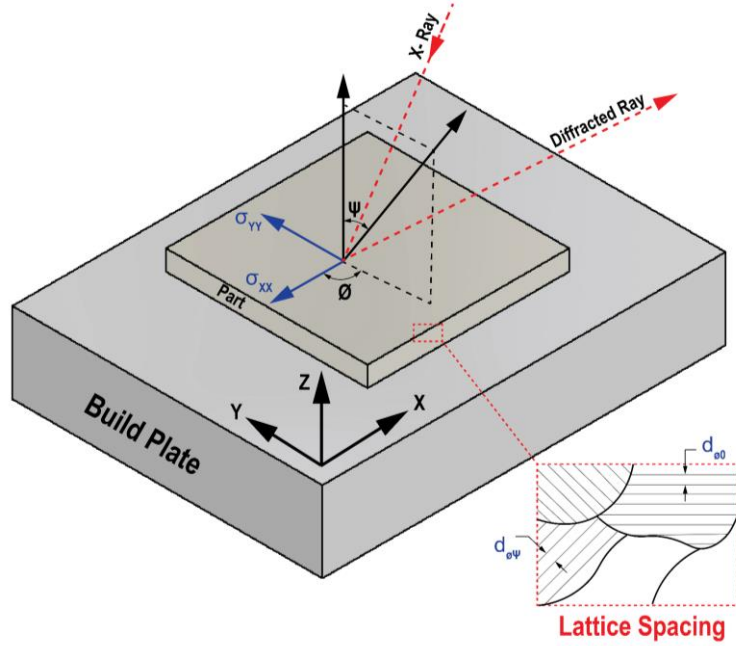


Figure 6.3: Definition of parameters used in X-ray stress measurement using  $\sin^2 \psi$  method.

#### 6.3.4.1 The $\sin^2 \psi$ method

The  $\sin^2 \psi$  method is a commonly employed technique in X-ray Diffraction (XRD) for the evaluation of residual stress in crystalline materials [93]. This method is based on the principle that the interplanar spacing of a crystal lattice changes under stress, and this change is reflected in the angle at which X-rays are diffracted according to Bragg's law. In the  $\sin^2 \psi$  methodology, the specimen is aligned at various tilt angles, denoted as  $\psi$ , relative to the incident X-ray beam, with the ensuing diffraction angles then measured. For each angle  $\psi$ , the lattice spacing, or  $d_{\psi}$ , is calculated. It is shown in *equation 35* that  $d_{\psi}$  exhibits a linear relationship with  $\sin^2 \psi$ . Within this analytical framework, lattice strain is deduced through a least squares regression analysis, applying the  $d_{\psi}$  and  $\sin^2 \psi$  values calculated from the experimental data [91]. The stress  $\sigma_{\theta}$  is calculated using the slope of the best-fit line and the elastic constant (Young's modulus,  $E$  and Poisson's ratio ( $\nu$ ) of the material [20]. When the intercept of the  $d_{\psi}$  vs  $\sin^2 \psi$  plot is zero:

$$d_{\psi 0} = d_0 - \left[ \left[ \frac{\nu}{E} \right]_{(hkl)} d_0 (\sigma_{XX} + \sigma_{YY}) \right] \quad (36)$$

$$d_{\phi 0} = \left[ 1 - \left[ \frac{\nu}{E} \right]_{(hkl)} (\sigma_{XX} + \sigma_{YY}) \right] \quad (37)$$

This is equal to the unstressed lattice spacing, denoted as  $d_0$ , reduced by the contraction induced by the Poisson's ratio, which is influenced by the aggregate of the principal stresses. The slope of the plot is:

$$\frac{\partial d_{\phi\psi}}{\partial \sin^2\psi} = \left[ \left( \frac{1+\nu}{E} \right)_{(hkl)} \sigma_{\phi} d_0 \right] \quad (38)$$

$$\sigma_{\phi} = \left( \frac{E}{1+\nu} \right)_{(hkl)} \frac{1}{d_0} \left( \frac{\partial d_{\phi\psi}}{\partial \sin^2\psi} \right) \quad (39)$$

The unstressed lattice spacing,  $d_0$  is generally unknown. However, because  $E \gg (\sigma_{XX} + \sigma_{YY})$  the value of  $d_{\phi 0}$  from *equation 37* differs from  $d_0$  by not more than  $\pm 1$ , and  $\sigma_{\phi}$  may be approximated to this accuracy using:

$$\sigma_{\phi} = \left( \frac{E}{1+\nu} \right)_{(hkl)} \frac{1}{d_{\phi 0}} \left( \frac{\partial d_{\phi\psi}}{\partial \sin^2\psi} \right) \quad (40)$$

Where, the lattice spacing,  $d_{\phi\psi}$  is a linear function of  $\sin^2\psi$ . Consequently, stress can be ascertained by measuring lattice spacings at various  $\psi$  angles. A linear relationship between lattice spacing and  $\sin^2\psi$  is established through the application of least squares regression.

This method allows for the accurate determination of uniaxial or biaxial residual stresses, and it is particularly useful for thin films and surface layers where stresses often develop during manufacturing or operational processes [22], [93], [133], [134], [135], [136]. It should be noted that the  $\sin^2\psi$  method assumes that the stress state is biaxial and the material is isotropic and linearly elastic. Deviations from these assumptions may require corrections or alternative methods for accurate stress analysis.

The  $\sin^2\psi$  method with single angular coordinate is applied in all work undertaken in this research. In this approach, the sample remains fixed in one orientation, and only the tilt angle ( $\psi$ ) is varied to obtain different measurements of lattice spacing. The limitation here is that this approach only captures the residual stress component along a specific direction. Therefore, to fully characterise the state of biaxial stress, the sample would have to be reorientated manually and the experiment repeated along different axes. PANalytical's X'Pert3 Powder X-ray diffraction system was used for the experiments.

After collecting the raw intensity data at each  $\psi$  angle, the accurate determination of peak positions is performed using Origin Pro software. Prior to determining the diffraction peak positions, the raw intensity measurements need to undergo correction for factors such as Lorentz polarization, absorption, and background noise. This correction process is carried out using XRD analysis software, specifically HighScore Plus from Malvern PANalytical. After establishing the precise peak position, the lattice spacing ( $d$ ) is calculated using *equation 27*. Subsequently, a plot of lattice spacing against  $\text{Sin}^2\psi$  is generated, and the slope is determined through linear regression analysis, which is created using Origin Pro software as shown in Figure 6.4.

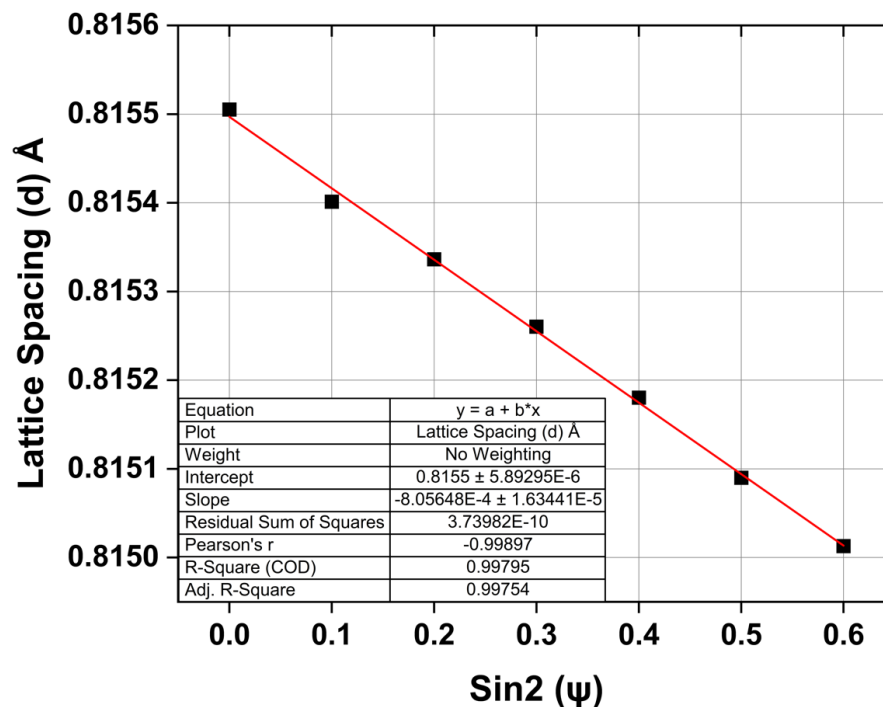


Figure 6.4: Illustrating a representative linear regression plot of  $\text{Sin}^2\psi$  against  $d$  for the  $\text{Sin}^2\psi$  residual stress methodology. This graph was generated using Origin Pro software.

The slope represents the lattice strain induced by the residual stress in the material resulting from the DAM process. By applying the obtained slope value and the lattice spacing distance in *equation 40*, the residual stress in the  $\sigma_{xx}$  direction can be determined. This process can be repeated to obtain values for the  $\sigma_{yy}$  direction.

## 6.4 Results

### 6.4.1 Single Line Scanning

The investigation into melt pool morphology and determination of the optimal process parameters for a single track of Ti6Al4V within the DAM process are addressed in *Chapter 5*. In this investigation, a constant hatch spacing of 200  $\mu\text{m}$  overlap was employed to generate multiple single lines, successively forming a layer with dimensions of 10  $\times$  10 mm using three, four, and five laser beams at scanning speeds of 50, 100, 150, 200, and 250 mm/min. Figure 6.5 shows plan view SEM images of the samples fabricated with five laser beams at different scanning speeds: (a) 250 mm/min, (b) 200 mm/min, (c) 150 mm/min, (d) 100 mm/min, and (e) 50 mm/min.

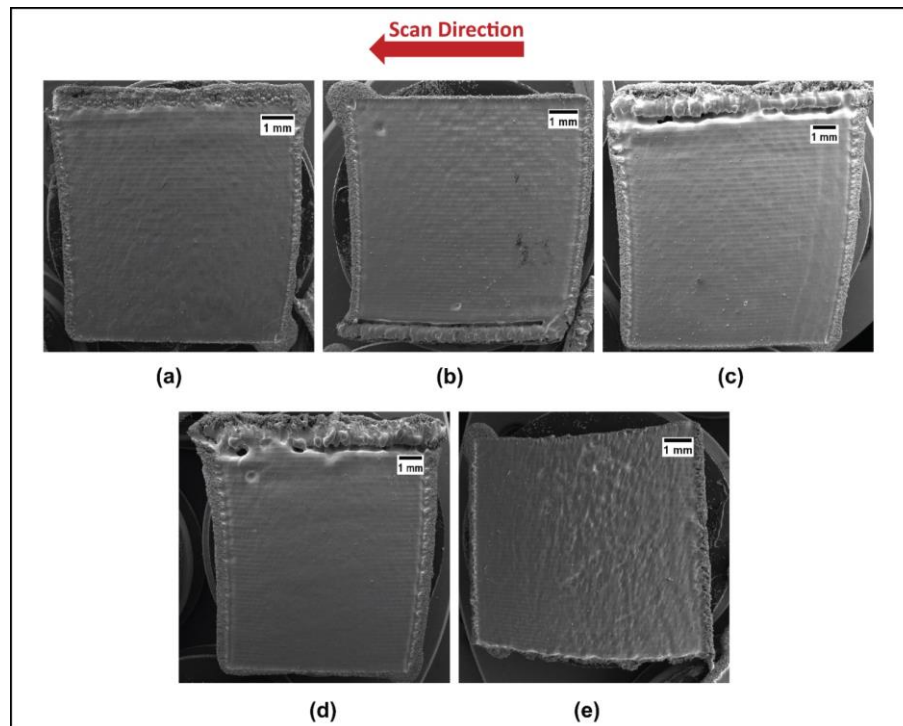


Figure 6.5: SEM images of the samples produced using five laser beams at (a) 250 mm/min, (b) 200 mm/min, (c) 150 mm/min, (d) 100 mm/min and (e) 50 mm/min.

All the samples underwent complete melting, and Figure 6.6 presents SEM images of the melt pool tracks generated with five laser beams at (a) 250 mm/min and (b) 50 mm/min.

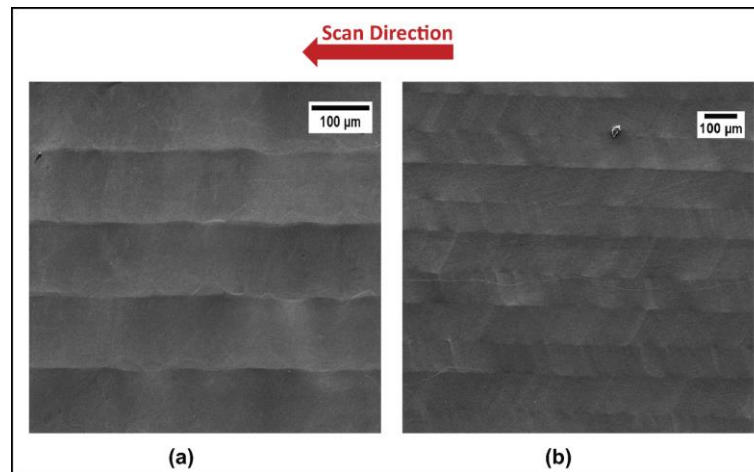


Figure 6.6: SEM images of samples produced using five laser beams at (a) 250 mm/min and (b) 50 mm/min. Both images are contributed to by 5 overlapping melt pools using the parallel scanning method.

Owing to the configuration of the laser channels in a close-packed array, the laser spots overlap, resulting in the creation of a single wider track. For various laser configurations of 3, 4, and 5 lasers, each with a hatch spacing of 200  $\mu\text{m}$ , the width of the laser beam and the degree of overlapping are detailed in Table 6.4. The hatch spacing has a direct impact on the build rate of the component. Therefore, it is important to gain an understanding of the influence of beam overlap on surface morphology. In these experiments, a consistent hatch spacing of 200  $\mu\text{m}$  was employed, resulting in beam overlaps of 8%, 47%, and 54% for configurations using 3, 4, and 5 laser beams, respectively.

<i>No. of lasers</i>	<i>Total power (W)</i>	<i>1/e<sup>2</sup> Beam Width (<math>\mu\text{m}</math>)</i>	<i>Beam Overlap</i>
<b>3</b>	<b>12</b>	<b>217</b>	<b>8%</b>
<b>4</b>	<b>16</b>	<b>294</b>	<b>47%</b>
<b>5</b>	<b>20</b>	<b>370</b>	<b>54%</b>

Table 6.4: The 1/e<sup>2</sup> beam diameter and the cumulative beam overlap generated with a 200  $\mu\text{m}$  hatch spacing.

The depth of the melted layer was investigated across different beam profiles, each utilising 3, 4, and 5 laser beams, with scanning speeds ranging from 50 to 250 mm/min. This examination was conducted with the aid of cross-sectional view SEM as depicted in Figure 6.7. Notably, the beam profile comprising 5 lasers produced a thicker layer, a result attributed to the increased energy density and 54% beam overlap. Nevertheless, it is worth noting that the beam configurations employing 4 and 3 lasers still managed to produce solid material with acceptable layer thicknesses. A beam overlap of at least 40 - 50%

offers an advantage in ensuring consistent layer thickness during the DAM process. Nonetheless, it is advisable to conduct a comprehensive and systematic analysis of beam overlap across various process parameters to establish the definitive processing window for Ti6Al4V during the DAM process.

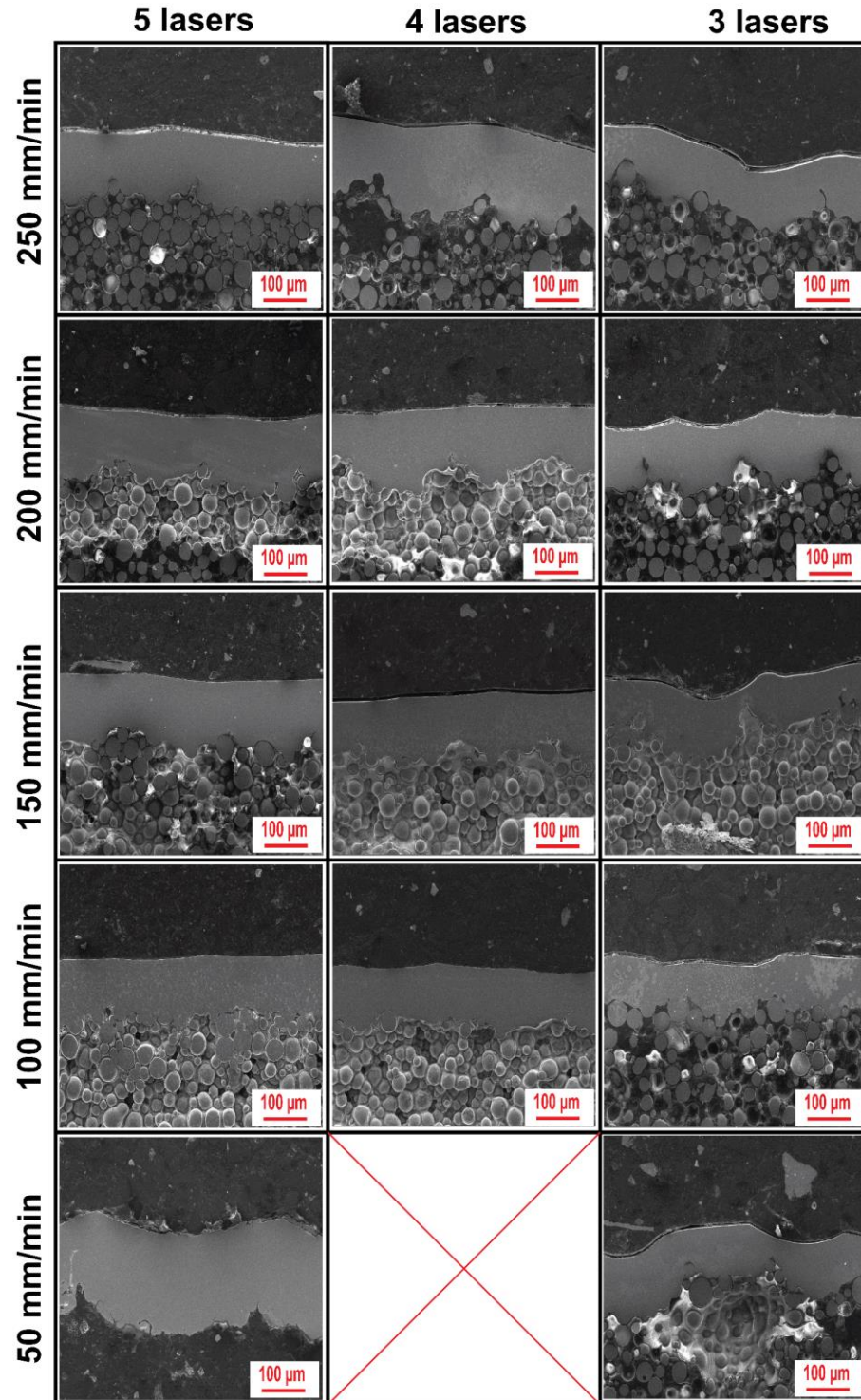


Figure 6.7: A figure depicting the melt pool depth, as determined through SEM, across different beam profiles involving 3, 4, and 5 laser beams, with scanning speeds varying from 50 to 250 mm/min.



### 6.4.2 Surface Roughness in DAM

Figure 6.8 shows images captured by a 3D optical microscope, depicting components subjected to processing at different scanning speeds, utilising beam profiles comprising three, four, and five lasers. Notably, each laser beam within these profiles is maintained at a power level of 4 W. The variation in the top surface roughness is marked, and the extracted values of root mean square surface roughness, denoted as  $R_a$ , are defined for each respective melted surface.

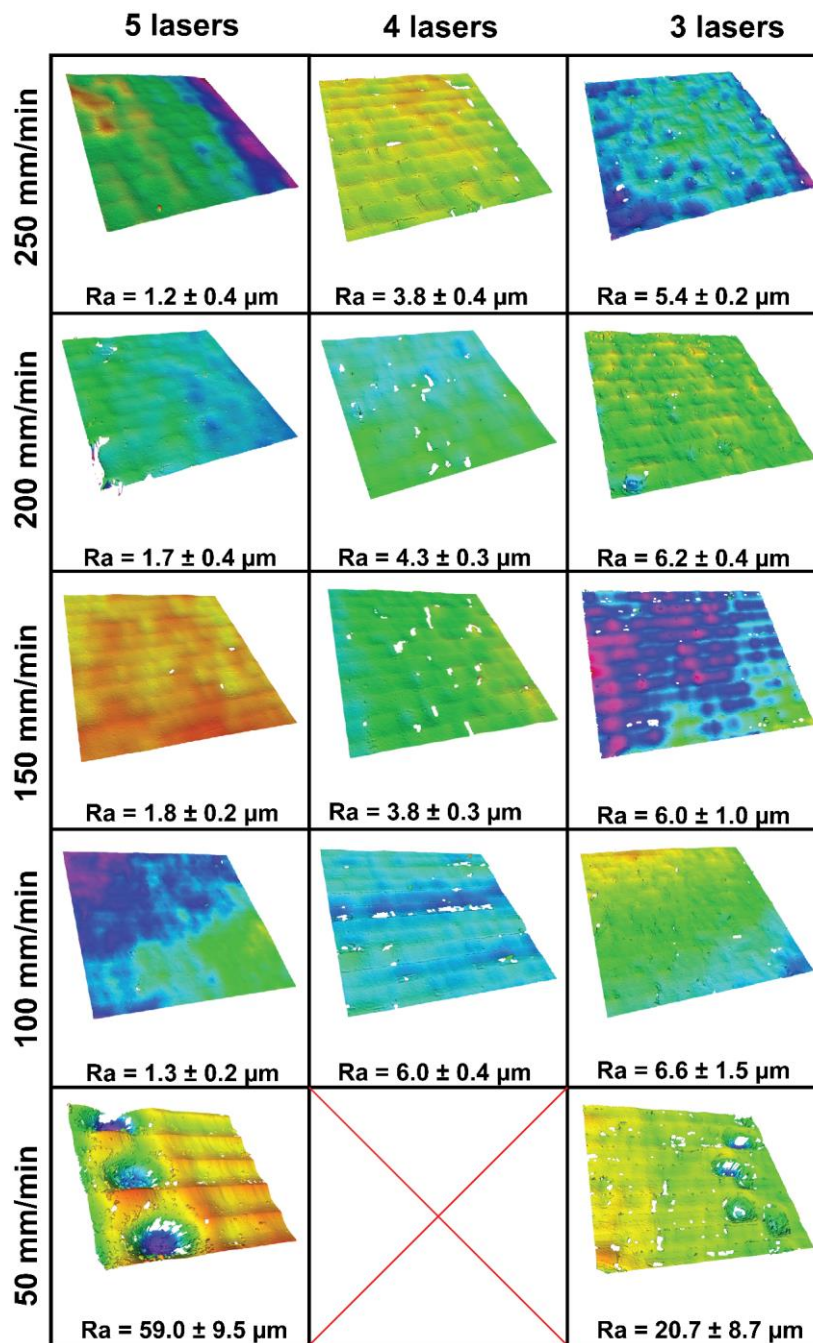


Figure 6.8: Surface roughness for different speeds and profiles, with corresponding r.ms roughness  $R_a$ .

During the DAM of Ti6Al4V, it was observed that the surface roughness improved with the addition of each laser in the beam profile. The  $R_a$  value for the beam profile with 3 lasers at 250 mm/min is 5.4  $\mu\text{m}$ . This roughness is reduced to 3.8  $\mu\text{m}$  and 1.2  $\mu\text{m}$  for the beam profile featuring four and five lasers, respectively. This improvement can be attributed to the increased beam overlap. Across the experiments, the hatch spacing for each beam profile was maintained at 200  $\mu\text{m}$ , resulting in beam overlaps of 8%, 47%, and 54% for the beam profiles with three, four, and five lasers, respectively. The increase in beam overlap correlates with improved surface roughness values. The increment in beam overlap allows for a more cohesive and uniform deposition of material, contributing to the observed enhancement in surface quality.

Although the correlation between scanning speed and surface roughness in DAM is not entirely evident, there is a general trend of improved surface roughness with increasing scanning speed. The unusually high surface roughness observed at a scanning speed of 50 mm/min is attributed to the excessive energy imparted during the process. A comparison of energy density, as conducted by Ref [6], further suggests that the optimal process window for Ti6Al4V lies between 100 and 300 mm/min when utilising a single row with five laser beams, with speeds below 100 mm/min considered excessive in terms of energy input.

In L-PBF, it is acknowledged that factors such as laser power, scanning speed, and hatch spacing exhibit a substantial impact on the surface roughness of the fabricated components. The interplay among these parameters governs the energy density imparted to the material, subsequently influencing the melt pool dynamics and solidification mechanisms, which are pivotal in determining the final surface morphology [137].

Ref [138] investigated the surface roughness of Ti6Al4V produced through L-PBF and developed a predictive model capable of estimating potential surface roughness for various processing parameters. Initially, the laser power significantly influences the powder melting process, with both low and high power levels contributing to elevated top-layer surface roughness. Inadequate power at lower levels may fail to fully melt larger powder particles, while excessive power at higher levels can result in spattering, leading to a coarse surface. Similarly, decreasing scanning speeds provides ample time for the

thorough melting of powder particles. Despite some discrepancies noted in the higher scanning speed region, this trend is anticipated to exhibit a consistent increase. The surface roughness values (Ra) obtained in this study for Ti6Al4V range between 2 and 38  $\mu\text{m}$ . Typically, as-built parts of Ti6Al4V processed using L-PBF exhibit a common Ra value falling within the range of 10 to 16  $\mu\text{m}$ .

### 6.4.3 Melt Pool Temperature Predicted by FE Models

The research presented in *Chapter 5* demonstrated that the melt pool temperature increased with the activation of each laser in the beam configuration. Similarly, within the simulations carried out for this chapter, the average melt pool temperature exhibited an increase in response to the addition of each laser and a reduction in scanning speed. The decrease in scanning speed resulted in higher energy density, thereby leading to an increase in temperature. *Figure 6.9* plots the average melt pool temperature extracted from the FEM simulations conducted for the laser configurations with 3, 4 and 5 lasers, while varying the scanning speed from 50 to 250 mm/min.

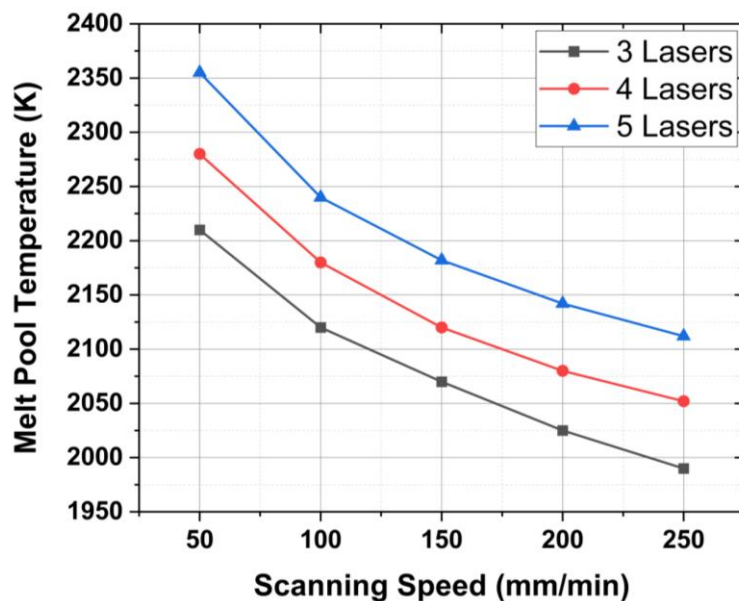


*Figure 6.9: The average temperature, as determined from simulations involving laser configurations with 3, 4, and 5 lasers, while varying the scanning speed from 50 to 250 mm/min.*

### 6.4.4 Cooling Rates Predicted by FE Models

The work presented in *Chapter 5* demonstrated that across different laser configurations within the array there was a noticeable reduction in the cooling rate for Ti6Al4V from the  $\beta$ -transus to the martensitic transformation

temperature during DAM. This reduction was in stark contrast to the reported rates in L-PBF and EB-PBF processes. In DAM, when a single laser was used at a scanning speed of 100 mm/min, the beam profile yielded a cooling rate of 778 K/s. Interestingly, this cooling rate decreased to 191 K/s when employing six lasers within the single array. The cooling rate for each beam configuration was measured using a thermal camera and compared against Analytical and FEM models. Throughout this study, the FEM models were constructed to predict the cooling rate of the multiple diode lasers in the DAM setup. Notably, the models consistently predicted higher cooling rates than those observed via thermal camera measurements. This difference primarily occurred from the omission of Marangoni convection effects in the models. Nevertheless, an important observation was made: the change in cooling rate derived from the thermal camera for one beam profile to another followed a similar trend in both the FEM models and the experimental measurements. This consistency highlights the utility of the FEM models in comprehending the behavior of cooling rates under varying processing conditions in the context of DAM.

The FEM model introduced in *Chapter 5* serves as the foundation for this research, with simulations being conducted for different laser configurations at varying scanning speeds. *Figure 6.10* illustrates the cooling rates, as derived from simulations involving laser configurations employing 3, 4, and 5 lasers, while also adjusting the scanning speed within the range of 50 to 250 mm/min. It is evident from the figure that the cooling rate exhibited a decrease with the incremental addition of each laser within the beam profile, concurrently reducing as the scanning speed was reduced. The most rapid cooling rate, reaching 8400 K/s, was predicted for the beam profile employing 3 lasers at a scanning speed of 250 mm/min. In contrast, the slowest cooling rate, at 1400 K/s, was observed in the simulation involving 5 lasers at a scanning speed of 50 mm/min.

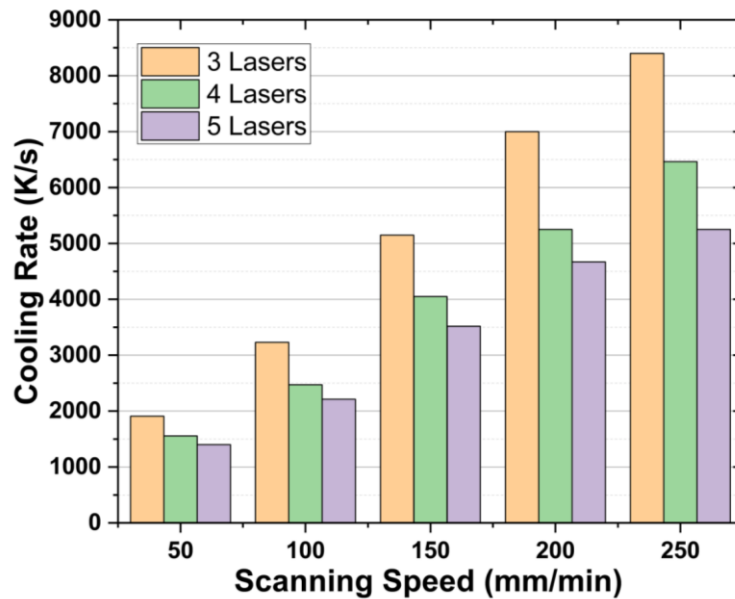


Figure 6.10: The cooling rates, as determined from simulations involving laser configurations with 3, 4, and 5 lasers, while varying the scanning speed from 50 to 250 mm/min.

#### 6.4.5 XRD Analysis

X-ray diffraction (XRD) is employed to confirm the presence of  $\alpha$  and  $\beta$  phases in Ti6Al4V samples produced using the DAM process. Figure 6.11, Figure 6.12, and Figure 6.13 display XRD phase analyses for samples created with 5, 4, and 3 lasers, respectively, at different scanning speeds. All the high intensity peaks in the XRD phase analyses of the samples consistently indicate the presence of the  $\alpha/\acute{\alpha}$  phases, characterized by a hexagonal closed-pack crystal structure. The  $2\theta$  locations of these  $\alpha/\acute{\alpha}$  peaks are similar across all the samples produced. In a typical L-PBF process, such as L-PBF, the melt pool created by the laser undergoes cooling, resulting in the complete transformation of the prior- $\beta$  phase into the acicular  $\acute{\alpha}$  martensitic phase. This transformation is primarily attributed to the exceptionally high cooling rates characteristic of the process. Nevertheless, when the alloy undergoes gradual cooling, the prior- $\beta$  transforms into Widmanstätten  $\alpha$  laths [139]. In some L-PBF samples, the presence of some  $\alpha$  laths can also be attributed to localised slow cooling effects. The crystal structure of both  $\alpha$  and  $\acute{\alpha}$  is identical, with both adopting a hexagonal closed-pack configuration. This similarity in crystal structure makes it challenging to distinguish between the peaks in the XRD results. Consequently, the peaks in the figures presented here are labelled as  $\alpha/\acute{\alpha}$  for clarity.

As discussed in *Chapter 2 section 2.10*, Ti6Al4V is classified as an  $\alpha + \beta$  alloy, featuring a  $\beta$  transus temperature that serves as a critical threshold below which the transformation into a typical  $\alpha + \beta$  duplex microstructure occurs. The cooling rate below this threshold plays a pivotal role in determining the resulting microstructure. In general, the rapid cooling rates in L-PBF prevent the formation of the  $\beta$  phase. In contrast, the build chamber temperature in EB-PBF reduces the cooling rate, enabling the formation of the  $\beta$  phase in the produced samples. However, all the samples produced, using the DAM process, utilising up to 5 lasers with scanning speeds ranging from 50 to 250 mm/min, consistently demonstrated the formation of the  $\beta$  phase, as can be seen in *Figure 6.11*, *Figure 6.12*, and *Figure 6.13*.

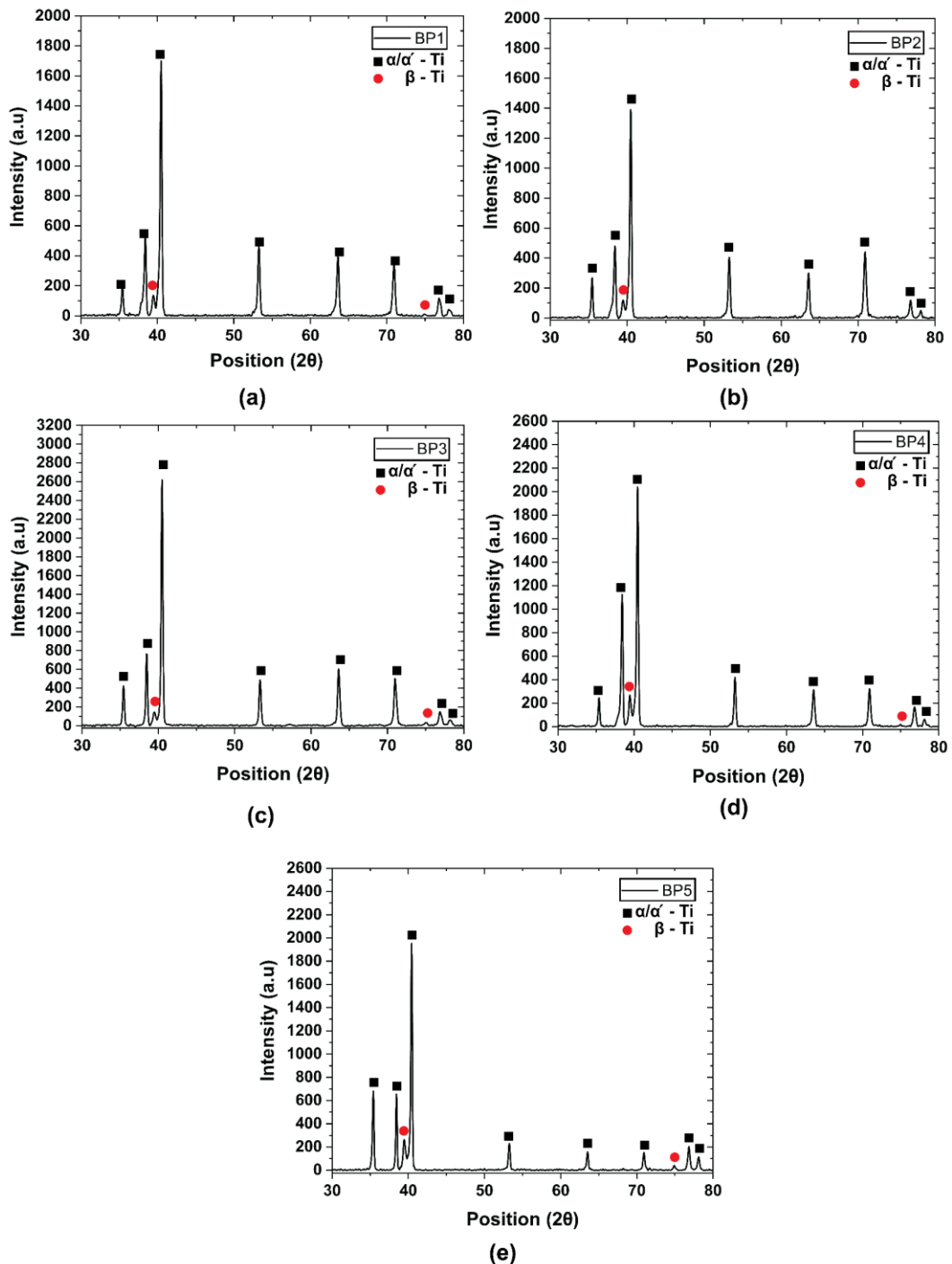


Figure 6.11: XRD phase analysis for the beam configuration with 5 Lasers illustrating for the scanning speed 250 mm/min; BP1 (a), 200 mm/min; BP2 (b), 150 mm/min; BP3 (c), 100 mm/min; BP4 (d), and 50 mm/min; BP5 (e).

The diffraction peak associated with the  $\beta$  phase is predominantly detected at a  $2\theta$  angle of  $39^\circ$ . Additionally, a secondary  $\beta$  phase is observed at around a  $2\theta$  angle of  $74$  to  $75^\circ$ . The  $\beta$  phases are indicated in the plots by red circle. The secondary  $\beta$  peak is absent in some samples, as evident in *Figure 6.11 (b)* and *Figure 6.12 (b)*. It is important to note that the intensity of the secondary  $\beta$  peak is considerably lower compared to all the other peaks in the diffraction data, making it susceptible to potential data errors.

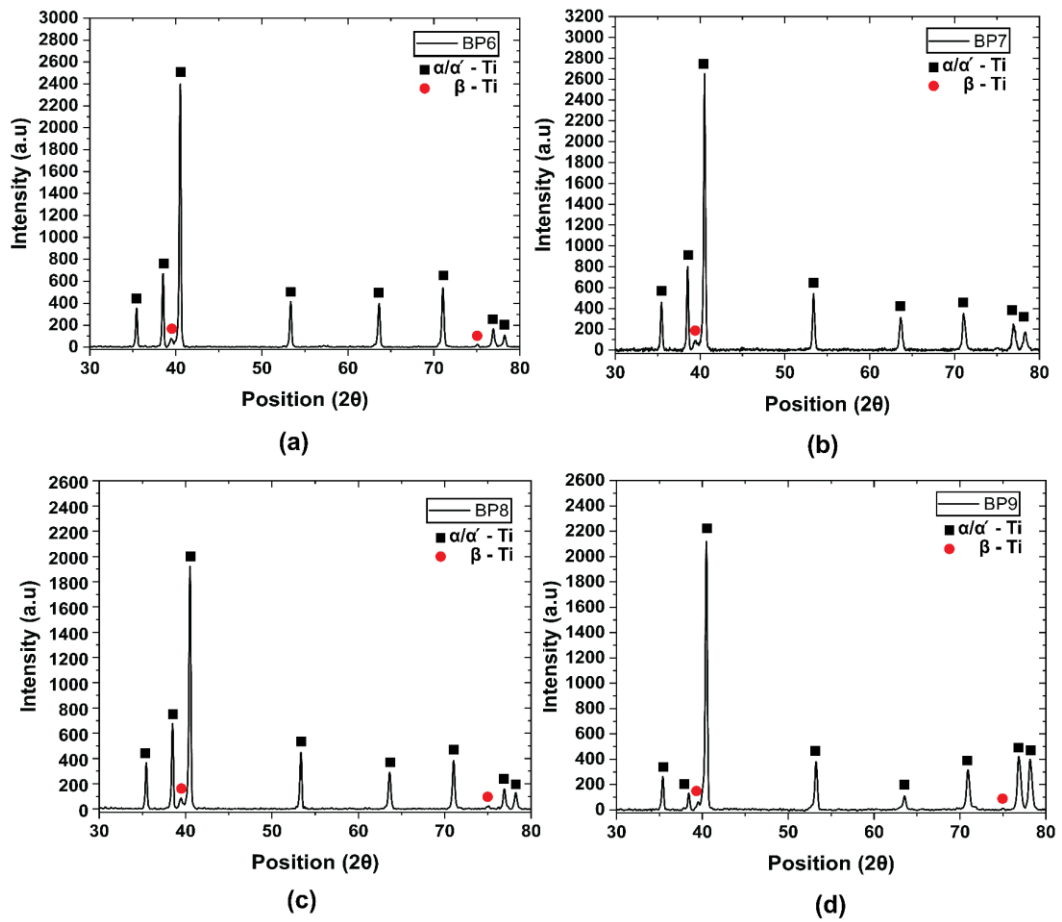


Figure 6.12: XRD phase analysis for the beam configuration with 4 Lasers illustrating for the scanning speed 250 mm/min; BP6 (a), 200 mm/min; BP7 (b), 150 mm/min; BP8 (c), and 100 mm/min; BP9 (d).



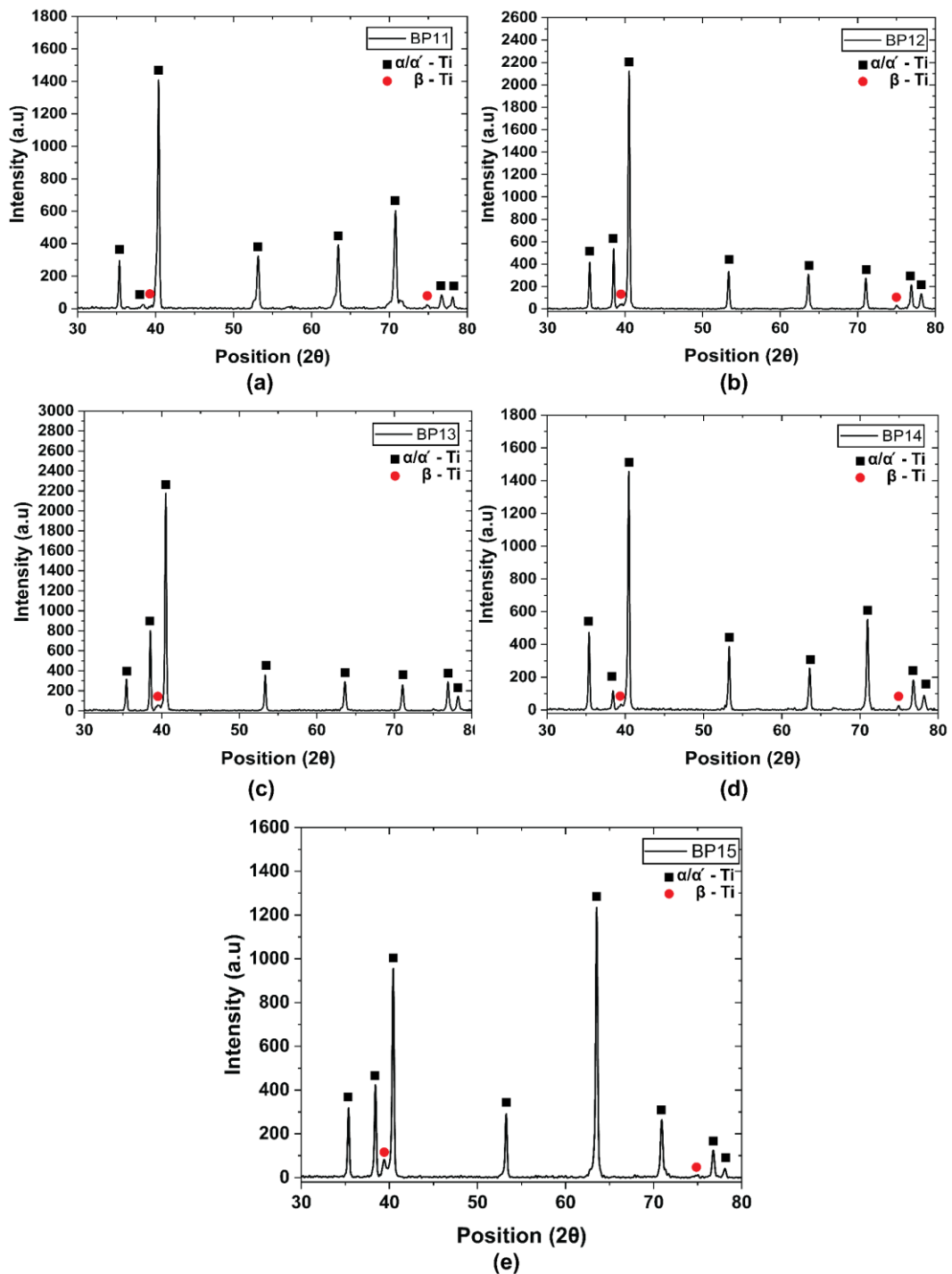


Figure 6.13: XRD phase analysis for the beam configuration with 3 Lasers illustrating for the scanning speed 250 mm/min; BP11 (a), 200 mm/min; BP12 (b), 150 mm/min; BP13 (c), 100 mm/min; BP14 (d), and 50 mm/min; BP15 (e).

#### 6.4.6 Residual Stress

The X-Ray diffraction technique used for residual stress measurement primarily gauges the strain present within the crystal lattice. This strain is an indication of the internal forces or stresses within the material, that have caused the lattice to deform. Residual stresses can arise due to various manufacturing processes, thermal treatments, or external loads and have the potential to distort

the regular spacing of the crystal lattice. By studying the changes in the diffraction pattern, we can determine the extent of this deformation or strain. Once we have measured the strain, the associated residual stress, which is responsible for inducing this strain, is then computed. This calculation is based on the principle that the distortion of the crystal lattice follows a linear elastic relationship, meaning that the lattice deformation is directly proportional to the applied stress. By understanding this relationship and knowing the properties of the material, we can accurately derive the residual stress from the measured strain [20], [23], [133], [135].

As discussed in Section 6.3.4.1, the slope of the tilt angle  $\sin^2\psi$  and lattice spacing ( $d$ ) yields the strain values. *Figure 6.14* depicts the  $d$  (21.3) versus  $\sin^2\psi$  plot for BP1 (5 lasers with a scanning speed of 250 mm/min) along the X axis (laser traverse direction). Whereas *Figure 6.15* shows the  $d$  (21.3) versus  $\sin^2\psi$  plot for BP1 along the Y axis (perpendicular to the laser traverse direction).

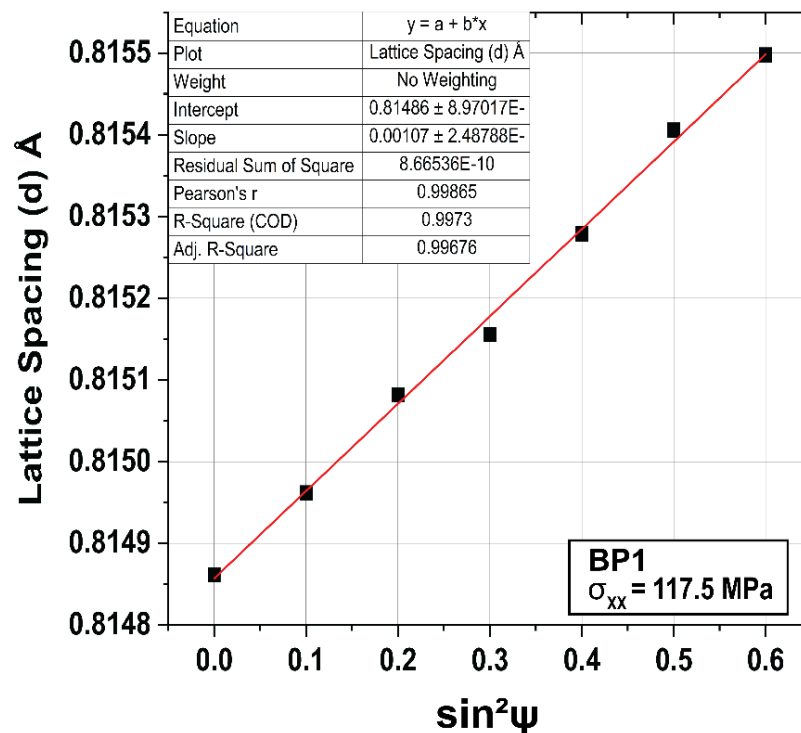


*Figure 6.14: Depicting the  $d$  (21.3) versus  $\sin^2\psi$  plot for two distinct configurations: BP1 (comprising 5 lasers with a scanning speed of 250 mm/min) along the X axis.*

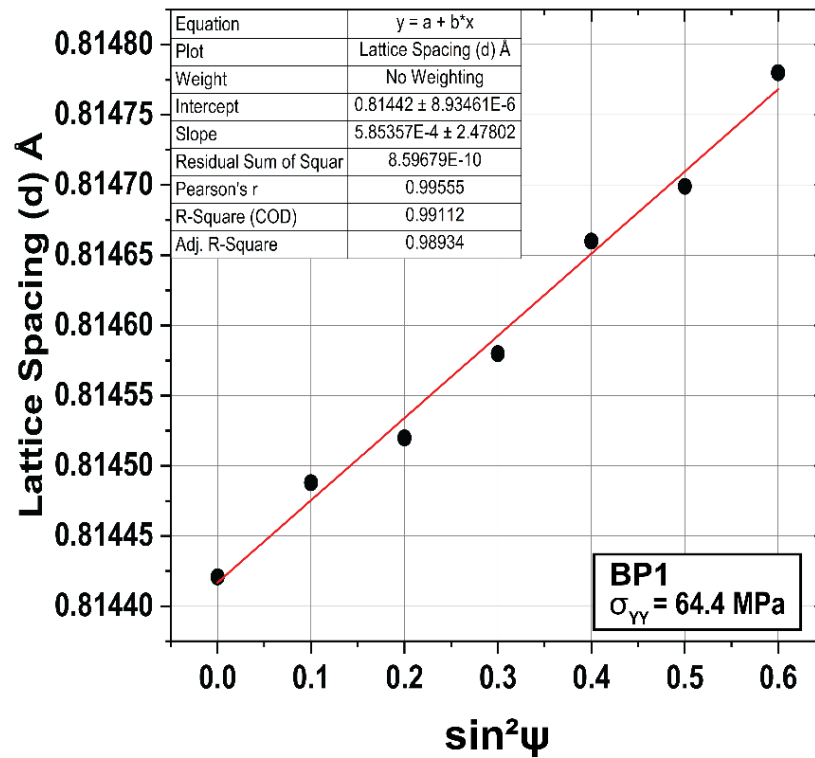


Figure 6.15: Figure 6.14: Depicting the  $d$  (21.3) versus  $\sin^2\psi$  plot for two distinct configurations: BP1 (comprising 5 lasers with a scanning speed of 250 mm/min) along the Y axis.

The residual stress values for each sample in both the X ( $\sigma_{XX}$ ) and Y ( $\sigma_{YY}$ ) directions are subsequently determined using *equation 13*. *Figure 6.16* illustrates the residual stress in the X and Y directions, as assessed from the samples through the XRD technique. The results indicate that residual stresses induced in the DAM process vary with the addition of each laser beam and the scanning speed. The lowest recorded residual stress value ( $\sigma_{YY}$ ) of 58.4 MPa, in the Y direction, was observed in a configuration utilizing 5 lasers with a scanning speed of 50 mm/min. Conversely, the highest value ( $\sigma_{XX}$ ) of 138.2 MPa was noted in the X direction in a setup employing 3 lasers with a scanning speed of 250 mm/min. This trend shows that residual stress decreases with the activation of each additional laser from 3 to 5, and also decreases with a reduction in scanning speed from 250 to 50 mm/min.

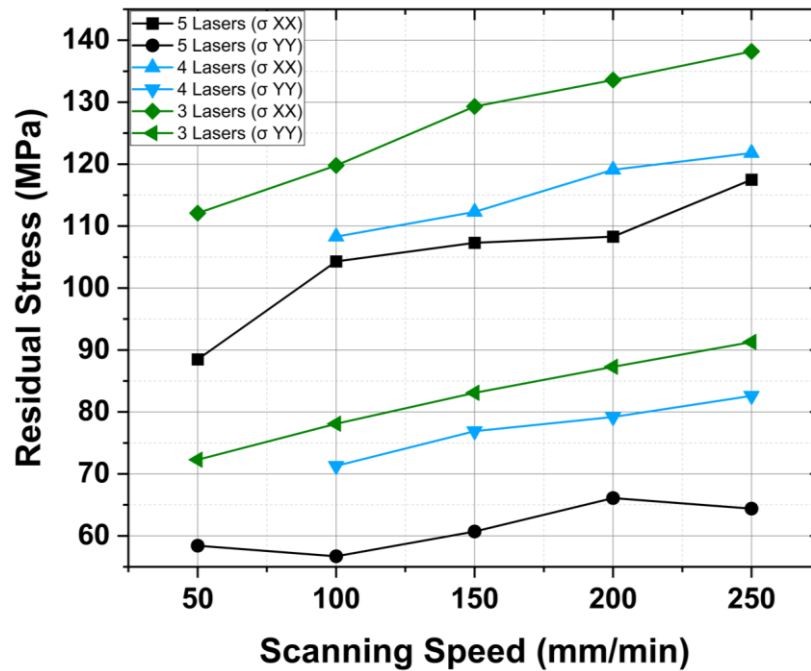


Figure 6.16: The residual stress in XX and YY directions, as determined from the samples using XRD technique involving laser configurations with 3, 4, and 5 lasers, while varying the scanning speed from 50 to 250 mm/min.

#### 6.4.7 Microstructure Characteristics During DAM of Ti6Al4V

As outlined in the literature review, microstructural changes in L-PBF are influenced by factors such as the elevated temperature of the melt pool, rapid cooling rates, steep temperature gradients, and the cyclic thermal variations inherent in the layered manufacturing process. These factors collectively lead to the development of a distinct microstructure when compared to conventional casting or forging techniques. An inherent feature of L-PBF is the phenomenon of oriented crystal growth, known as epitaxial nucleation. As a result of this process, newly forming cells exhibit the same crystallographic orientation as the grains in the previously solidified layers. This phenomenon is consistently observed not only between adjacent layers but also within individual layers due to the remelting process [140]. The microstructure of the as-built Ti6Al4V alloy typically comprises  $\alpha$  martensite. The solidification of the molten alloy initiates with the creation of the primary cubic  $\beta$  phase. The as-solidified beta phase exhibits a noticeable texture  $\{100\}$  and with the rapid cooling rates characteristic of L-PBF, the  $\beta$  phase undergoes transformation into  $\alpha$  martensite, which maintains a crystallographic orientation relationship with the parent  $\beta$  phase [3].

### 6.4.7.1 IPF Map

In DAM, all samples exhibit a microstructure characterised by both  $\alpha$  and  $\beta$  crystal structures, as demonstrated in the Inverse Pole Figure (IPF) map in Figure 6.17. An IPF is key in representing the crystal orientation in polycrystalline materials like Ti6Al4V, and is generated using Electron Backscatter Diffraction (EBSD). In the IPF, each color is assigned to a specific crystallographic direction, offering a visual insight into the texture of material and preferred crystal orientation. The crystallographic orientation direction in relation to the colour map for Ti – Alpha ( $\alpha$  phase in this case) and Ti – Beta ( $\beta$  phase) are given in the bottom left corner of the *Figure 6.17*. The EBSD analysis was performed using an Oxford Instruments® C-NANO EBSD detector at a 20 kV operation voltage. To optimise the balance between resolution and scanning duration, a step size of 0.1  $\mu\text{m}$  was chosen, along with a magnification of 650x, which was determined by the scanning area size.

For all the samples, EBSD analysis was conducted on an area measuring 250  $\mu\text{m}$  by 250  $\mu\text{m}$ , employing a fine step size of 0.1  $\mu\text{m}$ . This small step size enables high-resolution mapping, allowing for detailed examination of the microstructural features within the specified area. The IPF map provides confirmation of a basketweave-like  $\alpha$ - $\beta$  microstructure within the prior- $\beta$  grains, a pattern that is consistently observed across all processing conditions. The grain coarseness within the microstructure displays variations across different beam configurations and scanning speeds. Specifically, there is a slight increase in grain size with the activation of each additional laser beam, as well as with the reduction in scanning speed. The beam profile with 5 lasers at a scanning speed of 50 mm/min produces an average grain size of 1.9  $\mu\text{m}$ . Whereas, the beam profile with 3 laser at a scanning speed of 250 mm/min produces 1.07  $\mu\text{m}$  size grains. However, it is noteworthy that the scanning speed has a more pronounced impact on the differences in grain coarseness and crystallographic texture compared to the number of laser beams.

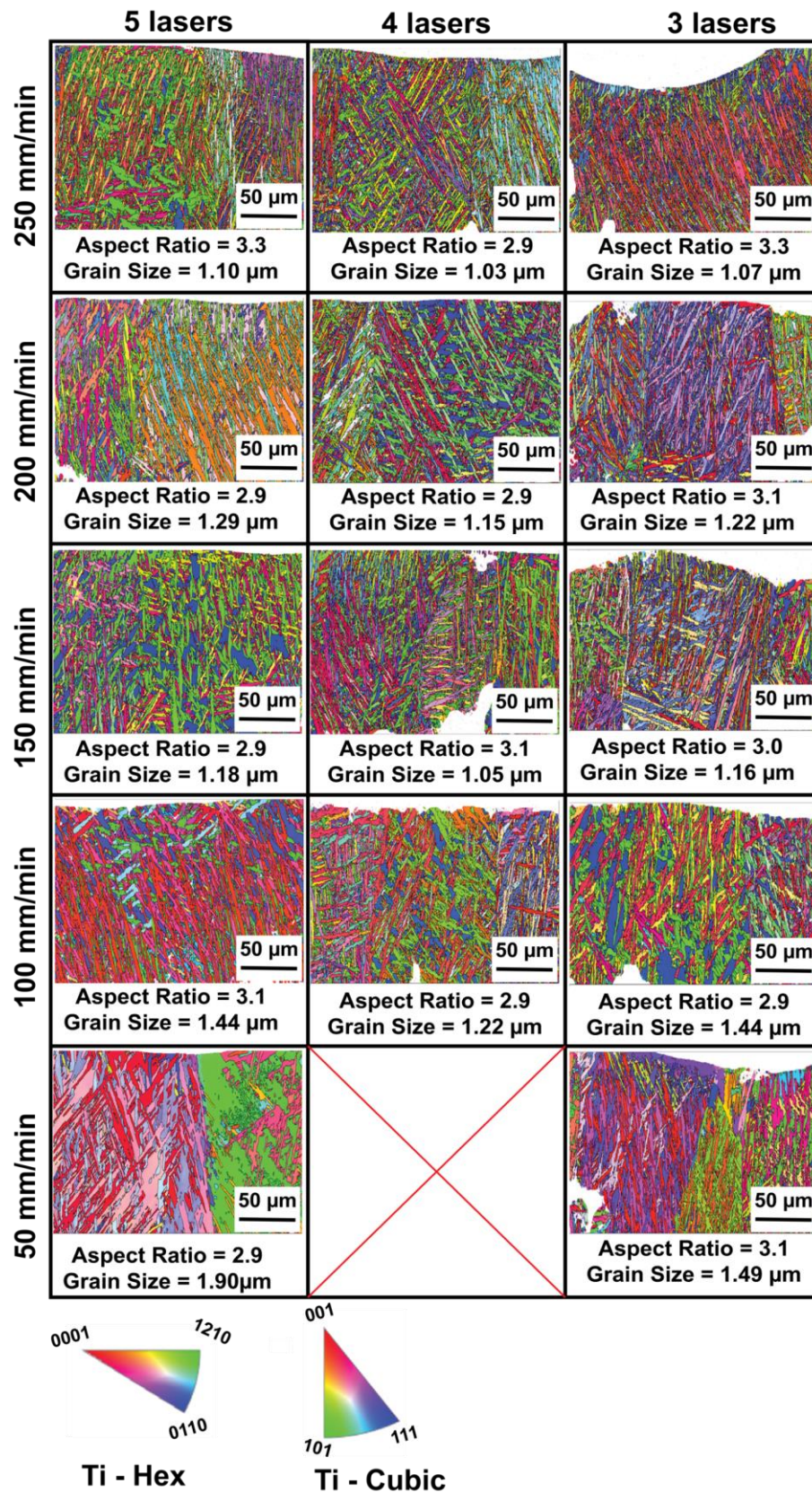


Figure 6.17: The IPF map as determined from the samples using EBSD technique involving laser configurations with 3, 4, and 5 lasers, while varying the scanning speed from 50 to 250 mm/min. The crystallographic orientation direction in relation to the colour map: Ti - Alpha is  $\alpha$  phase and Ti - Beta corresponds to  $\beta$  phase.

### 6.4.7.2 Pole Figure

A pole figure in EBSD is a graphical representation that shows the orientation of crystals in a sample. It plots the orientations of individual crystallites to identify the texture, or preferential alignment, within the material. The pole figures as shown in *Figure 6.18* shows the pole figures as determined from the samples for beam configurations with 5 lasers, while varying the scanning speed from 250 mm/min (a), 200 mm/min (b), 150 mm/min (c), 100 mm/min (d) and 50 mm/min (e). Similarly *Figure 6.19* and *Figure 6.20* illustrates the pole figures for the beam configurations with 4 and 3 lasers respectively.

The pole figures indicate that the  $\alpha$  texture exhibits greater intensity compared to the texture of the high-temperature  $\beta$  phase. Additionally, there is a obvious preference for the crystallographic orientation of the  $\alpha$  phase along the  $\{0001\}$  direction. The alterations in the texture of the  $\alpha$  phase do not display a strong correlation with either the scanning speed or the number of lasers employed. Similarly, the  $\beta$  phase exhibits a notable crystallographic orientation along the  $\{100\}$  and  $\{111\}$  directions. As the scanning speed was decreased during processing, the texture of the  $\beta$  phase in the material became more pronounced and concentrated, a trend evident in the pole figure across all three Ti-Cubic orientations. There appears to be an inconsistent reduction in the intensity of both the  $\alpha$  and  $\beta$  phases with respect to the number of lasers in the array, indicating a complex relationship between laser quantity and phase development. Additional experiments may be required to more definitively establish this relationship. Nevertheless, there is an indication of a marginal increase in the  $\alpha$  phase concentration as the number of lasers is reduced, suggesting a potential correlation between reduced laser count and  $\alpha$  phase development.

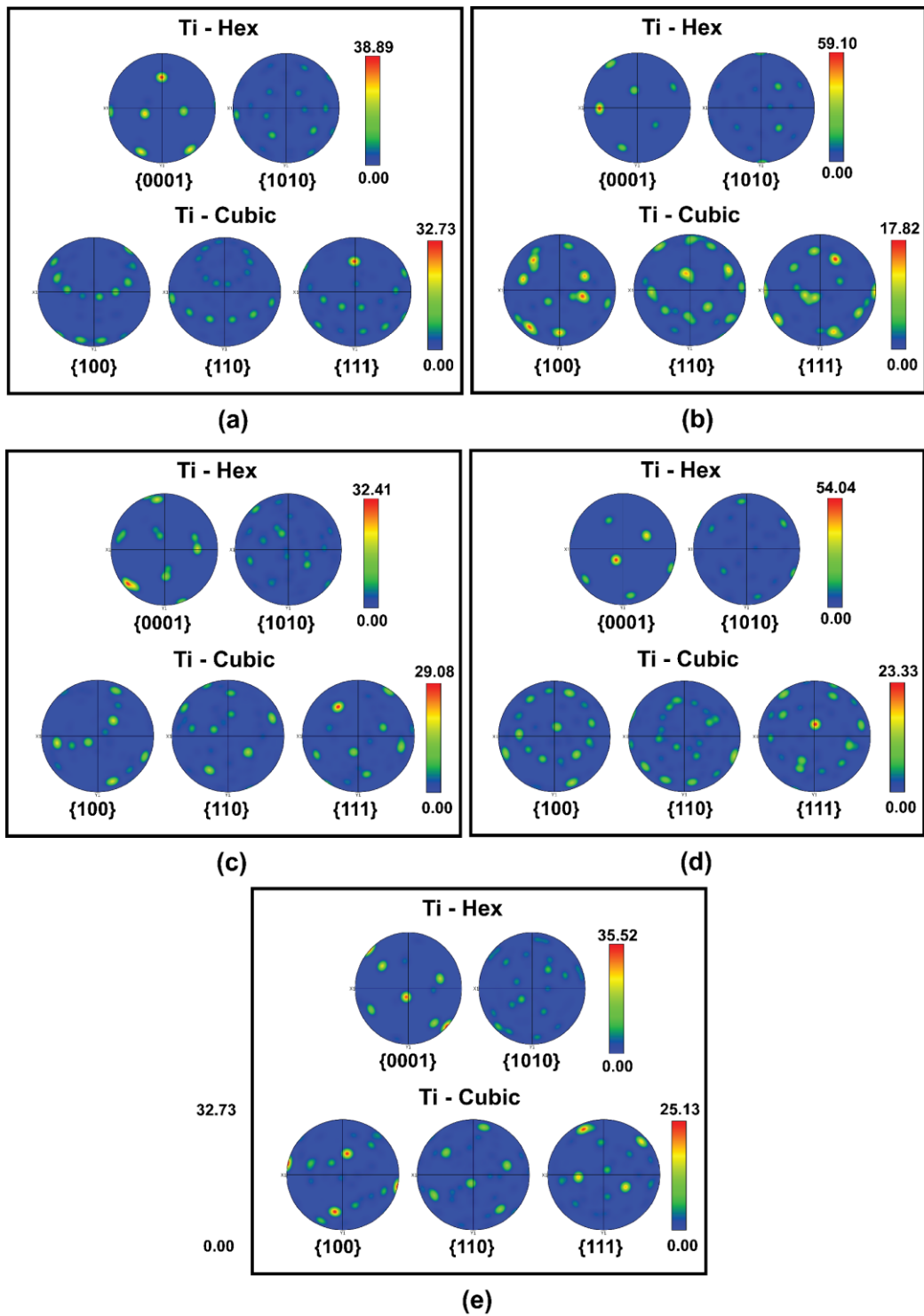


Figure 6.18: The pole figure as determined from the samples using EBSD technique involving laser configurations with 5 lasers, while varying the scanning speed from 250 mm/min (a), 200 mm/min (b), 150 mm/min (c), 100 mm/min (d) and 50 mm/min (e).



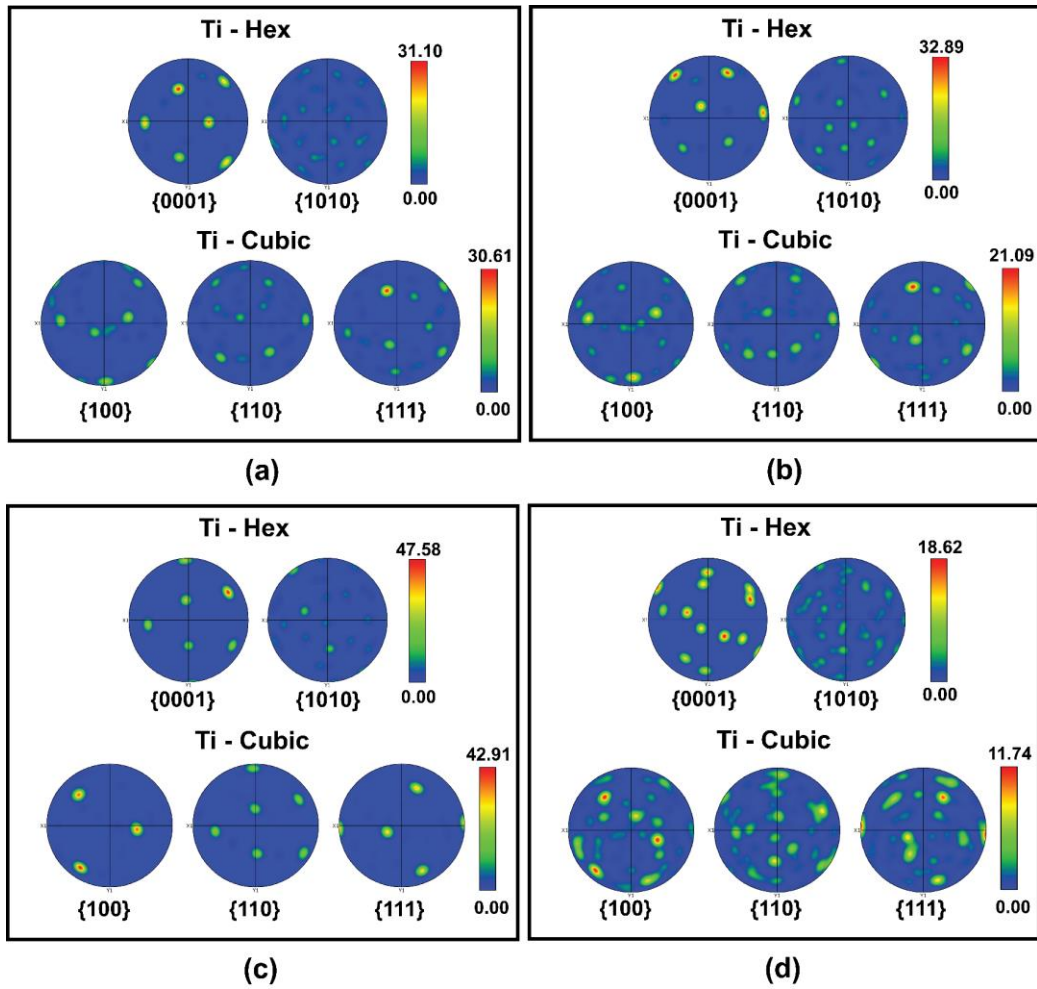


Figure 6.19: The pole figure as determined from the samples using EBSD technique involving laser configurations with 4 lasers, while varying the scanning speed from 250 mm/min (a), 200 mm/min (b), 150 mm/min (c), and 100 mm/min (d).

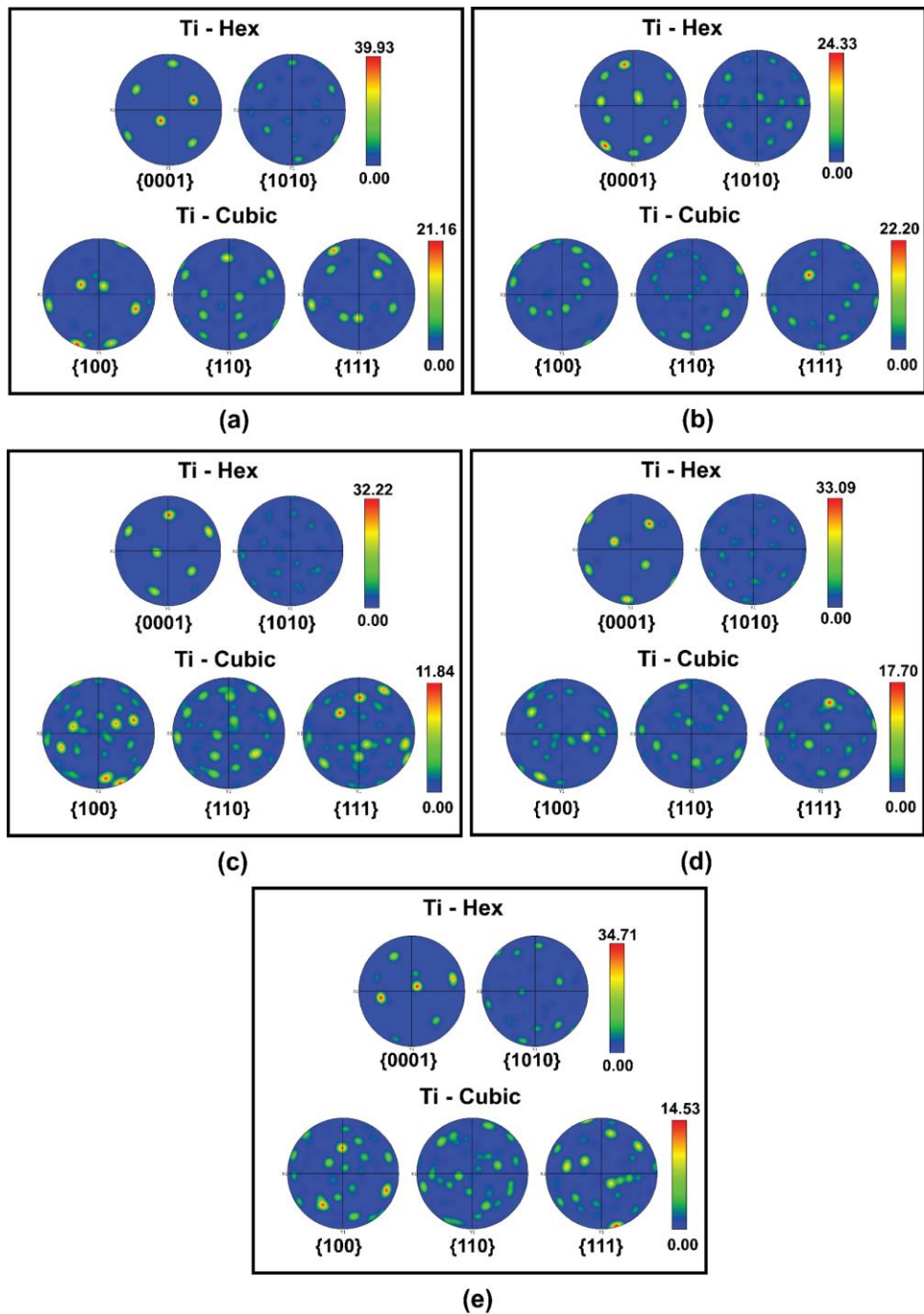


Figure 6.20: The pole figure as determined from the samples using EBSD technique involving laser configurations with 3 lasers, while varying the scanning speed from 250 mm/min (a), 200 mm/min (b), 150 mm/min (c), 100 mm/min (d) and 50 mm/min (e).

### 6.4.7.3 Phase Map

A phase map of the samples is shown in *Figure 6.21*, revealing the presence of a small amount of  $\beta$  phase in all samples. A phase map in EBSD is a graphical representation of the distribution and types of crystallographic phases present within a material sample. It is created by analysing the diffraction patterns

obtained from different regions of the sample, allowing for the identification of distinct phases based on their unique crystal structures.

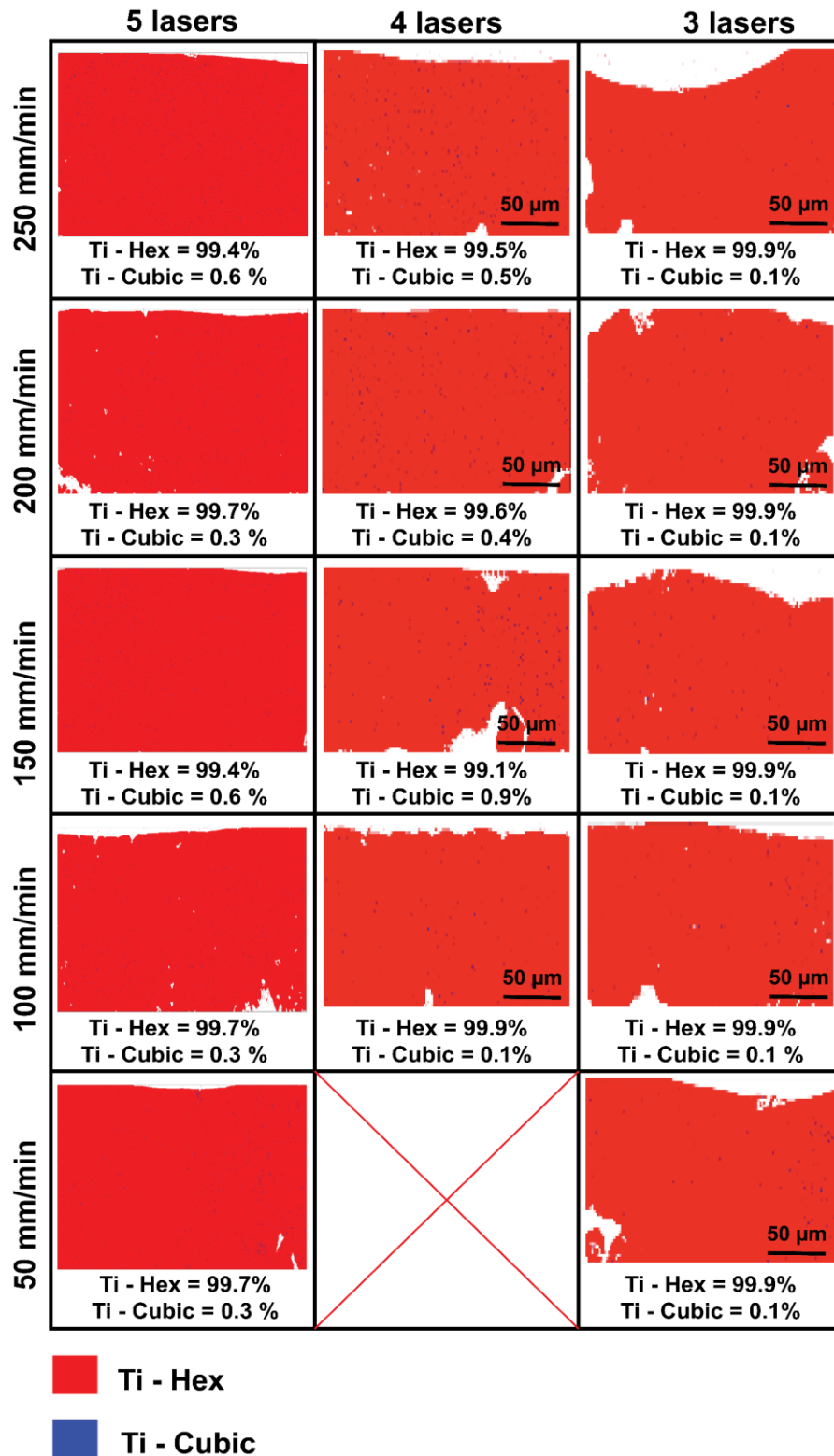


Figure 6.21: The phase map as determined from the samples using EBSD technique involving laser configurations with 3, 4, and 5 lasers, while varying the scanning speed from 50 to 250 mm/min.

The phase map presented in Figure 6.21 illustrates the microstructural composition of samples fabricated using 3, 4, and 5 lasers, with scanning speeds

varying between 50 and 250 mm/min. In this map, the Hexagonal Close-Packed (HCP)  $\alpha/\alpha'$  phase of Titanium (Ti-Hex) is depicted in red, indicating the areas where this phase predominates. Conversely, the Body-Centered Cubic (BCC)  $\beta$  phase of Titanium (Ti-Cubic) is represented in blue, differentiating it from the  $\alpha/\alpha'$  prime phase and showcasing the phase distribution within the samples resulting from the specified laser and scanning parameters. The content of  $\beta$  phase varies between 0.1% and 0.9%, and there appears to be no visible dependence on scanning speed or the number of lasers, as observed. However, the XRD results (*Figure 6.22*) show differences in the intensities of  $2\theta$  angles corresponding to  $\beta$  positions. This discrepancy can be attributed to the fact that X-ray measurements provide an average value over a length of 2.5 mm, whereas the EBSD phase map analyses a smaller area of  $250 \times 250 \mu\text{m}^2$ . Further experiments may be necessary to establish this relationship more conclusively.

## 6.5 Discussions

*Table 6.5* provides a comprehensive summary of the percentage variations in cooling rates as determined from simulations involving laser configurations with 3, 4, and 5 lasers, while varying the scanning speed from 50 to 250 mm/min. Analysis of these percentages reveals intriguing insights into the impact of scanning speed and the number of lasers on the cooling rate in the DAM process. The beam profile with 3 lasers at a scanning speed of 250 mm/min has the highest cooling rate of 8400 K/s and the rate of change is calculated from this highest value. Upon reducing the scanning speed from 250 mm/min to 200 mm/min, a 17% decrease in cooling rate becomes evident, emphasising the influence of slower scanning speeds on heat dissipation. Furthermore, as the laser count increased from 3 to 4, a 23% reduction in cooling rate was observed at 250 mm/min. This finding highlights the sensitivity of the cooling rate to the number of lasers active within the beam profile. Remarkably, the most significant cooling rate reduction of 83% was achieved when employing 5 laser beams at a scanning speed of 50 mm/min. This suggests that the combined effect of lower scanning speed and the simultaneous activation of additional lasers has a profound impact on the cooling rate in DAM. Similarly, it is known that higher laser power combined with a slower scanning speed can reduce the cooling rate in L-PBF processes [123].

3 Lasers		4 Lasers		5 Lasers	
Scanning Speed (mm/min)	Changes in Cooling Rate	Scanning Speed (mm/min)	Changes in Cooling Rate	Scanning Speed (mm/min)	Changes in Cooling Rate
50	77%	50	81%	50	83%
100	62%	100	71%	100	74%
150	39%	150	52%	150	58%
200	17%	200	38%	200	44%
250	0%	250	23%	250	38%

*Table 6.5: The percentage of changes in cooling rates, as determined from simulations involving laser configurations with 3, 4, and 5 lasers, while varying the scanning speed from 50 to 250 mm/min. The beam profile with 3 lasers at a scanning speed of 250 mm/min has the highest cooling rate of 8400 K/s. The rate of change is calculated from this highest value.*

The occurrence of the  $\beta$  phase without the implementation of pre-heating is a seldom-encountered phenomenon within both L-PBF and EB-PBF processes. Ref [139] demonstrated the induction of an  $\alpha + \beta$  microstructure in Ti6Al4V during L-PBF through utilisation of a distinctive approach. This method involved cyclic heating of the layers facilitated by a 90° rotation scanning strategy, along with the utilisation of a pre-heated build platform maintained at a temperature of 200° C. It is noteworthy that this research employed a low laser power of 42 W at a scanning speed of 58 mm/s, resulting in a notably low scanning speed when compared to the commercial L-PBF process for Ti6Al4V. Despite the application of this inventive approach leading to the production of an  $\alpha + \beta$  microstructure, the samples generated in this study exhibited a graded microstructure with residual porosity due to low energy density. Moreover, reduction in the laser power and scanning speed while employing a single laser in L-PBF results in a substantial corresponding reduction in throughput. Conversely, in the case of DAM, the slower speed is offset by the larger processing area of the laser beam array, ultimately enhancing throughput.

In *Figure 6.22*, an investigation is carried out regarding the intensity of XRD at the  $\beta$  phase, specifically at a  $2\theta$  angle of 39°. This examination is based on samples generated using laser configurations featuring 3, 4, and 5 lasers, with scanning speeds ranging from 50 to 250 mm/min. The data implies that the intensity of the  $\beta$  phase exhibits an incremental increase with the addition of each laser beam, as well as with a decrease in scanning speed. The intensity of a peak is intrinsically connected to the quantity of crystalline material contained within the sample and the extent to which the crystal planes are aligned to facilitate

diffraction. This observation underscores the heightened occurrence of  $\beta$  crystal formation within the DAM process as additional laser beams are incorporated, in parallel with a reduction in scanning speed. This alignment with the cooling rate further supports the notion that a gradual cooling process is recognised for its capacity to induce the formation of the  $\beta$  phase in Ti6Al4V [99].

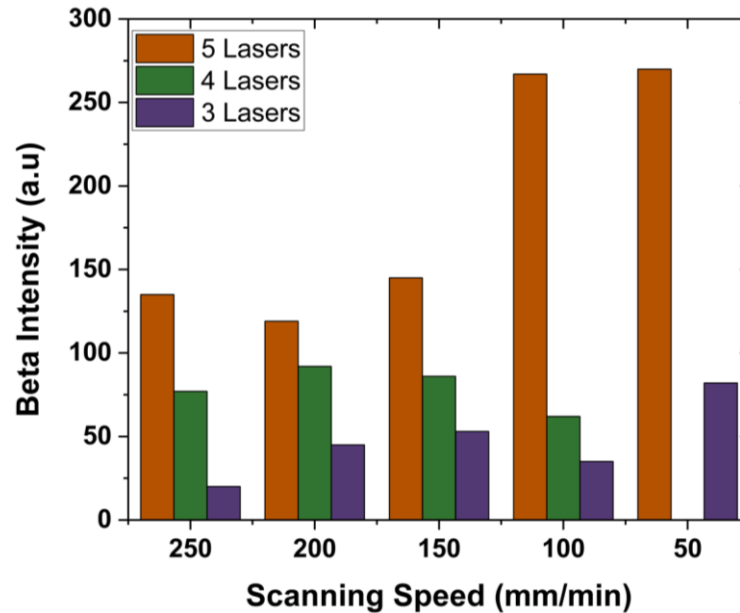


Figure 6.22: The intensity of XRD diffraction at the  $\beta$  phase at a  $2\theta$  angle of  $39^\circ$ , as determined from the samples involving laser configurations with 3, 4, and 5 lasers, while varying the scanning speed from 50 to 250 mm/min.

As outlined in Section 6.4.3, the microstructure of Ti6Al4V is affected by the cooling rate during the transition from the  $\beta$  transus temperature to the martensitic transformation temperature. A similar pattern was observed in the FEM simulations of the cooling rates for various parameters, as detailed in Table 6.5. The scanning speed played a role in influencing the rate of change in the percentage of cooling rates across different samples, which aligns with the observed growth in grain size.

In DAM, the inherent characteristic of a low cooling rate, combined with the ability to precisely regulate this rate through activation of multiple individually controlled diode lasers, presents a promising method for reduction of residual stress in the processed materials. Additionally, the potential for fine-tuning the cooling rate can be extended through the incorporation of additional rows within the laser array and adjustment of scanning speed. Furthermore, the residual stresses induced in the processing of Ti6Al4V using DAM are considerably lower than those reported for L-PBF (specified in Table 6.1), in the absence of substrate

pre-heating. The smallest residual stress observed in DAM is similar to the residual stress in L-PBF with a powder bed pre-heat temperature of approximately 450°C, as indicated in Table 6.2. The values presented in Table 6.2 represent the average residual stress in the build direction, which is generally lower than that of the top layer, as previously discussed. This suggests that the residual stress in DAM in the build direction could potentially be even lower than the values reported in this study. Moreover, implementing substrate pre-heating in the DAM process may further decrease the residual stress levels.

The fluctuations in residual stress correlate with the cooling rate, displaying a corresponding and consistent pattern. As the cooling rate decreased, the residual stress also decreased. Low cooling rates, particularly in the temperature range between the  $\beta$  transus and the martensitic transformation temperature, are known to effectively reduce residual stress in Ti6Al4V [141]. Increased laser power has been documented as a factor associated with a reduction in deformation resulting from residual stress [142]. In the context of laser cladding, it has been reported that reducing the feed rate, which is equivalent to the scanning speed in DAM or L-PBF, leads to a reduction in residual stress and resulting deformation [124]. The accumulation of elevated thermal residual stresses, attributed to the rapid cooling rate and temperature gradient, constitutes a significant challenge in the L-PBF built parts [127], [129], [143], [144].

## 6.6 Conclusions

The investigation in *Chapter 5* highlighted the efficacy of the DAM process in effectively regulating the cooling rate during manufacturing, through application of an individually controlled, fiber-coupled laser array. This control over cooling rates is achieved through laser activation and scanning speed adjustment. This Chapter further explored the influence of various beam profiles and scanning speeds on cooling rate changes in processed parts. DAM's inherent low cooling rates combined with precise control via individually managed diode lasers holds promise for reducing residual stress in manufactured components.

Notably, residual stresses in DAM-processed Ti6Al4V are considerably lower than those reported for L-PBF. The findings here indicate that residual stresses

in DAM are influenced by the number of laser beams and adjustments in scanning speed. The lowest recorded residual stress ( $\sigma_{YY}$ ) occurred in the Y direction, measuring 58.4 MPa in a configuration with 5 lasers at a scanning speed of 50 mm/min. Conversely, the highest stress ( $\sigma_{XX}$ ) of 138.2 MPa was observed in the X direction with 3 lasers at a scanning speed of 250 mm/min. A trend emerges, showing that residual stress decreases with the activation of additional lasers and with reduced scanning speed. Furthermore, the residual stress reduction with respect to the number of lasers scanning speed follows the trend of cooling rate derived from the FEM simulations as illustrated in *Figure 6.23*.

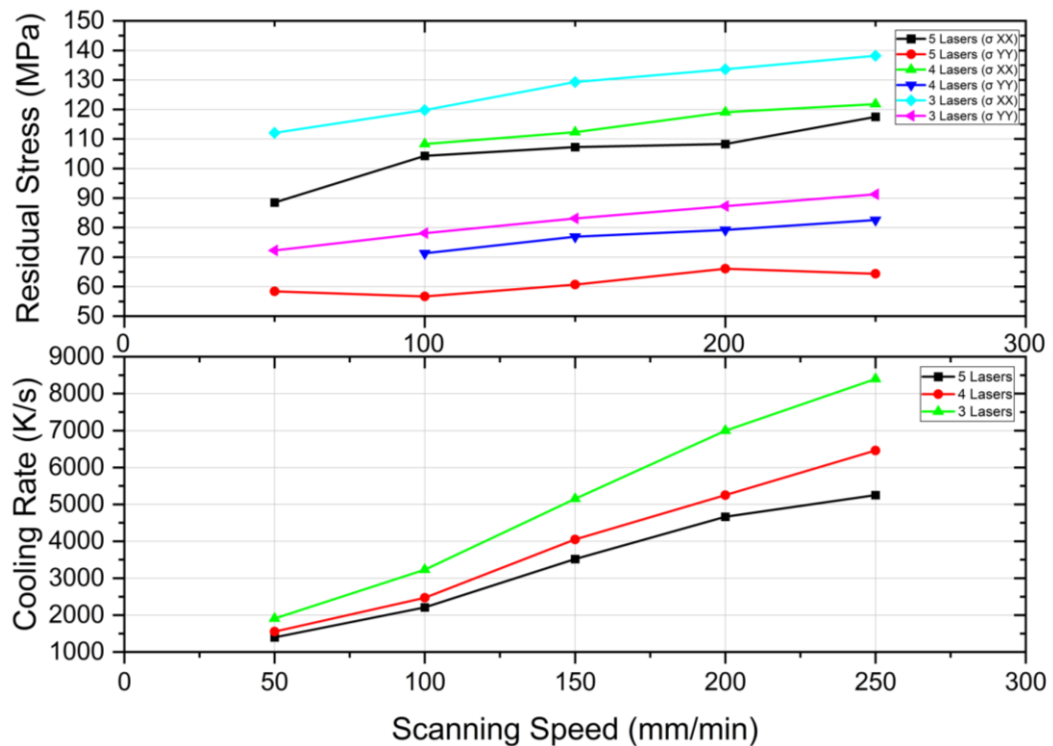


*Figure 6.23: Compares the residual stress in XX and YY direction at various scanning speeds (50 – 250 mm/min) with the cooling rate obtained from FEA analysis.*

Additionally, within the DAM process, all samples exhibit a microstructure that is characterised by both  $\alpha$  and  $\beta$  crystal structures. Grain coarseness varies across different beam configurations and scanning speeds, with scanning speed exerting a more significant influence on grain coarseness than the number of lasers. Pole figure analysis reveals a stronger  $\alpha$  texture compared to the high-temperature  $\beta$  phase, with a notable preference for the  $\{0001\}$  crystallographic orientation in the  $\alpha$  phase. The relationship between  $\alpha$  and  $\beta$  phase texture changes, scanning speed, and the number of lasers is not strongly correlated, and further experiments may be needed to ascertain this relationship with greater certainty.



## 7 Chapter 7: Conclusions and Future Work

### 7.1 Conclusions

This study investigates the behaviour of multi-laser interaction in Diode Area Melting (DAM) of Ti6Al4V, focusing on the activation of each laser beam within a single array at varying scanning speeds. Given that DAM is a relatively recent technique, there has been limited exploration into laser simulation with individually controlled diode laser beams. This research introduces both analytical and Finite Element Method (FEM) models to predict melt pool characteristics and cooling rates. In addition to modelling, a thermal camera was used to extract cooling rate data from the  $\beta$  transus to the martensitic transformation temperature. These empirical data were compared with predictions from the analytical and FEM models, providing a comprehensive understanding of the thermal dynamics in the process. For DAM modelling, the impact of the number of lasers on melt pool size and cooling rate was examined for a linear array of up to six diode lasers. The FEM approach demonstrated more accurate predictions of melt pool width and temperature. The cooling rate for Ti6Al4V from the  $\beta$ -transus to the martensitic transformation temperature was significantly lower than in L-PBF and EB-PBF processes, with a single laser yielding a cooling rate of 778 K/s and six lasers reducing it to 191 K/s. This cooling rate in DAM is approximately  $10^4$  orders of magnitude slower than in conventional L-PBF and comparable to certain casting processes. The reduction in cooling rate saturated with five lasers, with no additional reduction observed with further lasers.

The characteristic of lower cooling rates in DAM appears promising in reducing cooling rate related problems and thereby diminishing residual stresses in manufactured components. Notably, residual stresses in DAM-processed Ti6Al4V materials are significantly lower than those in L-PBF. These stresses are influenced by the number of laser beams and scanning speed adjustments, with the lowest and highest residual stresses recorded at different configurations and speeds. The minimum residual stress ( $\sigma_{yy}$ ) was observed in the Y direction (perpendicular to the laser traverse direction), registering at 58.4 MPa in a setup using 5 lasers with a scanning speed of 50 mm/min. On the other hand, the maximum stress ( $\sigma_{xx}$ ), amounting to 138.2 MPa, was recorded in the X

direction (laser traverse direction) when 3 lasers were operated at a scanning speed of 250 mm/min. The pattern of the result suggests a correlation where the residual stress reduces with the activation of each laser and reduction of scanning speeds.

In this study, detailed EBSD analysis was performed on Ti6Al4V samples, focusing on an area of 250  $\mu\text{m}$  by 250  $\mu\text{m}$  with a 0.1  $\mu\text{m}$  step size for high-resolution mapping. This approach confirmed a consistent basketweave-like  $\alpha$ - $\beta$  microstructure in all samples, with variations in grain coarseness influenced by different laser configurations and scanning speeds. Notably, grain size increased with additional lasers and slower scanning speed, with the greatest impact observed through reducing scanning speed. Pole figures revealed a stronger  $\alpha$  phase texture and a preference for its orientation along the  $\{0001\}$  direction, while the  $\beta$  phase showed significant orientations along the  $\{100\}$  and  $\{111\}$  directions, becoming more pronounced with slower scanning speeds. The phase map further highlighted the distribution of  $\alpha$  and  $\beta$  phases, showing variability in  $\beta$  phase content with no clear dependence on scanning speed or laser number. However, these findings, alongside XRD results indicating differences in  $\beta$  phase intensities, suggest a complex relationship between processing parameters and phase development, pointing to the need for further experiments to fully understand these dynamics.

## 7.2 Key Findings and Recommended Future Work

Key findings from the current study are summarized in *Table 7.1*. These findings reveal extensive opportunities for further development of the DAM methodology. *Table 7.1* also details future work associated with each finding, indicating potential areas for advancement.

Key Finding	Suggested Future Work
<p>An array of fibre-coupled diode lasers, each with a power of up to 4W, can be directly employed in the AM of metallic components. Activating each laser in the array expands the processing area, enabling the melting of larger areas at slower scanning speeds. Current research has successfully demonstrated the use of up to six lasers arranged in a single row within the array.</p>	<p>For future studies, it is advisable to expand this beam configuration to potentially include up to 100 lasers. This expansion would facilitate an evaluation of the throughput and build rate of the DAM process, offering insights into its competitive productivity relative to L-PBF.</p>

<p>Data derived from thermal camera measurements reveal that employing a single laser beam in DAM yielded a cooling rate of 778 K/s. When the setup was expanded to include six lasers, the cooling rate reduced significantly to 191 K/s. This rate of cooling in DAM is notably slower—approximately <math>10^4</math> orders of magnitude—compared to conventional L-PBF. Additionally, it was observed that the reduction in cooling rate reached a saturation point upon the integration of five lasers; subsequent addition of lasers did not result in further reductions in cooling rate.</p>	<p>Future work could explore adding multiple rows in the laser head array during the DAM process to better control the cooling rate. Utilising separate arrays for pre-heating, post-heating, and melting could enhance thermal management and improve component quality. This modification in laser configuration represents a promising area for further research in DAM technology.</p>
<p>Analytical and FEM models were developed to simulate the DAM process. The analytical solution provided quick estimates of melt pool width and temperature distribution around the melt pool but exhibited limitations in accuracy. FEM was well-suited for predicting melt pool width and depth and provided detailed information on temperature distribution. Although the models were not entirely accurate in predicting the cooling rate, the rate of change in cooling rate from one laser configuration and scanning speed to another showed a useful trend. This trend was useful in correlating cooling rate with residual stress formation, enhancing our understanding of these relationships.</p>	<p>It is essential to address the limitations of the current analytical and FEM methods, which do not adequately capture important phenomena such as Marangoni convective flow and phase changes during laser and powder material interaction. This necessitates the use of advanced tools like Computational Fluid Dynamics (CFD). It is recommended to employ an advanced CFD method, such as Laser Beamform as mentioned in Chapter 2, Section 2.6, to simulate the DAM process. Additionally, it has been observed that simulating DAM requires substantial computational time. Therefore, an optimised CFD solution should be used to better understand the dynamics and accurately predict cooling rates and thermal gradients during the DAM process.</p>
<p>Process parameters of DAM, such as laser beam profile (including spot spacing and dimensions), particle size distribution, emissivity, and conductivity of the powder, as well as laser power and scanning speed, significantly influence the morphology of melted single tracks and single layers, as well as the microstructure and surface roughness of DAM components.</p>	<p>Other process parameters that could be investigated include preheating temperatures and scanning strategies, such as the length of scanning vectors and the variable power of individual beams within the line-shaped multi-beam for overall beam intensity control. Additionally, the study of multiple layers and the mechanical properties of the 3D parts produced by DAM is essential to further understand and optimise the process.</p>
<p>It has been determined that the DAM technique allows for the near-net shaping and processing of Ti6Al4V using several low-power diode laser beams, which are individually addressable and non-deflected, to scan in parallel and selectively melt material from a powder bed. In the DAM processing of Ti6Al4V, the cooling rates are significantly reduced compared to those in L-PBF. Consequently, this results in the formation of <math>\beta</math>-grains within the samples, a phenomenon not achievable with L-PBF.</p>	<p>Future research should focus on refining the DAM process parameters popular engineering materials such as Inconel 718, stainless steels, and aluminium alloys. The preliminary experiments with Inconel 718 have revealed balling effects in several samples, indicating the need for a comprehensive analysis to determine the optimal processing parameters, which will extend the applicability of</p>

	DAM technology to a wider range of materials.
Residual stress measurements in this study focused on single-layer analyses of DAM-processed Ti6Al4V materials, which exhibited significantly lower residual stresses compared to those processed by L-PBF. A strong correlation was observed between residual stress and cooling rate, as derived from FEM simulations; a decrease in cooling rate corresponded with reduced residual stress.	For future work, it is strongly recommended to extend this study to multi-laser configurations along the build direction to observe how residual stress evolves during the construction of 3D shapes. Additionally, implementing in-situ monitoring of temperature evolution using a thermal camera could provide accurate temperature gradients. These gradients can be correlated with residual stress measurements to deepen our understanding of these dynamics in the DMA process.

*Table 7.1: The key findings of the current research and suggested areas for future work to advance DAM development.*

### 7.3 Summary

The unique attributes of DAM, such as lower residual stress, lower cooling rates, and enhanced area processing capabilities, position it as a potentially innovative approach within the L-PBF landscape, offering distinct advantages and new opportunities compared to the existing capabilities of L-PBF. A principal advantage of DAM is its capacity to process broader areas using multiple lasers. For instance, in a five-laser DAM configuration, the beam width extends to 370  $\mu\text{m}$ , significantly wider than in L-PBF. Expanding the process to include hundreds of diode lasers enables the coverage of millimetre-scale lengths, expanding area coverage and enhancing process efficiency. The ability to process wider areas with DAM can significantly increase the throughput of manufacturing processes, making it a more time-efficient and cost-effective solution for large-scale production.

With its inherently low residual stress and lower cooling rates, coupled with the capability to process wider areas, DAM offers distinct advantages over L-PBF. The low residual stress characteristic of DAM reduces the need for post-processing treatments, which are often necessary in L-PBF to relieve stresses and improve material properties. Additionally, DAM's lower scanning speeds result in reduced spattering, further enhancing the quality of the final product by leading to smoother surfaces and more precise geometries.

In summary, these unique attributes of DAM position it as a potentially revolutionary approach within the additive manufacturing landscape, offering distinct advantages and new opportunities compared to the existing capabilities of L-PBF.

\*\*\*

## References

- [1] I. Yadroitsev, I. Yadroitsava, and L. Mugwagwa, "Fundamentals of Laser Powder Bed Fusion of Metals," Elsevier, 2021, pp. 456–486.
- [2] S. Liu and Y. C. Shin, "Additive manufacturing of Ti6Al4V alloy: A review," *Mater Design*, vol. 164, p. 107552, 2019, doi: 10.1016/j.matdes.2018.107552.
- [3] M. G. Moletsane, P. Krakhmalev, N. Kazantseva, A. du Plessis, I. Yadroitsava, and I. Yadroitsev, "TENSILE PROPERTIES AND MICROSTRUCTURE OF DIRECT METAL LASER-SINTERED Ti6Al4V (ELI) ALLOY," *S. Afr. J. Ind. Eng.*, vol. 27, no. 3, pp. 110–121, 2016, doi: 10.7166/27-3-1667.
- [4] M. Zavala-Arredondo, K. M. Groom, and K. Mumtaz, "Diode area melting single-layer parametric analysis of 316L stainless steel powder," *Int J Adv Manuf Technology*, vol. 94, no. 5–8, pp. 2563–2576, 2018, doi: 10.1007/s00170-017-1040-4.
- [5] M. Zavala-Arredondo, H. Ali, K. M. Groom, and K. Mumtaz, "Investigating the melt pool properties and thermal effects of multi-laser diode area melting," *Int J Adv Manuf Technology*, vol. 97, no. 1–4, pp. 1383–1396, 2018, doi: 10.1007/s00170-018-2038-2.
- [6] M. Alsaddah, A. Khan, K. Groom, and K. Mumtaz, "Diode area melting of Ti6Al4V using 808 nm laser sources and variable multi-beam profiles," *Mater Design*, vol. 215, no. Phys. Proc. 12 2011, p. 110518, 2022, doi: 10.1016/j.matdes.2022.110518.
- [7] B.-A. Schuelke-Leech, "A model for understanding the orders of magnitude of disruptive technologies," *Technol. Forecast. Soc. Chang.*, vol. 129, pp. 261–274, 2018, doi: 10.1016/j.techfore.2017.09.033.
- [8] G. V. Overwalle and R. Leys, "3D Printing and Patent Law: A Disruptive Technology Disrupting Patent Law?," *Iic - Int Rev Intellect Prop Competition Law*, vol. 48, no. 5, pp. 504–537, 2017, doi: 10.1007/s40319-017-0602-1.
- [9] D. Mies, W. Marsden, and S. Warde, "Overview of Additive Manufacturing Informatics: 'A Digital Thread,'" *Integrating Mater Manuf Innovation*, vol. 5, no. 1, p. 6, 2016, doi: 10.1186/s40192-016-0050-7.
- [10] S. Afazov *et al.*, "Metal powder bed fusion process chains: an overview of modelling techniques," *Prog. Addit. Manuf.*, vol. 7, no. 2, pp. 289–314, 2022, doi: 10.1007/s40964-021-00230-1.
- [11] B. S. Institute, "BS EN ISO/ASTM 52900:2021: Additive manufacturing — General principles — Fundamentals and vocabulary." 2022.

- [12] T. DebRoy *et al.*, "Additive manufacturing of metallic components – Process, structure and properties," *Prog Mater Sci*, vol. 92, pp. 112–224, 2018, doi: 10.1016/j.pmatsci.2017.10.001.
- [13] M. Brandt, *Laser Additive Manufacturing*. 2017. doi: 10.1016/b978-0-08-100433-3.02001-7.
- [14] B. Dutta and F. H. (Sam) Froes, "The Additive Manufacturing (AM) of titanium alloys," *Met. Powder Rep.*, vol. 72, no. 2, pp. 96–106, 2017, doi: 10.1016/j.mprp.2016.12.062.
- [15] L. Xiao, W. Song, M. Hu, and P. Li, "Compressive properties and micro-structural characteristics of Ti–6Al–4V fabricated by electron beam melting and selective laser melting," *Mater Sci Eng*, vol. 764, p. 138204, 2019, doi: 10.1016/j.msea.2019.138204.
- [16] I. Yadroitsev, "Selective laser melting: Direct manufacturing of 3D-objects by selective laser melting of metal powders," LAP LAMBERT Academic Publishing, 2009, pp. 229–238.
- [17] F. Trevisan *et al.*, "On the Selective Laser Melting (SLM) of the AlSi10Mg Alloy: Process, Microstructure, and Mechanical Properties," *Materials*, vol. 10, no. 1, p. 76, 2017, doi: 10.3390/ma10010076.
- [18] B. Zhang, L. Dembinski, and C. Coddet, "The study of the laser parameters and environment variables effect on mechanical properties of high compact parts elaborated by selective laser melting 316L powder," *Mater Sci Eng*, vol. 584, pp. 21–31, 2013, doi: 10.1016/j.msea.2013.06.055.
- [19] G. Zhang *et al.*, "Element Vaporization of Ti-6Al-4V Alloy during Selective Laser Melting," *Metals-basel*, vol. 10, no. 4, p. 435, 2020, doi: 10.3390/met10040435.
- [20] I.C.Noyan and J. B. Cohen, *Residual Stress*, vol. 1. 1987.
- [21] H. Ali, H. Ghadbeigi, and K. Mumtaz, "Residual stress development in selective laser-melted Ti6Al4V: a parametric thermal modelling approach," *Int J Adv Manuf Technology*, vol. 97, no. 5–8, pp. 2621–2633, 2018, doi: 10.1007/s00170-018-2104-9.
- [22] I. Yadroitsava, S. Grewar, D. Hattingh, and I. Yadroitsev, "Residual Stress in SLM Ti6Al4V Alloy Specimens," *Mater. Sci. Forum*, vol. 828–829, pp. 305–310, 2015, doi: 10.4028/www.scientific.net/msf.828-829.305.
- [23] P. J. Withers and H. K. D. H. Bhadeshia, "Residual stress. Part 1 – Measurement techniques," *Mater Sci Tech Ser*, vol. 17, no. 4, pp. 355–365, 2001, doi: 10.1179/026708301101509980.
- [24] J. J. Beaman, D. L. Bourell, C. C. Seepersad, and D. Kovar, "Additive Manufacturing Review: Early Past to Current Practice," *J. Manuf. Sci. Eng.*, vol. 142, no. 11, 2020, doi: 10.1115/1.4048193.

- [25] R. Poprawe, K. Boucke, and D. Hoffman, *Tailored Light 1: High Power Lasers for Production*. Springer.
- [26] M. Zavala-Arredondo *et al.*, "Laser diode area melting for high speed additive manufacturing of metallic components," *Mater Design*, vol. 117, pp. 305–315, 2017, doi: 10.1016/j.matdes.2016.12.095.
- [27] C. Hinke *et al.*, "Additive Manufacturing: Perspectives for Diode Lasers," *2015 IEEE High Power Diode Lasers Syst. Conf. (HPD)*, pp. 39–40, 2015, doi: 10.1109/hpd.2015.7439684.
- [28] Y. Gu, H. Lu, Y. Fu, and Y. Cui, "High Power High Efficiency Diode Laser Stack for Processing," *IOP Conf. Ser.: Mater. Sci. Eng.*, vol. 317, no. 1, p. 012008, 2018, doi: 10.1088/1757-899x/317/1/012008.
- [29] J. Karp, V. Ostroverkhov, D. Bogdan, M. Graham, B. Mccarthy, and W. Carter, "Area melting with multi-laser arrays to increase build rate for metal powder bed fusion additive manufacturing," vol. 10909, p. 1090909, 2019, doi: 10.1117/12.2513892.
- [30] M. J. Matthews *et al.*, "Diode-based additive manufacturing of metals using an optically-addressable light valve," *Opt. Express*, vol. 25, no. 10, p. 11788, 2017, doi: 10.1364/oe.25.011788.
- [31] L. A. Coldren, S. W. Corzine, and M. L. Masanovic, "Diode Lasers and Photonic Integrated Circuits," 2nd, Ed., Wiley, 2012, pp. 1–44.
- [32] L. Li, "The advances and characteristics of high-power diode laser materials processing," *Opt. Lasers Eng.*, vol. 34, no. 4–6, pp. 231–253, 2000, doi: 10.1016/s0143-8166(00)00066-x.
- [33] S. Hengesbach *et al.*, "Brightness and average power as driver for advancements in diode lasers and their applications," pp. 93480B-93480B–18, 2015, doi: 10.1117/12.2085068.
- [34] Z.-N. Tian *et al.*, "Beam shaping of edge-emitting diode lasers using a single double-axial hyperboloidal micro-lens," *Opt Lett*, vol. 38, no. 24, p. 5414, 2013, doi: 10.1364/ol.38.005414.
- [35] B. Cheng, J. Lydon, K. Cooper, V. Cole, P. Northrop, and K. Chou, "Melt pool sensing and size analysis in laser powder-bed metal additive manufacturing," *J Manuf Process*, vol. 32, pp. 744–753, 2018, doi: 10.1016/j.jmapro.2018.04.002.
- [36] J. L. Bartlett, F. M. Heim, Y. V. Murty, and X. Li, "In situ defect detection in selective laser melting via full-field infrared thermography," *Addit Manuf*, vol. 24, pp. 595–605, 2018, doi: 10.1016/j.addma.2018.10.045.
- [37] R. Wester, "Tailored Light 2," Rein, Ed., Springer-Verlag GmbH Germany, 2011, pp. 23–30.



- [38] M. Alsaddah, A. Khan, K. Groom, and K. Mumtaz, "Use of 450-808 nm diode lasers for efficient energy absorption during powder bed fusion of Ti6Al4V," *Int J Adv Manuf Technology*, pp. 1–20, 2021, doi: 10.1007/s00170-021-06774-4.
- [39] J. C. Ion, "Laser Processing of Engineering Materials," no. Lasers in Medical Science11986, pp. 188–199, 2005, doi: 10.1016/b978-075066079-2/50010-6.
- [40] J. Ciurana, L. Hernandez, and J. Delgado, "Energy density analysis on single tracks formed by selective laser melting with CoCrMo powder material," *Int J Adv Manuf Technology*, vol. 68, no. 5–8, pp. 1103–1110, 2013, doi: 10.1007/s00170-013-4902-4.
- [41] C. Y. Yap, C. K. Chua, and Z. L. Dong, "An effective analytical model of selective laser melting," *Virtual Phys Prototyp*, vol. 11, no. 1, pp. 21–26, 2016, doi: 10.1080/17452759.2015.1133217.
- [42] M. Zavala-Arredondo *et al.*, "Use of power factor and specific point energy as design parameters in laser powder-bed-fusion (L-PBF) of AlSi10Mg alloy," *Mater Design*, vol. 182, p. 108018, 2019, doi: 10.1016/j.matdes.2019.108018.
- [43] U. S. Bertoli, A. J. Wolfer, M. J. Matthews, J.-P. R. Delplanque, and J. M. Schoenung, "On the limitations of Volumetric Energy Density as a design parameter for Selective Laser Melting," *Mater Design*, vol. 113, pp. 331–340, 2017, doi: 10.1016/j.matdes.2016.10.037.
- [44] R. Wester, "Tailored Light 2," 2011, pp. 93–100.
- [45] S. A. Khairallah, A. T. Anderson, A. Rubenchik, and W. E. King, "Laser powder-bed fusion additive manufacturing: Physics of complex melt flow and formation mechanisms of pores, spatter, and denudation zones," *Acta Mater*, vol. 108, pp. 36–45, 2016, doi: 10.1016/j.actamat.2016.02.014.
- [46] C. X. Zhao *et al.*, "The effect of oxygen on transitional Marangoni flow in laser spot welding," *Acta Mater*, vol. 58, no. 19, pp. 6345–6357, 2010, doi: 10.1016/j.actamat.2010.07.056.
- [47] J. Coleman *et al.*, "Sensitivity of Thermal Predictions to Uncertain Surface Tension Data in Laser Additive Manufacturing," *J. Heat Transf.*, vol. 142, no. 12, 2020, doi: 10.1115/1.4047916.
- [48] I. Yadroitsev, I. Yadroitsava, P. Bertrand, and I. Smurov, "Factor analysis of selective laser melting process parameters and geometrical characteristics of synthesized single tracks," *Rapid Prototyp. J.*, vol. 18, no. 3, pp. 201–208, 2012, doi: 10.1108/13552541211218117.
- [49] V. Gunenthiram, P. Peyre, M. Schneider, M. Dal, F. Coste, and R. Fabbro, "Analysis of laser–melt pool–powder bed interaction during the selective laser melting of a stainless steel," *J. Laser Appl.*, vol. 29, no. 2, p. 022303, 2017, doi: 10.2351/1.4983259.

- [50] I. Yadroitsev, A. Gusarov, I. Yadroitsava, and I. Smurov, "Single track formation in selective laser melting of metal powders," *J. Mater. Process. Technol.*, vol. 210, no. 12, pp. 1624–1631, 2010, doi: 10.1016/j.jmatprotec.2010.05.010.
- [51] P. Bidare, I. Bitharas, R. M. Ward, M. M. Attallah, and A. J. Moore, "Fluid and particle dynamics in laser powder bed fusion," *Acta Mater.*, vol. 142, pp. 107–120, 2018, doi: 10.1016/j.actamat.2017.09.051.
- [52] U. S. Bertoli, A. J. Wolfer, M. J. Matthews, J.-P. R. Delplanque, and J. M. Schoenung, "On the limitations of Volumetric Energy Density as a design parameter for Selective Laser Melting," *Mater Design*, vol. 113, pp. 331–340, 2017, doi: 10.1016/j.matdes.2016.10.037.
- [53] W. King, A. T. Anderson, R. M. Ferencz, N. E. Hodge, C. Kamath, and S. A. Khairallah, "Overview of modelling and simulation of metal powder bed fusion process at Lawrence Livermore National Laboratory," *Mater. Sci. Technol.*, vol. 31, no. 8, pp. 957–968, 2015, doi: 10.1179/1743284714y.0000000728.
- [54] A. Raghavan, H. L. Wei, T. A. Palmer, and T. DebRoy, "Heat transfer and fluid flow in additive manufacturing," *J Laser Appl*, vol. 25, no. 5, p. 052006, 2013, doi: 10.2351/1.4817788.
- [55] V. Manvatkar, A. De, and T. DebRoy, "Spatial variation of melt pool geometry, peak temperature and solidification parameters during laser assisted additive manufacturing process," *Mater Sci Tech Ser*, vol. 31, no. 8, pp. 924–930, 2015, doi: 10.1179/1743284714y.0000000701.
- [56] M. Bayat *et al.*, "Keyhole-induced porosities in Laser-based Powder Bed Fusion (L-PBF) of Ti6Al4V: High-fidelity modelling and experimental validation," *Addit Manuf*, vol. 30, p. 100835, 2019, doi: 10.1016/j.addma.2019.100835.
- [57] T. F. Flint, J. D. Robson, G. Parivendhan, and P. Cardiff, "laserbeamFoam: Laser ray-tracing and thermally induced state transition simulation toolkit," *Softwarex*, vol. 21, p. 101299, 2023, doi: 10.1016/j.softx.2022.101299.
- [58] A. Bandyopadhyay and K. D. Traxel, "Invited Review Article: Metal-additive manufacturing — Modeling strategies for application-optimized designs," *Addit Manuf*, vol. 22, pp. 758–774, 2018, doi: 10.1016/j.addma.2018.06.024.
- [59] M. Chiumenti *et al.*, "Numerical modelling and experimental validation in Selective Laser Melting," *Addit Manuf*, vol. 18, pp. 171–185, 2017, doi: 10.1016/j.addma.2017.09.002.
- [60] B. Song, S. Dong, H. Liao, and C. Coddet, "Process parameter selection for selective laser melting of Ti6Al4V based on temperature distribution simulation and experimental sintering," *Int J Adv Manuf Technology*, vol. 61, no. 9–12, pp. 967–974, 2012, doi: 10.1007/s00170-011-3776-6.

- [61] F. H. Harlow and J. E. Welch, "Numerical Calculation of Time-Dependent Viscous Incompressible Flow of Fluid with Free Surface," *Phys. Fluids*, vol. 8, no. 12, p. 2182, 1965, doi: 10.1063/1.1761178.
- [62] P. E. R. Lopez, P. N. Jalali, J. Björkvall, U. Sjöström, and C. Nilsson, "Recent Developments of a Numerical Model for Continuous Casting of Steel: Model Theory, Setup and Comparison to Physical Modelling with Liquid Metal," *ISIJ Int.*, vol. 54, no. 2, pp. 342–350, 2014, doi: 10.2355/isijinternational.54.342.
- [63] X. Yin, I. Zarikos, N. K. Karadimitriou, A. Raoof, and S. M. Hassanizadeh, "Direct simulations of two-phase flow experiments of different geometry complexities using Volume-of-Fluid (VOF) method," *Chem. Eng. Sci.*, vol. 195, pp. 820–827, 2019, doi: 10.1016/j.ces.2018.10.029.
- [64] M. Khorasani *et al.*, "A comprehensive study on melt pool depth in laser-based powder bed fusion of Inconel 718," *Int J Adv Manuf Technology*, vol. 120, no. 3–4, pp. 2345–2362, 2022, doi: 10.1007/s00170-021-08618-7.
- [65] S. D. Nath, G. Gupta, M. Kearns, O. Gulsoy, and S. V. Atre, "Effects of layer thickness in laser-powder bed fusion of 420 stainless steel," *Rapid Prototyp. J.*, vol. 26, no. 7, pp. 1197–1208, 2020, doi: 10.1108/rpj-10-2019-0279.
- [66] Z. Young *et al.*, "Effects of Particle Size Distribution with Efficient Packing on Powder Flowability and Selective Laser Melting Process," *Materials*, vol. 15, no. 3, p. 705, 2022, doi: 10.3390/ma15030705.
- [67] T. M. Wischeropp, C. Emmelmann, M. Brandt, and A. Pateras, "Measurement of actual powder layer height and packing density in a single layer in selective laser melting," *Addit. Manuf.*, vol. 28, pp. 176–183, 2019, doi: 10.1016/j.addma.2019.04.019.
- [68] Y. S. Lee and W. Zhang, "Modeling of heat transfer, fluid flow and solidification microstructure of nickel-base superalloy fabricated by laser powder bed fusion," *Addit. Manuf.*, vol. 12, pp. 178–188, 2016, doi: 10.1016/j.addma.2016.05.003.
- [69] Y. Huang, M. B. Khamesee, and E. Toyserkani, "A comprehensive analytical model for laser powder-fed additive manufacturing," *Addit Manuf*, vol. 12, pp. 90–99, 2016, doi: 10.1016/j.addma.2016.07.001.
- [70] Y. Huang, M. B. Khamesee, and E. Toyserkani, "A comprehensive analytical model for laser powder-fed additive manufacturing," *Addit Manuf*, vol. 12, pp. 90–99, 2016, doi: 10.1016/j.addma.2016.07.001.
- [71] P. Promoppatum, S.-C. Yao, P. C. Pistorius, and A. D. Rollett, "A Comprehensive Comparison of the Analytical and Numerical Prediction of the Thermal History and Solidification Microstructure of Inconel 718 Products Made by Laser Powder-Bed Fusion," *Engineering-london*, vol. 3, no. 5, pp. 685–694, 2017, doi: 10.1016/j.eng.2017.05.023.

- [72] J. Ning, E. Mirkoohi, Y. Dong, D. E. Sievers, H. Garmestani, and S. Y. Liang, "Analytical modeling of 3D temperature distribution in selective laser melting of Ti-6Al-4V considering part boundary conditions," *J Manuf Process*, vol. 44, pp. 319–326, 2019, doi: 10.1016/j.jmapro.2019.06.013.
- [73] K. S. Kumar, "Analytical Modeling of Temperature Distribution, Peak Temperature, Cooling Rate and Thermal Cycles in a Solid Work Piece Welded by Laser Welding Process," *Procedia Mater. Sci.*, vol. 6, pp. 821–834, 2014, doi: 10.1016/j.mspro.2014.07.099.
- [74] H. Yang, Z. Li, and S. Wang, "The Analytical Prediction of Thermal Distribution and Defect Generation of Inconel 718 by Selective Laser Melting," *Appl Sci*, vol. 10, no. 20, p. 7300, 2020, doi: 10.3390/app10207300.
- [75] R. Ganeriwala and T. I. Zohdi, "A coupled discrete element-finite difference model of selective laser sintering," *Granul Matter*, vol. 18, no. 2, p. 21, 2016, doi: 10.1007/s10035-016-0626-0.
- [76] Y. Woo, T. Hwang, I. Oh, D. Seo, and Y. Moon, "Analysis on selective laser melting of WC-reinforced H13 steel composite powder by finite element method," *Adv Mech Eng*, vol. 11, no. 1, p. 1687814018822200, 2019, doi: 10.1177/1687814018822200.
- [77] B. Schoinochoritis, D. Chantzis, and K. Salonitis, "Simulation of metallic powder bed additive manufacturing processes with the finite element method: A critical review," *Proc Institution Mech Eng Part B J Eng Manuf*, vol. 231, no. 1, pp. 96–117, 2014, doi: 10.1177/0954405414567522.
- [78] D. Yao *et al.*, "Numerical insights on the spreading of practical 316 L stainless steel powder in SLM additive manufacturing," *Powder Technol.*, vol. 390, pp. 197–208, 2021, doi: 10.1016/j.powtec.2021.05.082.
- [79] T. V. Rhijn, W. D. Preez, M. Maringa, and D. Kouprianoff, "An Investigation into the Optimization of the Selective Laser Melting Process Parameters for Ti6Al4V Through Numerical Modelling," *Jom-us*, vol. 75, no. 3, pp. 806–815, 2023, doi: 10.1007/s11837-022-05608-2.
- [80] F. Chen and W. Yan, "High-fidelity modelling of thermal stress for additive manufacturing by linking thermal-fluid and mechanical models," *Mater Design*, vol. 196, p. 109185, 2020, doi: 10.1016/j.matdes.2020.109185.
- [81] H. Zhang *et al.*, "An effective method for large-scale temperature simulation in SLM based on the finite difference," *Numer. Heat Transf., Part A: Appl.*, vol. 83, no. 5, pp. 503–521, 2023, doi: 10.1080/10407782.2022.2093020.
- [82] M. McMillan, M. Leary, and M. Brandt, "Computationally efficient finite difference method for metal additive manufacturing: A reduced-order DFAM tool applied to SLM," *Mater. Des.*, vol. 132, pp. 226–243, 2017, doi: 10.1016/j.matdes.2017.06.058.

- [83] X. He and J. Mazumder, "Transport phenomena during direct metal deposition," *J. Appl. Phys.*, vol. 101, no. 5, p. 053113, 2007, doi: 10.1063/1.2710780.
- [84] S. Wen and Y. C. Shin, "Modeling of transport phenomena during the coaxial laser direct deposition process," *J. Appl. Phys.*, vol. 108, no. 4, p. 044908, 2010, doi: 10.1063/1.3474655.
- [85] J. P. Kruth, L. Froyen, J. V. Vaerenbergh, P. Mercelis, M. Rombouts, and B. Lauwers, "Selective laser melting of iron-based powder," *J Mater Process Tech.*, vol. 149, no. 1–3, pp. 616–622, 2004, doi: 10.1016/j.jmatprotec.2003.11.051.
- [86] Z. Xiao *et al.*, "Study of residual stress in selective laser melting of Ti6Al4V," *Mater Design*, vol. 193, p. 108846, 2020, doi: 10.1016/j.matdes.2020.108846.
- [87] J.-P. Kruth, J. Deckers, E. Yasa, and R. Wauthlé, "Assessing and comparing influencing factors of residual stresses in selective laser melting using a novel analysis method," *Proc. Inst. Mech. Eng., Part B: J. Eng. Manuf.*, vol. 226, no. 6, pp. 980–991, 2012, doi: 10.1177/0954405412437085.
- [88] S. Chen, H. Gao, Y. Zhang, Q. Wu, Z. Gao, and X. Zhou, "Review on residual stresses in metal additive manufacturing: formation mechanisms, parameter dependencies, prediction and control approaches," *J Mater Res Technology*, vol. 17, pp. 2950–2974, 2022, doi: 10.1016/j.jmrt.2022.02.054.
- [89] M. Shiomi, K. Osakada, K. Nakamura, T. Yamashita, and F. Abe, "Residual Stress within Metallic Model Made by Selective Laser Melting Process," *CIRP Ann. - Manuf. Technol.*, vol. 53, no. 1, pp. 195–198, 2004, doi: 10.1016/s0007-8506(07)60677-5.
- [90] H. Ali, L. Ma, H. Ghadbeigi, and K. Mumtaz, "In-situ residual stress reduction, martensitic decomposition and mechanical properties enhancement through high temperature powder bed pre-heating of Selective Laser Melted Ti6Al4V," *Mater. Sci. Eng.: A*, vol. 695, pp. 211–220, 2017, doi: 10.1016/j.msea.2017.04.033.
- [91] A. Saerens, P. V. Houtte, B. Meert, and C. Quaeys, "Assessment of different X-ray stress measuring techniques for thin titanium nitride coatings," *J. Appl. Crystallogr.*, vol. 33, no. 2, pp. 312–322, 2000, doi: 10.1107/s0021889800000145.
- [92] F. Bocquet, P. Gergaud, and O. Thomas, "X-ray diffraction from inhomogeneous thin films of nanometre thickness: modelling and experiment," *J. Appl. Crystallogr.*, vol. 36, no. 1, pp. 154–157, 2003, doi: 10.1107/s0021889802019866.
- [93] T. Miyazaki and T. Sasaki, "A comparison of X-ray stress measurement methods based on the fundamental equation," *J. Appl. Crystallogr.*, vol. 49, no. 2, pp. 426–432, 2016, doi: 10.1107/s1600576716000492.

- [94] B. Wysocki, P. Maj, R. Sitek, J. Buhagiar, K. Kurzydłowski, and W. Świążzkowski, "Laser and Electron Beam Additive Manufacturing Methods of Fabricating Titanium Bone Implants," *Appl. Sci.*, vol. 7, no. 7, p. 657, 2017, doi: 10.3390/app7070657.
- [95] D. Chen *et al.*, "Research on in situ monitoring of selective laser melting: a state of the art review," *Int. J. Adv. Manuf. Technol.*, vol. 113, no. 11–12, pp. 3121–3138, 2021, doi: 10.1007/s00170-020-06432-1.
- [96] M. Khanzadeh, S. Chowdhury, M. A. Tschopp, H. R. Doude, M. Marufuzzaman, and L. Bian, "In-situ monitoring of melt pool images for porosity prediction in directed energy deposition processes," *Iise Transactions*, vol. 51, no. 5, pp. 437–455, 2019, doi: 10.1080/24725854.2017.1417656.
- [97] C. L. and M. Peters, *Titanium and Titanium Alloys : Fundamentals and Applications*. WILEY-VCH GmbH & Co. KGaA, 2003.
- [98] Lütjering and G. and J. C. Williams, "Titanium," 2nd, Ed., Springer, 2007, pp. 26–50.
- [99] T. Ahmed and H. J. Rack, "Phase transformations during cooling in  $\alpha+\beta$  titanium alloys," *Mater. Sci. Eng.: A*, vol. 243, no. 1–2, pp. 206–211, 1998, doi: 10.1016/s0921-5093(97)00802-2.
- [100] B. Vrancken, L. Thijs, J.-P. Kruth, and J. V. Humbeeck, "Heat treatment of Ti6Al4V produced by Selective Laser Melting: Microstructure and mechanical properties," *J. Alloy. Compd.*, vol. 541, pp. 177–185, 2012, doi: 10.1016/j.jallcom.2012.07.022.
- [101] S. S. Al-Bermani, M. L. Blackmore, W. Zhang, and I. Todd, "The Origin of Microstructural Diversity, Texture, and Mechanical Properties in Electron Beam Melted Ti-6Al-4V," *Metallurgical Mater Transactions*, vol. 41, no. 13, pp. 3422–3434, 2010, doi: 10.1007/s11661-010-0397-x.
- [102] S. Price, B. Cheng, J. Lydon, K. Cooper, and K. Chou, "On Process Temperature in Powder-Bed Electron Beam Additive Manufacturing: Process Parameter Effects," *J Manuf Sci Eng*, vol. 136, no. 6, p. 061019, 2014, doi: 10.1115/1.4028485.
- [103] B. Wysocki, P. Maj, R. Sitek, J. Buhagiar, K. Kurzydłowski, and W. Świążzkowski, "Laser and Electron Beam Additive Manufacturing Methods of Fabricating Titanium Bone Implants," *Appl Sci*, vol. 7, no. 7, p. 657, 2017, doi: 10.3390/app7070657.
- [104] M. J. Bermingham, S. D. McDonald, M. S. Dargusch, and D. H. StJohn, "Grain-refinement mechanisms in titanium alloys," *J Mater Res*, vol. 23, no. 1, pp. 97–104, 2008, doi: 10.1557/jmr.2008.0002.
- [105] P. A. Kobryn and S. L. Semiatin, "Microstructure and texture evolution during solidification processing of Ti–6Al–4V," *J Mater Process Tech*, vol. 135, no. 2–3, pp. 330–339, 2003, doi: 10.1016/s0924-0136(02)00865-8.

- [106] S. Yamamoto *et al.*, "Melting and solidification behavior of Ti-6Al-4V powder during selective laser melting," *Int J Adv Manuf Technology*, vol. 103, no. 9–12, pp. 4433–4442, 2019, doi: 10.1007/s00170-019-03384-z.
- [107] E. Mirkoohi, D. E. Seivers, H. Garmestani, and S. Y. Liang, "Heat Source Modeling in Selective Laser Melting," *Materials*, vol. 12, no. 13, p. 2052, 2019, doi: 10.3390/ma12132052.
- [108] T. Chande and J. Mazumder, "Estimating effects of processing conditions and variable properties upon pool shape, cooling rates, and absorption coefficient in laser welding," *J. Appl. Phys.*, vol. 56, no. 7, pp. 1981–1986, 1984, doi: 10.1063/1.334231.
- [109] K. C. Mills, "Recommended Values of Thermophysical Properties for Selected Commercial Alloys," in *Recommended Values of Thermophysical Properties for Selected Commercial Alloys*, Woodhead Publishing Ltd and ASM International, 2002, pp. 205–211.
- [110] I. Yadroitsev, P. Krakhmalev, and I. Yadroitsava, "Selective laser melting of Ti6Al4V alloy for biomedical applications: Temperature monitoring and microstructural evolution," *J Alloy Compd*, vol. 583, pp. 404–409, 2014, doi: 10.1016/j.jallcom.2013.08.183.
- [111] R. Zhang, L. Guessous, and G. C. Barber, "Investigation of the Validity of the Carslaw and Jaeger Thermal Theory under Different Working Conditions," *Tribol. Trans.*, vol. 55, no. 1, pp. 1–11, 2012, doi: 10.1080/10402004.2011.606961.
- [112] M. Tang, P. C. Pistorius, S. Narra, and J. L. Beuth, "Rapid Solidification: Selective Laser Melting of AlSi10Mg," *Jom-us*, vol. 68, no. 3, pp. 960–966, 2016, doi: 10.1007/s11837-015-1763-3.
- [113] A. Plotkowski, M. M. Kirka, and S. S. Babu, "Verification and validation of a rapid heat transfer calculation methodology for transient melt pool solidification conditions in powder bed metal additive manufacturing," *Addit Manuf*, vol. 18, pp. 256–268, 2017, doi: 10.1016/j.addma.2017.10.017.
- [114] E. Kannatey-Asibu, "Principles of Laser Materials Processing," Wiley, pp. 238–253.
- [115] J. Mazumder and W. M. Steen, "Heat transfer model for cw laser material processing," *J Appl Phys*, vol. 51, no. 2, pp. 941–947, 1980, doi: 10.1063/1.327672.
- [116] T. F. Flint, G. Parivendhan, A. Ivankovic, M. C. Smith, and P. Cardiff, "beamWeldFoam: Numerical simulation of high energy density fusion and vapourisation-inducing processes," *Softwarex*, vol. 18, p. 101065, 2022, doi: 10.1016/j.softx.2022.101065.
- [117] Y. S. Lee and W. Zhang, "Modeling of heat transfer, fluid flow and solidification microstructure of nickel-base superalloy fabricated by laser

powder bed fusion," *Addit Manuf*, vol. 12, pp. 178–188, 2016, doi: 10.1016/j.addma.2016.05.003.

[118] M. Markl and C. Körner, "Multiscale Modeling of Powder Bed--Based Additive Manufacturing," *Annu Rev Mater Res*, vol. 46, no. 1, pp. 1–31, 2015, doi: 10.1146/annurev-matsci-070115-032158.

[119] H. Caglar, A. Liang, K. Groom, and K. Mumtaz, "Multi-laser powder bed fusion of Ti6Al4V: Diode area melting utilizing low-power 450 nm diode lasers," *J. Mater. Process. Technol.*, vol. 325, p. 118303, 2024, doi: 10.1016/j.jmatprotec.2024.118303.

[120] H. Mizukami, Y. Shirai, A. Kawakami, and A. Mitchell, "Solidification Behavior of Ti-6Al-4V Alloy," *ISIJ Int.*, vol. 60, no. 11, pp. 2455–2461, 2020, doi: 10.2355/isijinternational.isijint-2020-089.

[121] F. Xiong, Z. Gan, J. Chen, and Y. Lian, "Evaluate the effect of melt pool convection on grain structure of IN625 in laser melting process using experimentally validated process-structure modeling," *J. Mater. Process. Technol.*, vol. 303, p. 117538, 2022, doi: 10.1016/j.jmatprotec.2022.117538.

[122] V. Manvatkar, A. De, and T. DebRoy, "Heat transfer and material flow during laser assisted multi-layer additive manufacturing," *J Appl Phys*, vol. 116, no. 12, p. 124905, 2014, doi: 10.1063/1.4896751.

[123] V. Manvatkar, A. De, and T. DebRoy, "Spatial variation of melt pool geometry, peak temperature and solidification parameters during laser assisted additive manufacturing process," *Mater. Sci. Technol.*, vol. 31, no. 8, pp. 924–930, 2015, doi: 10.1179/1743284714y.0000000701.

[124] F. Brückner, D. Lepski, and E. Beyer, "Modeling the Influence of Process Parameters and Additional Heat Sources on Residual Stresses in Laser Cladding," *J. Therm. Spray Technol.*, vol. 16, no. 3, pp. 355–373, 2007, doi: 10.1007/s11666-007-9026-7.

[125] I. Yadroitsev and I. Yadroitsava, "Evaluation of residual stress in stainless steel 316L and Ti6Al4V samples produced by selective laser melting," *Virtual Phys Prototyp*, vol. 10, no. 2, pp. 67–76, 2015, doi: 10.1080/17452759.2015.1026045.

[126] B. Cheng, S. Shrestha, and K. Chou, "Stress and deformation evaluations of scanning strategy effect in selective laser melting," *Addit. Manuf.*, vol. 12, pp. 240–251, 2016, doi: 10.1016/j.addma.2016.05.007.

[127] M. F. Zaeh and G. Branner, "Investigations on residual stresses and deformations in selective laser melting," *Prod. Eng.*, vol. 4, no. 1, pp. 35–45, 2010, doi: 10.1007/s11740-009-0192-y.

[128] A. V. Gusarov, M. Pavlov, and I. Smurov, "Residual Stresses at Laser Surface Remelting and Additive Manufacturing," *Phys. Procedia*, vol. 12, pp. 248–254, 2011, doi: 10.1016/j.phpro.2011.03.032.



- [129] I. Yadroitsev and I. Yadroitsava, "Evaluation of residual stress in stainless steel 316L and Ti6Al4V samples produced by selective laser melting," *Virtual Phys. Prototyp.*, vol. 10, no. 2, pp. 67–76, 2015, doi: 10.1080/17452759.2015.1026045.
- [130] P. Edwards and M. Ramulu, "Fatigue performance evaluation of selective laser melted Ti-6Al-4V," *Mater. Sci. Eng.: A*, vol. 598, pp. 327–337, 2014, doi: 10.1016/j.msea.2014.01.041.
- [131] I. van Zyl, I. Yadroitsava, and I. Yadroitsev, "RESIDUAL STRESS IN Ti6Al4V OBJECTS PRODUCED BY DIRECT METAL LASER SINTERING," *S. Afr. J. Ind. Eng.*, vol. 27, no. 4, pp. 134–141, 2016, doi: 10.7166/27-4-1468.
- [132] H. Ali, L. Ma, H. Ghadbeigi, and K. Mumtaz, "In-situ residual stress reduction, martensitic decomposition and mechanical properties enhancement through high temperature powder bed pre-heating of Selective Laser Melted Ti6Al4V," *Mater. Sci. Eng.: A*, vol. 695, pp. 211–220, 2017, doi: 10.1016/j.msea.2017.04.033.
- [133] E. Bemporad *et al.*, "A critical comparison between XRD and FIB residual stress measurement techniques in thin films," *Thin Solid Films*, vol. 572, pp. 224–231, 2014, doi: 10.1016/j.tsf.2014.09.053.
- [134] A. Takase, T. Ishimoto, N. Morita, N. Ikeo, and T. Nakano, "Comparison of Phase Characteristics and Residual Stresses in Ti-6Al-4V Alloy Manufactured by Laser Powder Bed Fusion (L-PBF) and Electron Beam Powder Bed Fusion (EB-PBF) Techniques," *Crystals*, vol. 11, no. 7, p. 796, 2021, doi: 10.3390/cryst11070796.
- [135] Y. Chen *et al.*, "Strategy of Residual Stress Determination on Selective Laser Melted Al Alloy Using XRD," *Materials*, vol. 13, no. 2, p. 451, 2020, doi: 10.3390/ma13020451.
- [136] J. S. R. M, S. P. AVS, N. B. K, and C. U, "Study of residual stresses and distortions from the Ti6Al4V based thin-walled geometries built using LPBF process," *Def. Technol.*, 2023, doi: 10.1016/j.dt.2023.01.002.
- [137] M. F. Sadali, M. Z. Hassan, F. Ahmad, H. Yahaya, and Z. A. Rasid, "Influence of selective laser melting scanning speed parameter on the surface morphology, surface roughness, and micropores for manufactured Ti6Al4V parts," *J. Mater. Res.*, vol. 35, no. 15, pp. 2025–2035, 2020, doi: 10.1557/jmr.2020.84.
- [138] V. Maitra and J. Shi, "Evaluating the Predictability of Surface Roughness of Ti-6Al-4V Alloy from Selective Laser Melting," *Adv. Eng. Mater.*, vol. 25, no. 14, 2023, doi: 10.1002/adem.202300075.
- [139] M. Simonelli, Y. Y. Tse, and C. Tuck, "The formation of  $\alpha + \beta$  microstructure in as-fabricated selective laser melting of Ti-6Al-4V," *J Mater Res*, vol. 29, no. 17, pp. 2028–2035, 2014, doi: 10.1557/jmr.2014.166.

- [140] P. Krakhmalev *et al.*, "Microstructure, Solidification Texture, and Thermal Stability of 316 L Stainless Steel Manufactured by Laser Powder Bed Fusion," *Metals*, vol. 8, no. 8, p. 643, 2018, doi: 10.3390/met8080643.
- [141] H. Ali, H. Ghadbeigi, and K. Mumtaz, "Processing Parameter Effects on Residual Stress and Mechanical Properties of Selective Laser Melted Ti6Al4V," *J Mater Eng Perform*, vol. 27, no. 8, pp. 4059–4068, 2018, doi: 10.1007/s11665-018-3477-5.
- [142] A. S. Wu, D. W. Brown, M. Kumar, G. F. Gallegos, and W. E. King, "An Experimental Investigation into Additive Manufacturing-Induced Residual Stresses in 316L Stainless Steel," *Met. Mater. Trans. A*, vol. 45, no. 13, pp. 6260–6270, 2014, doi: 10.1007/s11661-014-2549-x.
- [143] R. K. Ganeriwala *et al.*, "Evaluation of a thermomechanical model for prediction of residual stress during laser powder bed fusion of Ti-6Al-4V," *Addit Manuf*, vol. 27, pp. 489–502, 2019, doi: 10.1016/j.addma.2019.03.034.
- [144] M. Megahed, H.-W. Mindt, N. N'Dri, H. Duan, and O. Desmaison, "Metal additive-manufacturing process and residual stress modeling," *Integrating Mater Manuf Innovation*, vol. 5, no. 1, pp. 61–93, 2016, doi: 10.1186/s40192-016-0047-2.

## Appendix A: ANSYS ADPL Code

### Moving Gaussian Heat Source

```

/INPUT, HFLUX_func,1
      *DIM, HEAT_FLX1, TABLE,6,22, 1,12
! The last number corresponds to the ID number for the coordinate system.
      !
! Begin of equation:  $Q(x, y, t) = A * \exp(B * ((\{X\} - C)^2 + (\{Y\} - D * \{TIME\} - E)^2) / F + G)$ 
      *SET, HEAT_FLX1(0,0,1), 0.0, -999
      *SET, HEAT_FLX1(2,0,1), 0.0
      *SET, HEAT_FLX1(3,0,1), 0.0
      *SET, HEAT_FLX1(4,0,1), 0.0
      *SET, HEAT_FLX1(5,0,1), 0.0
      *SET, HEAT_FLX1(6,0,1), 0.0
*SET, HEAT_FLX1(0,1,1), 1.0, -1, 0, C, 0, 0, 2           ! "C" x coordinate
      *SET, HEAT_FLX1(0,2,1), 0.0, -2, 0, 1, 2, 2, -1
      *SET, HEAT_FLX1(0,3,1), 0, -1, 0, 2, 0, 0, -2
      *SET, HEAT_FLX1(0,4,1), 0.0, -3, 0, 1, -2, 17, -1
*SET, HEAT_FLX1(0,5,1), 0.0, -1, 0, D, 0, 0, 1           ! "D" laser speed
      *SET, HEAT_FLX1(0,6,1), 0.0, -2, 0, 1, -1, 3, 1
      *SET, HEAT_FLX1(0,7,1), 0.0, -1, 0, 1, 3, 2, -2
      *SET, HEAT_FLX1(0,8,1), 0.0, -2, 0, E, 0, 0, -1           ! "E" y coordinate
      *SET, HEAT_FLX1(0,9,1), 0.0, -4, 0, 1, -1, 2, -2
      *SET, HEAT_FLX1(0,10,1), 0.0, -1, 0, 2, 0, 0, -4
      *SET, HEAT_FLX1(0,11,1), 0.0, -2, 0, 1, -4, 17, -1
      *SET, HEAT_FLX1(0,12,1), 0.0, -1, 0, 1, -3, 1, -2
*SET, HEAT_FLX1(0,13,1), 0.0, -2, 0, F, 0, 0, -1           ! "F" 2*beam radius^2
      *SET, HEAT_FLX1(0,14,1), 0.0, -3, 0, 1, -1, 4, -2
*SET, HEAT_FLX1(0,15,1), 0.0, -1, 0, G, 0, 0, -3           ! "G" absorption*depth=0
      *SET, HEAT_FLX1(0,16,1), 0.0, -2, 0, 1, -3, 1, -1
*SET, HEAT_FLX1(0,17,1), 0.0, -1, 0, B, 0, 0, -2           ! "B" negative sign
      *SET, HEAT_FLX1(0,18,1), 0.0, -3, 0, 1, -1, 3, -2

```

```

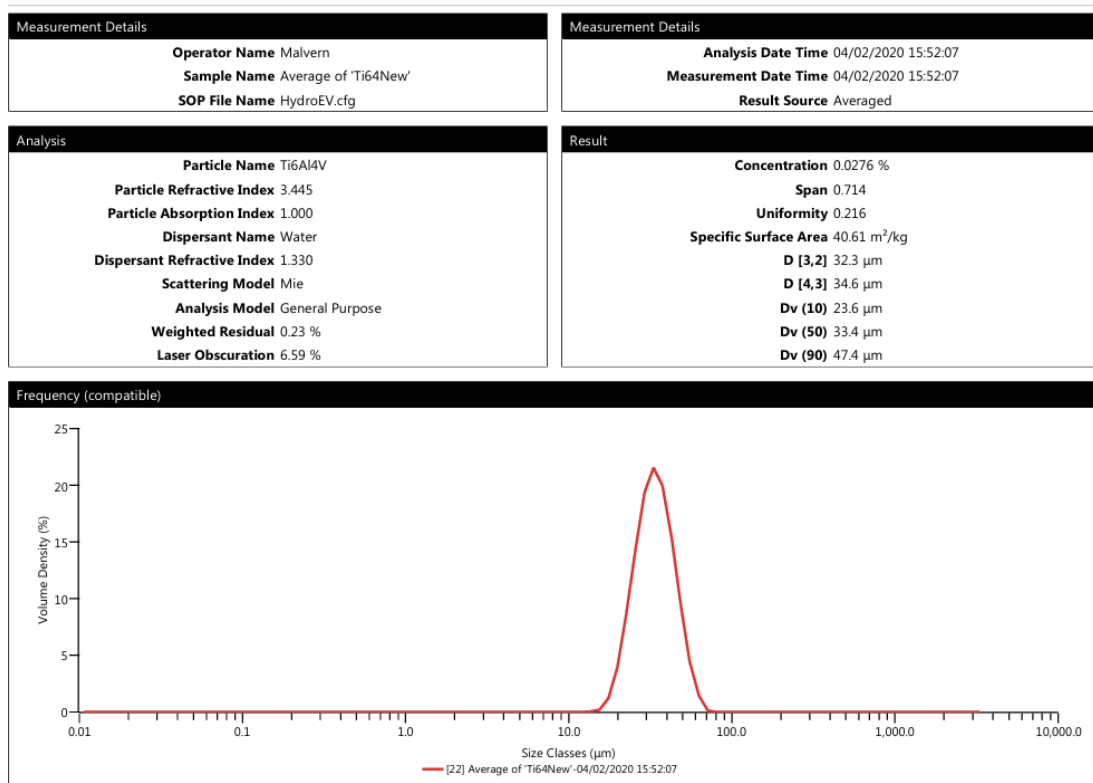
*SET, HEAT_FLX1(0,19,1), 0.0, -1, 7, 1, -3, 0, 0
*SET, HEAT_FLX1(0,20,1), 0.0, -2, 0, A, 0, 0, -1    !"A" Laser power
*SET, HEAT_FLX1(0,21,1), 0.0, -3, 0, 1, -2, 3, -1
*SET, HEAT_FLX1(0,22,1), 0.0, 99, 0, 1, -3, 0, 0
! End of equation: Q (x, y, t)=A*exp(B*(({X}-C)^2+({Y}-D*{TIME}-E)^2)/F+G)
sf, a1,hflux,%HEAT_FLX1% ! Replace a1 with a named selection.

```

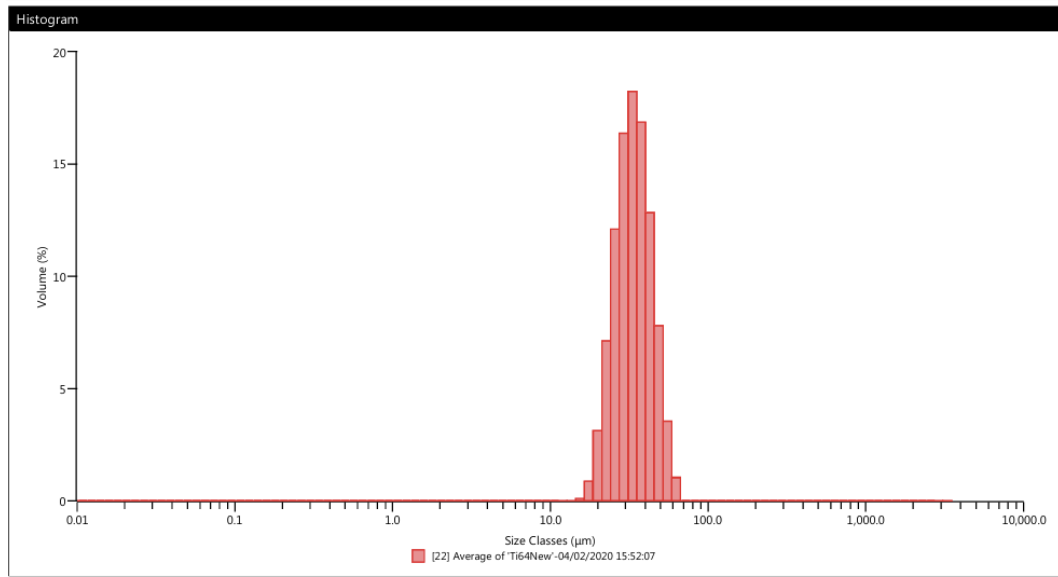
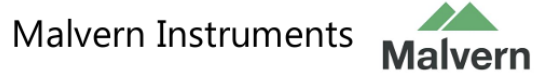
## Appendix B: Ti6Al4V Powder Data

### Analysis

Malvern Instruments

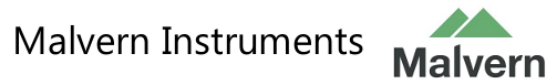


Analysis



Size (µm)	% Volume In	Size (µm)	% Volume In	Size (µm)	% Volume In	Size (µm)	% Volume In	Size (µm)	% Volume In
0.0100	0.00	0.166	0.00	2.75	0.00	45.6	7.80	756	0.00
0.0114	0.00	0.188	0.00	3.12	0.00	51.8	3.54	859	0.00
0.0129	0.00	0.214	0.00	3.55	0.00	58.9	1.04	976	0.00
0.0147	0.00	0.243	0.00	4.03	0.00	66.9	0.00	1110	0.00
0.0167	0.00	0.276	0.00	4.58	0.00	76.0	0.00	1260	0.00
0.0189	0.00	0.314	0.00	5.21	0.00	86.4	0.00	1430	0.00
0.0215	0.00	0.357	0.00	5.92	0.00	98.1	0.00	1630	0.00
0.0244	0.00	0.405	0.00	6.72	0.00	111	0.00	1850	0.00
0.0278	0.00	0.460	0.00	7.64	0.00	127	0.00	2100	0.00
0.0315	0.00	0.523	0.00	8.68	0.00	144	0.00	2390	0.00
0.0358	0.00	0.594	0.00	9.86	0.00	163	0.00	2710	0.00
0.0407	0.00	0.675	0.00	11.2	0.00	186	0.00	3080	0.00
0.0463	0.00	0.767	0.00	12.7	0.00	211	0.00	3500	0.00
0.0526	0.00	0.872	0.00	14.5	0.10	240	0.00		
0.0597	0.00	0.991	0.00	16.4	0.88	272	0.00		
0.0679	0.00	1.13	0.00	18.7	3.13	310	0.00		
0.0771	0.00	1.28	0.00	21.2	7.13	352	0.00		
0.0876	0.00	1.45	0.00	24.1	12.09	400	0.00		
0.0995	0.00	1.65	0.00	27.4	16.37	454	0.00		
0.113	0.00	1.88	0.00	31.1	18.23	516	0.00		
0.128	0.00	2.13	0.00	35.3	16.86	586	0.00		
0.146	0.00	2.42	0.00	40.1	12.83	666	0.00		

Analysis



Trend						
	Record Number	Sample Name	Dx (10) (µm)	Dx (50) (µm)	Dx (90) (µm)	
	22	Average of 'Ti64New'	23.6	33.4	47.4	
Mean			23.6	33.4	47.4	
1xStd Dev			0.00	0.00	0.00	
1xRSD (%)			0.00	0.00	0.00	

Appendix C: COSHH assessment form for Ti6Al4V

Ti6Al4V COSHH ASSESSMENT FORM





Reference no: MS12012028

Date: 12 January 2020

processing Titanium (Ti6Al4V) using Diode Area Melting 2.0 (DAM 2.0)

Location: C05, The Royal Exchange Building
<b>Overall risk rating = Low</b>
Summary: <ol style="list-style-type: none"> <li>1. Purging argon in the chamber.</li> <li>2. Selective scanning of the powder bed using a 450 nm, 4W diode laser.</li> <li>3. Elimination of differential pressure gradient from the chamber, if any.</li> <li>4. Cleaning up the chamber.</li> </ol>

<b>Detailed description of task and work practice information:</b>			
<ol style="list-style-type: none"> <li>1. The chamber would be purged with argon after the atmospheric air is expelled using a vacuum pump. The argon gas cylinder should be handled by an individual trained in gas cylinder handling.</li> <li>2. After the chamber has been purged with argon, the powder would be wiped on to the levelled powder bed, after which a diode laser (808 nm, 4.5 W) would selectively scan the powder bed, melting the metal powder. The laser system should be handled by an individual who has cleared the online laser safety training of the university.</li> <li>3. Upon successful completion of selective scanning of the metal powder, i.e. completion of the fabrication of the component, the lasers are turned off, the wipers and pistons are returned to the 'home' position. The pistons are allowed to cool down.</li> <li>4. The differential pressure in the chamber would be eliminated by using the pressure release valve. The chamber would then be opened.</li> <li>5. The residual powder would be scooped up into containers using a spoon. After the majority of the powder has been scooped up, the residual material would be scrubbed clean using isopropyl alcohol.</li> </ol>			
<b>Hazard information:</b>			
Commercial name of substance(s):		1. Ti6Al4V powder, Renishaw powder (15-45 µm)	
Supplier details:		Carpenter Technology Corporation 1735 Market Street, 15th Floor Philadelphia, PA 19103 United States Tel: +1 610-208-2000	
Hazardous substances in use/contained within products used: (include any available workplace exposure limits from EH40/2005)		<b>Substances</b>	
		<ol style="list-style-type: none"> <li>1. Titanium (85 – 95%) CAS: 7440-32-6</li> <li>2. Aluminium (5 – 7%) CAS: 7429-90-5</li> <li>3. Vanadium (3 – 5%) CAS: 7440-62-2</li> </ol>	
<b>Associated risk phrases:</b>			
H334	May cause allergy/asthma/breathing difficulties if inhaled	H351	May cause cancer in the lungs
H317	May cause allergic skin reaction	H372	Causes damage to respiratory tract and lungs
H280	Contains gas under pressure	H330	Fatal if inhaled
Supplier material safety data sheet (MSDS) available?		Yes	
<b>HAZARD RATING:</b>		Medium	
<b>Exposure information:</b>			
Physical form of substance:		<ol style="list-style-type: none"> <li>1. Powder</li> <li>2. Gas</li> </ol>	
Approximate amount of material used (per working day):		<ol style="list-style-type: none"> <li>1. 1 kg</li> <li>2. 20 L</li> </ol>	
Who might be exposed to the hazardous substance(s):		Operator(s)	
Potential routes of exposure:		<ol style="list-style-type: none"> <li>a. Inhalation</li> <li>b. Dermal</li> </ol>	
Potential consequences of exposure:		<ol style="list-style-type: none"> <li>a. Bronchial irritation</li> <li>b. Potential allergic skin reaction</li> </ol>	

Approximate daily duration of exposure:	
<input type="checkbox"/> Less than 30 mins	<input type="checkbox"/> 30 mins – 1 hr
<input type="checkbox"/> 2 – 4 hrs	<input type="checkbox"/> 4 – 8 hrs
	<input checked="" type="checkbox"/> 1 – 2 hrs
	<input type="checkbox"/> More than 8 hrs
Location of task:	
<input type="checkbox"/> Outside	<input type="checkbox"/> Inside – poorly ventilated
<input type="checkbox"/> Confined space	<input checked="" type="checkbox"/> Inside – well ventilated
<input type="checkbox"/> Other: please specify	
Any additional activities that could increase exposure potential (such as maintenance):	NA
Any at-risk groups or individuals to be aware of:	NA
<b>POTENTIAL EXPOSURE RATING:</b>	Low
Hierarchy of control measures:	
Can the substance be eliminated or a less hazardous alternative used? (if not, explain why)	No (the choice of material is important for the results expected from the experiment)
Existing engineering controls:	
Personal Protective Equipment:	
<input type="checkbox"/> Eye/face protection? (state type/class required)	<input checked="" type="checkbox"/> Protective gloves? (State type/class required)
	
<input checked="" type="checkbox"/> Protective clothing? (state type/class required)	<input checked="" type="checkbox"/> Masks/respirators? (3M 6898 with A1 filters)
	
Details of instruction / information / training provided to employees:	1. Lab induction to get access to the facility 2. Gas cylinder training to handle argon cylinders 3. Laser training to handle diode laser(s)
Other control measures:	1. Oxygen sensor to be kept inside the chamber to monitor the oxygen levels. The lab has oxygen sensors as well to ensure safe oxygen amounts in the working environment.
Details of any exposure monitoring:	NA
Details of any health surveillance required:	NA
Other precautions and emergency procedures:	
Any specific storage precautions (include quantities held on site):	NA
Any specific release, spillage, fire or disposal precautions:	1. Dust clouds should be avoided 2. Avoid moisture and humid environment
<b>RESIDUAL EXPOSURE RATING:</b>	Low
<b>OVERALL RISK RATING (hazard rating x resid. exposure rating) =</b>	

Any further action required:		No	
Assessed by:	Sarath Alayil Veetil	Reviewed by:	Dr Kamran A Mumtaz
Date assessed:	12/01/2020	Date reviewed:	12/01/2020
Review before:	12/01/2022	Next review:	12/01/2022

\*\*\*\*